ISSN 2475-742X (Print)
ISSN 3066-2427 (Online)

CPSS Transactions on Power Electronics and Applications

VOLUME 10 NUMBER 2 JUNE 2025

REGULAR PAPERS

A PUBLICATION OF THE CHINA POWER SUPPLY SOCIETY

CPSS Transactions on Power Electronics and Applications

CPSS Transactions on Power Electronics and Applications (CPSS TPEA) is sponsored and published by China Power Supply Society and technically co-sponsored by IEEE Power Electronics Society. It publishes original and high quality peer reviewed papers in the field of power electronics and its applications. With the goal of promoting the technology of power electronics including concepts, theory, modeling and control, analysis and simulation, emerging technology and applications, CPSS TPEA is expected to be a favorable platform to strengthen information exchange in this area. Interested authors are welcome to submit your papers via the Manuscript Central (https://mc03.manuscriptcentral.com/tpea-cpss) online submission system. You can find more information on our website: http://tpea.cpss.org.cn.

Hardware Implementation of Sudoku, Optimal Sudoku, Sky-Scrapper, Novel Shade Dispersion and Magic Matrix Shifting PV Reconfiguration Techniques With MPPT Algorithm to Enhance Maximum Power

Vinaya CHAVAN, Suresh MIKKILI, and Gaurav KUMAR

***Abstract*—This research paper investigates the performance of reconfiguration methods by integrating the MPPT algorithm. This study examines the performance of various PV array reconfiguration techniques based on power extraction, efficiency, and reliability. The effectiveness of reconfiguration methods has been evaluated through simulation, followed by hardware experimentation under partial shading cases. The methodology involves implementing and testing conventional TCT and other physical PV array reconfiguration methods by integrating the P&O MPPT algorithm with each reconfiguration method, and the performance of the combined system is evaluated under voltage and current curves, power extraction, MPPT tracking efficiency, and % steady state oscillations. Hardware experiments validate the proposed approach using a PV system prototype.**

***Index Terms*—Maximum power point, novel shade dispersion and magic matrix shifting PV reconfiguration techniques, optimal Sudoku, shading conditions, sky-scrapper, Sudoku.**

I. Introduction

THE photovoltaic (PV) system is a potential renewable energy technology for electricity production. However, solar radiation, temperature, and partial shade may substantially impact their effectiveness. Due to the difference in power output between shaded and unshaded modules within a PV array, partial shading circumstances, in particular, may result in significant power losses.

Different strategies have been devised to minimize the negative impacts of partial shade and improve the power generation from PV arrays. Reconfiguration is one solution to enhance power extraction through shade dispersion. Under shading circumstances, using MPPT tends to make the PV system work at its maximum power point (MPP). The Perturb and Observe (P&O) algorithm is a popular MPPT algorithm for its efficiency, simplicity, and compatibility. The static reconfiguration approach includes reconfiguring the panel position of PV modules to distribute shade.

MPPT algorithms significantly increase the efficiency of PV systems by continuing to monitor and maintain the PV array's MPP. The researcher discusses various MPPT methods, like input variables based on conventional MPPT methods, intelligent MPPT methods, optimization-based MPPT methods and hybrid MPPT methods by combining two or more MPPT methods. The performance of MPPT integration is compared based on their tracking speed, control of external variations, power efficiency, algorithm complexity, implementation cost, etc. [1]−[2]. The MPPT system extracts the maximum obtainable power by adjusting the operating point to ensure maximum energy extraction, compensating for changes in temperature, shading, and other environmental factors. The P&O algorithm is comprehensively researched and employed to track maximum power in PV systems.

The research in [3] combines fractional short-circuit current measurement with the P&O technique to enhance the accuracy and efficiency of MPPT. It offers improved tracking performance and eliminates the need for additional sensors to develop a cost-effective solution for PV systems. Authors in [3] introduce an improved adaptive P&O method focusing on enhancing the performance of the power tracking by incorporating adaptive step size and modified perturbation strategies. It aims to achieve faster and more efficient MPPT under varying environmental circumstances. [4] explores the integration of an improved P&O algorithm with artificial bee colony optimization to enhance the P&O method's effectiveness in tracking the extreme power under shading situations. The research in [5] aims to assess the impact of PSC on the P&O algorithm's performance and provides insights into mitigating cross-coupling effects for efficient MPPT operation in PV systems. Therefore, this P&O method has been selected for research.

The PV array reconfiguration static and dynamic reconfiguration approaches for mitigating partial shading influence

Manuscript received January 02, 2024; revised June 26, 2024 and January 21, 2025; accepted March 06, 2025. Date of publication June 30, 2025; date of current version April 18, 2025. This work was supported in part by Science and Engineering Research Board, Department of Science and Technology, Ministry of Science and Technology, India under the grant EEQ/2021/000294.
(Corresponding author: Suresh Mikkili.)

V. Chavan is with the Department of Electrical Engineering, AMGOI Vathar Tarf VTarfon, Maharashtra, India (e-mail: chavanvinaya19@gmail.com).

S. Mikkili and G. Kumar are with the Department of Electrical and Electronics Engineering, National Institute of Technology Goa, India (e-mail: mikkili.suresh@nitgoa.ac.in; gauravkumar@nitgoa.ac.in).
Digital Object Identifier 10.24295/CPSSTPEA.2025.00013

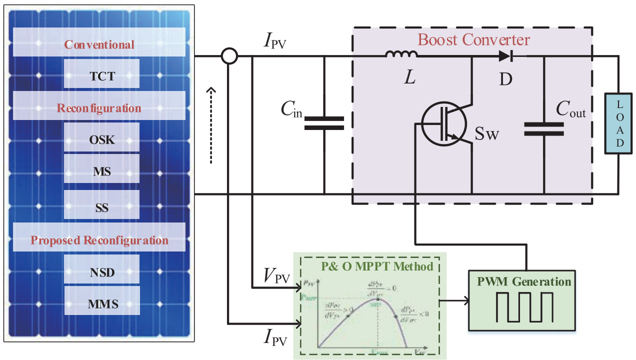

Fig. 1. The architecture of the PV array reconfiguration with MPPT.

process pertain to modifying the spatial arrangement of photovoltaic modules in an array [6]. It can be done electrically or physically. The number of modules and configuration depend on the desired system capacity and available space. There are various sensor-less PV array reconfiguration methods like shifting-based reconfiguration, Sudoku (SK) [6] optimal Sudoku (OSK) [7], [8] improved versions of Sudoku methods [9]−[11] square puzzle-based reconfigurations, dominance square (DS) [12], competence square (CS) [13] magic square puzzle based [14] and other reconfigurations, skyscraper reconfiguration (SS) Lo Shu technique [15] recently proposed reconfigurations[11], [16], [17], novel shade dispersion method (NSD) [18], [19], magic matrix shifting (MMS) [20] etc. The above-mentioned concept presents many potential advantages, including optimizing energy generation by redistributing the shading effect. For conventional configuration, conventional MPPT fails under partial shading conditions. Therefore, in recent years, reconfiguring a PV array by integrating the MPPT algorithm with an available PV system has attracted substantial interest in improving power extraction under partial shade situations.

This work has focused on designing and optimizing reconfiguration circuits, creating control algorithms, and assessing reconfigured PV system performance when connected to MPPT under various shading patterns.

The research objective is to investigate the performance of the conventional TCT configuration and static PV array reconfiguration techniques when integrated with perturb and observe the P&O MPPT algorithm. The study aims to evaluate the effectiveness of different static reconfiguration techniques in enhancing the power output and the effect of reconfiguration on the performance of the P&O MPPT algorithm. The results of this research will help to understand how to effectively use static PV array reconfiguration strategies for maximizing power extraction efficiency in actual applications.

This work proposed two novel methods (MMS and NSD) to reconfigure the 4×4 PV array to extract the maximum power under partial shading conditions. The novelty of work is:

1. Dynamic performance of reconfiguration has been examined through hardware implementation validation and analysis of I-V and P-V curves for all considered reconfiguration

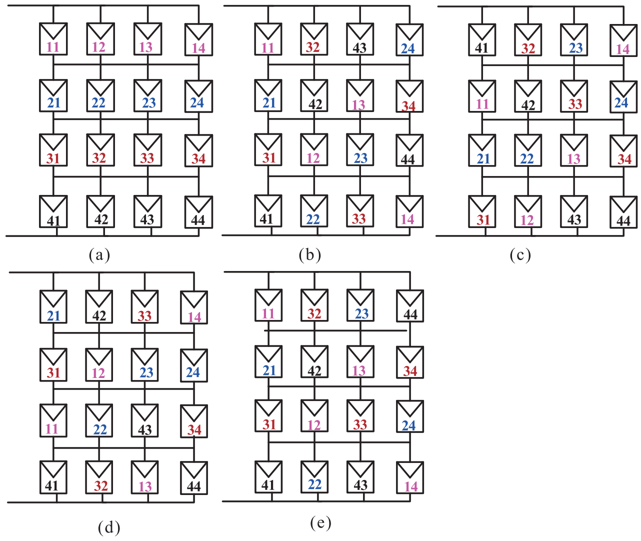

Fig. 2. PV array topology under Case-I shading condition. (a) TCT, (b) OSK, (c) SS, (d) NSD, (e) MMS.

methods.

2. This work is implemented using the 8-bit AVR microcontroller, which is an effective solution for practical implementation compared to other microcontrollers like DSP or FPGA.

II. Modeling of PV System

Fig. 1 shows the reconfigured PV array with the MPPT algorithm to provide the pulse to boost converter which transfers power to the load. MPPT optimizes the power output of the PV module. This paper focuses on the various techniques used in a PV array reconfiguration with different shading conditions that integrate the MPPT algorithm.

A. Reconfiguration of Photovoltaic Array

In this paper, a sensor-less PV array reconfiguration has been deliberated. Panels are exchanged according to OSK, SS, and the recently proposed MMS reconfiguration. For comparison, the proposed methods with a conventional TCT configuration have been used. The panel position for all the methods is shown in Fig. 2. Table I contains the comparison and required formula for MPPT integration. For NSD and MMS reconfiguration, algorithms are given below:

Step 1: Submatrix Dimensions (NSD and MMS)

m *is* number of rows, n is number of columns, and a *is* total number of elements such that $a = m \times n$.

Thus, the matrix M is an $m \times n$ matrix.

Initially, $M_{i,j}$=0,

Where, $1 \leqslant i \leqslant m$ and $1 \leqslant j \leqslant n$

For NSD: $m < n$

For MMS: $m > n$

Step 2: Filling the submatrix (NSD and MMS):

Start at the first position $M_{1,1}$ and begin placing numbers from 1 to a, incrementing the row and column indices. Feed-forward rule: After placing number k in position $M_{i,j}$,

TABLE I
COMPARASION OF VARIOUS RECONFIGURATION WITH MPPT INTEGRATION

Array Topology	Theoretical Basis	Key Formulas	Reconfiguration with MPPT Integration
TCT	Interconnects PV modules in a mesh-like structure to improve current sharing and reduce mismatch losses.	Current sharing: $I_{\text{tied}}=\frac{\sum_{k=1}^{n} I_k}{n}$ Voltage remains constant: $V_{\text{tied}}=V_{\text{module}}$	Total array power is: $P_{\text{array}}=I_{\text{tied}}\times V_{\text{tied}}$ MPPT adjusts for optimal power: $\eta_{\text{MPPT}}=\frac{P_{\text{MPP}}}{P_{\text{array}}}$
OSK	Ensures a unique arrangement of PV modules to minimize mismatch losses and balance power under fixed shading conditions.	Minimize mismatch loss: $L=\sum_{i=1}^{m}\sum_{j=1}^{n}(P_{\text{avg}}-P(i,j))^2$	The total array power is calculated as: $P_{\text{array}}=\sum_{i=1}^{m}\sum_{j=1}^{n}P(i,j)$ MPPT ensures: $\eta_{\text{MPPT}}=\frac{P_{\text{MPP}}}{P_{\text{array}}}$
SS	Maximizes visibility of PV modules to sunlight by placing taller or unshaded modules in strategic positions.	Maximize visibility: $P_{\text{visible}}=\sum_{i,j}Visible(i,j)\times P(i,j)$	Visibility impacts total power: $P_{\text{array}}=P_{\text{visible}}$ MPPT adjusts to optimize power as: $\eta_{\text{MPPT}}=\frac{P_{\text{MPP}}}{P_{\text{array}}}$
NSD	The submatrix structure equalize the row currents. Modules are repositioned physically, and shading is dispersed logically within a column.	Row current equalization: $I_{\text{row}}=\frac{\sum_{i=1}^{n} I_{i,j}}{n}$ Achieves logical shifting of rows to satisfy magic constant 21 for 2×3 submatrix structure	The total array power is calculated as: $P_{\text{array}}=\sum_{i=1}^{m}\sum_{j=1}^{n}P_{\text{Reconfigured } i,j}$ MPPT extracts maximum power by dynamically tracking: $\eta_{\text{MPPT}}=\frac{P_{\text{MPP}}}{P_{\text{array}}}$
MMS	The submatrix-based approach uses logical shifts and horizontal folds (HF) to reposition PV modules.	Submatrix formation: $m\times n=a$ where a is the total matrix size. Row current equalization is achieved using submatrix shifts to satisfy the magic number	After reconfiguration, power is: $P_{\text{array}}=\sum_{i=1}^{m}\sum_{j=1}^{n}P_{\text{Reconfigured } i,j}$ MPPT ensures maximum power extraction: $\eta_{\text{MPPT}}=\frac{P_{\text{MPP}}}{P_{\text{array}}}$

place number k+1 in the next row and next column. If $m < n$ when placing the next number after filling a column, skip one column. Position for number k: Let k be the number to be placed,
where, $1 \leqslant k \leqslant a$

For each k value update the row and column indices as:

$$i_k=\left|\frac{k-1}{n}\right|+1, \tag{1}$$

$$j_k=k-1 \mod n+1 \tag{2}$$

Step 3: Skipping columns (NSD and MMS) (*if m < n*)

If $m < n$, then after filling the matrix by moving to the next column, we skip one column.

If $j_k \geqslant n$, then instead of moving to j_k+1, we place the next number in j_k+2.

$$j_k=\begin{cases} j_k+1 & \text{if } j_k<n \\ j_k+2 & \text{if } j_k\geqslant n \end{cases} \tag{3}$$

Step 4: Matrix Completion

We continue placing numbers from $k = 1$ to $k = a$.

B. Maximum Power Point Tracking (MPPT) Algorithm

The P&O MPPT involves introducing perturbations to the voltage or current during operation, in the P-V curve of the solar panel, at maximum power, the slope of the curve is zero ($\frac{dP_{\text{PV}}}{dP_{\text{PV}}}=0$). The real-time measurement of the voltage and current of the PV panel is done to calculate the slope of the curve. Changes in the power (ΔP_{PV}) and voltage (ΔV_{PV}) are calculated using (4) and (5):

$$\Delta P_{\text{PV}}=P_{\text{current}}-P_{\text{previous}} \tag{4}$$

$$\Delta V_{\text{PV}}=V_{\text{current}}-V_{\text{previous}} \tag{5}$$

The decision of duty ratio change of the boost converter is made by calculating the slope and region of the P-V curve. If ΔP_{PV} is greater than zero and $\Delta V_{\text{PV}}>0$, V_{PV} will increase by ΔV_{step}. If $\Delta V_{\text{PV}}<0$, V_{PV} will reduced by ΔV_{step}. If ΔP_{PV} is less than zero and $\Delta V_{\text{PV}}>0$, V_{PV} will decrease by ΔV_{step} to achieve MPP. If $\Delta V_{\text{PV}}<0$, V_{PV} will increased by ΔV_{step} to achieve MPP. The converter output voltage depends on the duty cycle of the converter. For the boost converter, if the duty cycle is increased then, the output voltage will reduced. In order to transfer the maximum power from PV to load, the load impedance and source impedance should be equal. To match the impedances, a boost converter is used between the source and load.

$$Z_{\text{in}}=(1-d)^2 Z_{\text{out}} \tag{6}$$

where Z_{in} is the input impedance of the boost converter d is the duty ratio of the converter switching pulse applied to the switch, and Z_{out} is the output impedance of the converter. It is observed from (6) that input impedance depends on the duty cycle.

The sensors sense the voltage and current of PV, and the processed signal is given to the ADC (10-bit) of the AVR microcontroller calculates the output power P_{PV}, and compares it

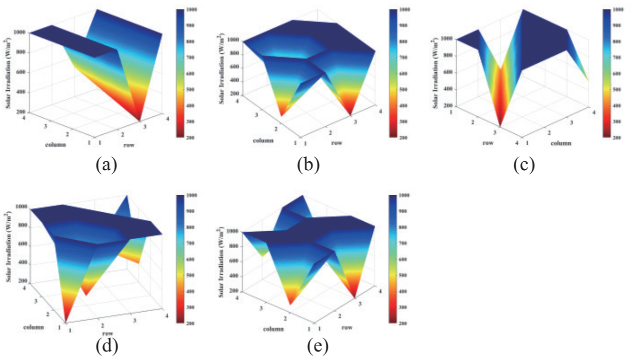

Fig. 3. Case-I shading condition and shade dispersion for (a) TCT, (b) OSK, (c) SS, (d) NSD, (e) MMS.

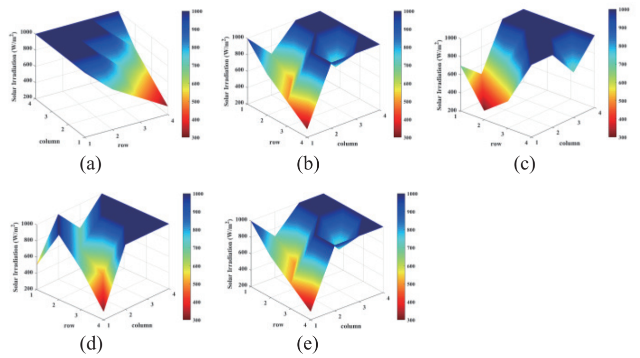

Fig. 5. Case-III shading condition and shade dispersion for (a) TCT, (b) OSK, (c) SS, (d) NSD, (e) MMS.

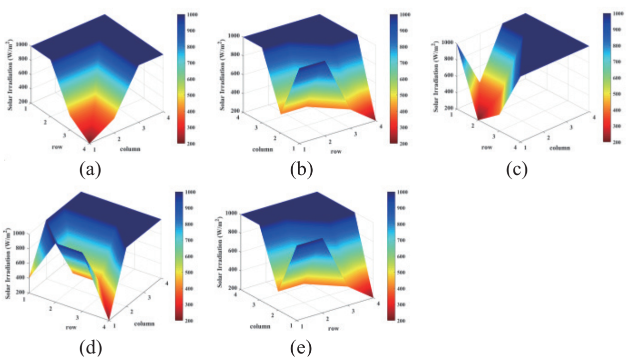

Fig. 4. Case-II shading condition and shade dispersion for (a) TCT, (b) OSK, (c) SS, (d) NSD, (e) MMS.

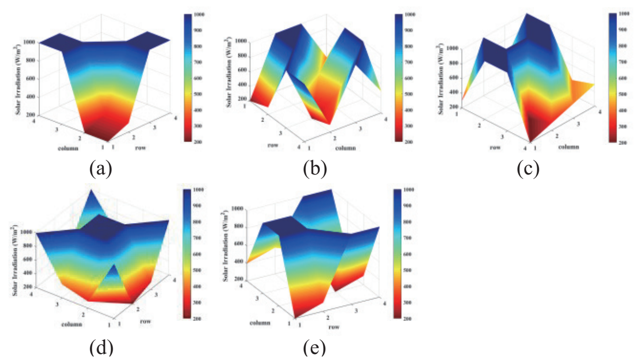

Fig. 6. Case-IV shading condition and shade dispersion for (a) TCT, (b) OSK, (c) SS, (d) NSD, (e) MMS.

to $P_{previous}$. Suppose that $P_{current} > P_{previous}$, the PWM duty cycle is raised to maximize PV panel power. If $P_{current}$ is smaller than $P_{previous}$, the duty cycle is lowered to restore extreme capacity.

C. DC-DC Converter

DC-DC converters reconfigure the PV module connections and voltage levels within the array. These converters enable optimal power transfer by adapting the voltage and current levels to match the load impedance to the source impedance to transfer the maximum power from source to load.

Overall, the PV array reconfiguration with MPPT system architecture aims to maximize the energy output of the PV array by dynamically optimizing the module connections and adjusting the operating point to track the MPP under varying environmental conditions.

III. Partial Shading Conditions and Shade Pattern

In PV array reconfiguration, specific shading conditions such as Case-I, Case-II, Case-III, and Case-IV are selected to evaluate and optimize system performance under various real-world scenarios. Case-I shading simulates typical shadows from horizontal obstructions like buildings and trees, while Case-II shading assesses edge effects and performance impacts from shadows at array corners. Case-III shading represents irregular shading patterns from non-uniform obstructions, and Case-IV shading simulates unpredictable, real-world shading from clouds, debris, and temporary obstructions. These real-world shading conditions improve the PV array to minimize the mismatch power loss, hence improving efficiency.

This paper considers four realistic shading conditions. First is Case-I, shown in Fig. 3, which has five irradiance levels: 200 W/m^2, 300 W/m^2, 400 W/m^2, 500 W/m^2, and 1000 W/m^2. Second Case-II shading in Fig. 4 has three levels of irradiation: 200 W/m^2, 400 W/m^2, and 1000 W/ m^2.

Case-III shade condition consists of four irradiance levels: 300 W/m^2, 500 W/m^2, 700 W/m^2, and 1000 W/m^2, and RM PSC with five irradiance levels: 200 W/m^2, 300 W/m^2, 400 W/m^2, 500 W/m^2 and 1000 W/m^2. In Fig. 3 to Fig. 6(a), subfigures portray the PSC for TCT configuration and (b), (c), (d), and (e). Gives the shade dispersion for OSK, SS, NSD, and MMS methods for considering four shading cases.

The performance of the reconfiguration is investigated with the P&O MPPT method based on power tacked by the MPPT algorithm, % tracking efficiency of the MPPT algorithm, and steady-state power oscillations in percent. The performance is investigated and discussed in section four.

IV. Results and Discussion

The performance of various panel placement topologies

TABLE II
MPPT ALGORITHM PERFORMANCE FOR DIFFERENT PV ARRAY TOPOLOGIES UNDER SHADE CASE-I

Array Topology	GMPP at STC	V_{oc}	I_{sc}	V_{mp}	I_{mp}	P_{mp}	V_{mppt}	I_{mppt}	P_{mppt}
TCT	40	29.17	1.86	17.23	1.66	28.67	23.44	0.90	21.11
OSK	40	29.04	1.62	24.24	1.37	33.14	25.49	1.31	32.30
SS	40	29.17	1.62	24.35	1.31	31.78	21.73	1.35	29.25
NSD	40	29.17	1.58	24.12	1.35	32.63	25.43	1.21	30.85
MMS	40	29.04	1.62	24.24	1.37	33.14	24.49	1.35	32.49

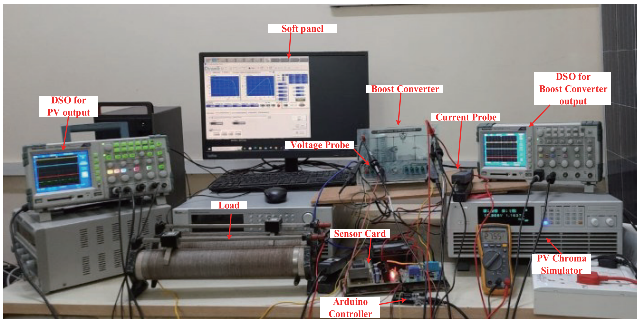

Fig. 7. Experimental prototype to evaluate the performance of reconfiguration techniques.

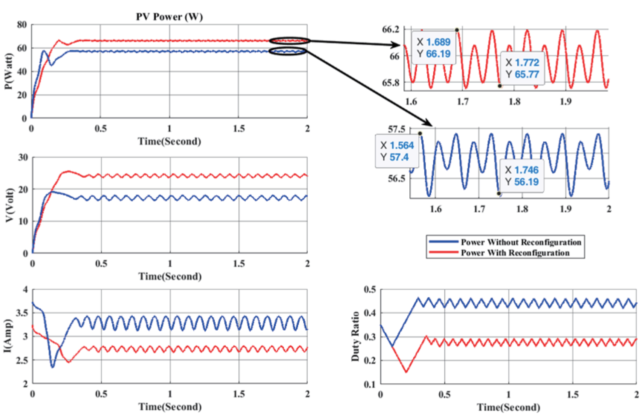

Fig. 8. Simulated PV system power, voltage, and current for conventional TCT and OSK, SS, and MMS reconfiguration methods with P&O MPPT under Case-I shading.

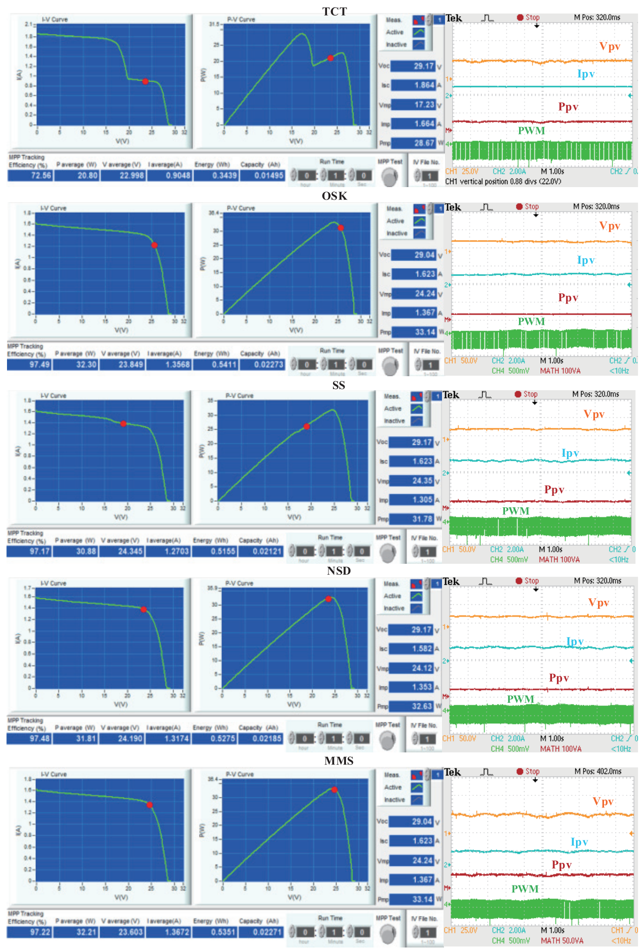

Fig. 9. Experimental result under Case-I shading condition for TCT connection, OSK, SS, NSD, and MMS reconfiguration.

named TCT, OSK, SS, NSD, and MMS has been investigated with conventional P&O MPPT under PSC. The performance is analyzed in both MATLAB simulation and real-time hardware implementation as shown in Fig. 7.

The tests are carried out using a PV panel with an operational voltage of 6 V±5%, an operating current of 833 mA±5%, and an open circuit voltage of 7 V±5%, and a short circuit current of 916 mA±5%. It is used for PV chroma, with the highest PV power on Chroma solar array simulation soft panel 62000 H series being used for 80 W. Chroma has limitations for current. Therefore, the scaling factor 0.5 is employed, resulting in a short circuit current of 1.83 A and output power of 40 W at STC.

A. PSC-Case-I

As shown in Fig. 8, all the reconfiguration methods work efficiently, and reconfiguration improves by 8.79 with 1% of reduced steady-state oscillations in power output. The corresponding experimental result validation is given in Table II. Fig. 9 shows I-V and P-V curves, and performance evaluation is given in Fig.10. It shows that with MPPT integration, MMS is the best reconfiguration with the highest power tracking efficiency of 97.49%, and output power 32.49 W power and least 4.47% power oscillations.

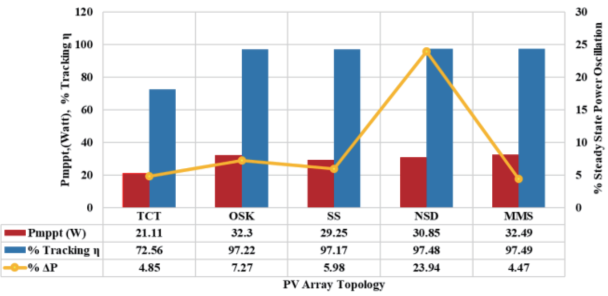

Fig. 10. Performance evaluation under Case-I shade.

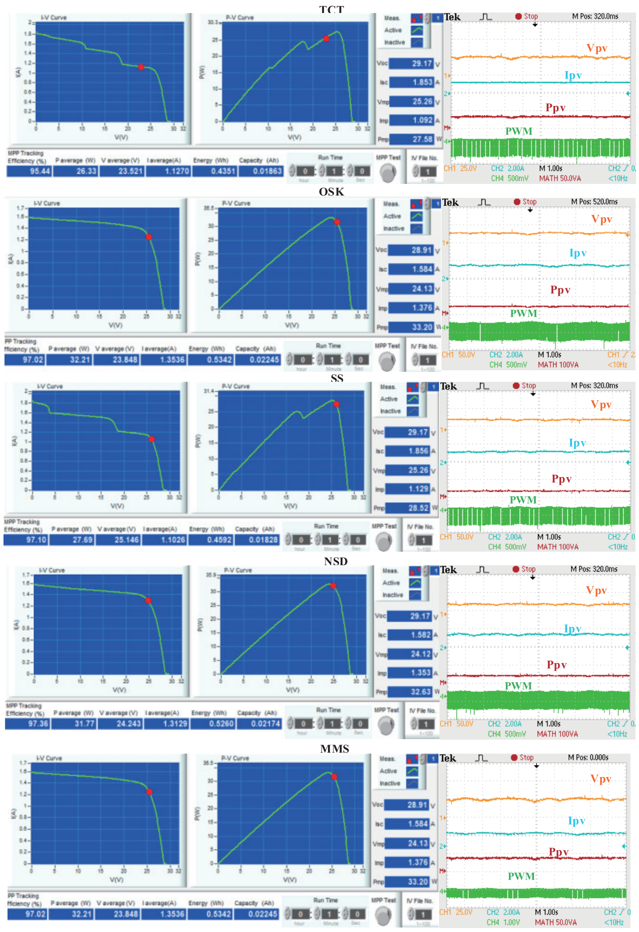

Fig. 11. The experimental result under Case-II shading condition for TCT connection, OSK, SS, NSD, and MMS reconfiguration.

B. PSC-Case-II

The corresponding experimental result validation is given in Table III and Fig. 11. In Fig. 12, simulation results show that under Case-II, MMS and OSK give the highest power of 66 W and the least steady-state power oscillations of 0.2% with the P&O algorithm. For other reconfigurations and TCT, there are 1.3% of steady-state power oscillations and an average of 56.5 W of power generation.

The performance assessment depicted in Fig. 13 reveals that when integrated with MPPT, MMS is the most optimal reconfiguration for power tracking efficiency. This configuration achieves an impressive 32.09 W power output, corresponding to 97.02% efficiency. Additionally, this configuration exhibits the lowest level of power oscillations, at a mere 4.47%.

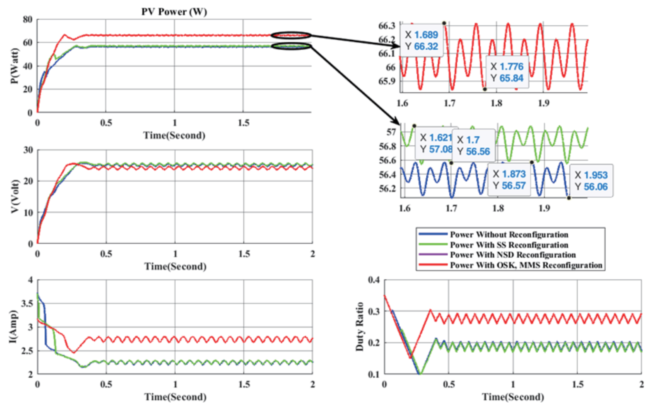

Fig. 12. Simulated power, voltage, and current of PV system for conventional TCT, OSK, SS, NSD, and MMS reconfiguration methods with P&O MPPT under Case-II.

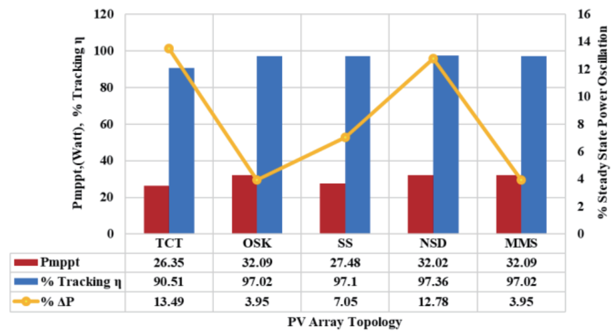

Fig. 13. Performance evaluation under Case-II shade.

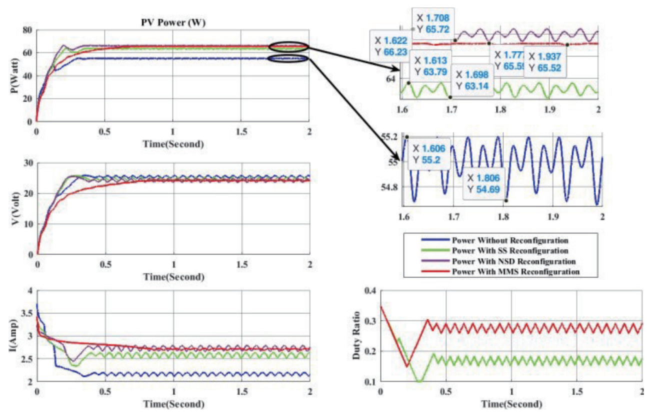

Fig. 14. Simulated PV system power, voltage, and current for conventional TCT and OSK, SS, NSD, and MMS reconfiguration methods with P&O MPPT under Case-III shading.

C. PSC-Case-III

Fig. 14 shows the simulation results under Case-III, with P&O power point tracking. NSD gives the highest power, oscillating between 65.7 W and 66.23 W. MMS is beside it, giving 65.52 W

TABLE III
MPPT ALGORITHM PERFORMANCE FOR DIFFERENT PV ARRAY TOPOLOGIES UNDER SHADE CASE-II

Array Topology	GMPP at STC	V_{oc}	I_{sc}	V_{mp}	I_{mp}	P_{mp}	V_{mppt}	I_{mppt}	P_{mppt}
TCT	40	29.17	1.85	25.26	1.09	27.58	25.24	1.09	26.35
OSK	40	28.91	1.58	24.13	1.38	33.20	25.20	1.27	32.09
SS	40	29.17	1.86	25.26	1.13	28.52	25.95	1.06	27.48
NSD	40	29.17	1.58	24.12	1.35	32.63	24.69	1.31	32.02
MMS	40	28.91	1.58	24.13	1.38	33.20	25.20	1.27	32.09

Fig. 15. Experimental result under Case-III shading condition for TCT connection, OSK, SS, NSD, and MMS reconfiguration.

tracked power with negligible oscillations. Fig. 15 shows the experimental results with I-V and P-V curves. Fig. 16 and Table IV give the experimental result validation on the 40 W system.

The analysis presented in Fig. 16 demonstrates that when the PV system is combined with MPPT integration, OSK and MMS reconfiguration attain a notable power output of 32.16 W, corresponding to an efficiency of 97.58%. Moreover, the MMS configuration maintains power stability with the most minor power oscillations at 3.99%.

D. PSC-Case-IV

In Fig. 17, simulation results show that under Case-IV, MMS

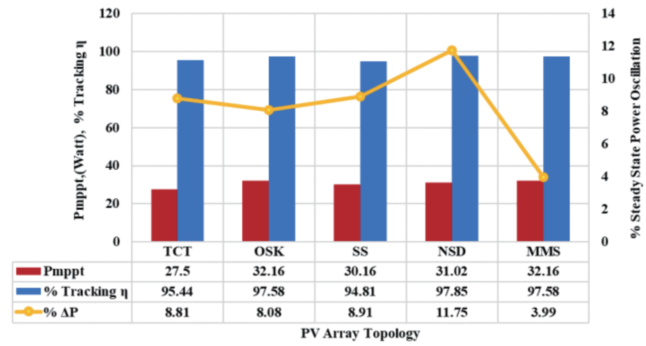

Fig. 16. Performance evaluation under Case-III shade.

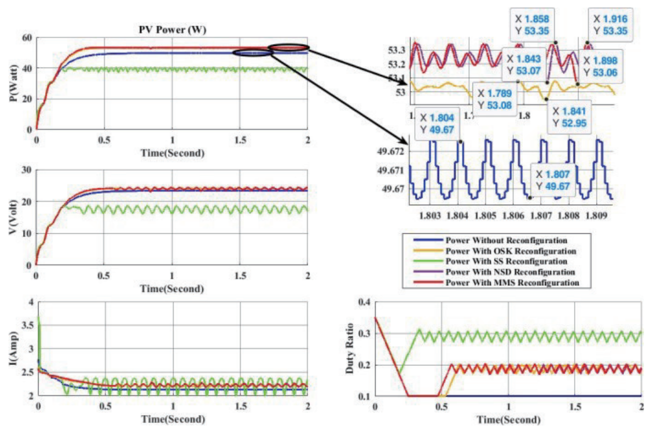

Fig. 17. Simulated PV system power, voltage, and current for conventional TCT and OSK, SS, NSD, and MMS reconfiguration methods with P&O MPPT under Case-IV shading.

and NSD give the highest power of 53 W and the least steady state power oscillations with the P&O algorithm.

The corresponding experimental result validation is given in Table V, Fig. 18, and Fig. 19. It shows that for MMS reconfiguration P&O, the MPPT algorithm gives the uppermost power tracking efficiency of 97.8%, providing 25.56 W power with the lowest 4.91% steady state power oscillations.

V. CONCLUSION

In this paper, the performance of newly proposed reconfigurations (NSD&MMS), shifting-based reconfiguration (OSK), puzzle-based reconfiguration (SS), and conventional configuration (TCT) have been investigated with the integra-

TABLE IV
MPPT ALGORITHM PERFORMANCE FOR DIFFERENT PV ARRAY TOPOLOGIES UNDER SHADE CASE-III

Array Topology	GMPP at STC	V_{oc}	I_{sc}	V_{mp}	I_{mp}	P_{mp}	V_{mppt}	I_{mppt}	P_{mppt}
TCT	40	29.17	1.09	25.26	1.09	27.58	22.76	1.13	27.50
OSK	40	29.17	1.71	24.12	1.36	32.80	24.30	1.35	32.16
SS	40	29.17	1.72	24.57	1.30	31.99	25.47	1.22	30.16
NSD	40	29.04	1.71	24.24	1.36	32.85	25.56	1.21	31.02
MMS	40	29.17	1.71	24.12	1.36	32.80	24.30	1.35	32.16

TABLE V
MPPT ALGORITHM PERFORMANCE FOR DIFFERENT PV ARRAY TOPOLOGIES UNDER SHADE CASE-IV

Array Topology	GMPP at STC	V_{oc}	I_{sc}	V_{mp}	I_{mp}	P_{mp}	V_{mppt}	I_{mppt}	P_{mppt}
TCT	40	28.63	1.39	24.57	1.04	25.50	24.41	1.04	25.43
OSK	40	28.63	1.30	24.12	1.10	26.58	23.82	1.11	26.40
SS	40	28.63	1.85	17.58	1.15	20.15	19.06	0.89	15.96
NSD	40	28.63	1.29	24.12	1.11	26.70	24.58	1.07	26.36
MMS	40	28.63	1.29	24.12	1.11	26.70	22.15	1.15	25.56

Fig. 18. Experimental result under Case-IV shading condition for TCT connection, OSK, SS, NSD, and MMS reconfiguration.

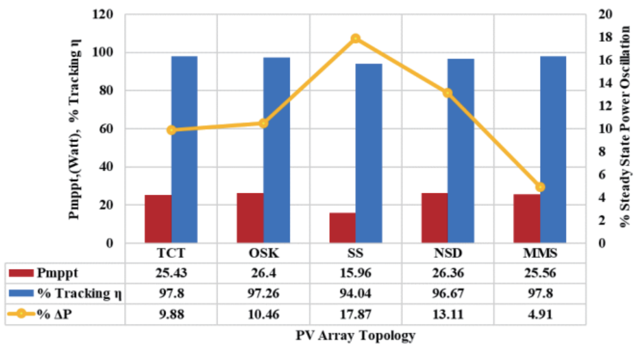

Fig. 19. Performance evaluation under Case-IV shade.

tion of traditional P&O MPPT under PSC on 4×4 PV array structures. The effectiveness of the proposed reconfiguration is evaluated through both simulation studies followed by experimental studies under complex PSCs in terms of tracked GMPP, tracking efficiency, and percent steady state power oscillations around MPP. From the results, it is revealed that the proposed reconfiguration with the conventional P&O MPPT method significantly tracks the GMPP with higher tracking efficiency and also with less steady state oscillation around the GMPP compared to conventional MPPT, which can limit use of filters.

REFERENCES

[1] N. Karami, N. Moubayed, and R. Outbib, "General review and classification of different MPPT techniques," in *Renewable and Sustainable Energy Reviews*, vol. 68, pp. 1–18, Feb. 2017.

[2] M. Mao, L. Cui, Q. Zhang, K. Guo, L. Zhou, and H. Huang, "Classification and summarisation of solar photovoltaic MPPT techniques: A review based on traditional and intelligent control strategies," in *Energy Reports*, vol. 6, pp. 1312–1327, Nov. 2020.

[3] H. A. Sher, A. F. Murtaza, A. Noman, K. E. Addoweesh, K. Al-Haddad, and M. Chiaberge, "A new sensorless hybrid MPPT algorithm based on fractional short-circuit current measurement and P&O MPPT," in *IEEE Transactions on Sustainable Energy*, vol. 6, no. 4, pp. 1426–1434, Oct. 2015.

[4] D. Pilakkat and S. Kanthalakshmi, "An improved P&O algorithm integrated with artificial bee colony for photovoltaic systems under partial shading conditions," in *Solar Energy*, vol. 178, pp. 37–47, Jan. 2019.

[5] S. R. Pendem and S. Mikkili, "Assessment of cross-coupling effects in PV string-integrated-converters with P&O MPPT algorithm under various partial shading patterns," in *CSEE Journal of Power and Energy Systems*, vol. 8, no. 4, pp. 1013–1028, Jul. 2022.

[6] S. Mikkili, K. A. Bapurao, and P. K. Bonthagorla, "Sudoku and optimal Sudoku reconfiguration techniques for power enhancement of partial shaded solar PV system," in *Journal of The Institution of Engineers (India): Series B*, vol. 103, pp. 1793–1807, Jul. 2022.

[7] S. G. Krishna and T. Moger, "Optimal SuDoKu reconfiguration technique for total-cross-tied PV array to increase power output under non-uniform irradiance," in *IEEE Transactions on Energy Conversion*, vol. 34, no. 4, pp. 1973–1984, Dec. 2019.

[8] S. G. Krishna and T. Moger, "Improved SuDoKu reconfiguration technique for total-cross-tied PV array to enhance maximum power under partial shading conditions," in *Renewable and Sustainable Energy Reviews*, vol. 109, pp. 333–348, Jul. 2019.

[9] B. Aljafari, D. S, B. C, P. K. Balachandran, and T. S. Babu, "Power enhanced solar PV array configuration based on calcudoku puzzle pattern for partial shaded PV system," in *Heliyon*, vol. 9, no. 5, May 2023.

[10] A. Kumar and R. Agarwal, "Enhancement of power output of partially shaded photovoltaic system using optimal Sudoku puzzle based triple-tied-cross-link reconfiguration techniques," in *Engineering Research Express*, vol. 5, no. 4, Dec. 2023.

[11] P. R. Satpathy, S. B. Thanikanti, B. Aljafari, N. Nwulu, R. Sharma, and K. Balasubhramanian, "Investigation of multiple Sudoku PV array reconfiguration architectures under partial shading," in *2023 International Conference in Advances in Power, Signal, and Information Technology (APSIT)*, Bhubaneswar, India, 2023, pp. 786–791.

[12] B. Dhanalakshmi and N. Rajasekar, "Dominance square based array reconfiguration scheme for power loss reduction in solar PhotoVoltaic (PV) systems," in *Energy Conversion and Management*, vol. 156, pp. 84–102, Jan. 2018.

[13] B. Dhanalakshmi and N. Rajasekar, "A novel competence square based PV array reconfiguration technique for solar PV maximum power extraction," in *Energy Conversion and Management*, vol. 174, pp. 897–912, Oct. 2018.

[14] M. S. S. Nihanth, J. P. Ram, D. S. Pillai, A. M. Y. M. Ghias, A. Garg, and N. Rajasekar, "Enhanced power production in PV arrays using a new skyscraper puzzle based one-time reconfiguration procedure under partial shade conditions (PSCs)," in *Solar Energy*, vol. 194, pp. 209–224, Dec. 2019.

[15] R. Venkateswari and N. Rajasekar, "Power enhancement of PV system via physical array reconfi guration based Lo Shu technique," in *Energy Conversion and Management*, vol. 215, Jan. 2020.

[16] I. U. Khalil and A. U. Haq, "A modified chess knight reconfiguration approach for mitigating power losses in PV systems," in *Energy Reports*, vol. 11, pp. 2204–2219, Jun. 2024.

[17] V. Narayanaswamy, R. Ayyanar, C. Tepedelenlioglu, D. Srinivasan, and A. Spanias, "Optimizing solar power using array topology reconfiguration with regularized deep neural networks," in *IEEE Access*, vol. 11, pp. 7461–7470, 2023.

[18] V. C. Chavan and S. Mikkili, "Hardware implementation of sensor-less matrix shifting reconfiguration method to extract maximum power under various shading conditions," in *CPSS Transactions on Power Electronics and Applications*, vol. 8, no. 4, pp. 384–396, Dec. 2023.

[19] V. C. Chavan, S. Mikkili, and T. Senjyu, "Experimental validation of novel shade dispersion PV reconfiguration technique to enhance maximum power under PSCs," in *CPSS Transactions on Power Electronics and Applications*, vol. 8, no. 2, pp. 137–147, Jun. 2023.

[20] V. Chavan and S. Mikkili, "Hardware implementation of proposed and conventional PV array reconfiguration techniques to extract maximum power under various shading conditions," in *International Journal of Circuit Theory and Applications*, Jun. 2023.

Vinaya Chavan received the B.Tech. Degree in Electrical Engineering (EE) from Rajaram bapu Institute of Technology, Sakharale, Maharashtra, India 2012. She received an M.E. degree in Electrical Power System Engineering (EPS) from the Government College of Engineering Karad, Maharashtra, India, in 2015. She has completed her PhD Electrical and Electronics Engineering at the National Institute of Technology Goa, India. She works as an assistant professor in the Department of Electrical Engineering at Ashokrao Mane Group of Institutions (AMGOI) Vathar Tarf VTarfon, Maharashtra, India. Her research interests include applications of renewable energy sources, Smart Electric Grid, Power Electronics Applications to Power System.

Suresh Mikkili received an M.Tech. and Ph.D. in Electrical Engineering from the National Institute of Technology, Rourkela, India, in 2008 and 2013. He is currently working as an Associate Professor in the department of EEE at the National Institute of Technology Goa, India. He was the Head of the EEE department at NIT Goa from June 2014 to November 2015 and Dean of Student Welfare at NIT Goa from September 2015 to July 2019. He is serving as a BoG Member and Center Charge of B.Tech Admissions at NIT Goa. His research interests include intelligent electric grids, electric vehicles, grid-connected/stand-alone PV systems, wireless power transfer, power quality issues, and applications of soft computing techniques. He has authored "Power Quality Issues: Current Harmonics," published by the CRC Press, Taylor & Francis Group, August 2015, ISBN 9781498729628. He has reported the results of his research (135+ articles) in reputed international journals (SCI/SCI-E) and at international conferences (Annual/Bi-Annual). Personal link: https://orcid.org/0000-0002-5802-3390, https://nitgoa.irins. org/profile/141228.

Gaurav Kumar is a Ph.D. student in the Electrical and Electronics Engineering Department of the National Institute of Technology, Goa. He completed an M.Tech. Degree in Power Electronics and Power Systems from the National Institute of Technology, Goa, India, in 2017. His research interests include electric vehicles, renewable energy, and DC-DC converters. He achieved the MHRD scholarship during his M.Tech. Degree.

Space Vector Modulation Strategy for Common-Mode Voltage Suppression in the Reduced Switch Count Three-Level Inverter With Unbalanced Neutral-Point Voltages

Zhiyuan CHU, Changwei QIN, Xiaoyan LI, Jingyang FANG, Lei YANG, and Yanling ZHANG

***Abstract*—The reduced switch count three-level inverter (RSC TLI) has been proposed to save the system cost of the conventional three-level inverter. In some special applications, the RSC TLI should be operated with simultaneous lower common-mode voltage (CMV) and unbalanced neutral-point voltage (NPV) conditions. For this reason, this article further proposes a space vector modulation (SVM) strategy that fulfills the above requirements. First, the basic vectors with low CMV amplitudes are selected, and four basic vectors are employed to synthesize the reference vector and achieve NPV flexible control. The duty cycles of the employed basic vectors are obtained by a novel indirect method, and the appropriate switching sequences are designed to further reduce the current harmonic and keep lower switching losses. Finally, the separate control of capacitor voltages is achieved by using a closed-loop control approach to optimally regulate the duty cycles of different basic vectors. Compared with the conventional strategy, the proposed scheme can reduce the CMV magnitude by half and is applicable to unbalanced NPV conditions. The feasibility and effectiveness are verified by experiments.**

***Index Terms*—Common-mode voltage (CMV) suppression, reduced switch count three-level inverter (RSC TLI), space vector modulation (SVM), unbalanced neutral-point voltages (NPVs).**

I. Introduction

DUE to the advantages of low output current harmonics, high efficiency, and low switching voltage stress, multi-level inverters are widely used in medium-voltage applications, such as photovoltaic (PV) power generation, energy storage, and motor drives [1], [2]. Among them, the three-level inverter (TLI) has been attracted much attention because of its high reliability and simple structure [3], [4].

The reduced switch count three-level inverter (RSC TLI) only contains ten switches and still maintains the multi-level output waveform. Compared to the commonly-used neutral-point-clamped (NPC) TLI and T-type TLI, the RSC TLI reduces two switches [5]. However, the output states of the RSC TLI cannot exceed two at the same time owing to the coupling effects of the coupled unit and independent unit [6]. Thus, the modulation strategies of NPC TLI and T-type TLI cannot be directly employed in the RSC TLI.

Being similar with the NPC and T-type TLI, the neutral-point voltage (NPV) of the RSC TLI is commonly kept to be balanced [7]. However, in some particular cases, the NPV should be controlled to be unequal [8], [9]. For example, the voltages across two dc-link capacitors in centralized PV inverter are generally regulated to be different for realizing separate maximum power point tracking (MPPT) of PV arrays [10]. In high-power ac drive systems, two rectifiers are used to improve the power rating, but the output voltages of both rectifiers are likely to be unequal [11]. Unfortunately, the output currents will be distorted by unbalanced NPVs. Many scholars have investigated the above issues. An asymmetric strategy for the separate dc links of TLI was introduced in [12]. Zhang et al. presented an improved vector synthesis strategy, but the computational difficulty was increased [13]. To solve this issue, a simplified pulse width modulation (PWM) strategy was proposed in [14], which reduced the computational difficulty. The virtual space vector modulation (VSVM) strategy was demonstrated to be suitable for both balanced and unbalanced NPVs [15]. To improve the system efficiency, two different discontinuous PWM (DPWM) strategies were investigated [16], [17]. For the NPC three-level rectifier, a zero-sequence component injection method was proposed [18]. However, this method cannot be applied to arbitrary unbalanced NPVs and arbitrary power factor conditions at the same time. In order to suppress the leakage current, a DPWM was proposed in [19]. Unfortunately, above methods cannot be directly employed for RSC TLI since this

Manuscript received November 14, 2024; revised January 28, 2025; accepted March 02, 2025. Date of publication June 30, 2025; date of current version April 18, 2025. This work was supported in part by Taishan Scholar Project of Shandong Province under the Grant tsqn202312223, Natural Science Foundation of Shandong Province under the Grant ZR2024MF039, and Development Plan for Youth Innovation Team of Higher Education Institutions in Shandong Province under the Grant 2023KJ127. (*Corresponding author: Changwei Qin, Xiaoyan Li, and Jingyang Fang*.)

Z.Chu, C. Qin, X. Li, L. Yang, and Y. Zhang are with the School of Information and Electrical Engineering and Shandong Key Laboratory of Smart Buildings and Energy Efficiency, Shandong Jianzhu University, Jinan 250101, China (e-mail: 2022085105@stu.sdjzu.edu.cn; qinchangwei20@sdjzu.edu.cn; xylee2023@sdjzu.edu.cn; 2023080103@stu.sdjzu.edu.cn; zhangyanling19@sdjzu.edu.cn).

J. Fang is with the School of Control Science and Engineering, Shandong University, Jinan 250061, China (e-mail: jingyangfang@sdu.edu.cn).

Digital Object Identifier 10.24295/CPSSTPEA.2025.00010

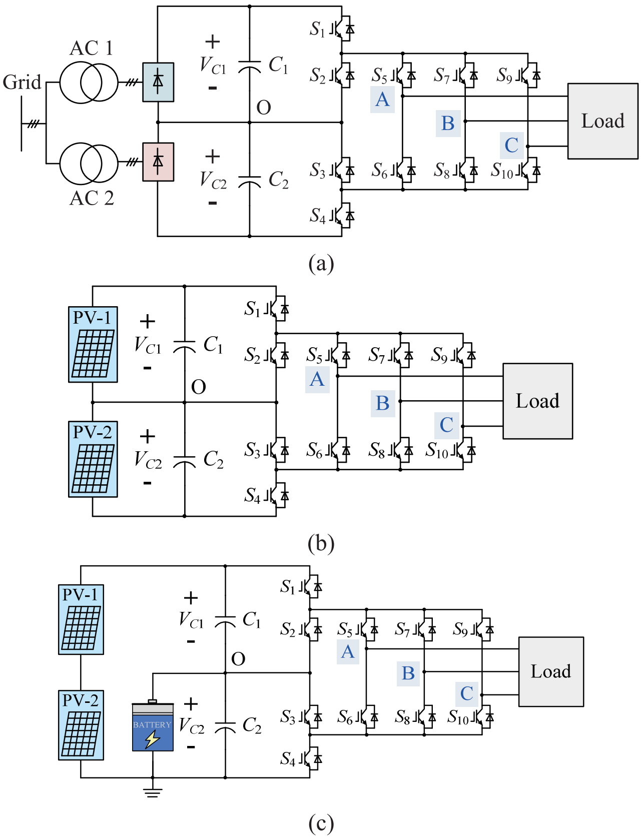

Fig. 1. Three configurations of the RSC TLI with unbalanced NPV conditions. (a) AC drive system. (b) Centralized PV inverter. (c) MPC connected PV–battery hybrid system.

topology is unable to generate medium vectors. For the RSC TLI, an improved virtual SVM (IVSVM) was put forward with unbalanced NPVs, which can enhance the quality of output currents [11]. However, the common-mode voltage (CMV) is very high.

The CMV is generated by the high-frequency action of the switches, which leads to a number of harmful issues. In transformerless PV inverters, the high CMV amplitude triggers the leakage current, which deteriorates the quality of output currents and even threatens the safety of human beings [20]. In motor drive systems, the CMV causes electromagnetic interference (EMI) and generates enormous bearing currents, which decreases the lifetime of the bearings and even damage motors [21].

Presently, the CMV suppression strategies can be categorized into hardware-based and software-based approaches. For hardware-based approaches, the common-mode inductors and common-mode transformers are utilized to suppress the CMV, which however increase the size and volume of the system. Software-based approaches can suppress the CMV only by modifying the modulation strategy, which is a significant benefit. In order to eliminate the CMV of TLI a modulation strategy based on medium and zero vectors was offered in [22], but the dc voltage utilization was decreased. In [23], the large, medium and zero-vector modulation (LMZVM) strategy was presented to reduce the CMV amplitude to one-sixth of dc voltage. Unfortunately, the above two strategies cannot realize active NPV control. Based on [23], a large, medium, small and zero-vector modulation (LMSZVM) strategy was introduced to simultaneously reduce the CMV and control NPV [24]. In [20], a carrier-based PWM (CBPWM) strategy was investigated, which suppressed the CMV with unbalanced NPVs by limiting the range of zero-sequence component. A data-driven strategy for CMV suppression was investigated in [25]. Unfortunately, the strategy requires a large inductor since it is essentially a type of predictive control. An optimal space vector-based hybrid PWM scheme was introduced to simultaneously reduce CMV and line current ripple [26]. However, the output currents of the method are not satisfactory due to discarding the zero vectors [27]. Yan et al. proposed a carrier-based discontinuous SVM (DSVM) method to suppress the CMV [28]. However, this method cannot flexibly regulate the NPV. In addition, a CMV reduction method-based flexible power control was proposed for PV-battery hybrid systems [29].

However, the above modulation strategies are only applicable to the NPC and T-type TLIs. For the RSC TLI, a modulation strategy was suggested in [30], which simultaneously reduced the CMV and controls the NPV balance. However, this method merely considers balanced NPV condition and cannot be applied to unbalanced NPVs.

Aiming at the above-mentioned issues, this article presents a novel SVM strategy for suppressing the CMV in the RSC TLI with unbalanced NPVs. The innovation consists of the following four points.

1) The CMV magnitudes of the basic vectors with unbalanced NPVs are analyzed. The basic vectors with low CMV magnitudes are retained. Meanwhile, this paper reveals the relationship between the basic vectors for the RSC TLI and the dc unbalancing coefficient, and the space vector diagrams (SVD) for different dc unbalancing coefficients are established to suppress the CMV.

2) Based on the established SVD, each sector is further divided into two regions. four basic vectors are optimally selected to synthesize the reference vector in all regions, and a degree of control freedom is provided to flexibly control the capacitor voltages. The duty cycles of the basic vectors are obtained by using an indirect method, and the appropriate switching sequences are designed.

3) The separate control of capacitor voltages is achieved by modifying the duty cycles of the selected basic vectors, and the quality of output currents remains unaffected.

4) In order to validate the feasibility of the presented strategy, extensive experimental tests have been carried out. The obtained results of different modulation indices and dc unbalancing coefficients indicate that the presented strategy can ensure the good waveforms of the output currents. Furthermore, the separate control of capacitor voltages for the proposed strategy can be verified by the short transient process.

This article is outlined as follows: Section II displays the working principle of the RSC TLI with unbalanced NPVs. The proposed modulation strategy is elaborated in Section III. The experimental results are provided in Section IV. Some concluding remarks are given in Section V.

TABLE I
BASIC VECTORS AND CMVS OF THE RSC TLI

Type	Vectors	CMV	Vectors	CMV
Large	[PNN]	$(V_{C1}-2V_{C2})/3$	[NPP]	$(2V_{C1}-V_{C2})/3$
	[PPN]	$(2V_{C1}-V_{C2})/3$	[NNP]	$(V_{C1}-2V_{C2})/3$
	[NPN]	$(V_{C1}-2V_{C2})/3$	[PNP]	$(2V_{C1}-V_{C2})/3$
P-Type Small	[POO]	$V_{C1}/3$	[PPO]	$2V_{C1}/3$
	[OPO]	$V_{C1}/3$	[OPP]	$2V_{C1}/3$
	[OOP]	$V_{C1}/3$	[POP]	$2V_{C1}/3$
N-Type Small	[ONN]	$-2V_{C2}/3$	[OON]	$-V_{C2}/3$
	[NON]	$-2V_{C2}/3$	[NOO]	$-V_{C2}/3$
	[NNO]	$-2V_{C2}/3$	[ONO]	$-V_{C2}/3$
Zero	[PPP]	V_{C1}	[NNN]	$-V_{C2}$
	[OOO]	0		

II. WORKING PRINCIPLE OF THE RSC TLI WITH UNBALANCED NPVS

Two different configurations of the RSC TLI with unbalanced NPV conditions are displayed in Fig. 1(a) and (b), in which two PV arrays or rectifiers are used to implement the separate MPPT control or increase the power rating, and the unbalanced NPV conditions occur. Furthermore, the topology of the multiport dc-ac converter (MPC) connected to PV-battery hybrid system is shown in Fig. 1(c). It can be seen that one of the voltage-dividing capacitors of the RSC TLI is connected to the battery as a new dc port, while the original dc-link remains as the other dc port connected to two PV arrays. The unbalanced NPVs can also occur if the voltage across PV array is not equal to the voltage across the battery. Therefore, the starting point of the proposed strategy is reasonable.

In order to make the analysis easier, the dc unbalancing coefficient φ is expressed as:

$$\varphi = \frac{V_{C1} - V_{C2}}{V_{C1} + V_{C2}} = \frac{V_{\text{diff}}}{V_{\text{dc}}} \tag{1}$$

where V_{C1} and V_{C2} are the voltages across capacitors C_1 and C_2, respectively. V_{diff} is the voltage difference across C_1 and C_2. V_{dc} is the total dc-link voltage.

It can be seen that the dc φ ranges from −1 to 1. From (1), V_{C1} and V_{C2} can be expressed as:

$$\begin{cases} V_{C1} = \dfrac{1+\varphi}{2} V_{\text{dc}} \\ V_{C2} = \dfrac{1-\varphi}{2} V_{\text{dc}} \end{cases} \tag{2}$$

Being similar with the conventional NPC and T-type TLI, the RSC TLI has three output voltage states, as, P, O, and N. Choosing the neutral-point (O) as the reference, the corresponding output voltages are V_{C1}, 0, and $-V_{C2}$, respectively.

The CMV is represented by v_{cm}, which is defined as the average value of three-phase output voltages v_{ao}, v_{bo}, and v_{co} [20], as expressed by (3).

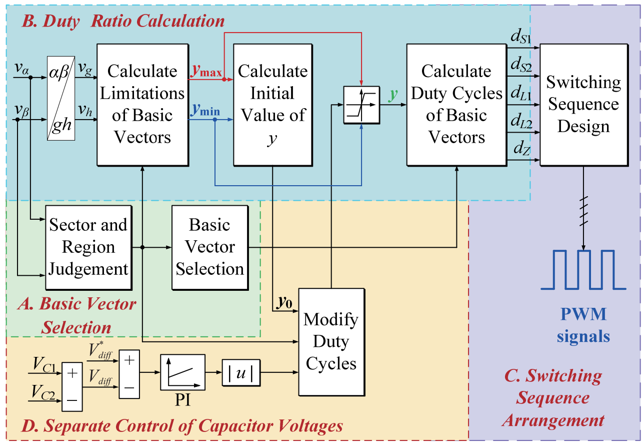

Fig. 2. Control diagram of the proposed strategy.

$$v_{\text{cm}} = \frac{v_{\text{ao}} + v_{\text{bo}} + v_{\text{co}}}{3} \tag{3}$$

Limited by the circuit constraints, the medium vectors in conventional NPC or T-type TLIs cannot be generated, and the conventional SVM strategy cannot be directly applied in the RSC TLI [6]. With the unbalanced NPV conditions, Table I summarizes the CMV of the basic vectors, which are calculated based on (3). It is easy to see that the CMV magnitudes are relatively high for basic vectors in red color. Therefore, the CMV can be suppressed by discarding the basic vectors marked in red color, while the remaining vectors are used to synthesize the reference vector. Based on this principle, the proposed SVM strategy for CMV suppression will be elaborated in the next section.

III. PROPOSED SVM STRATEGY FOR CMV SUPPRESSION

The proposed SVM strategy for CMV suppression in the RSC TLI with unbalanced NPVs includes four parts. Fig. 2 shows the control diagram of the proposed strategy. In part A, the basic vector selection is introduced to suppress the CMV. The duty cycle calculation of the basic vectors is presented in part B. In part C, the switching sequence is properly arranged. Finally, the separate control of capacitor voltages is achieved by using a closed-loop control approach to optimally regulate the duty cycles of different basic vectors.

A. Basic Vector Selection

Based on the CMV analysis above, Fig. 3 shows the SVD with different DC unbalancing coefficients (φ) of the proposed SVM strategy. The amplitude of small vectors will be affected by the dc unbalancing coefficient, and the large and zero vectors are not affected. The SVD is divided into 6 sectors, and each sector is further divided into two regions (regions A and B).

Taking sector I as an example, the sector contains small vector V_{S1} [POO], small vector V_{S2} [OON], large vector V_{L1} [PNN], large vector V_{L2} [PPN], and zero vector V_Z [OOO], which are expressed as:

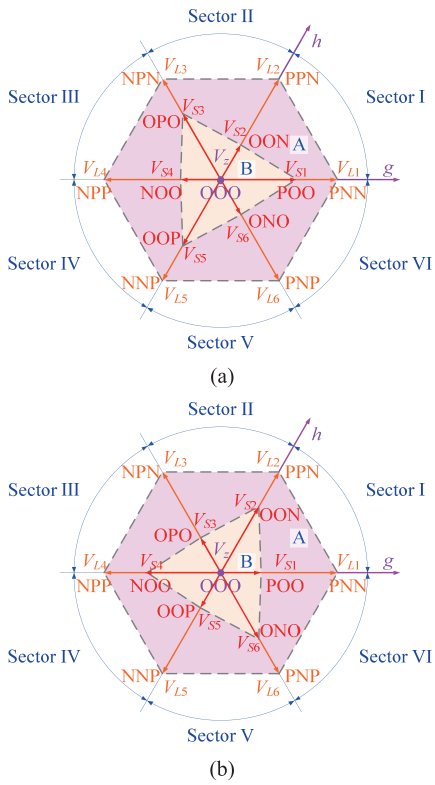

Fig. 3. SVD of the proposed strategy. (a) $\varphi > 0$. (b) $\varphi < 0$.

$$\begin{cases} V_{S1} = \dfrac{1+\varphi}{3} V_{dc} \cdot e^{j0} \\ V_{S2} = \dfrac{1-\varphi}{3} V_{dc} \cdot e^{j\frac{\pi}{3}} \\ V_{L1} = \dfrac{2}{3} V_{dc} \cdot e^{j0} \\ V_{L2} = \dfrac{2}{3} V_{dc} \cdot e^{j\frac{\pi}{3}} \\ V_Z = 0 \end{cases} \tag{4}$$

When the reference vector locates in region A, four nearest basic vectors are used to synthesize the reference vector. Since both P-type and N-type small vectors are contained in this region, the NPV can be flexibly controlled. While for region B, the basic vector generally selected according to the nearest three-vector principle, which cannot realize the separate control of capacitor voltages. To cope with the difficulty, a large vector is added, which means that four vectors are adopted to synthesize the reference vector. In this way, a novel control degree of freedom can be generated, and the NPV control can be achieved. Table II shows the basic vector selection for different regions of each sector.

B. Duty Ratio Calculation

To simplify the calculation, the 60° coordinate system is employed. v_g and v_h are the g-axis and h-axis components, which can be expressed as:

TABLE II
THE BASIC VECTOR SELECTION IN DIFFERENT SECTORS

Sector	Region A	Region B
I	[POO], [OON], [PNN], [PPN]	[OOO], [POO], [OON], [PNN] or [PPN]
II	[OON], [OPO], [PPN], [NPN],	[OOO], [OON], [OPO], [PPN] or [NPN]
III	[OPO], [NOO], [NPN], [NPP]	[OOO], [OPO], [NOO], [NPN] or [NPP]
IV	[NOO], [OOP], [NPP], [NNP]	[OOO], [NOO], [OOP], [NPP] or [NNP]
V	[OOP], [ONO], [NNP], [PNP]	[OOO], [OOP], [ONO], [NNP] or [PNP]
VI	[ONO], [POO], [PNP], [PNN]	[OOO], [ONO], [POO], [PNP] or [PNN]

$$\begin{cases} v_g = v_\alpha - \dfrac{\sqrt{3}}{3} v_\beta \\ v_h = \dfrac{2\sqrt{3}}{3} v_\beta \end{cases} \tag{5}$$

where v_α and v_β are two components of reference vector in orthogonal coordinate system. The duty ratio calculation in regions A and B are analyzed as follows:

1) Region A of Sector I: In this region, four basic vectors are selected to synthesize reference vector, and the volt-second balance equation is written as follows:

$$\begin{cases} V_{S1} \cdot d_{S1} + V_{S2} \cdot d_{S2} + V_{L1} \cdot d_{L1} + V_{L2} \cdot d_{L2} = V_{ref} \\ d_{S1} + d_{S2} + d_{L1} + d_{L2} = 1 \end{cases} \tag{6}$$

where d_{S1}, d_{S2}, d_{L1} and d_{L2} are the duty cycles of V_{S1}, V_{S2}, V_{L1} and V_{L2}, respectively. V_{ref} is the reference vector. (6) is further simplified by substituting (4) into (6) as follows:

$$\begin{cases} \dfrac{1+\varphi}{3} \cdot V_{dc} \cdot d_{S1} + \dfrac{2}{3} \cdot V_{dc} \cdot d_{L1} = v_g \\ \dfrac{1-\varphi}{3} \cdot V_{dc} \cdot d_{S2} + \dfrac{2}{3} \cdot V_{dc} \cdot d_{L2} = v_h \\ d_{S1} + d_{S2} + d_{L1} + d_{L2} = 1 \end{cases} \tag{7}$$

It is worthwhile to start by assuming that the duty cycle of the P-type small vector d_{S1} is a known quantity, whose value is y, and the corresponding detailed solution is given in subsection D. On this assumption, d_{S2}, d_{L1} and d_{L2} can be obtained:

$$\begin{cases} d_{S2} = \dfrac{1}{1+\varphi} \cdot \dfrac{2V_{dc} - 3v_g - 3v_h}{V_{dc}} - \dfrac{1-\varphi}{1+\varphi} \cdot y \\ d_{L1} = \dfrac{3}{2} \cdot \dfrac{v_g}{V_{dc}} - \dfrac{1+\varphi}{2} \cdot y \\ d_{L2} = \dfrac{1}{2} \cdot \left[\dfrac{3v_h}{V_{dc}} - \dfrac{1-\varphi}{1+\varphi} \cdot \dfrac{2V_{dc} - 3v_g - 3v_h}{V_{dc}} + \dfrac{(1-\varphi)^2}{1+\varphi} \cdot y \right] \end{cases} \tag{8}$$

As the duty cycles of each basic vector take values between 0 and 1, the range of y can be expressed as:

$$\begin{cases} y < \dfrac{1}{1-\varphi} \cdot \dfrac{2V_{dc} - 3v_g - 3v_h}{V_{dc}} \cdot \dfrac{1}{1+\varphi} \cdot \dfrac{3v_g}{V_{dc}} \\ y < \dfrac{1}{1+\varphi} \cdot \dfrac{3v_g}{V_{dc}} \\ y > \dfrac{1}{1-\varphi} \cdot \dfrac{2V_{dc} - 3v_g - 3v_h}{V_{dc}} - \dfrac{1+\varphi}{(1-\varphi)^2} \cdot \dfrac{3v_h}{V_{dc}} \end{cases} \tag{9}$$

Thus, the maximum value (y_{max}) and minimum value (y_{min}) of y are given in (10) and (11), respectively.

$$y_{max} = \min\left\{ 1, \frac{1}{1-\varphi} \cdot \frac{2V_{dc} - 3v_g - 3v_h}{V_{dc}}, \frac{1}{1+\varphi} \cdot \frac{3v_g}{V_{dc}} \right\} \tag{10}$$

$$y_{min} = \max\left\{ 0, \frac{1}{1-\varphi} \cdot \frac{2V_{dc} - 3v_g - 3v_h}{V_{dc}} - \frac{1+\varphi}{(1-\varphi)^2} \cdot \frac{3v_h}{V_{dc}} \right\} \tag{11}$$

For convenient calculation, the initial value of y (y_0) is taken as the arithmetic mean of its maximum and minimum values, as shown in (12).

$$y_0 = \frac{y_{max} + y_{min}}{2} \tag{12}$$

By substituting (12) into (8), the duty cycles of other basic vectors can be derived.

2) Region B of Sector I: In this region, the NPV can be flexibly controlled by adding a large vector to synthesize the reference vector, which is classified into two cases according to the difference between the reference value of voltage difference across C_1 and C_2 (V^*_{diff}) and V_{diff}.

Case 1: If $V^*_{diff} \leqslant V_{diff}$, four basic vectors [OOO], [POO], [OON], and [PPN] are adopted to synthesize the reference vector. In this case, the volt-second balance equation is as follows:

$$\begin{cases} V_Z \cdot d_Z + V_{S1} \cdot d_{S1} + V_{S2} \cdot d_{S2} + V_{L2} \cdot d_{L2} = V_{ref} \\ d_Z + d_{S1} + d_{S2} + d_{L2} = 1 \end{cases} \tag{13}$$

where V_Z denotes [OOO]. d_Z is the duty cycle of V_Z.

If the duty cycle d_{L2} of the large vector is considered as a known quantity y, the above equations can be expressed as:

$$\begin{cases} d_{L2} = y \\ d_{S1} = \dfrac{1}{1+\varphi} \cdot \dfrac{3v_g}{V_{dc}} \\ d_{S2} = \dfrac{1}{1-\varphi} \cdot \left(\dfrac{3v_h}{V_{dc}} - 2y \right) \\ d_Z = 1 - y - \dfrac{1}{1+\varphi} \cdot \dfrac{3v_g}{V_{dc}} - \dfrac{1}{1-\varphi} \cdot \left(\dfrac{3v_h}{V_{dc}} - 2y \right) \end{cases} \tag{14}$$

It can be seen that d_{S1} is not related to d_{L2}, but d_{S2} will be decreased by increasing d_{L2}. It is known that the P-type small vector decreases the voltage across C_1 and increase the voltage across C_2. The N-type small vector has the opposite effects.

TABLE III
SWITCHING STATES OF ZERO VECTORS FOR THE RSC TLI

Vectors	ON switches	Vectors	ON switches
$[OOO]_{-1}$	{2, 3, 5, 8, 10}	$[OOO]_{-2}$	{2, 3, 5, 7, 10}
$[OOO]_{-3}$	{2, 3, 6, 7, 10}	$[OOO]_{-4}$	{2, 3, 6, 7, 9}
$[OOO]_{-5}$	{2, 3, 6, 8, 9}	$[OOO]_{-6}$	{2, 3, 5, 8, 9}

Consequently, increasing the duty cycle of the large vector will reduce the difference between V^*_{diff} and V_{diff}.

By restricting the duty cycle of the basic vectors, y_{max} and y_{min} are denoted as (15) and (16), respectively.

$$y_{min} = \max\left\{ 0, \frac{1-\varphi}{(1+\varphi)^2} \cdot \frac{3v_g}{V_{dc}} + \frac{1}{1+\varphi} \cdot \frac{3v_h}{V_{dc}} - \frac{1-\varphi}{1+\varphi} \right\} \tag{15}$$

$$y_{max} = \min\left\{ 1, \frac{1}{2} \cdot \frac{3v_h}{V_{dc}} \right\} \tag{16}$$

Case 2: When $V^*_{diff} > V_{diff}$, [OOO], [POO], [OON], and [PNN] are adopted to synthesize the reference vector. The duty cycles of basic vectors can be expressed as:

$$\begin{cases} d_{L1} = y \\ d_{S1} = \dfrac{1}{1+\varphi} \cdot \left(\dfrac{3v_g}{V_{dc}} - 2y \right) \\ d_{S2} = \dfrac{1}{1-\varphi} \cdot \dfrac{3v_h}{V_{dc}} \\ d_Z = 1 - y - \dfrac{1}{1-\varphi} \cdot \dfrac{3v_h}{V_{dc}} - \dfrac{1}{1+\varphi} \cdot \left(\dfrac{3v_g}{V_{dc}} - 2y \right) \end{cases} \tag{17}$$

Similarly, y_{max} and y_{min} can be denoted as follows:

$$y_{min} = \max\left\{ 0, \frac{1+\varphi}{(1-\varphi)^2} \cdot \frac{3v_h}{V_{dc}} + \frac{1}{1-\varphi} \cdot \frac{3v_g}{V_{dc}} - \frac{1+\varphi}{1-\varphi} \right\} \tag{18}$$

$$y_{max} = \min\left\{ 1, \frac{3v_g}{2V_{dc}} \right\} \tag{19}$$

The value of y is obtained from the output of proportional-integral (PI) regulator, whose steps will be given Subsection D. The duty cycles of each basic vector can be obtained by substituting the obtained y into (14) or (17).

C. Switching Sequence Design

In order to reduce the harmonics of output currents and to keep lower switching losses, the appropriate switching sequences for different cases are carefully designed. It should be noted that the zero vector [OOO] contains six redundant states, so different states should be selected for different sectors. Table III displays the zero vectors with low CMV magnitudes and the corresponding switching states.

To further reduce the harmonics of the output currents, the switching sequences are arranged symmetrically on both sides.

TABLE IV
SWITCHING SEQUENCES IN DIFFERENT SECTORS

Sector	Region	Switching sequence
	A	[OON]–[PPN]–[PNN]–[POO]–…
I	B ($V^*_{diff} \leqslant V_{diff}$)	[OON]–[PPN]–[POO]–$[OOO]_{-1}$–…
	B ($V^*_{diff} > V_{diff}$)	[OON]–$[OOO]_{-1}$–[POO]–[PNN]–…
	A	[OON]–[PPN]–[NPN]–[POO]–…
II	B ($V^*_{diff} \leqslant V_{diff}$)	[OON]–[PPN]–[OPO]–$[OOO]_{-3}$–…
	B ($V^*_{diff} > V_{diff}$)	[OON]–$[OOO]_{-3}$–[OPO]–[NPN]–…
	A	[NOO]–[NPP]–[NPN]–[OPO]–…
III	B ($V^*_{diff} \leqslant V_{diff}$)	[NOO]–[NPP]–[OPO]–$[OOO]_{-3}$–…
	B ($V^*_{diff} > V_{diff}$)	[NOO]–$[OOO]_{-3}$–[OPO]–[NNP]–…
	A	[NOO]–[NPP]–[NNP]–[OOP]–…
IV	B ($V^*_{diff} \leqslant V_{diff}$)	[NOO]–[NPP]–[OOP]–$[OOO]_{-5}$–…
	B ($V^*_{diff} > V_{diff}$)	[NOO]–$[OOO]_{-5}$–[OOP]–[NNP]–…
	A	[ONO]–[PNP]–[NNP]–[OOP]–…
V	B ($V^*_{diff} \leqslant V_{diff}$)	[ONO]–[PNP]–[OOP]–$[OOO]_{-5}$–…
	B ($V^*_{diff} > V_{diff}$)	[ONO]–$[OOO]_{-5}$–[OOP]–[NNP]–…
	A	[ONO]–[PNP]–[PNN]–[POO]–…
VI	B ($V^*_{diff} \leqslant V_{diff}$)	[ONO]–[PNP]–[POO]–$[OOO]_{-1}$–…
	B ($V^*_{diff} > V_{diff}$)	[ONO]–$[OOO]_{-1}$–[POO]–[PNN] –…

For simplicity, the former half of the switching sequences of different sectors are provided in Table IV.

The switching sequence in region A of sector I is designed as: [OON]–[PPN]–[PNN]–[POO]–[PNN]–[PPN]–[OON]. Region A contains both the P-type small vector and the N-type small vector, and the capacitor voltages can be controlled independently, so one sequence is used. Region B is only able to select different large vectors [PNN] or [PPN] according to different NPVs, thus two switching sequences are needed to realize separate control of capacitor voltages. Moreover, all switching sequences are initiated and terminated by the N-type small vector.

D. Separate Control of Capacitor Voltages

To realize the separate control of capacitor voltages, a PI regulator is employed. To be specifics, the difference between V^*_{diff} and V_{diff} is fed to the PI regulator. The absolute value of its output (y_{np}) is used to modify the duty cycle of the basic vectors, which can be expressed as:

$$y_{np} = \left| \left(k_p + \frac{k_i}{s} \right) \cdot (V^*_{diff} - V_{diff}) \right| \tag{20}$$

where k_p and k_i are the parameters of the PI regulator.

The separate control of capacitor voltages is available in three cases, which are indicated as follows:

Case 1: When the reference vector is located in the region A and $V^*_{diff} \leqslant V_{diff}$, the duty cycle of the P-type small vector should be increased, so y is modified as:

$$y = y_0 + y_{np} \tag{21}$$

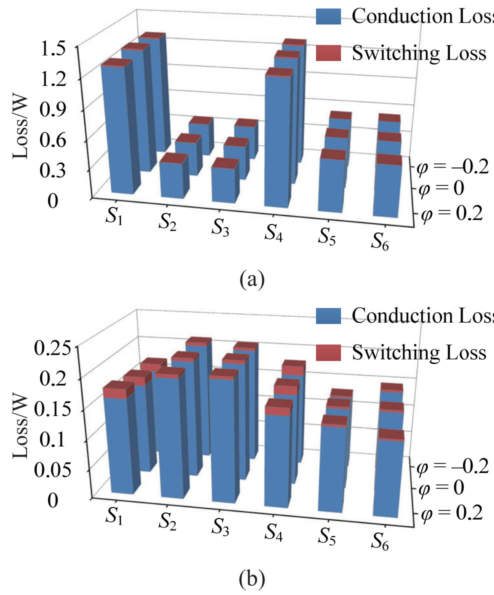

Fig. 4. Losses of power switches for the RSC TLI. (a) $m = 0.8$. (b) $m = 0.4$.

Case 2: When the reference vector is located in the region A and $V^*_{diff} > V_{diff}$, the duty cycle of the P-type small vector should be decreased, so y is modified as:

$$y = y_0 - y_{np} \tag{22}$$

Case 3: When the reference vector is located in the region B, it is sufficient to set the duty cycle of the large vector directly to be y_{np} for easy calculation, which is expressed as:

$$y = y_{np} \tag{23}$$

In addition, the modified duty cycle of the basic vectors should satisfy the above limitations, as expressed by (24).

$$y_{min} < y < y_{max} \tag{24}$$

E. Loss Analyses of Power Switches

Since the topology of the RSC TLI is symmetrical, the voltage stress and loss of S_5 is identical to those of S_7 and S_9, and the same conclusion can be obtained for other switches. Therefore, it is sufficient to analyze only power switches S_1–S_6. In addition, the losses of power switches can be categorized into switching losses and conduction losses.

To visually demonstrate the losses of the proposed strategy, Fig. 4 shows the losses of the proposed strategy for the RSC TLI, which is obtained via PLECS Blockset and MATLAB/Simulink. It can be seen that the losses of power switches are mainly conduction losses and switching losses are very small. When $\varphi = 0.2$, the losses of S_1, S_2, and S_5 are slightly greater than those of S_4, S_3, and S_6. On the contrary, when $\varphi = -0.2$, the losses of S_1, S_2, and S_5 are slightly smaller than those of S_4, S_3, and S_6, respectively. As m is increased, the losses of the power switches are increased correspondingly, because the magnitude of output current is increased.

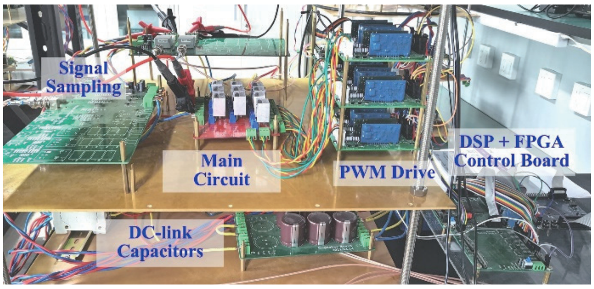

Fig. 5. Photograph of the experimental test rig.

TABLE V
PARAMETERS FOR THE EXPERIMENTAL TESTS

Parameters	Values
DC-link voltage (V_{dc})	100 V
DC-link capacitors (C_1 and C_2)	1410 μF
Fundamental frequency (f)	50 Hz
Switching frequency (f_{sw})	12.5 kHz
Sampling period (T_s)	80 μs
Dead-time (t_d)	2 μs
Resistive-inductive (RL) load	10 Ω, 7 mH

IV. Experimental Results

A hardware-based RSC-TLI test rig is designed and built to verify the validity of proposed strategy, as depicted in Fig. 5. Three-phase output voltages are measured, and CMV is obtained by using (3). The digital signal processor TMS320F28335 and field programmable gate array XC3S500E are adopted as controllers. One dc source is adopted as the dc power supply to verify the feasibility and correctness of the separate control of capacitor voltages in this article [16], [31].

The measurements of CMV waveforms experimentally are conducted, and the digital storage oscilloscope RTO2014 from Rohde & Schwarz is further utilized, which can support the mathematical calculation in (3). To be specific, three-phase pole voltages (v_{ao}, v_{bo}, and v_{co}) are measured, and the CMV waveform is obtained by the MATH function in RTO2014. The rest of the photos were captured via the oscilloscope MDO3024 from Tektronix.

In order to effectively demonstrate the advantages of the proposed SVM strategy, the methods in [11] and [30] are used for comparisons. For the convenience of the following description, the method in [11], the method in [30], and the proposed SVM strategy are denoted as Method-1, Method-2, and Method-3, respectively. The parameters for the experimental tests are presented in Table V.

A. Experimental Results in Steady State

In order to investigate the operating performance in regions A and B of each sector, two modulation indices are chosen, which include 0.8 and 0.4. When V^*_{diff} is equal to 20 V, the experimental results are shown in Fig. 6.

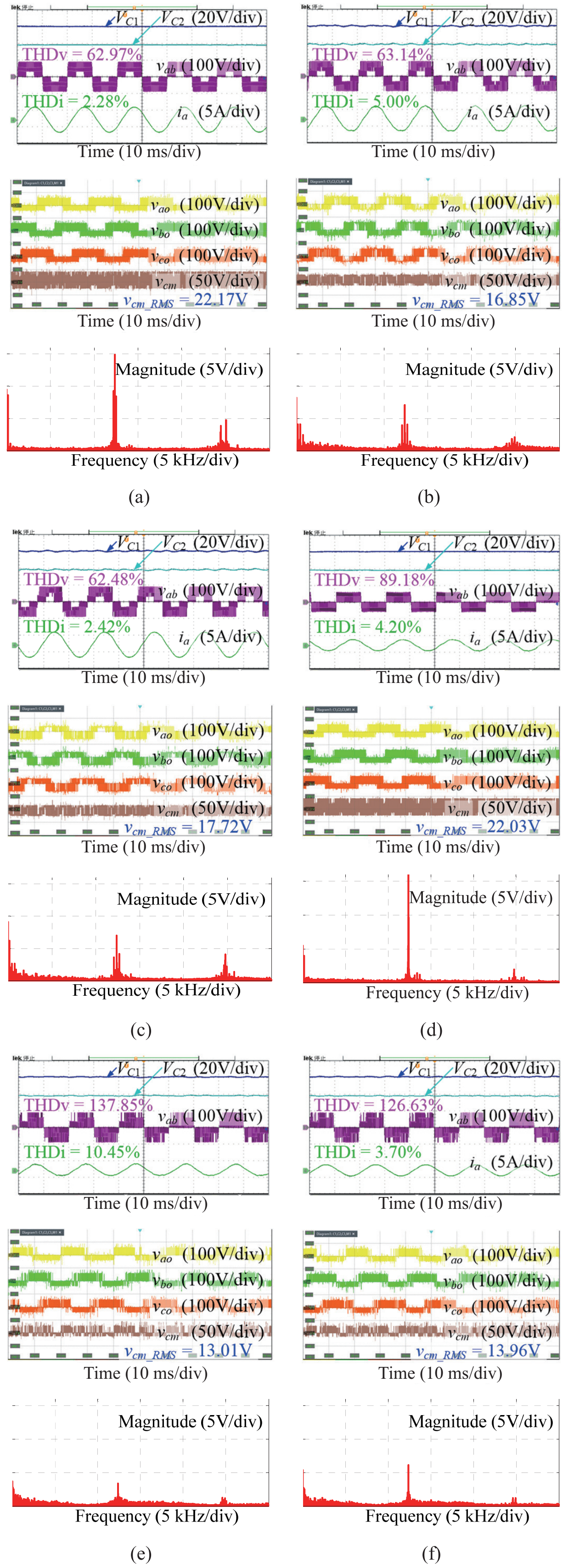

Fig. 6. Experimental results for positive unbalancing coefficient (φ = 0.2). (a) Method-1, m = 0.8. (b) Method-2, m = 0.8. (c) Method-3, m = 0.8. (d) Method-1, m = 0.4. (e) Method-2, m = 0.4. (f) Method-3, m = 0.4.

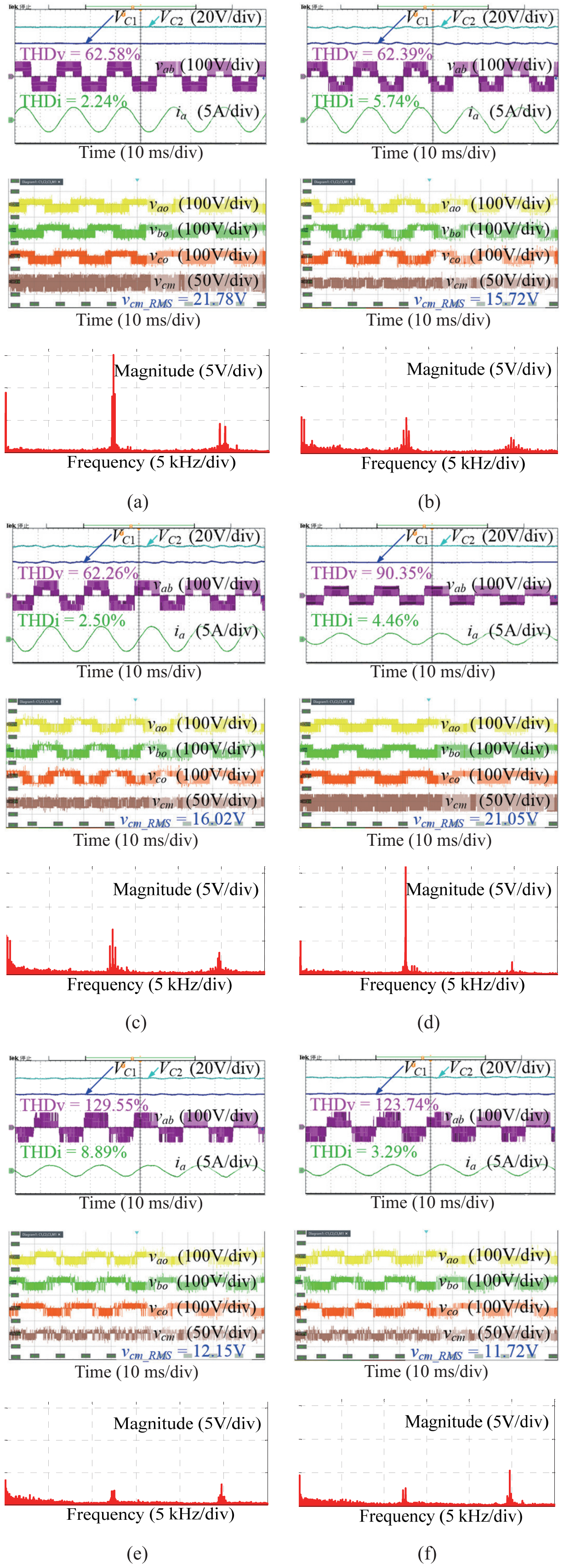

Fig. 7. Experimental results for negative unbalancing coefficient (φ = –0.2). (a) Method-1, m = 0.8. (b) Method-2, m = 0.8. (c) Method-3, m = 0.8. (d) Method-1, m = 0.4. (e) Method-2, m = 0.4. (f) Method-3, m = 0.4.

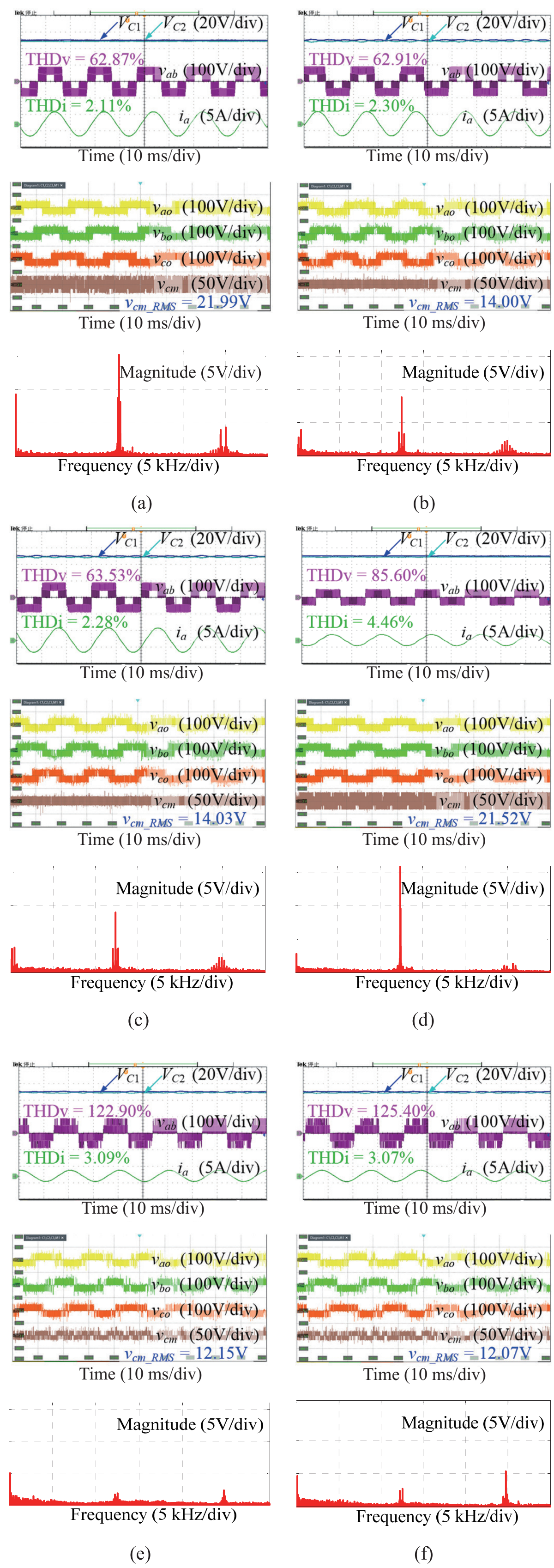

Fig. 8. Experimental results with balanced NPV condition (φ = 0). (a) Method-1, m = 0.8. (b) Method-2, m = 0.8. (c) Method-3, m = 0.8. (d) Method-1, m = 0.4. (e) Method-2, m = 0.4. (f) Method-3, m = 0.4.

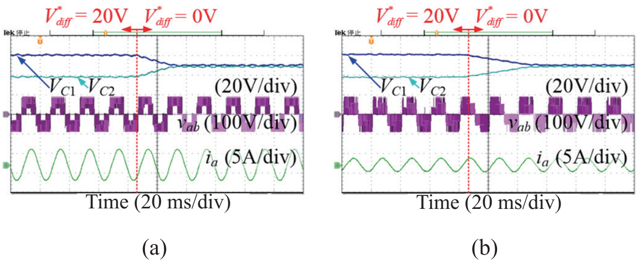

Fig. 9. Dynamic experimental waveforms from positive dc unbalancing coefficient to balanced NPV condition for Method-3. (a) $m = 0.8$. (b) $m = 0.4$.

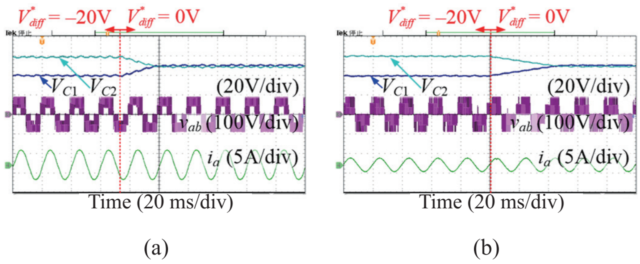

Fig. 10. Dynamic experimental waveforms from negative dc unbalancing coefficient to balanced NPV condition for Method-3. (a) $m = 0.8$. (b) $m = 0.4$.

Fig. 6(a) − (c) shows the experimental waveforms when the modulation index $m = 0.8$. The line voltages for three methods are five levels. The total harmonic distortion (THD) of output current (THDi) for Method-1 is the minimum, whose value is 2.28%. However, Method-1 synthesizes the reference vector by using all basic vectors, which has the root-mean-square (RMS) value of CMV as high as 22.17 V. Although Method-2 can suppress the CMV, the quality of output currents is obviously degraded, whose THDi is high as 5.00%. Compared to Method-1, the CMV amplitude for Method-3 is reduced by half. Compared with Method-2, the THDi for Method-3 is reduced to 2.42%, and the quality of output currents is significantly improved. Thus, Method-3 can suppress the CMV while ensuring high quality of output currents.

Fig. 6(d) − (f) shows the experimental waveforms when $m = 0.4$. Being similar to the previous results, the RMS values of the CMV are reduced by 40.94% and 36.63% for Method-2 and Method-3, when comparing with Method-1, respectively. In contrast to $m = 0.4$, the quality of output currents for Method-3 is significantly better than that of Method-1, whose THDi is equal to 3.70%.

When V^*_{diff} is equal to −20 V, the experimental results are shown in Fig. 7. Same as when $\varphi = 0.2$, Method-1 has the highest CMV. Method-2 can suppress the CMV. However, the output currents are distorted. Method-3 can suppress the CMV while maintaining the well quality of output currents.

When $\varphi = 0$, the experimental results are displayed in Fig. 8. The CMV for Method-1 are still the highest. There is almost no difference in the overall performance of Method-2 and Method-3. Therefore, the proposed modulation strategy is also applicable to the condition with balanced NPVs.

The spectra of the CMV are gained by using MATLAB to better analyze the CMV performance, which are offered in Figs. 6 − 8, respectively. The major components of CMV for Method-3 are reduced at different frequencies compared to Method-1. In conclusion, all the results confirm CMV suppression properties of the proposed modulation strategy.

B. Dynamic Experimental Results

When V^*_{diff} is manually changed, the experimental results for Method-3 are illustrated in Figs. 9 and 10. It can be clearly seen that Method-3 is able to regulate V_{C1} and V_{C2} separately. Moreover, satisfactory waveforms of output currents are guaranteed with balanced and unbalanced NPV conditions.

V. Conclusion

In this article, a novel SVM strategy for CMV suppression in the RSC TLI with unbalanced NPVs was proposed. The basic vectors with low CMV magnitudes were chosen, which suppressed the CMV. Based on SVD with unbalanced NPVs, four basic vectors were selected to synthesize the reference vector. The duty cycles of basic vectors were calculated by using an indirect method, and the appropriate switching sequences were designed. By modifying the duty cycle of basic vectors, the separate control of capacitor voltages was accomplished. The CMV magnitudes were decreased by half in comparison with the conventional modulation strategy. What's more, the proposed SVM strategy was simultaneously applicable to balanced and unbalanced NPV conditions. The effectiveness of the proposed method was verified by experiments.

It is reported that, the technology in this article is still at the theoretical research stage presently, and the equipment for industrialization is not available. For the industrial equipment based on centralized TLI, the similar modulation strategy that is suitable for both balanced and unbalanced NPVs can be implemented via the digital controller. Doing so, when some non-ideal factors result in unbalanced NPV conditions, the quality of output currents will not be negatively affected.

References

[1] H. Kanakri, E. C. D. Santos, and M. Rizkalla, "Twelve-step voltage source inverter: a three-phase six-levels inverter using planar transformers," in *CPSS Transactions on Power Electronics and Applications,* vol. 9, no. 1, pp. 263–273, Sept. 2024.

[2] Y. Yang, J. Pan, H. Wen, M. Fan, R. Chen, L. He, M. Xie, M. Norambuena, L. Xu, and J. Rodriguez, "Model predictive current control with low complexity for single-phase four-level hybrid-clamped converters," in *IEEE Transactions on Transportation Electrification,* vol. 7, no. 3, pp. 983–999, Sept. 2021.

[3] J. Chen, D. Jiang, and Q. Li, "Attenuation of conducted EMI for three-level inverters through PWM," in *CPSS Transactions on Power Electronics and Applications,* vol. 3, no. 2, pp. 134–145, Jun. 2018.

[4] Z. Dong, C. Wang, and Q. Cheng, "A hybrid modulation method with the maximum controllable range of the neutral-point current for three-level NPC," in *IEEE Transactions on Transportation Electrification,* vol. 8, no. 4, pp. 4444–4455, Dec. 2022.

[5] X. Xing, M. Jing, C. Du, C. Qin, C. Liu, and Z. Chen, "An adaptive model predictive control for reduced switch count three-level inverter," in *IEEE Journal of Emerging and Selected Topics in Power Electronics,* vol. 11, no. 1, pp. 453–464, Feb. 2023.

[6] C. Qin, X. Xing, and Y. Jiang, "Topology and space vector modulation method for the reduced switch count quasi-Z-source three-level inverter,"

in *IEEE Transactions on Industrial Electronics,* vol. 70, no. 5, pp. 4332–4344, May 2023.

[7] C. Wang, Z. Li, X. Si, and H. Xin, “Control of neutral-point voltage in three-phase four-wire three-level NPC inverter based on the disassembly of zero level,” in *CPSS Transactions on Power Electronics and Applications,* vol. 3, no. 3, pp. 213–222, Sept. 2018.

[8] Y. Zou, Y. Xing, L. Zhang, Z. Zheng, X. Liu, H. Hu, T. Wang, and Y. Wang, “Dynamic-space-vector discontinuous PWM for three-phase Vienna rectifiers with unbalanced neutral-point voltage,” in *IEEE Transactions on Power Electronics,* vol. 36, no. 8, pp. 9015–9026, Aug. 2021.

[9] Z. Zhang, B. Li, G. Zhang, G. Wang, Z. Huang, B. Hu, T. Long, and D. Xu, “Optimized carrier-based DPWM strategy adopting self-adjusted redundant clamping modes for Vienna rectifiers with unbalanced dc links,” in *IEEE Transactions on Power Electronics,* vol. 38, no. 2, pp. 1622–1634, Feb. 2023.

[10] U. M. Choi, F. Blaabjerg, and K. B. Lee, “Control strategy of two capacitor voltages for separate MPPTs in photovoltaic systems using neutral-point-clamped inverters,” in *IEEE Transactions on Industry Applications,* vol. 51, no. 4, pp. 3295–3303, Jul.-Aug. 2015.

[11] C. Qin and X. Li, “Improved virtual space vector modulation scheme for the reduced switch count three-level inverter with balanced and unbalanced neutral-point voltage conditions,” in *IEEE Transactions on Power Electronics,* vol. 38, no. 2, pp. 2092–2104, Feb. 2023.

[12] Y. Park, S.-K. Sul, C.-H. Lim, and S.-H. Lee, “Asymmetric control of DC-link voltages for separate MPPTs in three-level inverters,” in *IEEE Transactions on Power Electronics,* vol. 28, no. 6, pp. 2760–2769, Jun. 2013.

[13] Z. Zhang, A. Chen, X. Xing, and C. Zhang, “Space vector modulation based control strategy of three-level inverter for separate MPPTs in photovoltaic system,” in *Proceedings of IEEE 8th International Power Electronics and Motion Control Conference,* 2016, pp. 2394–2400.

[14] Z. Ye, Y. Xu, X. Wu, G. Tan, X. Deng, and Z. Wang, “A simplified PWM strategy for a neutral-point-clamped (NPC) three-level converter with unbalanced dc links,” in *IEEE Transactions on Power Electronics,* vol. 31, no. 4, pp. 3227–3238, Apr. 2016.

[15] X. Wu, G. Tan, Z. Ye, G. Yao, Z. Liu, and G. Liu, “Virtual-space-vector PWM for a three-level neutral-point-clamped inverter with unbalanced dc-links,” in *IEEE Transactions on Power Electronics,* vol. 33, no. 3, pp. 2630–2642, Mar. 2018.

[16] X. Wu, G. Tan, G. Yao, C. Sun, and G. Liu, “A hybrid PWM strategy for three-level inverter with unbalanced dc links,” in *IEEE Journal of Emerging and Selected Topics in Power Electronics,* vol. 6, no. 1, pp. 1–15, Mar. 2017.

[17] M. M. Hashempour, M. Yang, and T. Lee, “An adaptive control of DPWM for clamped-three-level photovoltaic inverters with unbalanced neutral-point voltage,” in *IEEE Transactions on Industry Applications,* vol. 54, no. 6, pp. 6133–6148, Nov.-Dec. 2018.

[18] P. Zhang, X. Wu, B. Li, Li Ding, J. Long, W. Zhang, and Y. Li, “A zero-sequence component injection PWM scheme for three-level neutral point clamped rectifiers with unbalanced dc-link voltages,” in *IEEE Transactions on Industrial Electronics,* vol. 12, no. 3, pp. 5420–5430, Jun. 2024.

[19] Y. Zou, L. Zhang, Y. Xing, H. Zhuge, X. Shen, Y. Zhang, and Y. Lu, “An optimized DPWM with reduced leakage current for three-phase three-level inverters with unbalanced neutral-point voltage,” in *IEEE Transactions Power Electronics,* vol. 12, no. 3, pp. 16346–16360, Dec. 2024.

[20] C. Qin, X. Li, X. Xing, C. Zhang, and G. Zhang, “Common-mode voltage reduction method for three-level inverter with unbalanced neutral-point voltage conditions,” in *IEEE Transactions on Industrial Informatics,* vol. 17, no. 10, pp. 6603–6613, Oct. 2021.

[21] M. Jing, C. Du, X. Xing, Z. Chen, and C. Wen, “The switching decomposition pulse width modulation with reduced common mode voltage for reduced switch counts neutral point clamped inverter,” in *IET Power Electronics,* vol. 16, no. 4, pp. 612–630, Nov. 2022.

[22] M. C. Cavalcanti, K. C. de Oliveira, A M. de Farias, F. A. S. Neves, G. M. S. Azevedo, and F. C. Camboim, “Modulation techniques to eliminate leakage currents in transformerless three-phase photovoltaic systems,” in *IEEE Transactions on Industrial Electronics,* vol. 57, no. 4, pp. 1360–1368, Apr. 2010.

[23] J. S. Lee and K. B. Lee, “New modulation techniques for a leakage current reduction and a neutral-point voltage balance in transformerless photovoltaic systems using a three-level inverter,” in *IEEE Transactions on Power Electronics,* vol. 29, no. 4, pp. 1720–1732, Apr. 2014.

[24] C. Qin, C. Zhang, X. Xing, X. Li, A. Chen, and G. Zhang, “Simultaneous common-mode voltage reduction and neutral-point voltage balance scheme for the quasi-Z-source three-level T-type inverter,” in *IEEE Transactions on Industrial Electronics,* vol. 67, no. 3, pp. 1956–1967, Mar. 2020.

[25] Y. Huang, T. Liu, Q. Ren, A. Chen, H. Zhang, and W. Wang, “Data-driven predictive control strategy to improve robust performance for three-level inverters with reduced common-mode voltage,” in *IEEE Journal of Emerging and Selected Topics in Power Electronics,* vol. 12, no. 4, pp. 3823–3834, Aug. 2024.

[26] K. Nanshikar and S. Das, “Optimal space vector-based hybrid PWM scheme in terms of common-mode voltage and line current ripple,” in *IEEE Transactions on Power Electronics,* vol. 39, no. 11, pp. 14478–17792, Nov. 2024.

[27] X. Tang, X. Yuan, S. Niu, and K. T. Chau, “High-efficient multivector model predictive control with common-mode voltage suppression,” in *IEEE Journal of Emerging and Selected Topics in Power Electronics,* vol. 12, no. 3, pp. 2674–2885, Jun. 2024.

[28] Q. Yan, H. Chen, T. Zhao, X. Yuan, L. Zhang, and R. Zhao, “A carrier-based discontinuous space-vector PWM for common-mode voltage reduction in dual-input three-level T-type inverters with unbalanced neutral-point voltages,” in *IEEE Transactions on Power Electronics,* vol. 39, no. 9, pp. 11020–11033, Feb. 2024.

[29] Z. Li, X. Xing, C. Liu, C. Wen, and R. Zhang, “Common-mode voltage reduction method-based flexible power control for multiport DC-AC converter in PV-battery hybrid system,” in *IEEE Journal of Emerging and Selected Topics in Power Electronics,* vol. 12, no. 3, pp. 2744–2757, Jun. 2024.

[30] X. Li, C. Qin, Z. Chu, and J. Fang, “A novel modulation scheme for simultaneous common-mode voltage reduction and neutral-point voltage balance in the reduced switch count quasi-Z-source three-level inverter,” in *IEEE Transactions on Power Electronics,* vol. 38, no. 10, pp. 12035–12047, Oct. 2023.

[31] X. Pang, A. Chen, X. Li, Z. Zhong, and X. Liu, “Carrier-based fault tolerant control strategies for three-level T-type inverter with unbalanced neutral-point voltage,” in *IEEE Journal of Emerging and Selected Topics in Power Electronics,* vol. 12, no. 4, pp. 4154–4164, Aug. 2024.

Zhiyuan Chu received the B.S. degree in building electricity and intelligence in 2022 from Shandong Jianzhu University, Jinan, China, where he is currently working toward the M.S. degree in control engineering. His current research interests include modulation strategies of multi-level converters.

Changwei Qin received the Ph.D. degree in electrical engineering from Shandong University, Jinan, China, in 2019. In 2020, he joined Shandong Jianzhu University, where he is currently an Associate Professor. His current research interests include control of multi-level converters and impedance source converters.

Xiaoyan Li received the Ph.D. degree in electrical engineering from Shandong University, Jinan, China, in 2020. From 2021 to 2023, she was a Postdoctoral Research Fellow with Shandong University, Jinan, China. In 2023, she joined Shandong Jianzhu University, where she is currently a Full Professor. Her current research interests include control of multi-level converters and power quality control.

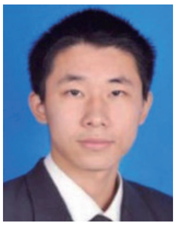

Jingyang Fang received the B.Sc. and M.Sc. degrees in electrical engineering from Xi'an Jiaotong University, Xi'an, China, in 2013 and 2015, respectively, and the Ph.D. degree from the School of Electrical and Electronic Engineering, Nanyang Technological University, Singapore, in 2019.

From May 2018 to August 2018, he was a Visiting Scholar with the Institute of Energy Technology, Aalborg University, Aalborg, Denmark. From August 2018 to August 2019, he was a Research Fellow with School of Electrical and Electronic Engineering, Nanyang Technological University, Singapore. From August 2019 to August 2021, he was a Postdoctoral Researcher with the Duke University and TU Kaiserslautern. Since August 2021, he has joined School of Control Science and Engineering, Shandong University as a Full Professor. His research interests include power quality control, stability analysis and improvement, renewable energy integration, and digital control in more-electronics power systems.

Dr. Fang is a recipient of the Humboldt Research Fellowship, two IEEE Prize Paper Awards, one Best Presenter Award, and the IEEE JESTPE Star Reviewer Award. He received the Chinese Government Award for Outstanding Self-Financed Students Abroad in 2018 and the Best Thesis Award from NTU in 2019. He was World's Top 2% Highly Cited Scientists ranked by Stanford University.

Lei Yang received the B.S. degree in electrical engineering and automation in 2023 from Shandong Jianzhu University, Jinan, China, where he is currently working toward the M.S. degree in control science and engineering. His current research interests include modulation strategies of multi-level converters.

Yanling Zhang received the M.S. degree in control science and engineering from Northeastern University, Shenyang, China, in 2009. She is currently an experimentalist with the School of Information and Electrical Engineering, Shandong Jianzhu University. Her research interests include embedded system design.

Battery Cluster Fault-Tolerant Control for High Voltage Transformerless Grid-Tied Battery Energy Storage System

Xiqi WU, Shuai GAO, YiLin LIU, Rui LI, Xinyu JIANG, and Xu CAI

***Abstract*—The battery fault-tolerant operation is one of the important issues for such a large-capacity cascaded H-bridge converter-based battery energy storage system (BESS). Conventional redundant method by bypassing whole SMs at ac-side may lead to insufficient modulation ratio margin and waste the potential of healthy H-bridge part. First, the comparison of ac-side bypassing submodules (SMs) with dc-side disconnecting cluster is made; and the concept of new battery cluster fault tolerance strategy is discussed. In order to give full play to the grid voltage support capability of the faulty module, a battery cluster fault tolerance operating control combining proposed fault-tolerant strategy and optimal zero sequence voltage injection is proposed in this paper. As a result, it can effectively enhance the capability of handling battery warnings and failure and is able to tolerate any number of faulty battery cluster modules. Besides, state of charge(SOC) balancing of healthy SMs and capacitor voltage balancing of faulty SMs are incorporated into control algorithm. At last, effectiveness of the proposed battery fault tolerance strategy is thoroughly verified in BESS of 10 kV/5 MW and 14 SMs per phase by MATLAB/Simulink simulations and hardware-in-loop experiment.**

***Index Terms*—Battery energy storage system, cascaded H-bridge, fault tolerance, redundant control.**

I. Introduction

SALE-up application of energy storage is necessary for a high proportion of fluctuating wind and solar new energy sources. Battery energy storage is the fastest growing energy storage method, and the scale of energy storage power plant is moving from hundred MWh level to GWh level [1]−[3]. The technical bottleneck hindering the large capacity of single energy storage is variations of battery cells due to the inconsistent manufacturing process and the inhomogeneous operating environment. The inconsistency of battery cells leads to the barrel effect between series-connected battery cells and the circulating current effect between parallel-connected battery clusters, which reduces the available capacity of the battery, increases the loss of the battery system, and the local cell faults are prone to trigger the safety problems [4], [5]. As result, the single unit capacity of traditional battery energy storage system (BESS) based on two-level converter generally does not exceed 1 MW due to the limitation by technologies such as battery safety, cells grouping method and battery management system (BMS).

Transformerless grid-tied BESS (TGT-BESS) is based on cascaded H-bridge (CHB) converter and has a highly modular configuration, which facilitates capacity expansion and redundancy design, and can be connected MVAC or HVAC without the bulky line-frequency transformer, eliminating losses caused by linear fractional transformation (LFT) [6], [7]. All of the aforementioned advantages favor the usage of TGT-BESS in the large-capacity energy storage application such as grid-side and new energy plant side. As shown in Fig. 1, the large-capacity battery stack is separated as numerous individual cluster units connected to each H-bridge circuit, which avoids the circulating current in the battery stack, reduces the system cycle loss and improves the system safety at the same time [8]. Compared with the traditional BESS, TGT-BESS features the large-capacity of single converter unit, requiring fewer parallel units to form a large-scale energy storage power plant. These results in a simpler power plant structure and control strategy, which render energy storage system have faster response as well as avoid stability problems [9], [10].

However, a big challenge brought by a large single-unit capacity is the reliability of system operation. Long time, stable and safe grid-tied operation for such a highly energy-concentrated BESS relies on the reliability from two aspects: power switches and battery cells. Therefore, the capability of faulty tolerance and postfault operation are critical issues [11]. On the one hand, the higher grid-tied voltage level increases the number of cascades, and more power switches are used. Thus, each H-bridge module may become a potential point of failure due to short-circuiting or open-circuiting of the power devices, which increases the probability of system failure [12]. Many fault-tolerant approaches have been proposed for multilevel

Manuscript received November 18, 2024; revised February 02, 2025; accepted March 06, 2025. Date of publication June 30, 2025; date of current version April 18, 2025. This work was supported in part by National Key R&D Program of China under the Grant 2023YFB4204400. *(Corresponding author: Rui Li.)*

X. Wu, Y. Liu, R. Li, and X. Cai are with the Key Laboratory of Control of Power Transmission and Conversion, School of Electronics, Information and Electrical Engineering, Shanghai Jiao Tong University, Shanghai 200240, China (e-mail: wuxiqi@sjtu.edu.cn; yilinliu@sjtu.edu.cn; liruiqd@sjtu.edu.cn; xucai@sjtu.edu.cn).

S. Gao and X. Jiang are with the Guangzhou Zhiguang Energy Storage Technology Co., Ltd., Guangzhou 510760, China (e-mail: gaoshuai@gzzg.com.cn; jiangxinyu@gzzg.com.cn).

Digital Object Identifier 10.24295/CPSSTPEA.2025.00011

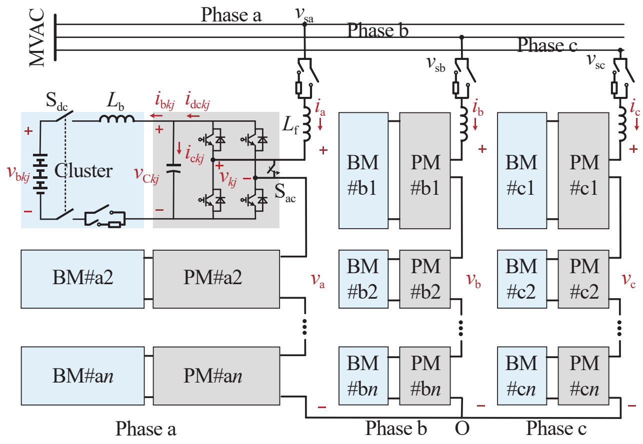

Fig. 1. Circuit diagram of TGT-BESS.

converters in different applications and mainly focus on faults intrigued by power switches [13]–[15], which can be divided into two categories: hardware redundancy method and software control technique.

The hardware method is implemented by adding redundant submodules (SMs). The redundant modules work at hot standby or cold standby states depending to whether they are active or not in normal conditions. In [16], a redundant SM is employed in each of the three phases and operates in hot standby mode. In case of a fault, the faulty module and one non-faulty module in the other two phases are bypassed simultaneously. However, added redundant modules in each phase increases the hardware cost and size of the system, especially in battery application. Just a cold standby redundancy module is employed for three-phase legs in [17], [18]. In normal operation, the redundant module is in the bypass state; when the fault occurs, the redundant module is inserted into faulty phase through a switch network to ensure that the operating state of system is the same as before the fault. Although the system cost effectively is lowered since only one redundant module is needed, this method has strong limitations and is only applicable to the situation where a single power module (PM) of the system fails.

Software methods adjust the control strategy to allow the system to continue to operate after faulty module is bypassed [19], [20]. Symmetrical bypass method is used in [21] and then capacitor voltage of the non-faulty module is enhanced to maintain a constant sum of dc voltage, allowing the system to still emit the original reactive capacity. However, this method not only increases the voltage level of the filter capacitors and power switches but also is not suitable for BESS due to clamped effect by battery voltage. In [22], [23], unsymmetrical bypass method is used for BESS. After bypassing the faulty module, a zero-sequence voltage is injected to achieve the maximum magnitude of the three-phase balanced line voltage [24]. While avoiding the occurrence of over-modulation, the method also maintains battery SOC equalization in energy storage systems. A fault-tolerant control method is proposed in [25] for the occurrence of open-circuit and short-circuit faults in the switch. Instead of bypassing the whole module directly after the fault, the faulty module is switched from full-bridge mode to fault-tolerant half-bridge mode by changing its modulation strategy [26]. At this situation, the output ac voltage of SM is only half of the rated voltage, and the faulty module still has the power output and voltage support capability. Since this fault-tolerant mode introduces a dc voltage bias in the faulty phase, it is necessary to inject a dc component of equal amplitude in the non-faulty phase as well, so as not to affect the grid-connected current waveform [27].

Compared with power devices, massive battery cells, as an energy carrier, are more prone to occurrence of some warnings or failures: such as internal short-circuiting of cells, excessive voltage or temperature difference of cells within a cluster, overcharging or over-discharging or overheating of cells [28]. Especially at the end of the system charging and discharging, there will often be a battery cell that firstly reaches the cut-off voltage, resulting in shutdown and reduction of BESS capacity utilization. In response to this kind of situation, state-of-art studies take conventional fault-tolerant method of directly bypassing the faulty SMs like handling failure of power switches in [16]–[24].

On this ground, this article presents a new battery cluster fault tolerance strategy for TGT-BESS, which takes advantage of the healthy power H-bridge part of the faulty SMs, where they are still able to generate ac voltage to support grid voltage. The main technical contributions of this article are summarized as follows:

1) Instead of directly bypassing the faulty module through the ac bypass switch after a cluster fault occurs, the faulty cluster is disconnected through the dc circuit breaker. The faulty module is switched from charge or discharge mode to reactive fault-tolerant mode and continues to operate, giving full play to the grid voltage support capability of the faulty module.

2) The proposed strategy is able to tolerate any number of faulty battery cluster modules, while other nonfaulty modules can still continue to absorb or release energy. This is important to improve the system capacity utilization at the end of charging and discharging.

3) A battery clusters fault-tolerant control strategy incorporating third harmonic voltage injection (THVI) is proposed to avoid the risk of system downtime due to insufficient modulation ratio margins caused by the traditional direct ac bypass of SMs.

The rest of this paper is organized as follows: the conventional SM ac-side directly-bypassing and a new battery cluster fault tolerance strategy are discussed in Section II. A battery cluster fault tolerance operating control for TGT-BESS combining fault-tolerant strategy, zero sequence voltage injection and the balancing control of capacitor voltage of faulty SMs and SOC of healthy SMs are theoretically analyzed in Section III. The effectiveness of proposed control scheme is verified by offline simulation and hardware-in-loop (HIL) experiment in Section IV. The conclusions are given in Section V.

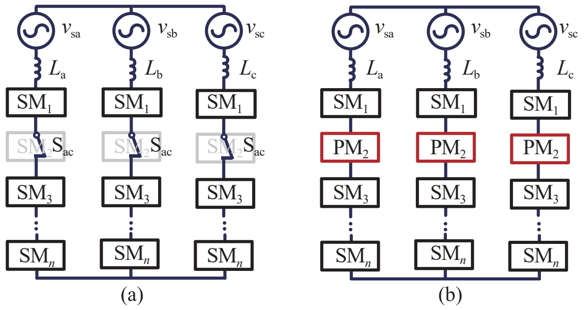

Fig. 2. Fault tolerance methods. (a) Directly bypassing whole SM at ac side. (b) Exiting battery cluster at dc side.

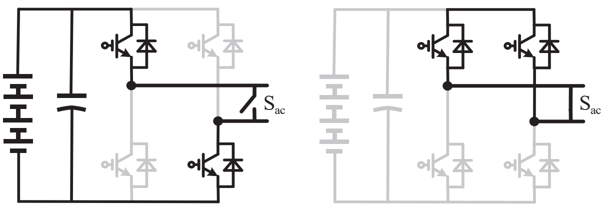

Fig. 3. Ac-side bypassing process.

II. Conventional SM Bypass Method and a New Battery Fault-Tolerant Strategy

A. System Configuration

Fig. 1 shows the circuit schematic of TGT-BESS. It is composed of n SMs per phase and each SM comprises PM and battery module (BM). PM is an H-bridge converter with a filter capacitor C, which is the main circuit of static synchronous compensator. BM contains a battery cluster, its BMS, a dc soft-start circuit, a dc circuit breaker S_{dc} and a filter inductor L_b. The H-bridge cells are connected in series on their ac side; then, the output terminal is connected to medium-voltage grid directly through a filter inductor L_f and an ac soft-start circuit. A set of two thyristor switches S_{ac} is utilized to bypass the whole H-bridge SM.

In Fig. 1, v_{kj} and i_{dckj} represent the ac side voltage and dc side current of jth H-bridge cell in k phase, where k = a, b, c stands for the phase and $j = 1, 2, \ldots, n$ stands for the H-bridge cell number. v_{Ckj}, v_{bkj} and i_{bkj} represent capacitor voltage, battery voltage and current of jth H-bridge cell in k phase. v_k and i_k represent the CHB converter output voltage and phase current of k phase.

B. SM AC-Side Directly-Bypassing Method

As shown in Fig. 2(a), the conventional fault-tolerant method directly bypasses whole fault SM by ac-side switches. Fig. 3 shows two states of this process. After receiving fault diagnosis information from BMS, the healthy H-bridge first output a zero level; and then the bypassing switches turn on to avoid short circuit. Simultaneously at other phases, two healthy SMs at the same position are also bypassed for physical symmetry of three-phase arms. Furthermore, the modulation voltage of rest SMs should be enlarged to match the grid voltage and carriers also need to be arranged. Usually, one or more reductant SMs are employed and operate in hot standby duty to avoid over-modulation after quitting fault SMs.

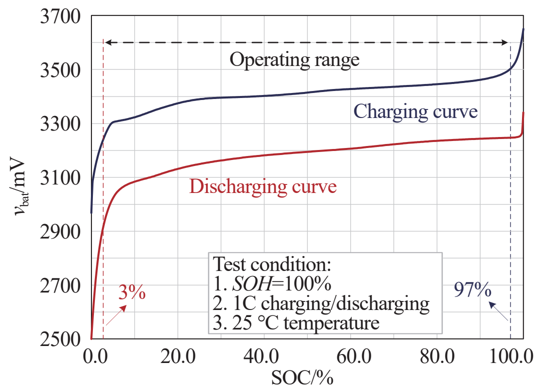

Fig. 4. Charging and discharging curves of battery output voltage to SOC.

For Lithium battery application, the output port has a wide voltage range during its whole SOC area as shown in Fig. 4. Therefore, configuration of battery should take the minimum port voltage into account and it is the terminal voltage during discharging process that decides whether the set of battery configuration meets the grid-tied requirement. Fig. 4 shows that the 1C charging curve is always much higher than the discharging curve, which means the charging operation has lower risk of overmodulating. In order to avoid overcharging and over discharging, threshold values of port voltage at charging and discharging state are set at 2.90 V and 3.50 V, which corresponds to 3% and 97% SOC at 1C condition, respectively.

Taking 35kV/20MW/20MWh TGT-BESS as an example, 2703.2V-rated cells are connected in series to form an 864V-rated battery cluster. Each phase leg has 38 SMs in normal operation and only contains one redundant SM considering the minimum 2.9 V cell voltage. After bypassing some fault SMs, low SOC range are cut down and the utilization ratio of capacity is reduced gradually as the fault number increases. Therefore, the conventional ac-side directly bypassing method has limited capability of fault tolerance operation while the potential of healthy power H-bridge modules that may exist is also wasted.

C. A New Battery Cluster Fault Tolerance Strategy

Based on aforementioned discussion, Lithium battery has significantly greater probability of occurrence of warning or fault than semiconductor switch, especially at charge and discharge terminal. As a result, H-bridge part after removing battery cluster can also be made full use of and may have some potential to be exploited further.

Thereby, a new battery cluster fault tolerance strategy is proposed as shown in Fig. 2(b). After receiving fault diagnosis or battery warning information from BMS, battery clusters are disconnected from H-bridge and PM part continues to operate in main circuit. Assuming that voltage drop of grid-side filtering

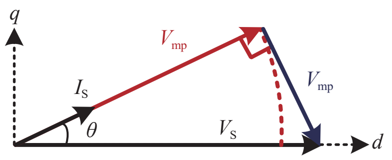

Fig. 5. Phase diagram of modulation voltage.

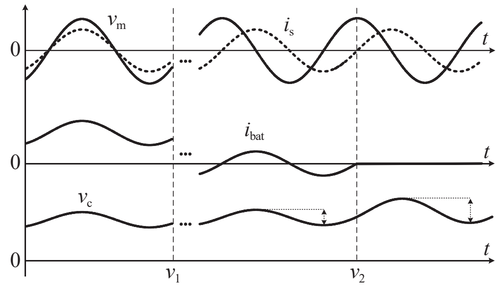

Fig. 6. Key waveforms during battery cluster exiting process.

inductor is ignored, the fundamental frequency element of output voltage of converter is equivalent to grid voltage V_s, which also equals to converter modulation signals. Fig. 5 shows phase diagram of modulation voltage of healthy SMs and fault-tolerant PMs. The modulation of converter is decomposed into two vectors: modulation voltage of healthy SMs V_{mp} is in phase with grid-side current I_s and modulation voltage of PMs V_{mq} is perpendicular with I_s. Their relationship can be expressed as following:

$$V_{mp} = \sqrt{V_S^2 - V_{mq}^2} \tag{1}$$

In this situation, the power factor of system deviates from unity value, where healthy SMs continues to be charged and discharged while faulty SMs operate in mode of reactive power due to absence of battery active power.

Beneficially, non-faulty SMs should not output a voltage which amplitude is nearly identical to grid voltage like the conventional directly bypassing SMs. Due to the voltage support brought by the PMs of faulty SMs, the voltage amplitude outputted by rest healthy SMs is reduced as (1) and their overmodulation after occurrence of fault is avoided.

Fig. 6 shows key waveform of SMs during battery cluster exiting process to illustrate the principle of proposed fault tolerance strategy:

State 1[t_0–t_1]: SM operates in discharging or charging state and its modulation voltage has the same or opposite phase as the phase current. It can be seen that battery current and capacitor voltage all have a dc bias value. A fluctuating component due to pulsating power of single-phase topology.

State 2[t_1–t_2]: Receiving fault diagnosis or battery warning information at t_1, its modulation voltage vector is regulated to be orthogonal with phase current vector. Thus, battery cluster stops charging or discharging and its dc bias current is removed. In this state, the cross zero point of battery current is always detected.

State 3[t_2–t_3]: At a certain cross zero point of t_2, a turn-off signal is given to dc circuit breaker and the faulty cluster is disconnected from its PM. And this H-bridge part continues to operate in mode of reactive power to support the grid voltage.

III. Proposed Battery Cluster Fault Tolerance Control for CHB-Based BESS

From aforementioned analysis, when whole faulty SMs are directly bypassed at ac side, the modulation margin of rest SMs is reduced gradually and this may result in overmodulation. The strategy of battery cluster exiting at dc side make full use of potential of non-faulty H-bridge power part to support grid voltage. However, more complex control is required to achieve SOC balancing of healthy SMs and capacitor voltage balancing of faulty SMs. Thereby, this section represents a battery cluster fault tolerance operating control for TGT-BESS combining proposed fault-tolerant strategy and zero sequence voltage injection to minimize reactive power of system.

A. Battery Cluster Fault Tolerance Control Based on THVI and Proposed Battery Cluster DC-Side Exiting Strategy

As shown in Fig. 5, when faulty SMs provide voltage support by their H-bridge part for converter, the system should output a certain reactive power. As the amplitude that should be outputted by faulty SMs increases, the ratio of reactive to active power becomes more and more large. This will lead to a uncomplete range of four quadrant operation. In order to enhance power factor of system as much as possible after occurrence of battery warning or fault, the proposed battery cluster fault tolerance strategy is improved by optimal THVI and analyzed in this part.

In order to more easily implement the fault tolerance, symmetrical exiting strategy is used, where three battery clusters at the same position of different phases are disconnected from their respective PMs when any cluster has a fault. Hence, the charging or discharging power should be regulated as follow:

$$P_{sys} = \operatorname{sgn}(P_{set}) \cdot \min\left(\left| P_{set} \right|, \frac{n - n_{fal}}{n} P_{nom} \right) \tag{2}$$

where P_{set} and P_{nom} denote the set target power and normalized active power when all batteries work well. n_{fal} represents the number of faulty SMs in each phase.

To simplify the analysis, the following assumptions are established.

1) The voltage drop of grid-side filtering inductor is neglected and the amplitude of modulation voltage of each phase V_m is equal to that of grid phase voltage V_s.

2) Inner-phase SOC of non-faulty SMs is well balanced and their sum dc voltage V_{bat} is equal to $(n-n_{fal})v_{bat}$, where v_{bat} is battery voltage of each healthy SMs.

3) Inner-phase capacitor voltage of faulty SMs is well balanced and their sum dc voltage V_C is equal to $n_{fal}v_C$, where v_C is capacitance voltage of each faulty PMs.

Defining the amplitude of injected third harmonic voltage (THV) as V_{THV}, when non-faulty SMs have enough margin to

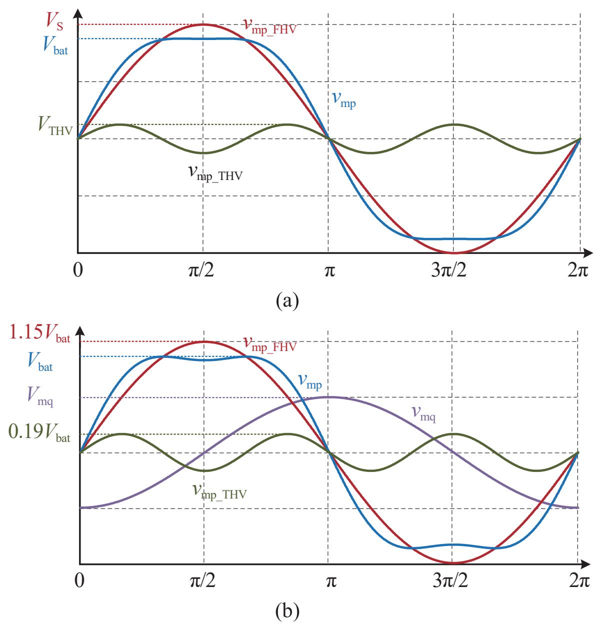

Fig. 7. Schematic diagram of modulation voltage of faulty and non-faulty SMs. (a) $\sqrt{3}/2\,V_s \leqslant V_{bat} < V_s$. (b) $V_{bat} < \sqrt{3}/2\,V_s$.

generate modulation voltage, the grid voltage is supported only by non-faulty SMs.

$$\begin{cases} V_{mp} = V_S \\ V_{mq} = 0,\ V_{bat} = (n - n_{fal}) v_{bat} \geqslant V_S \\ V_{THV} = 0 \end{cases} \tag{3}$$

If $V_{bat} < V_s$, THV is injected to enhance dc voltage utilization ratio of healthy SMs as shown in Fig. 7(a). Assuming that non-faulty SMs can output a voltage with its amplitude of the first harmonic voltage (FHV) equal to V_s, the modulation voltage of healthy SMs can be expressed as

$$v_{mp} = V_s \sin(\omega t) + V_{THV} \sin 3\omega t \tag{4}$$

Take the derivative of (4) as

$$\left.\frac{dv_{mp}}{d\omega t}\right|_{\omega t=\theta_0} = V_S \cos\theta_0 + 3V_{THV}\cos 3\theta_0 = 0 \tag{5}$$

θ_0 represents the angle at the peak value of v_{mp}, which results in

$$\sin\theta_0 = \sqrt{\frac{V_S + 3V_{THV}}{12V_{THV}}} \tag{6}$$

Substitute (6) into (4), an extreme value of the function v_{mp} is solved as

$$v_{mp\_ext1} = \frac{V_S + 3V_{THV}}{3}\sqrt{\frac{V_S + 3V_{THV}}{3V_{THV}}} \tag{7}$$

It is easy to solve another extreme value of the function v_{mp} at the extreme point of $\pi/2$ as

$$v_{mp\_ext2} = V_S - V_{THV} \tag{8}$$

On this basis, the amplitude of modulation voltage of non-faulty SMs can be derived as

$$v_{mp\_max} = \begin{cases} v_{mp\_ext2},\ V_{THV} \leqslant \dfrac{V_S}{9} \\ v_{mp\_ext1},\ V_{THV} > \dfrac{V_S}{9} \end{cases} \tag{9}$$

Take the derivative of (7)

$$\frac{dv_{mp\_max}}{dV_{THV}} = \frac{6V_{THV} - V_S}{6V_{THV}}\sqrt{\frac{V_S + 3V_{THV}}{3V_{THV}}} = 0 \tag{10}$$

From (7), when $V_{THV} = V_s/6$, v_{mp_max} has the minimum value as

$$V_{mp\_min} = \frac{\sqrt{3}}{2} V_S \tag{11}$$

When $V_{mp\_min} \leqslant V_{bat}$, THVI can help non-faulty SMs to generate modulation voltage. As shown in Fig. 7(a), the amplitude of modulation voltage of non-faulty SMs after injecting THV is equal to V_{bat}. The amplitude of injected THV can be calculated as

$$V_{THV} = \begin{cases} V_S - V_{bat}, V_{bat} \geqslant \dfrac{8}{9} V_S \\ f(V_S, V_{bat}), V_{bat} < \dfrac{8}{9} V_S \end{cases} \tag{12}$$

In (12), the function $f(V_s, V_{bat})$ is calculate according to the equation that (7) is equal to V_{bat} and is derived as

$$f(V_S, V_{bat}) = \left(\sqrt{\frac{V_S^2 V_{bat}^4}{36} - \frac{V_{bat}^6}{27}} - \frac{V_S V_{bat}^2}{6}\right)^{\frac{1}{3}} - \frac{V_S}{3} + \frac{V_{bat}^2}{3\left(\sqrt{\dfrac{V_S^2 V_{bat}^4}{36} - \dfrac{V_{bat}^6}{27}} - \dfrac{V_S V_{bat}^2}{6}\right)^{\frac{1}{3}}} \tag{13}$$

In this situation, faulty SMs are still not required to output voltage to support grid voltage, and the following equation can be obtained:

$$\begin{cases} V_{mp} = V_S \\ V_{mq} = 0 \end{cases},\ \frac{\sqrt{3}}{2} V_S \leqslant V_{bat} < V_S \tag{14}$$

In (14), V_{THV} is equal to (12).

When the sum dc voltage of non-faulty SMs is not enough high to match the grid voltage even though the optimal THV with amplitude has been injected, to wit $V_{mp\_min} > V_{bat}$, faulty SMs are required to output voltage to some extent.

As seen from (11) and according to duality theory, it is not difficult to obtain the maximum amplitude of FHV that can be generated by non-faulty SMs and its corresponding injected THV as

TABLE I
SIMULATION MODEL PARAMETERS

Parameters	Symbol	Values
Cascaded number per phase	n	14
System active power/capacity	P_{nom}/Q_{nom}	5 MW
Rated voltage of BM	V_{bat}	720 V
Battery internal resistor	r_{bat}	0.1 Ω
Grid line-to-line voltage	V_{grid}	10 kV
DC filtering capacitor	C_{dc}	10 mF
DC filtering inductor	L_{dc}	2 mH
Grid-side filtering inductor	L_f	6 mH
SM switching frequency	f_{sw}	1 kHz

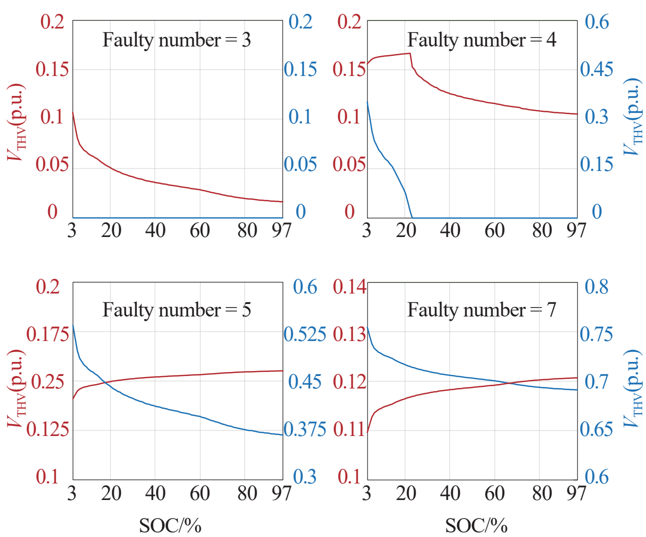

Fig. 8. Curves of THV by healthy SMs and supporting voltage by faulty SMs at different number of faulty SMs during whole discharging SOC range.

$$V_{mp}=\frac{2}{\sqrt{3}}V_{bat}, V_{THV}=\frac{\sqrt{3}}{9}V_{bat} \tag{15}$$

Accordingly, the amplitude of output voltage that should be generated by faulty SMs to support grid voltage can be deduced as

$$V_{mq}=\sqrt{V_S^2-V_{mp}^2}=\sqrt{V_S^2-\frac{4}{3}V_{bat}^2} \tag{16}$$

In this case as depicted in Fig. 7(b), the following equation can be obtained:

$$\begin{cases} V_{mp}=\dfrac{2}{\sqrt{3}}V_{bat} \\ V_{mq}=\sqrt{V_S^2-\dfrac{4}{3}V_{bat}^2}, \ V_{bat}<\dfrac{\sqrt{3}}{2}V_S \\ V_{THV}=\dfrac{\sqrt{3}}{9}V_{bat} \end{cases} \tag{17}$$

Based on aforementioned discussion about three cases, the target reactive power of system should be set as

$$Q_{sys}=\begin{cases} 0, V_{bat}\geqslant\dfrac{\sqrt{3}}{2}V_S \\ \dfrac{\sqrt{3V_S^2-4V_{bat}^2}}{2V_{bat}}P_{sys}, V_{bat}<\dfrac{\sqrt{3}}{2}V_S \end{cases} \tag{18}$$

On this ground, considering the systematic parameters given in Table I, Fig. 8 shows THV by healthy SMs and supporting voltage by faulty SMs at different number of faulty SMs during whole discharging SOC range. It is obvious that higher voltage outputted by faulty SMs is needed as faulty number increases and battery SOC decreases. By contrast, THV has limited the reductant capability while faulty SMs mainly bear the function of supporting voltage as occurrence of more and more faulty SMs.

B. Capacitor Voltage Average Value and Balancing Control of Faulty PMs

Once the battery cluster is removed from SMs, their capacitor voltage is not anymore clamped by the battery. Therefore, the sum of capacitor voltage in a phase should be control actively to track a reference value and capacitor voltage of all PMs in a phase should be balanced in real-time.

As shown in Fig. 5, in order to ensure that the modulation voltage of faulty SMs is always orthogonal with grid current, its components on dq axis should be set as

$$\begin{cases} V_{Qd}=V_{mq}\cos\left(\dfrac{\pi}{2}-\theta\right)=V_{mq}\sin\theta \\ V_{Qq}=V_{mq}\sin\left(\dfrac{\pi}{2}-\theta\right)=-V_{mq}\cos\theta \end{cases} \tag{19}$$

Then, three-phase modulation voltage V_{Ck} of faulty SMs are obtained by dq/abc transformation as depicted in Fig. 9(a). To stabilize the sum of capacitor voltage in each phase, the capacitor average voltage per phase V_{Ck_avg} should be equal to the reference value V_{C_ref} and a PI controller is utilized for superposing a voltage ΔV_{Ck}, which is in-phase or antiphase with its phase current i_k. The superposed voltage can be realized by

$$\Delta V_{Ck}=\left(k_{p,1}+\frac{k_{i,1}}{S}\right)(V_{C\_ref}-V_{Ck\_avg})i_k \tag{20}$$

where $k_{p,1}$ and $k_{i,1}$ are proportion and integral coefficients of the capacitor voltage PI controller, respectively.

Furthermore, the modulation voltage of each faulty SMs can be obtained

$$v_{Cki}=\frac{v_{Ck}+\Delta v_{Ck}}{n_{fal}} \tag{21}$$

For balancing capacitor voltage of inner phase faulty SMs, a PI controller is utilized for superposing a voltage Δv_{Cki}, which is in-phase or antiphase with its phase current i_k. The superposed voltage can be realized by

$$\Delta v_{Cki}=\left(k_{p,2}+\frac{k_{i,2}}{S}\right)(v_{Ck\_avg}-v_{Cki})i_k \tag{22}$$

where $k_{p,2}$ and $k_{i,2}$ are proportion and integral coefficients of the

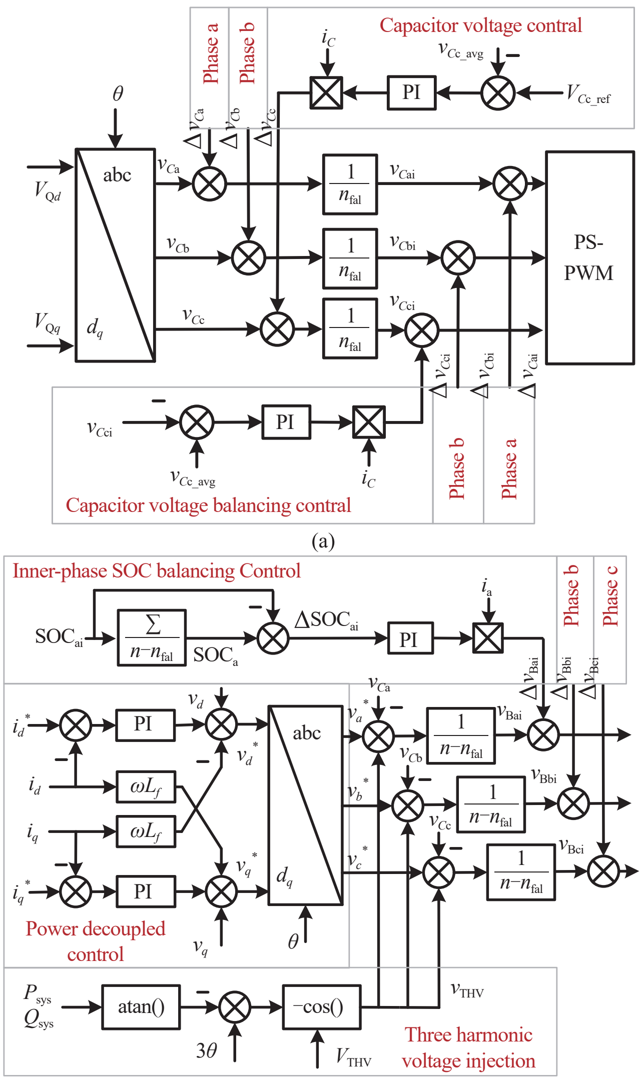

(a)

(b)

Fig. 9. Control schematic diagram. (a) Capacitor voltage control of faulty SMs . (b) SOC balancing control of non-faulty SMs.

capacitor voltage balancing PI controller, respectively.

C. Inner-Phase SOC Balancing Control of Non-Faulty SMs

As shown in Fig. 9(b), power decoupled control at *dq* axis is utilized to control grid-side active and reactive power and generate whole modulation voltage v_k^* of three-phase arms. After subtracting modulation voltage of faulty SMs, the modulation voltage v_{Bki} of each non-faulty SMs can be obtained as

$$v_{BKi}=\frac{v_K^*+v_{\mathrm{THV}}-v_{CK}}{n-n_{\mathrm{fal}}} \tag{23}$$

As shown in Fig. 9(b), the phase of THV should be identical with FHV generated by non-faulty SMs and it can be expressed as

$$v_{\mathrm{THV}}=-V_{\mathrm{THV}}\cos\left[3\theta-\operatorname{atan}\left(\frac{Q_{\mathrm{sys}}}{P_{\mathrm{sys}}}\right)\right] \tag{24}$$

Similarly, for balancing SOC of inner phase non-faulty SMs, a PI controller is utilized for superposing a voltage ΔV_{Bki}, which is in-phase or anti-phase with its phase current i_k. The superposed voltage can be realized by

$$\Delta v_{Bki}=\left(k_{\mathrm{p},3}+\frac{k_{\mathrm{i},3}}{S}\right)(SOC_k-SOC_{ki})i_k \tag{25}$$

where $k_{\mathrm{p},3}$ and $k_{\mathrm{i},3}$ are proportion and integral coefficients of the SOC balancing PI controller, respectively.

IV. Verification and Discussion

A. Software Offline Simulation

To verify the effectiveness of the proposed fault-tolerance algorithm based on the strategy of battery cluster exiting at dc side, simulation models of the three-phase 10 kV TGT-BESS are built using MATLAB/Simulink. Structural diagram of the simulation model is shown in Fig. 1 and Table I lists the main system parameters.

The steady-state and dynamic-state control performance of TGT-BESS under the proposed fault-tolerance algorithm are validated through various studies. At the beginning of simulation, the system output nominal 5 MW active power and the power factor is unity. The voltage of batter cluster is set at the minimum value 670 V. In order to test the proposed approach, three battery clusters are exited at 0.1 s and more two clusters are disconnected at 0.3 s and 0.5 s, respectively. Fig. 10(a) and (b) shows three-phase active and reactive power and grid-connected current waveform of the system, respectively. It can be observed that at 0.1–0.3 s (Case 1) the reactive power is zero, which means that no voltage should be output by faulty 3 SMs and is consistent with analysis in Fig. 8. In addition, at 0.3–0.5 s (Case 2) and 0.5–0.8 s (Case 3), a certain reactive power is output to ensure that rest healthy SMs can continuous to discharge.

Fig. 10(c) shows the average value of capacitor voltage of each phase faulty SMs and Fig. 10(d) shows the waveforms of modulation voltage of faulty SMs, respectively. Although at 0.1–0.3 s no voltage is needed to support grid voltage, faulty SMs output will output a small voltage after fault occurrence to control the capacitor voltage to follow its given reference 900 V. At Cases 2 and 3, the voltage by faulty SMs is enlarged to 0.5 V_s and 0.75 V_s. Fig. 10(e) indicates injected THV at different cases and its amplitude complies with analytical calculation.

Capacitor voltage waveforms of all faulty and healthy SMs in phase a are depicted in Fig. 10 (f), (g) and (h). At 0.1 s, three faulty SMs disconnect their battery and their capacitor voltage are charged to 900 V. In this case, no fluctuating voltage is observed owing to zero reactive power. At 0.3 s, capacitor voltage of #1–3 decreases and that of #4–5 increases, which is attributed to capacitor voltage balancing algorithm. Finally, their voltages are stable at 900 V and have a certain fluctuated component.

THVI helps to decrease the modulation ratio and healthy SMs can output a as large first harmonic component as pos-

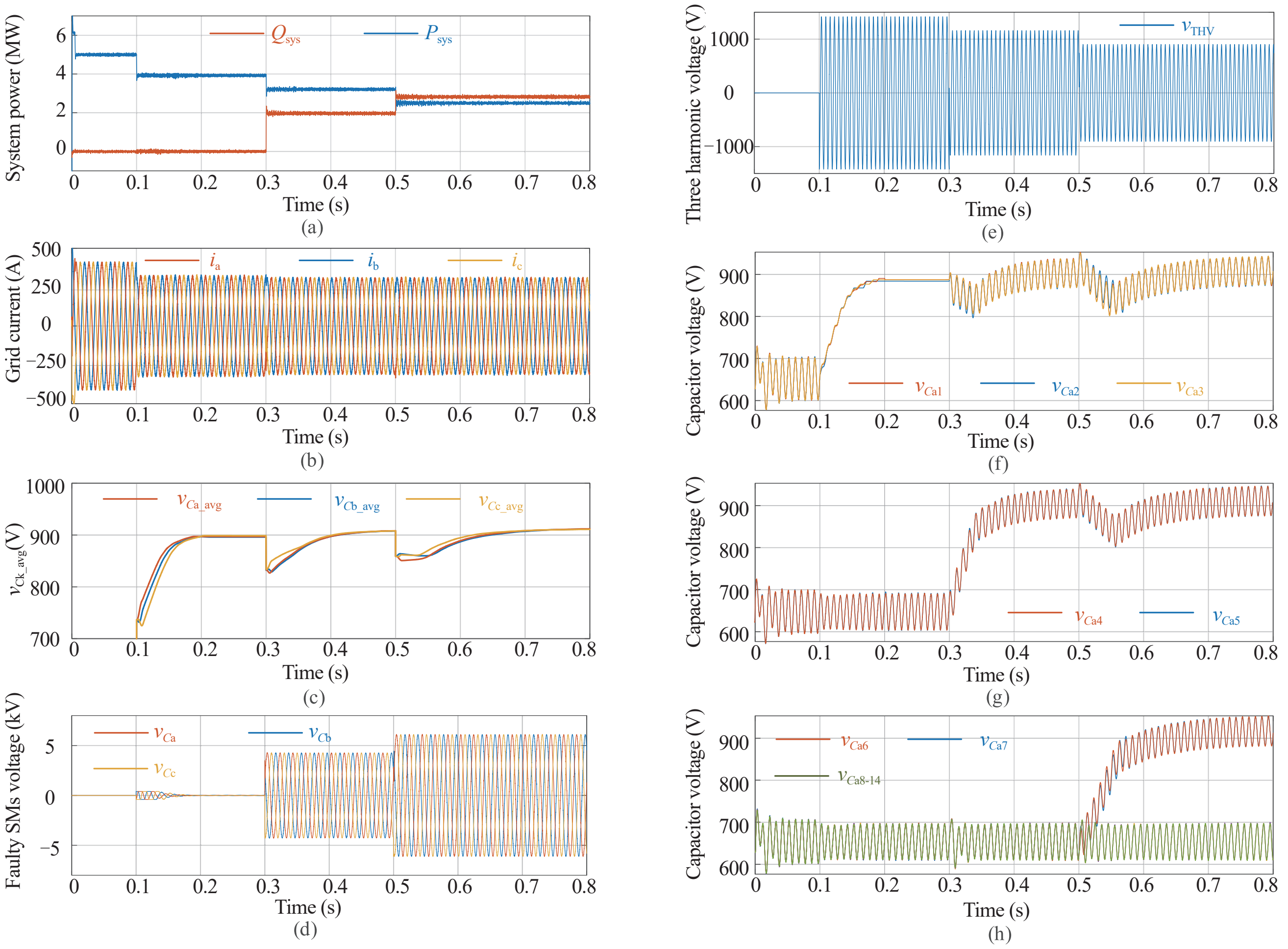

Fig. 10. Simulation results of the proposed battery cluster fault tolerance strategy. (a) System active and reactive power. (b) Grid side current. (c) Average value of capacitor voltage of faulty SMs. (d) Modulation voltage of faulty SMs. (e) Injected THV. (f) Capacitor voltage waveforms of #1−3 SMs in phase a. (g) Capacitor voltage waveforms of #4−5 SMs in phase a. (h) Capacitor voltage waveforms of #6−14 SMs in phase a.

sible. This is reflected in the modulation voltage waveforms of three-phase non-faulty SMs around 0.1 s as shown in Fig. 11(a1)−(a3). Similar effects can be observed around 0.3 s and 0.5 s in Fig. 11(b1)−(b3) and (c1)−(c3). After superimposing THV over the modulation signals, output voltage waveforms of faulty and healthy SMs are demonstrated in Fig. 11 (a4)−(a5), which are step wave and overmodulation is avoided. This verifies the effectiveness of zero sequence voltage injection to minimize reactive power of system.

For the purpose of validating proposed battery cluster fault tolerance operating control for TGT-BESS combining proposed fault-tolerant strategy and optimal zero sequence voltage injection, modulation ratio of healthy and faulty SMs of proposed fault-tolerance method at different faulty number are demonstrated in Fig. 12. Correspondingly, the modulation ratio of conventional bypassing method is obtained by simulation. It can be seen that the conventional method has critical margin at the occurrence of two clusters. However, avoidance of overmodulation of not only healthy SMs and faulty SMs can always be guaranteed at any number faulty SMs with proposed algorithm.

B. HIL Experiment

To verify the feasibility of implementing proposed control technique in actual digital controller, an HIL experimental platform is constructed, as shown in Fig. 13. Detailed switching circuits of the TGT-BESS are established in the real-time digital simulator MT-8020, and all control algorithms in Fig. 9 are implemented in the controller framework composed of a TMS320C28346 DSP and an XC6SLX25 FPGA. The parameters of the main circuit are same with that listed in Table I. The difference of between offline and real-time models is that only one phase arm and 14 SMs run in simulator since the DSP+FPGA controller has maximum 60 PWM channels. In spite of this, all key control methods can be tested and verified completely with such a single phase system.

Seven SMs are set in sequence with occurrence of faulty signals and Fig. 14 gives key waveforms to illustrate the process before and after fault under employing proposed fault-tolerance method. Grid voltage and current waveforms are captured to show that the system always has enough modulation ratio margin to control grid current after battery clusters are disconnected from H-bridges. At the situation with

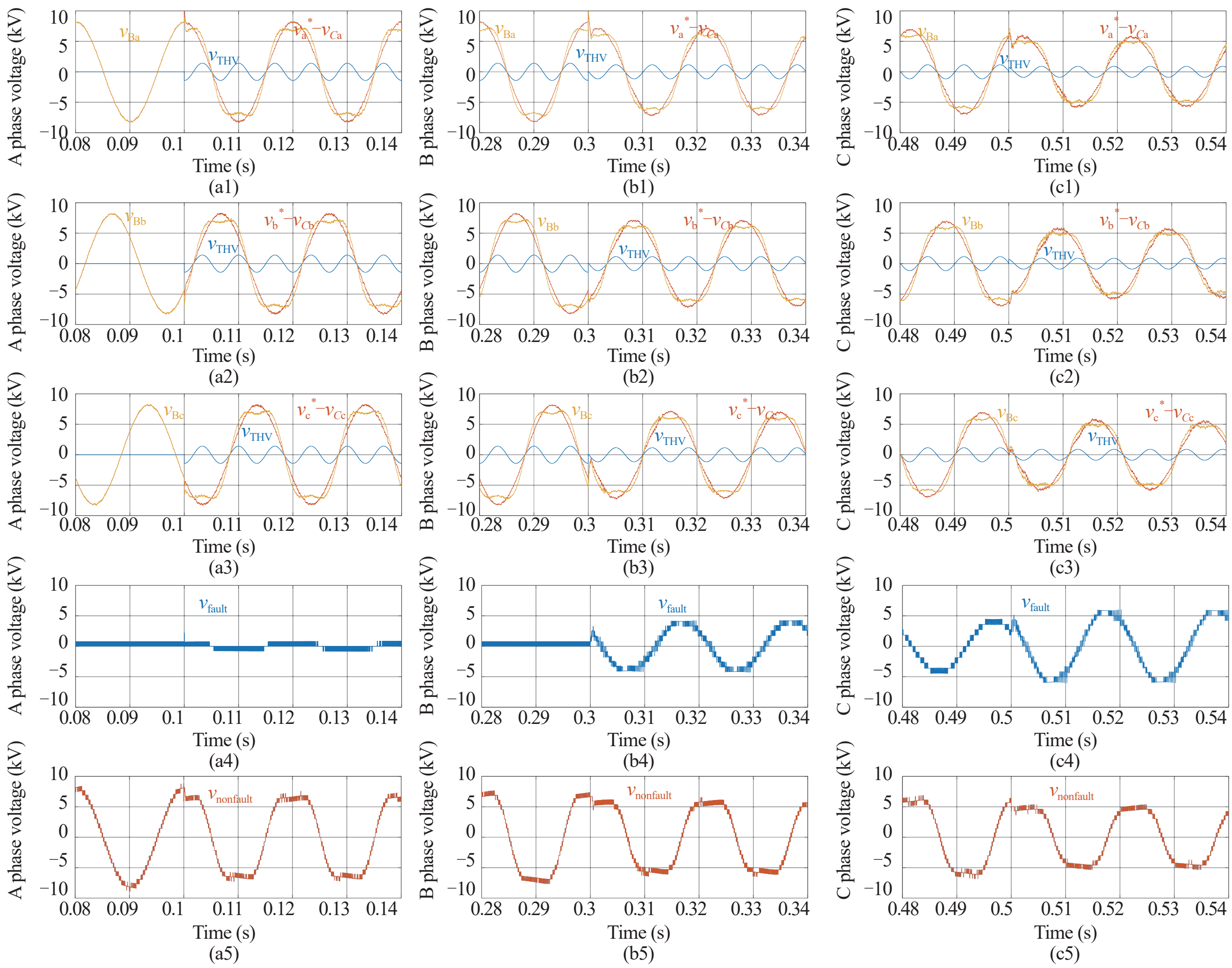

Fig. 11. Simulation results of three-phase modulation voltage of nonfaulty SMs and the output voltage by faulty and nonfaulty SMs. (a1–a5) Around the occurrence of 5 battery clusters fault. (b1–b5) Around the occurrence of 3 battery clusters fault. (c1–c5) Around the occurrence of 7 battery clusters fault.

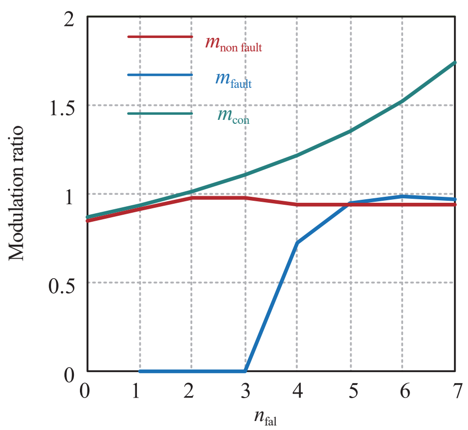

Fig. 12. Simulated modulation ratio of conventional bypassing method and healthy and faulty SMs of proposed fault-tolerance method at different faulty number.

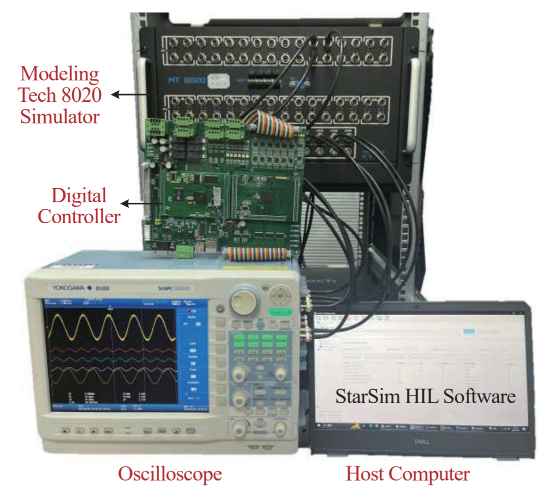

Fig. 13. HIL experimental platform.

one faulty SM, as can be seen, faulty SMs modulation voltage and THV all are zero and the whole dc-side voltage of 13 healthy SMs is still higher than the amplitude of grid voltage. This is corresponding with (3). When 2 and 3 faulty SMs are formed, injecting a certain THV can help to avoid system over-modulation and faulty SMs is also no required to output volt-

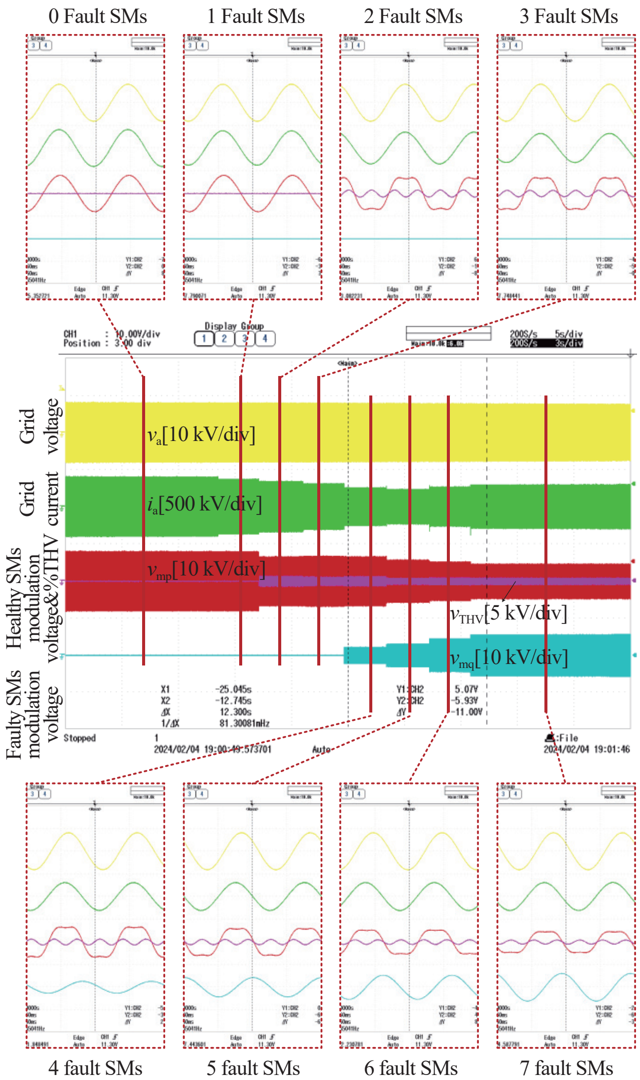

Fig. 14. Key voltage and current waveforms during the process of continuous occurrence of seven faulty SMs.

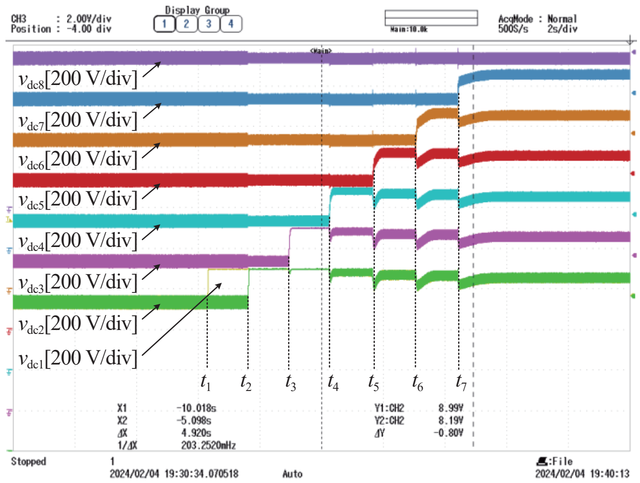

Fig. 15. Capacitor voltage waveforms of #1-8 SMs during the process of continuous occurrence of seven faulty SMs.

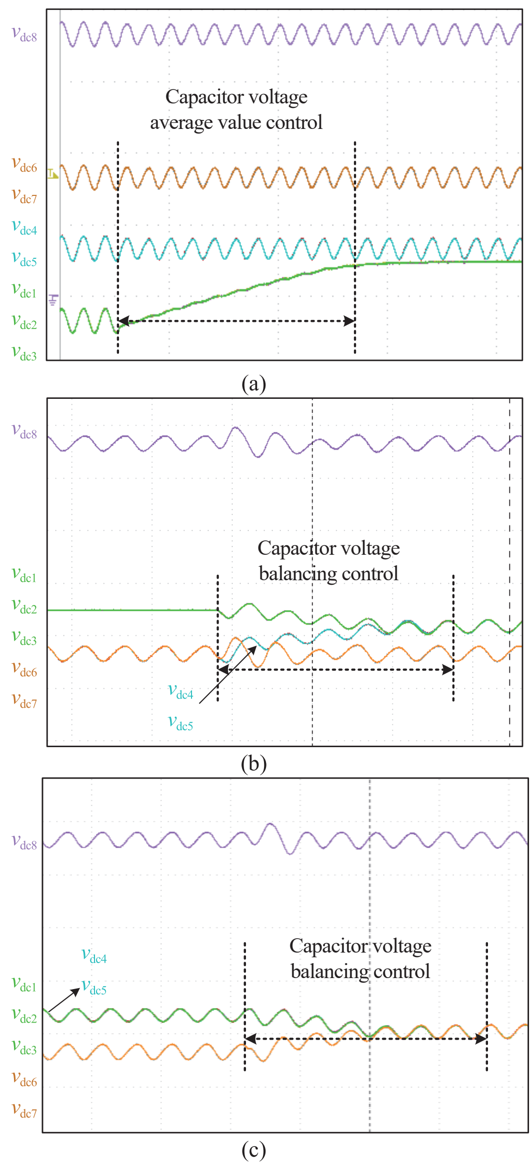

Fig. 16. Enlarged capacitor voltage waveforms of #1−8 SMs.

age, which is corresponding with (14). Definitely, with more faulty battery clusters are disconnected, only injecting THV has no ability to make the whole battery voltage match the grid voltage. According to (18), faulty SMs should output a certain passive voltage and power to render healthy SMs to continuously operate in charging or discharging mode. It is obvious that faulty SMs modulation voltage gradually increases as more faulty SMs occur.

In order to show the fault-tolerance process of each faulty SMs, dc-side voltage waveforms are observed by 8 channels oscilloscope as shown in Fig. 15. Due to healthy SMs have nearly identical dynamic and stable actions, only eighth SM is observed and the ninth to fourth SMs are be regarded as the same with it. From Fig. 15, before faulty SMs output supported voltage, the capacitor voltage of #1−3 SMs is fast charged to 900 V after battery is cut off. When faulty SMs output passive power, there is also fluctuating voltage superposing over capacitor voltage. As shown in Fig. 16(a), capacitor voltage average value control as (20) renders the average voltage of faulty SMs track to its reference although they do not need to output power at stable state. Meanwhile, when another two SMs operate in fault-tolerance mode as Fig. 16(b) and (c), capacitor voltage balancing control make all faulty SMs voltage to be equalized first and then charged. This is in consistent with theoretical analysis and offline simulation.

V. Conclusion

In this article, a fault tolerance strategy for multi-battery clusters of TGT-BESS is proposed to ensure the continuous and reliable operation of the large-capacity system. Disconnecting warning or faulty battery by itself dc breaker rather than bypassing whole SMs with ac bypass circuitry, the H-bridge part of faulty SMs can continue to operate as a reactive device. Advantageously, the faulty SMs are made the use of and has the capability of outputting a reactive voltage, which help to decrease the modulation voltage by rest healthy SMs and avoid overmodulation. Furthermore, a battery cluster fault tolerance operating control for TGT-BESS combining proposed fault-tolerant strategy and optimal zero sequence voltage injection is proposed to tolerate any number of faulty battery cluster modules. At last, a 10 kV/5 MW TGT-BESS for principal validation is built in simulation platform of MATLAB/Simulink and a HIL experimental platform. The simulation and experimental results all verify the feasibility of the proposed fault tolerance operating control under occurrence of multi-clusters fault. However, it can be seen that this method will change the steady-state operating point and power factor of the system. Further research is needed on fault isolation and fault-tolerant operation strategies that do not affect the external characteristics of the system. The binary star modular multilevel topology is expected to solve this problem in future research.

References

[1] S. Vazquez, S. M. Lukic, E. Galvan, L. G. Franquelo, and J. M. Carrasco, "Energy storage systems for transport and grid applications, " in *IEEE Transactions on Industrial Electronics*, vol. 57, no. 12, pp. 3881–3895, Dec. 2010.

[2] B. Dunn, H. Kamath, and J.-M. Tarascon, "Electrical energy storage for the grid: A battery of choices, " in *Science*, vol. 334, no. 6058, pp. 928–935, Nov. 2011.

[3] F. Calero, C. A. Cañizares, K. Bhattacharya, C. Anierobi, I. Calero, M. F. Z. de Souza, M. Farrokhabadi, N. S. Guzman, W. Mendieta, D. Peralta, B. V. Solanki, N. Padmanabhan, and W. Violante, "A review of modeling and applications of energy storage systems in power grids," in *Proceedings of the IEEE*, vol. 111, no. 7, pp. 806–831, Jul. 2023.

[4] X. Li and S. Wang, "Energy management and operational control methods for grid battery energy storage systems," in *CSEE Journal of Power and Energy Systems*, vol. 7, no. 5, pp. 1026–1040, Sept. 2021.

[5] M. Liu, X. Cao, C. Cao, P. Wang, C. Wang, J. Pei, H. Lei, X. Jiang, R. Li, and J. Li, "A review of power conversion systems and design schemes of high-capacity battery energy storage systems," in *IEEE Access*, vol. 10, pp. 52030–52042, 2022.

[6] L. Maharjan, S. Inoue, and H. Akagi, "A transformerless energy storage system based on a cascade multilevel PWM converter with star configuration," in *IEEE Transactions on Industry Applications*, vol. 44, no. 5, pp. 1621–1630, Sept.-Oct. 2008.

[7] C. Liu, N. Gao, X. Cai, and R. Li, "Differentiation power control of modules in second-life battery energy storage system based on cascaded H-bridge converter," in *IEEE Transactions on Power Electronics*, vol. 35, no. 6, pp. 6609–6624, Jun. 2020.

[8] C. Liu, X. Cai, and Q. Chen, "Self-adaptation control of second-life battery energy storage system based on cascaded H-bridge converter," in *IEEE Journal of Emerging and Selected Topics in Power Electronics*, vol. 8, no. 2, pp. 1428–1441, Jun. 2020.

[9] J. I. Y. Ota, T. Sato, and H. Akagi, "Enhancement of performance, availability, and flexibility of a battery energy storage system based on a modular multilevel cascaded converter (MMCC-SSBC)," in *IEEE Transactions on Power Electronics*, vol. 31, no. 4, pp. 2791–2799, Apr. 2016.

[10] L. Maharjan, S. Inoue, H. Akagi, and J. Asakura, "State-of-charge (SOC)-balancing control of a battery energy storage system based on a cascade PWM converter," in *IEEE Transactions on Power Electronics*, vol. 24, no. 6, pp. 1628–1636, Jun. 2009.

[11] H. Xue, J. He, Y. Ren, and P. Guo, "Seamless fault-tolerant control for cascaded H-bridge converters based battery energy storage system," in *IEEE Transactions on Industrial Electronics*, vol. 70, no. 4, pp. 3803–3813, Apr. 2023.

[12] L. Xiong, F. Zhuo, X. Liu, Z. Xu, and Y. Zhu, "Fault-tolerant control of CPS-PWM-based cascaded multilevel inverter with faulty units," in *IEEE Journal of Emerging and Selected Topics in Power Electronics*, vol. 7, no. 4, pp. 2486–2497, Dec. 2019.

[13] Q. Xiao, Y. Jin, H. Jia, Y. Tang, A. F. Cupertino, Y. Mu, R. Teodorescu, F. Blaabjerg, and J. Pou, "Review of fault diagnosis and fault-tolerant control methods of the modular multilevel converter under submodule failure," in *IEEE Transactions on Power Electronics*, vol. 38, no. 10, pp. 12059–12077, Oct. 2023.

[14] S. Yang, Y. Tang, and P. Wang, "Seamless fault-tolerant operation of a modular multilevel converter with switch open-circuit fault diagnosis in a distributed control architecture," in *IEEE Transactions on Power Electronics*, vol. 33, no. 8, pp. 7058–7070, Aug. 2018.

[15] B. Li, S. Shi, B. Wang, G. Wang, W. Wang, and D. Xu, "Fault diagnosis and tolerant control of single IGBT open-circuit failure in modular multilevel converters," in *IEEE Transactions on Power Electronics*, vol. 31, no. 4, pp. 3165–3176, Apr. 2016.

[16] W. Song and A. Q. Huang, "Fault-tolerant design and control strategy for cascaded H-bridge multilevel converter-based STATCOM," in *IEEE Transactions on Industrial Electronics*, vol. 57, no. 8, pp. 2700–2708, Aug. 2010.

[17] N. Bisht and A. Das, "A circuit topology of cascaded H-bridge STATCOM to operate with multiple faulty bypassed cells," in *IEEE Transactions on Industry Applications*, vol. 57, no. 5, pp. 5345–5355, Sept.-Oct. 2021.

[18] R Ahmadi, M. Aleenejad, H. Mahmoudi, and S. Jafarishiadeh, "Reduced number of auxiliary H-bridge power cells for post-fault operation of three phase cascaded H-bridge inverter," in *IET Power Electronics*, vol. 12, no. 11, pp. 2923–2931, Aug. 2019.

[19] B. Mirafzal, "Survey of fault-tolerance techniques for three-phase voltage source inverters," in *IEEE Transactions on Industrial Electronics*, vol. 61, no. 10, pp. 5192–5202, Oct. 2014.

[20] S. Farzamkia, H. Iman-Eini, A. Khoshkbar-Sadigh, and M. Noushak, "A software-based fault-tolerant strategy for modular multilevel converter using DC bus voltage control," in *IEEE Journal of Emerging and Selected Topics in Power Electronics*, vol. 9, no. 3, pp. 3436–3445, Jun. 2021.

[21] Y. Neyshabouri and H. Iman-Eini, "A new fault-tolerant strategy for a cascaded H-bridge based STATCOM," in *IEEE Transactions on Industrial Electronics*, vol. 65, no. 8, pp. 6436–6445, Aug. 2018.

[22] L. Maharjan, T. Yamagishi, H. Akagi, and J. Asakura, "Fault-tolerant operation of a battery-energy-storage system based on a multilevel cascade PWM converter with star configuration," in *IEEE Transactions on Power Electronics*, vol. 25, no. 9, pp. 2386–2396, Sept. 2010.

[23] P. Lezana and G. Ortiz, "Extended operation of cascade multicell converters under fault condition," in *IEEE Transactions on Industrial Electronics*, vol. 56, no. 7, pp. 2697–2703, Jul. 2009.

[24] Y. Yu, G. Konstantinou, B. Hredzak, and V. G. Agelidis, "Operation of cascaded H-bridge multilevel converters for large-scale photovoltaic

power plants under bridge failures," in *IEEE Transactions on Industrial Electronics*, vol. 62, no. 11, pp. 7228–7236, Nov. 2015.

[25] Q. Xiao, L. Chen, Y. Jin, Y. Mu, A. F. Cupertino, H. Jia, Y. Neyshabouri, T. Dragičević, and R. Teodorescu, "An improved fault-tolerant control scheme for cascaded H-bridge STATCOM with higher attainable balanced line-to-line voltages," in *IEEE Transactions on Industrial Electronics*, vol. 68, no. 4, pp. 2784–2797, Apr. 2021.

[26] Y. Neyshabouri, K. K. Monfared, H. Iman-Eini, and M. Farhadi-Kangarlu, "Symmetric cascaded H-bridge multilevel inverter with enhanced multi-phase fault tolerant capability," in *IEEE Transactions on Industrial Electronics*, vol. 69, no. 9, pp. 8739–8750, Sept. 2022.

[27] H. Xue, J. He, and P. Guo, "Fault-tolerance control of battery energy storage system based on cascaded H-bridge converter," in *High Voltage Engineering*, vol. 46, no. 10, pp. 3418–3430, Sept. 2020.

[28] M. T. Lawder, B. Suthar, P. W. C. Northrop, S. De, C. M. Hoff, O. Leitermann, M. L. Crow, S. Santhanagopalan, and V. R. Subramanian, "Battery energy storage system (BESS) and battery management system (BMS) for grid-scale applications," in *Proceedings of the IEEE*, vol. 102, no. 6, pp. 1014–1030, Jun. 2014.

Xiqi Wu received the bachelor's degree in electrical engineering from Nanjing University of Aeronautics and Astronautics, China, in 2019 and received the Ph.D. degree from Shanghai Jiaotong University in 2024.

Since 2024, he has been with the Key Laboratory of Control of Power Transmission and Conversion (Shanghai Jiaotong University), Ministry of Education, Minhang District, Shanghai, China, where he is currently a post doctor. His current research interests include key technologies of battery energy storage system, renewable energy power conversion and grid forming control.

Shuai Gao received the master's degree in power electronics and power drives from Hefei University of Technology, China, in 2020.

His current research interests include high voltage energy storage system and new electricity system.

Yilin Liu received the bachelor's degree in electrical engineering from Southwest Jiaotong University, Chengdu, China, in 2022. She is currently working toward the Ph.D. degree in electrical engineering with the Key Laboratory of Control of Power Transmission and Conversion, Shanghai Jiao Tong University, Ministry of Education, Shanghai, China.

Her current research interests include key technologies of battery energy storage system and renewable energy power conversion.

Rui Li received the Ph.D. degree in electrical engineering from Zhejiang University, Hangzhou, China, in 2010.

From 2008 to 2009, he was an Academic Guest with the Power Electronic Systems Laboratory, Swiss Federal Institute of Technology, Zürich, Switzerland. From 2014 to 2015, he was a Postdoctoral Research Scholar with the Center for Advanced Power Systems, Department of Electrical and Computer Engineering, College of Engineering, Florida State University, Tallahassee, FL, USA. Since 2010, he has been with the Department of Electrical Engineering, School of Electronics, Information and Electrical Engineering, Shanghai Jiao Tong University, Shanghai, China, where he is currently an Professor since 2019. His current research interest includes the application of power electronics in renewable energy conversion. He was a recipient of the IEEE Power Electronics Society Transactions Second Prize Paper Award, in 2015.

Xinyu Jiang received the master's degree in electrical insulation and high voltage technology from Xi'an Jiaotong University, China, in 1997.

His current research interests include high voltage energy storage system and new electricity system.

Xu Cai received the B.Eng. degree from Southeast University, Nanjing, China, in 1983, the M.Sc. and the Ph.D. degrees from China University of Mining and Technology, Jiangsu, China, in 1988 and 2000, respectively.

He was with the Department of Electrical Engineering, China University of Mining and Technology, as an Associate Professor from 1989 to 2001. He joined Shanghai Jiao Tong University, as a Professor from 2002 and is a director of Wind Power Research Center of Shanghai Jiao Tong University from 2008 and vice director of State Energy Smart Grid R&D Center (Shanghai) from 2010 to 2013. His special fields of interest lie in power electronics and renewable energy exploitation and utilization, including wind power converters, wind turbine.

Multi-Functional V2G Interface With Improved Dynamic Response for Shunt Compensation

Arpitkumar J. PATEL and Amit V. SANT

***Abstract*—This paper proposes a multi-functional vehicle-to-grid (M-V2G) interface based on the new fundamental active current (FAC) extraction method for shunt compensation (SC) with enhanced dynamic response. The M-V2G operates in four modes, namely (A) active power injection (API), (B) API and SC, (C) API and partial SC, and (D) SC. The proposed FAC extraction method involves processing the *d*-axis current of non-linear load through the cascaded band-stop filter. The resulting signal comprises a dc and an ac component with six times the fundamental frequency. For balanced currents, FAC is derived as the value of this signal sampled at the absolute peak value of its derivative. For unbalanced load currents, FAC extraction considers (i) the average of six consecutive samples, or (ii) inclusion of an additional BSF with a center frequency corresponding to the 6th harmonic is included. The second option provides a faster dynamic response. M-V2G interface is controlled based on the FAC and commanded API. The proposed technique ensures accurate FAC estimation without complex computations, as evident from the pseudo-code and experimental studies. Further, the experimental results confirm its effectiveness, feasibility, and practical viability. The M-V2G interface with the proposed FAC estimation scheme increases power quality and VA utilization of the V2G interface.**

***Index Terms*—Battery, electric vehicles, multi-functional control, shunt compensation, vehicle-to-grid (V2G).**

I. Introduction

ELECTRIC vehicles (EVs) have emerged as a cleaner alternative to internal combustion (IC) based vehicles. On the other hand, for the utility, the rising number of EVs poses challenges of increased energy demand, network congestion, and power quality (PQ) issues [1]–[3]. The grid-interfaced EV charger requires an ac-dc converter at the grid side. Using a diode-based ac-dc converter at the input stage of an EV charger may be economical. However, the diode rectifier injects harmonic currents into the grid. The impact of EV charging stations on grid PQ is discussed in [4]–[5]. Further, the increasing usage of power converters in industrial, domestic, and commercial sectors deteriorates the PQ by harmonic current injection into the grid. The PQ issue is further compounded by the ever-increasing nonlinear loads [6]. The harmonic currents in the grid are responsible for the increased line losses, line congestion, mal-operation of control and protective equipment, and reduced power transfer capability [7]. PQ issues are prone to increase upon the installation of EV charging stations on a larger scale. Hence, mitigating the PQ issues at the charging station is necessary. [2] and [8] suggest the installation of a distributed static compensator (DSTATCOM) and shunt active power filter (SAPF) at the charging station to nullify current harmonics. In EV chargers, using pulse width modulated (PWM) rectifiers in place of diode-based rectifiers is beneficial with respect to the PQ concerns as it offers a unity power factor and reduces total harmonic distortion (THD) at the grid end. Moreover, the EV charger can facilitate bi-directional power flow with PWM rectifiers, provided that the bi-directional dc-dc converter is employed. This enables EV chargers to perform vehicle-to-grid (V2G) operations to offer ancillary services to the grid. The V2G operation refers to the power flow from the EV to the grid, while the grid-to-vehicle (G2V) operation refers to charging the EV battery from the grid.

EV chargers can operate in V2G mode and perform active power injection (API) to meet the active power demand of load (APDL) [9]. Such operation may not always result in complete utilization of the interface's VA capacity. Moreover, the issue of PQ degradation due to other nonlinear loads at the station premises needs to be addressed. The IGBT-based ac-dc interface of the EV charger holds a power structure similar to that of SAPF. This enables the utilization of the V2G interface to mitigate the harmonic currents drawn by the other loads at the station premises. The implementation, however, necessitates additional control loops. The multi-functional control of V2G ensures the implementation of requisite shunt compensation (SC) and/or traditional charging or API operations. Hence, for increased VA utilization and addressing current related PQ issues, a multifunctional-V2G (M-V2G) interface can be controlled to perform API and SC, which can compensate for the harmonic currents and reactive power demand of load (RPDL). For providing SC through the V2G interface, estimation of the fundamental active component (FAC) of load current is essential. This paper introduces a new FAC extractor (FACE) that offers computational simplicity, fast dynamic response, and accurate FAC estimation, even under unbalanced load conditions. The proposed M-V2G interface operates in four distinct modes, namely, (A) API, (B) API and SC, (C) API with partial SC, and (D) SC only. The proposed technique enhances VA

Manuscript received November 20, 2024; revised February 28, 2025; accepted March 27, 2025. Date of publication June 30, 2025; date of current version April 18, 2025. No funding was received to assist with the preparation of this manuscript. *(Corresponding author: Arpitkumar J. Patel.)*

Both authors are with the Department of Electrical Engineering, School of Energy Technology, Pandit Deendayal Energy University, Gandhinagar, India (e-mail: arpit.pphd20@sot.pdpu.ac.in; amit.sant@sot.pdpu.ac.in).

Digital Object Identifier 10.24295/CPSSTPEA.2025.000016

TABLE I
COMPARATIVE ANALYSIS OF M-V2G INTERFACE

Operating Modes	[9]	[11]	[12]	[13]	[14]	[15]	Proposed
API	✓	✓	✓	✗	✗	✗	✓
API and HCM	✗	✗	✗	✗	✓	✓	✓
API and RPC	✗	✗	✓	✗	✓	✓	✓
API and Partial SC	✗	✗	#	✗	✗	✗	✓
SC Only	✗	✗	✓	✓	✗	✗	✓

HCM and RPC indicate harmonic current mitigation and reactive power compensation. # indicates RPC only

utilization and PQ, even when the battery is unavailable for V2G operations.

V2G operation supports the grid by providing active power support. Several studies demonstrate how effectively V2G operations can be managed to maintain a better voltage profile in the distribution network [10]. Earlier work focused on traditional V2G operation, which could only support the grid through API [9], [11]. The interface is redundant when an EV is unavailable. Authors in [12] have investigated the V2G operation involving reactive power compensation. However, harmonic current mitigation with the V2G interface has not been explored. Control of V2G for SC with Lyapunov function is reported by Çelik [13]. However, SC with multi-functional control involving simultaneous API and SC has not been explored.

[14]–[15] have presented a V2G interface with simultaneous API and SC. However, with SC, the VA rating of the interface may be exceeded, leading to operational constraints. Thus, an advanced M-V2G interface is needed to dynamically allocate VA capacity between API and SC while preventing overloading. Furthermore, the impact of different operating modes on PQ enhancement and system utilization remains underexplored in existing studies. The operating modes reported for V2G interfaces in various references are given in Table I. When the V2G interface supplies only active power to the load, the %THD of the supply current tends to increase [16].

For the implementation of SC, estimation of the FAC of load current is mandatorily needed. FACE based on generalized integrators, second-order filters, self-tuning filters, etc., are reported in the literature [7], [17]–[19]. These methods extract the input signal's fundamental component using second or higher-order transfer functions. While effective in isolating the fundamental component, these methods inherently exhibit slower dynamic responses due to the filtering stages involved. The transient response of such systems is further limited by the need for sufficient filtering to ensure accuracy. Moreover, these methods require precise tuning of multiple control parameters, which adds to the complexity. The computational burden of these techniques also poses challenges for real-time applications, especially when higher-order or multiple filtering stages are involved, requiring additional processing resources.

Least mean square (LMS) based FAC extraction techniques are also widely reported in the literature [17], [20]–[21]. LMS algorithms employ adaptive filtering structures, providing flexibility in harmonic order selection. However, LMS-based techniques require intensive computational resources and their dynamic and steady-state performance highly depends on the learning rate, μ. A higher μ leads to a faster dynamic response but introduces oscillations in steady-state conditions [22]–[23]. Conversely, a lower μ ensures accurate estimation at the cost of sluggish dynamic response [22]–[23]. LMS algorithms with variable learning rates (VLR), as reported in [24]–[27], mitigate this issue but increase the computational burden. Additionally, improper selection of μ may lead to instability [26]–[27]. This factor limits the practical usability of LMS for high-speed FACE in M-V2G applications.

[28]–[29] have explored artificial neural network (ANN)-based techniques for FAC extraction. ANN-based approaches require pre-training on large datasets corresponding to load profiles. However, their accuracy is compromised when the operating conditions deviate from the training dataset [29]. Furthermore, ANN implementations demand significant memory and processing power, making them less viable for real-time V2G control. Their reliance on extensive pre-training also reduces adaptability in dynamic grid conditions.

[2] and [30] introduced the moving window min-max (MWM) technique for FAC extraction. The MWM technique is simpler to implement, as it does not involve explicit filtering mechanisms and exhibits a faster dynamic response (approximately half a cycle). However, in intermediate calculations, the maximum and minimum values of the d-axis load current must be determined. Since no filtering is applied, accuracy is compromised when the sensed signals contain noise. In practical scenarios, this increases susceptibility to distortions, which can reduce the effectiveness of SC operation. Alternately, a computationally simple FACE with a faster dynamic response is required to facilitate seamless transitions between the operating modes of the M-V2G interface.

This paper presents an M-V2G interface with improved dynamic response for SC. As reported in [16], four operating modes of M-V2G, namely (A) API, (B) API and SC, (C) API and partial SC, and (D) SC, are considered in this paper. The improved dynamic response for SC is obtained with the proposed FACE unit. The proposed FACE is simpler to implement and provides an accurate estimation of FAC. The key idea behind the proposed algorithm is that for a signal containing dc and ac quantity, the dc quantity can be determined by sampling

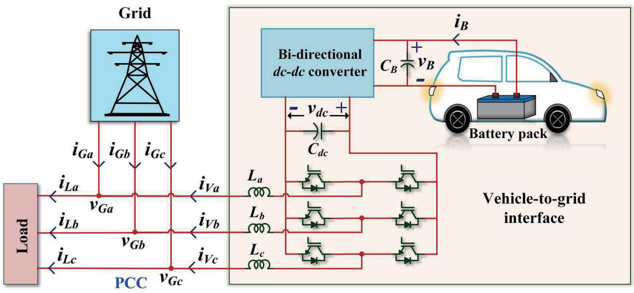

Fig. 1. Power circuit of M-V2G interface.

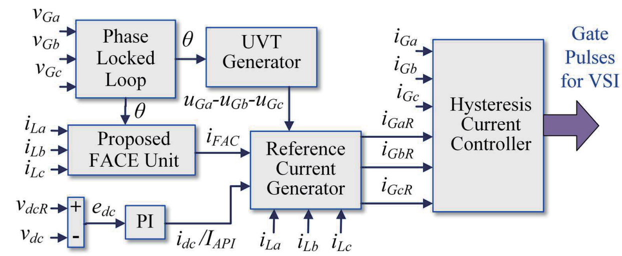

Fig. 2. Control circuit of M-V2G interface.

the signal at the peak of its derivate. This idea can be implemented for FAC extraction using d-axis load current, wherein the signal comprises both ac and dc quantities. The dc quantity represents the FAC of load current. The proposed FACE unit samples the d-axis load current, i_{Ld}, at the absolute peak value of di_{Ld}/dt. Before this, i_{Ld} has been processed through cascaded band-stop filters (CBSFs). This filtering stage is required to eliminate higher-order harmonics so that only the lowest-order harmonic is present. The dynamic response of a second-order band-stop filter is faster when tuned to attenuate higher-order harmonics at their respective center frequencies than when set for the fundamental frequency. Hence, the overall dynamic response is not significantly impacted by the involvement of a cascaded band-stop filtering stage. Further, the obtained signal at the output of CBSFs is sampled at the absolute peak of its derivative. This sampled value represents the FAC of load current, i_{FAC}, which should be drawn from the grid to ensure SC. The mathematical basis of the proposed FACE is discussed in detail in further sections. Further frequency and time domain analysis are provided to validate fast dynamic response and accuracy for FAC extraction. The FACE method is computationally efficient, ensuring fast dynamic response and ripple-free steady-state operation. Unlike LMS-based approaches, it does not require iterative adaptation or learning rate tuning. Compared to ANN-based techniques, it eliminates the dependency on pre-trained models, making it more suitable for real-time operation. Further, the performance analysis of the M-V2G interface, based on the experimental studies, with the proposed FACE unit under four modes reveals its feasibility and practicability. With the merits of accurate and fast FAC extraction, computational simplicity, and ease of implementation, the FACE unit stands out as a key contribution. Furthermore, the proposed M-V2G control strategy ensures that even when API is not feasible due to battery unavailability, the voltage source inverter (VSI) can still be utilized for SC, improving overall system efficiency. This multi-functional operation enhances PQ at the point of common coupling (PCC) and maximizes the utilization of the V2G interface.

To summarize, the key contributions of this work are: (i) M-V2G operation enabling increased VA utilization, even in the absence of a battery for API operation, (ii) a novel FACE algorithm with fast dynamic response for the implementation of SC using the M-V2G interface, (iii) frequency response analysis and step response analysis conducted to validate effective filtering and rapid dynamic response, and (iv) experimental validation of the four operating modes, demonstrating the feasibility and practical implementation of the proposed FACE-based control for the V2G interface.

II. Operation of Multi-Functional V2G Interface

The EV charger employs ac-dc and dc-dc converters to charge EV batteries from the grid. The charging process of EV batteries from the grid refers to G2V operation. EVs can provide auxiliary services to the grid, such as grid support through API. Such operation of an EV charger wherein power flows from the EV battery to the grid is referred to as the V2G operation. For EVs to facilitate V2G operations, the employed converters in the interface should be bidirectional. Fig. 1 shows the power circuit of the M-V2G interface, comprising a battery interfaced with the grid through a bidirectional dc-dc converter and VSI. VSI is interfaced with the grid through coupling inductors, L_a-L_b-L_c. In Fig. 1, v_{Ga}-v_{Gb}-v_{Gc} are grid voltages at the PCC with frequency ω and phase angle θ, i_{Ga}-i_{Gb}-i_{Gc} are grid currents, i_{La}-i_{Lb}-i_{Lc} are load currents, i_{Va}-i_{Vb}-i_{Vc} are currents supplied by the V2G interface, C_{dc} is the dc-link capacitor, v_{dc} is the dc-link voltage, and v_B-i_B are battery voltage and battery current. For the traditional V2G operation, EVs are required. The V2G interface is redundant in case (i) batteries are not available for the V2G operations and (ii) the state of charge (SOC) of the battery is not adequate. Also, in case the available battery has a lower capacity than the rating of the V2G interface, the interface will not be utilized to its maximum rating. This work proposes multi-functional control of the V2G interface with a fast dynamic response for SC.

The block diagram depiction of multi-functional control of the V2G interface is mentioned in Fig. 2. The phase-locked loop (PLL) algorithm processes v_{Ga}-v_{Gb}-v_{Gc} and computes phase angle, θ. Based on estimated θ, unit vector templates (UVTs), u_{Ga}-u_{Gb}-u_{Gc}, are computed. The proposed FACE unit utilizes i_{La}-i_{Lb}-i_{Lc} and θ for the computation of FAC of load current denoted as i_{FAC}. With the two-stage system, as shown in Fig. 1, the dc-dc converter will feed power at the dc-link for API. For G2V operation, ac-dc conversion is required. It is accomplished by regulating the dc-link voltage. When dc-dc draws power from dc-link for charging the battery pack, v_{dc} starts decreasing. On the contrary, when the dc-dc converter injects power into the dc-link from the battery pack, v_{dc} starts rising. The dc-link voltage control loop regulates v_{dc} by drawing power from the grid when required for the battery charging and injecting

TABLE II
OPERATION AND REFERENCE CURRENT FOR EACH MODE

Current	Mode	Operation		Reference Current for V2G Interface $i_{VxR}(t)$	
		API	SC		
$i_{VxR}(t)$	A	✓	✗	$i_{VxR}(t) = I_{API}\ u_{Gx}(t)$	(1)
	B	✓	✓	$i_{VxR}(t) = I_{API}\ u_{Gx}(t) + i_{SCx}(t)$	(2)
	C	✓	Δ	$i_{VxR}(t) = I_{API}\, u_{Gx}(t) + K\, i_{SCx}(t)$ $K=(I_{RM} - I_{API}) / max\{z_a, z_b, z_c\}$	(3) (4)
	D	✗	✓	$i_{VxR}(t) = i_{SCx}(t)$	(5)
$i_{SCx}(t)$	B, C, D	-	-	$i_{SCx}(t) = i_{Lx}(t) - i_{FAC}(t)\, u_{Gx}(t)$	(6)
$i_{GxR}(t)$	A, B, C, D	-	-	$i_{GxR}(t) = i_{Lx}(t) - i_{VxR}(t)$	(7)

✓ - ✗ - Δ correspondingly indicates that the functionality can be, cannot be, or is partially implemented.

power to the grid during API operation. v_{dc} is compared with a reference voltage, v_{dcR} and the resulting dc-link voltage error, e_{dc}, is processed by the proportional-integral (PI) controller for computing the peak value of active current to be injected into the grid for regulation of v_{dc}, denoted as i_{dc}. It is to be noted that i_{dc} represents active power consumed by the VSI on account of losses and active power demanded or injected by the dc-dc converter. Neglecting the losses compared to the active power being exchanged at the dc-link, i_{dcR} can be represented as I_{API}. I_{API} represented as the peak value of FAC of injected currents at PCC. The corresponding product of I_{API} and u_{Ga}-u_{Gb}-u_{Gc}, denoted as i_{dcRa}-i_{dcRb}-i_{dcRc}, represents the instantaneous values of active current to be injected into the grid for regulation of v_{dc}. The dc-link voltage control loop facilitates ac-dc conversion during battery charging and dc-ac conversion during API operation. Based on the active operating mode, I_{API}, i_{La}-i_{Lb}-i_{Lc}, and i_{FAC}, reference grid currents, denoted as i_{GaR}-i_{GbR}-i_{GcR}, are determined. Based on i_{GaR}-i_{GbR}-i_{GcR} and i_{Ga}-i_{Gb}-i_{Gc}, hysteresis current controller generates gate pulses for the VSI of M-V2G interface.

The multi-functional operation of the V2G interface refers to the implementation of SC alongside traditional API operation. The power interface between the grid and the vehicle is designed based on the charging requirement of the battery. However, when implementing V2G operation, the batteries may not be discharged at full capacity, or sometimes lower capacity batteries are available for V2G operation. In such a scenario, the power interface may not be operated at its rated capacity. To increase the utilization of the V2G interface, SC can be implemented for the other loads at the station premise alongside API. This not only increases VA utilization of the V2G interface but also helps in improving the PQ. The four operating modes of the proposed M-V2G interface are (A) API only, (B) API and SC, (C) API with partial SC, and (D) SC only. For each mode, Table II shows the functionality, reference current for the V2G interface, $i_{VxR}(t)$, currents for SC, $i_{SCx}(t)$, and reference grid currents, $i_{GxR}(t)$, through (1)-(7). Mode-A implements traditional V2G with API only. Hence, $i_{VxR}(t)$ is the product of reference API, I_{API}, and respective UVT, $u_{Gx}(t)$, which are obtained using PLL. x in subscript denotes phase a, b, or c.

Although the traditional API operation assists the grid in supplying active power to the load, it does not resolve the harmonic current injection issue due to other nonlinear loads at the station. To increase VA utilization of the V2G interface and improve the PQ at the PCC, Mode-B implements M-V2G operation with concurrent API and SC. $i_{SCx}(t)$ is computed as per (6). $i_{VxR}(t)$ is the sum of $i_{SCx}(t)$ and $[I_{API}u_{Gx}(t)]$. It is to be noted that the V2G interface is designed based on the charging requirements. In case of an increase in load at the PCC, the V2G interface might run at overload. When the peak current capacity of VSI, I_{RM}, is exceeded, Mode-C is used, where $i_{VxR}(t)$ can be computed as per (3) and $i_{SCx}(t)$ is scaled by the scaling factor K. K is defined in (4), where z_x is the absolute peak of $i_{SCx}(t)$ computed over a cycle. API in Mode-C is as per I_{API}, and only SC is scaled. A similar approach is reported in [16] and [31] for the multi-functional control of battery and solar photovoltaic systems. Mode-D is activated when no battery is available. Only SC takes place in Mode-D, and the V2G interface only provides $i_{SCx}(t)$. The Mode-D operation of the V2G interface increases the utilization of the V2G interface by implementing SC even when the batteries are not available for the API operation. Thus, Modes A, B, and C require the grid to partially support the APDL. Modes B and D fully provide the required SC, whereas Mode-C performs partial SC as per the available VA ratings. In Modes A and C, the grid provides for the current harmonics and RPDL fully and partially, respectively. In Modes B, C, and D, the FACE unit needs to compute i_{FAC} for implementing SC.

Mode A to C can be implemented when the battery is fully charged. API and API with full or partial shunt compensation can be implemented with the battery fully charged. With API, the battery gets discharged. Even Mode-D can be activated in such a scenario, provided API is not to be carried out. Ideally, the battery will not discharge with Mode-D, and the V2G interface will be utilized for SC. On the other hand, when the battery is fully depleted, Mode A to C cannot be activated. In such a scenario, only Mode-D can be activated. No API will take place. However, SC will be carried out to enhance PQ and improve the overall utilization of the charging infrastructure. For Modes B, C, and D, computation of i_{FAC} is required to perform SC.

TABLE III
PSEUDO-CODE FOR THE PROPOSED FACE

Operation	Mathematical Operation	
Initialize sampling instant n as 1		
Sample i_{La} - i_{Lb} - i_{Lc} and obtain $u_{Ga}(n)$ - $u_{Gb}(n)$ - $u_{Gc}(n)$ from the PLL.		
Compute i_{Ld}	$i_{Ld}(n) = (2/3)\times\sum_{x=a,b,c} i_{Lx}(n)\, u_x(n)$	(8)
	$= i_{FAC}(n)+\sum_{l=2,6,12,18,24} M_l(n) \sin[l\theta(n)+\varphi_l]$	(9)
Compute i_y	For a balanced system, $i_y(n) = i_{FAC}(n) + M_6(n) \sin[6\theta(n)+\varphi_6]$	(10)
	For an unbalanced system, $i_y(n) = i_{FAC}(n) + \sum_{l=2,6} M_l(n) \sin(l\theta(n)+\varphi_l)$	(11)
Compute $\lvert pi_y \rvert$	For a balanced system, $\lvert pi_y(n) \rvert = \lvert 6M_6(n) \cos[6\theta(n)+\varphi_6] \rvert$	(12)
	For an unbalanced system, $\lvert pi_y(n) \rvert = \lvert \sum_{l=2,6} lM_6(n) \cos[l\theta(n)+\varphi_l] \rvert$	(13)
Update i_{FAC}	$J(n) = \lvert pi_y(n) \rvert$	(14)
	Condition: $J(n-1) \geqslant J(n)$ & $J(n-1) \geqslant J(n-2)$	(15)
	$i_{FAC}(n) = i_y(n-1)$	(16)
Repeat the process with $n = n + 1$.		

III. PROPOSED FACE UNIT

The d-axis load current for non-linear loads comprises a dc and several ac components. For a signal comprising an ac and a dc quantity, the sampling of the signal at the absolute peak of its derivative represents the dc component. This logic does not right away apply to the extraction of FAC as multiple ac signals are present in the d-axis load current. CBSFs processes the d-axis load current to remove all ac components other than the lowest order harmonic in order to get around the problem before sampling or computing the derivative. The FAC of load current can now be computed by sampling the obtained signal at the peak of its derivative.

Table III shows the procedure for the proposed FACE unit, with p as the differential operator. Based on the input samples, the d-axis load current, i_{Ld}, is determined as per (8). To remove high-frequency noise, i_{Ld} is low pass filtered with a cut-off frequency, δ, of 1000 Hz. As shown in (9), where l is the order of harmonic and φ_l is the phase-shift angle of l^{th} harmonic, i_{Ld} comprises of i_{FAC} as the dc component and multiple ac components representing the harmonics. If there was only one ac component in i_{Ld}, then i_{FAC} could be determined as the sample of i_{Ld} at the absolute peak of its derivative. To apply this idea, the 12th, 18th, and 24th harmonic present in i_{Ld} are filtered out by processing it through CBSF having a center frequency, δ_b, of 12ω, 18ω, and 24ω, respectively. The step response analysis of the band stop filter (BSF) reveals a faster dynamic response with higher δ_b. As shown by (10)–(11), in addition, i_{FAC} to the output of CBSF, i_y, comprises the 6th harmonic and 2nd plus 6th harmonic for balanced and unbalanced currents, respectively. Here, M_l is the peak magnitude of the lth harmonic.

The proposed idea necessitates the determination of the

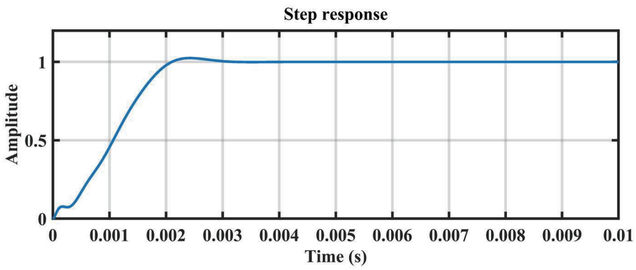

Fig. 3. Step response of CBSF implemented for balanced loading conditions.

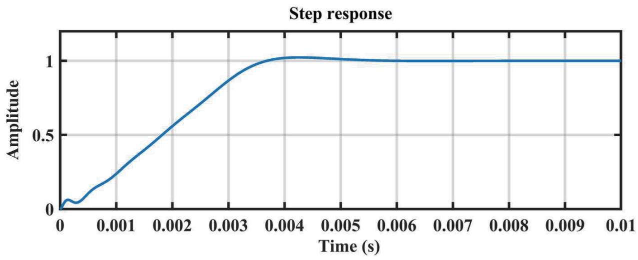

Fig. 4. Step response of CBSF implemented for unbalanced loading conditions.

peak of $\lvert pi_y \rvert$, which is given by (12)–(13) for balanced and unbalanced cases. With J defined by (14), when the conditions specified in (15) are satisfied, i_{FAC} is updated as per (16). For the balanced case, $i_{FAC}(n) = i_y(n-1)$, which can be estimated by sampling i_y at the peak of $\lvert pi_y(n) \rvert$. At the peak of $\lvert pi_y(n) \rvert$, $p^2 i_y(n)$, given by (17), is equated to zero, and the roots (i.e. θ) are determined. Since $M_6 > 0$, $p^2 i_y(n) = 0$ holds true when $\sin[(6\theta(n)+\varphi_6] = 0$, which leads to $[6\theta(n)+\varphi_6] = \pi$ or 2π. At θ, given by (18), $i_y(n) = i_{FAC}(n)$. This proves the proposed idea.

For an unbalanced case, as two ac quantities present in i_y. Hence, i_{FAC} cannot be estimated by sampling i_y at the peak of $\lvert pi_y \rvert$. The use of BSF to eliminate the 2nd harmonic can resolve the issue, but the response time for BSF is higher for the 2nd order harmonic. Alternately, if 6th harmonic is eliminated using BSF, then similar approach as given by (14)–(16) is followed. T_R, the maximum time for computing the new value of i_{FAC} upon change in load, is given by (19), where t_L-t_{CBSF}-t_h correspondingly indicate the response time of LPF, response time of BSFs involved, and maximum time between the instants of load change and next peak of $\lvert pi_y(n) \rvert$. The step response for CBSF under balanced and unbalanced load conditions are shown in Figs. 3 and 4, respectively. Based on the step response analysis using MATLAB's stepinfo function, T_R for balanced and unbalanced cases is determined as 4.3 ms and 9.6 ms, respectively. Hence, for instant change in load, the new value of FAC will be estimated within 9.6 ms. Further, bode plots for CBSF utilized for balanced and unbalanced conditions are shown in Figs. 5 and 6, respectively. It is to be observed from bode plots that the higher order harmonics are attenuated as magnitude/attenuation at their frequencies is very close to zero.

$$p^2 i_y(n) = -36M_6(n) \sin[6\theta(n)+\varphi_6] \quad (17)$$

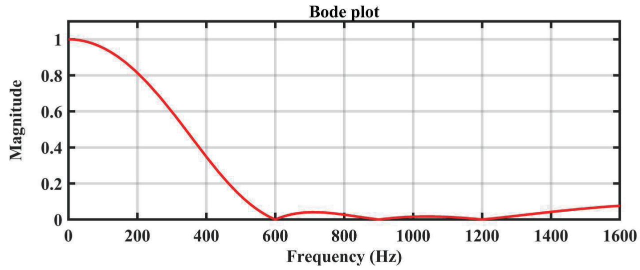

Fig. 5. Bode plot of CBSF implemented for balanced loading conditions.

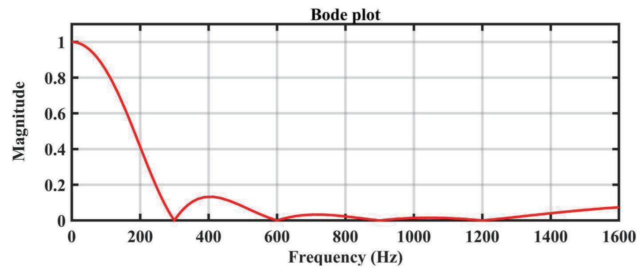

Fig. 6. Bode plot of CBSF implemented for unbalanced loading conditions.

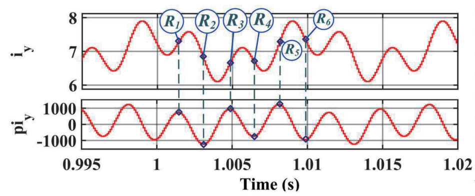

	Time	i_y
R_1	1.0014	7.29364
R_2	1.0031	6.71699
R_3	1.0048	6.65082
R_4	1.0064	6.70822
R_5	1.0081	7.28529
R_6	1.0098	7.35129
Average		7.001

Fig. 7. i_y and pi_y for unbalanced loading.

$$\theta = [(\pi - \varphi_6)/6] \text{ or } [(2\pi - \varphi_6)/6] \tag{18}$$

$$T_{\mathrm{R}} = t_{\mathrm{L}} + t_{\mathrm{CBSF}} + t_h \tag{19}$$

Another approach is proposed for the estimation of i_{FAC} under unbalanced conditions. For the unbalanced case, as per (11) and (13), there would be two ac quantities present in $i_y(n)$ and $|pi_y(n)|$. Now, i_{FAC} cannot be estimated by sampling i_y at the peak of $|pi_y|$. As presented earlier, the use of BSF to eliminate either the 2nd or 6th harmonic can resolve the issue. The elimination of the 2nd harmonic would incur increased response time compared to proceeding with the elimination of the 6th harmonic component. However, one more filtering stage would be required. Another approach is presented wherein an additional filter for removing either the 2nd or 6th harmonic is not required. For unbalanced load currents, i_y and pi_y are shown in Fig. 7. i_y sampled at the peak of $|pi_y|$ over a 10 ms duration (i.e. time period of 2nd harmonic) are given by R_1-R_6. These six consecutive samples are stored in an array based on first-in-last-out, and as per (20), the average of six samples represents i_{FAC} as given in (21). As shown in Fig. 7, the average of R_1-R_6 is 7.001 A, which is equal to i_{FAC}. This approach of computing i_{FAC} based on averaging the values of i_y sampled at the peak of $|pi_y|$ over a 10 ms duration has a larger response time than the

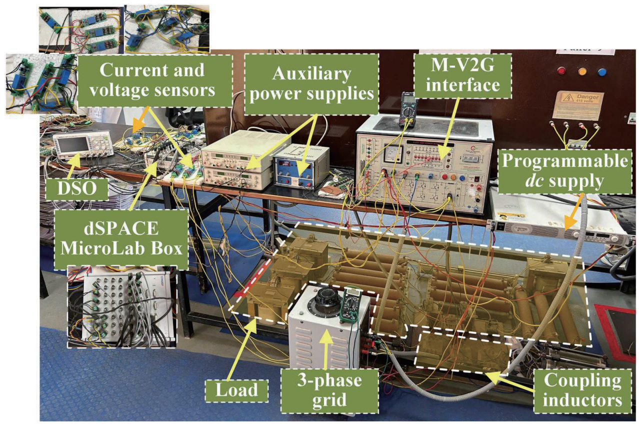

Fig. 8. Experimental prototype model of M-V2G controlled with the proposed FACE.

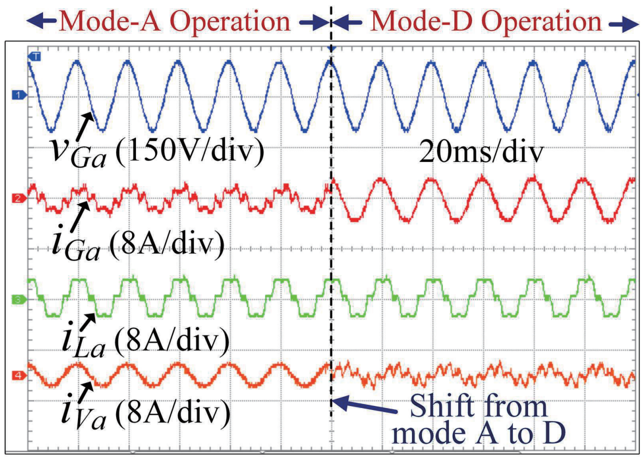

Fig. 9. Performance analysis of M-V2G interface with the proposed FACE. v_{Ga}-i_{Ga}-i_{La}-i_{va} for mode transition from Mode A-D.

previous approach. Further, FAC estimated with the proposed FACE unit will be utilized by the overall control algorithm to implement various operating modes of the M-V2G interface. The proposed FACE offers accurate estimation and a fast dynamic response and is easier to implement.

$$\text{For } j = 5{:}1,\ \mathrm{A}(j+1) = \mathrm{A}(j)\ \&\ A(1) = i_y(n) \tag{20}$$

$$i_{\mathrm{FAC}} = \frac{1}{6}\sum_{k=1}^{6} A(k) \tag{21}$$

IV. Results and Discussions

Experimental studies are performed to validate the performance of the M-V2G interface controlled with the proposed FACE unit. The experimental setup is shown in Fig. 8. The V2G interface comprises a 3-phase grid-tied VSI employing IGBTs SKM100GB12T4. v_{Gx} is 70.7 V, and nominal grid frequency is 50 Hz. The value of L_{x} is 10 mH. The value of C_{dc} is 1500 μF. The control algorithm, comprising overall multi-functional control comprising the proposed FACE unit, is

TABLE IV
LIST OF PARAMETERS USED IN EXPERIMENTAL STUDY

Parameter	Value
Supply	3-phase, 122.47 V ac voltage
Nominal supply frequency	50 Hz
IGBT part no.	SKM100GB12T4
L_a - L_b - L_c	10 mH
C_{dc}	1500 µH
Controller	dSPACE MicroLab Box 1202
Voltage sensors	LV25-P/SP2
Current sensors	LA55-P/SP1

Load Configurations

	Load (Ω) I	II	III	IV	V	VI	Load Parameters (Ω)
R_{DBR}	50	25	50	50	25	25	Impedance/phase of the 3-phase R-L load
	--	--	Z_1	Z_1	Z_1	Z_1	$Z_1 = 50 + j\omega 0.2$
Z_{LIN}	--	--	Z_1	Z_1	Z_1	Z_1	$Z_2 = 32 + j\omega 0.03$
	--	--	Z_1	Z_2	Z_1	Z_2	

TABLE V
MEASURED PEAK VALUES AND %THD OF i_{Ga}-i_{La}-i_{Va} FOR THE FOUR OPERATING MODES

Mode	Peak Value i_{Ga}	i_{La}	i_{Va}	%THD i_{Ga}	i_{La}	i_{Va}
Mode-A	2.1	3.1	2.0	38.0	19.6	4.6
Mode-B	3.2	4.3	3.0	4.0	15.0	30.0
Mode-C	5.8	6.9	3.4	6.7	13.3	25.0
Mode-D	3.5	3.1	2.3	3.5	20.3	61.0

implemented in dSPACE MicroLab Box 1202. For feedback, LV25-P/SP2 voltage sensors and LA55-P/SP1 current sensors are used. Load comprises of parallel connection of 3-phase uncontrolled rectifier with a load resistance of R_{DBR} and 3-phase RL load. The list of parameters used in experimental studies are given in Table IV. Programmable dc power supply emulates EV battery and bi-directional dc-dc converter.

Figs. 9 and 10 show the performance analysis of the M-V2G interface with the proposed FACE for phase-a. Figs. 9 and 10 exhibit performance during transitions from Modes A-D and B-C, respectively. The peak magnitudes (PMs) and THD of i_{Ga}-i_{La}-i_{Va} are indicated in Table V for each mode. With Load-I, for Modes A and D, i_{La} is non-sinusoidal with PM and THD of 3.1-3.1 A and 19.6%-20.3%. In Fig. 9, during Mode-A, the M-V2G interface performs API with I_{API} of 2.0 A. Hence, i_{Va} is sinusoidal with %THD<5. i_{Ga} caters to RPDL, current harmonics of load, and the remaining APDL. It is now equal to (i_{La}-i_{Va}), and it provides RPDL fully and APDL partially. Hence, the THD of i_{Ga} exceeds 5%. Now, if the battery is unavailable, the system shifts to Mode-D and M-V2G interface performs SC as per the proposed FACE unit to deliver i_{SCa}. Hence, i_{Va} is highly distorted. But, i_{Ga} is sinusoidal and in-phase with v_{Ga} as it needs to cater to APDL only. Thus, with Mode-D, the system is not redundant when the battery is unavailable and performs PQ enhancement.

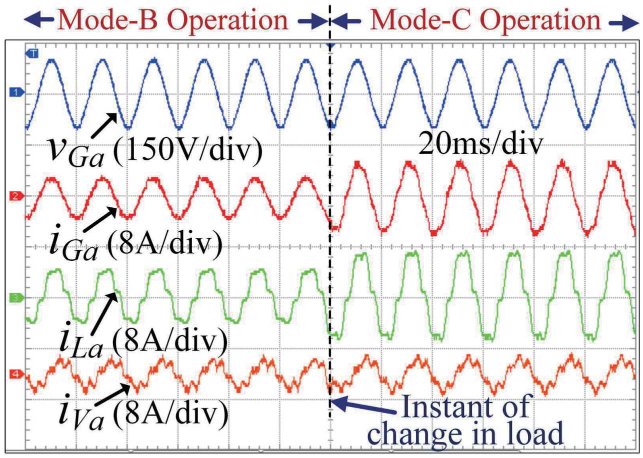

Fig. 10. Performance analysis of M-V2G interface with the proposed FACE. v_{Ga}-i_{Ga}-i_{La}-i_{va} for mode transition from Mode B-C.

TABLE VI
POWER ANALYSIS FOR THE FOUR OPERATING MODES

Mode	Load	Grid P_G (W)	Q_G (VAr)	Load P_L (W)	Q_L (VAr)	M-V2G Interface P_V (W)	Q_V (VAr)
A	I	214	136	472	147	258	11
B	III	467	−2	567	285	100	287
C	V	812	179	912	508	100	329
D	I	505	0	465	146	−40	146

Fig. 10 shows the M-V2G operation for Mode B-C. In Mode-B, the M-V2G interface performs API to partially meet the APDL and SC. Load-III is present in Mode-B. As a result of SC implemented by the M-V2G interface, i_{Va} is non sinusoidal and i_{Ga} is sinusoidal with %THD<5. Mode-C is initiated with Load-V and I_{RM} - I_{API} as 4.0-1.0A, and K = 0.645. K<1 indicates partial SC. Hence, 64.5% of i_{SCa} is supplied by the M-V2G interface and the remaining is catered by the grid. With partial SC as per I_{RM} limit, M-V2G interface ensures that the THD of i_{Ga} is less than that of i_{La}. The proposed FACE unit facilitates seamless operation and transitions between M-V2G functionalities. Such M-V2G operation increases VA utilization while adhering to VA ratings.

The active and reactive power supplied by the grid, P_G - Q_G, supplied by the M-V2G interface, P_V - Q_V, and consumed by the load, P_L - Q_L, are given in Table VI. In Mode-A, P_V partially meets the APDL and does not perform SC. Hence, the grid caters to the remaining APDL. As SC is absent, $Q_L = Q_G$. Also, the harmonic currents are fed from the grid. In Mode-B, as the M-V2G interface performs SC and API, $Q_V = Q_L$, $Q_G = 0$, and

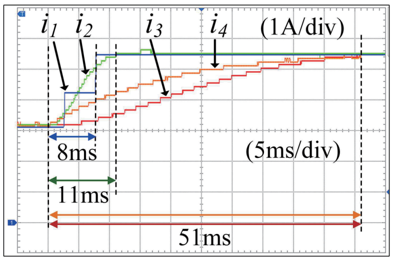

Fig. 11. Dynamic response analysis for balanced load.

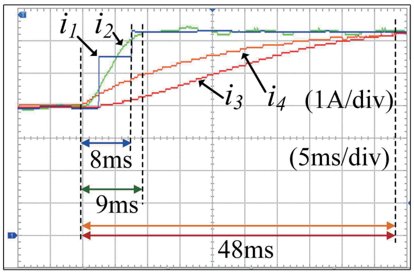

Fig. 12. Dynamic response analysis for unbalanced load (Load-IV to Load-VI).

APDL is met by the grid and M-V2G interface. Hence, $P_L = P_G + P_V$. In Mode-C, partial SC is implemented by the interface to avoid its overloading, $Q_L = Q_G + Q_V$. Also, the M-V2G interface now partially caters to APDL. With the unavailability of a battery, the operation shifts to Mode-D, wherein SC is performed by the V2G interface. Hence, $Q_G = 0$ and $Q_L = Q_V$. Now, as APDL is met by the grid, $P_L = P_G$.

Figs. 11 and 12 show the steady-state and dynamic response for i_1 - i_4 for balanced and unbalanced loads with time to reach the new steady state indicated individually. i_1 - i_4 respectively denote the FAC computed with the proposed method, synchronous reference frame theory (SRFT) with filter cut-off frequency, δ, of 50 Hz, SRFT with $\delta = 10$ Hz, and LMS algorithm with $\mu = 0.01$, reported in [20]. The comparison of the FAC extraction with these four methods is given in Table VII, while the estimated values are mentioned in Table VIII. With the change from Load-I to Load-II, i_1 has the fastest dynamic response, and i_3 has a sluggish response. With larger δ, i_2 has a faster response as compared to i_3. However, as observed from Fig. 12, with the unbalanced loading (Load IV to VI), the higher δ cannot fully attenuate the 2^{nd} harmonics, and hence ripples are observed in the steady state. However, this is not the case with the proposed method; no ripples are observed in the steady-state, even for unbalanced loading. LMS algorithm exhibits a slower dynamic response for the given μ and considered loads. The optimal selection of a variable μ can improve the response, but the computational complexity will significantly increase. The experimental studies validate the fast, dynamic and accurate steady-state response of the proposed FACE.

TABLE VII
Comparison of Face based on Experimental Studies

FACE	Load	SRF δ=50 Hz	SRF δ=10 Hz	ADALINE - LMS	Proposed
Ripples	Balanced	Less	Not observed	Not observed	Not observed
	Unbalanced	High	Not observed	Not observed	Not observed
Transition Time (ms)	Balanced	11	51	51	8
	Unbalanced	9	48	48	8

TABLE VIII
Estimated Values with Different FAC Extraction Techniques

Load	Average value of FAC estimated with the proposed SRFT with δ=50 Hz, SRFT with δ=10 Hz, and LMS algorithm with μ=0.01 for Loads I, II, IV and VI (A)			
	i_1	i_2	i_3	i_4
I	3.0	3.0	3.0	3.05
II	5.3	5.3	5.3	5.4
IV	3.9	3.9	3.9	3.9
VI	6.2	6.2	6.2	6.3

V. Conclusion

This paper proposes an M-V2G interface with a new FACE unit for improved dynamic response for SC. The reported M-V2G operation performs (A) API only, (B) API and SC, (C) API and partial SC, and (D) SC only. FACE is mandatorily needed for Modes B, C, and D. A new FACE unit is proposed, which offers the benefits of computation simplicity, ease of implementation, fast dynamic response, and ripple-free steady-state response. The merits of the proposed scheme are evident from the presented comparative analysis. Also, the fast dynamic response offered by the proposed extraction scheme results in a seamless transition among the various operating modes. If a signal comprising of an ac and a dc component is sampled at the absolute peak of its derivative, then the sample value is the dc component. With non-linear loads, the d-axis load current comprises a dc and several ac components. Hence, this logic is not directly applicable to FAC extraction. To circumvent the issue, before sampling or computing the derivative, the d-axis load current is processed through CBSF to remove all ac components except the lowest-order harmonic. Now, the value sampled as per the concept mentioned earlier represents the FAC of load current. The excellent harmonic attenuation capability and fast dynamic response of the CBSF are evident from the presented frequency and step response analysis. Mathematical derivations for the FACE and steps for controlling the M-V2G interface for each mode are discussed in detail. Further, the performance of M-V2G has been experimentally validated for the four operating modes. Such multi-functional operation can result in PQ enhancement through SC, support the grid through API, improve the VA utilization of the M-V2G interface, and facilitate the use of the interface even when the battery is unavailable.

References

[1] S. S. Letha, M. H. J. Bollen, and T. Busatto, and Á. Espín-Delgado, "Power quality issues of electro-mobility on distribution network—An overview," in *Energies*, vol. 16, no. 13, Jun. 2023.

[2] A. J. Patel and A.V Sant, "Power quality enhancement for charging station with moving window min-max algorithm-based shunt active power filter," in *Energy Reports*, vol. 8, pp. 86–91, Oct. 2022.

[3] D. Çelik and M. E. Meral, "A coordinated virtual impedance control scheme for three-phase four-leg inverters of an electric vehicle to grid (V2G)," in *Energy*, vol. 246, May 2022.

[4] M. R. Khalid, M. S. Alam, A. Sarwar, and M. J. Asghar, "A Comprehensive review on electric vehicles charging infrastructures and their impacts on power-quality of the utility grid," in *ETransportation*, vol. 1, Aug. 2019.

[5] S. Behera, N V. R. Naik, A. K. Panda, and S. K. Behera, "A dual control strategy for improved power quality in grid-tied off-board bidirectional electric vehicle charger," in *Electric Power Systems Research*, vol. 236, Nov. 2024.

[6] R. K. Lenka, A. K. Panda, and L. Senapati, "Grid integrated multifunctional EV charging infrastructure with improved power quality," in *Journal of Energy Storage*, vol. 76, Jan. 2024.

[7] A. J. Patel and A. V. Sant, "EV charging station with cascaded low-pass filtering scheme-based control of unified power quality conditioner," in *Clean Energy*, vol. 6, no. 5, pp. 738–761, Oct. 2022.

[8] C. Balasundar, C. K. Sundarabalan, J. Sharma, N. S. Srinath, and J. M. Guerrero, "Design of power quality enhanced sustainable bidirectional electric vehicle charging station in the distribution grid," in *Sustainable Cities and Society*, vol. 74, Nov. 2021.

[9] Y. Wang, J. -W. Yang, W. -J. Kim, T. -H. Kwon, T. Lee, and S. -J. Park, "Second harmonic current suppression and dynamic response improvement for V2G system," in *IEEE Transactions on Power Electronics*, vol. 38, no. 8, pp. 9566–9580, Aug. 2023.

[10] S. Das, P. Thakur, A. K. Singh, and S. N. Singh, "Optimal management of vehicle-to-grid and grid-to-vehicle strategies for load profile improvement in the distribution system," in *Journal of Energy Storage*, vol. 49, May 2022.

[11] A. Zabetian-Hosseini, G. Joós, and B. Boulet, "Control design for effective usage of electric vehicles in V2G-enabled DC charging stations," in *IEEE Transactions on Power Delivery*, vol. 38, no. 6, pp. 4335–4346, Dec. 2023.

[12] A. A. Ghani, V. K. Ramachandaramurthy, and J. Y. Yong, "Design of a master power factor controller for an industrial plant with solar photovoltaic and electric vehicle chargers," in *Electrical Engineering*, vol. 104, no. 1, pp. 13–25, Feb. 2022.

[13] D. Çelik, "Lyapunov based harmonic compensation and charging with three phase shunt active power filter in electrical vehicle applications," in *International Journal of Electrical Power & Energy Systems*, vol. 136, Mar. 2022.

[14] K. Srivastava, S. Kumar, and R. Maurya, "A robust BCNMCC based variance smoothing approach for SPV based grid integrated EV battery charging system," in *Journal of Energy Storage*, vol. 72, Nov. 2023.

[15] R. K. Lenka, A. K. Panda, R. Patel, and J. M. Guerrero, "PV integrated multifunctional off-board EV charger with improved grid power quality," in *IEEE Transactions on Industry Applications*, vol. 58, no. 5, pp. 5520–5532, Sept.-Oct. 2022.

[16] A. J. Patel and A. V. Sant, "A new fundamental active current extraction scheme for multifunctional control of V2G interface," in *Journal of Energy Storage*, vol. 86, May 2024.

[17] A. V. Sant, "Shunt active power filtering with reference current generation based on dual second order generalised integrator and LMS algorithm," in *Energy Reports*, vol. 8, pp. 886–893, Nov. 2022.

[18] S. Ahmed, G. Madjid, M. Youcef, and T. Hamza, "Real-time control of an active power filter under distorted voltage condition," in *International Journal of Power Electronics and Drive Systems*, vol. 2, no. 4, pp. 424–433, Dec. 2012.

[19] C. Singh, G. Kumar, H. Kumar, and A. Arora, "Power quality enhancement using adaptive notch filter in grid distribution system," in *2023 3rd International Conference on Intelligent Technologies (CONIT)*, Hubli, India, 2023, pp. 1–6.

[20] A. Kumar and P. Kumar, "Power quality improvement for grid-connected PV system based on distribution static compensator with fuzzy logic controller and UVT/ADALINE-based least mean square controller," in *Journal of Modern Power Systems and Clean Energy*, vol. 9, no. 6, pp. 1289–1299, Nov. 2021.

[21] S. K. Patel, S. R. Arya, and R. Maurya, "Optimal step LMS-based control algorithm for DSTATCOM in distribution system," in *Electric Power Components and Systems*, vol. 47, no. 8, pp. 675–691. Aug. 2019.

[22] Q. Niu and T. Chen, "A new variable step size LMS adaptive algorithm," in *2018 Chinese Control and Decision Conference (CCDC)*, Shenyang, China, 2018, pp. 1–4.

[23] N. Gupta, M. Morey, M. M. Garg, and A. Kumar, "An experimental investigation of variable-step-size affine projection sign based algorithm for power quality enhanced grid-interactive solar PV system," in *Electric Power Systems Research*, vol. 228, Mar. 2024.

[24] S. Roy, F. Chishti, B. Singh, and B. K. Panigrahi, "GNLMP control for solar PV-battery based microgrid with Ms-EPLL synchronization," in *IEEE Transactions on Industry Applications*, vol. 58, no. 5, pp. 6599–6611, Sept.-Oct. 2022.

[25] A. Parida and B. Subudhi, "A variable step size robust least mean logarithmic square-based control scheme for improved power quality of grid-interfaced PV system," in *IEEE Transactions on Smart Grid*, vol. 13, no. 3, pp. 2086–2093, May 2022.

[26] B. Singh, S. K. Dube, and S. R. Arya, "Hyperbolic tangent function-based least mean-square control algorithm for distribution static compensator," in *IET Generation, Transmission & Distribution*, vol. 8, no. 12, pp. 2102–2113, Dec. 2014.

[27] P. A. C. Lopes, "Analysis of the LMS and NLMS algorithms using the misalignment norm," in *Signal, Image and Video Processing*, vol. 17, pp. 3623–3628, May 2023.

[28] A. Bhattacharya and C. Chakraborty, "A shunt active power filter with enhanced performance using ANN-based predictive and adaptive controller," in *IEEE Transactions on Industrial Electronics*, vol. 58, no. 2, pp. 421–428, Feb. 2011.

[29] M. Qasim and V. Khadkikar, "Application of artificial neural networks for shunt active power filter control," in *IEEE Transactions on Industrial Informatics*, vol. 10, no. 3, pp. 1765–1774, Aug. 2014.

[30] A. J. Patel and A. V. Sant, "Moving window min-max algorithm-based control of UPQC at EV charging station," in *2023 IEEE 3rd International Conference on Smart Technologies for Power, Energy and Control (STPEC)*, Bhubaneswar, India, 2023, pp. 1–6.

[31] A. V. Sant, V. Khadkikar, W. Xiao, H. Zeineldin, and A. Al-Hinai, "Adaptive control of grid connected photovoltaic inverter for maximum VA utilization," in *IECON 2013-39th Annual Conference of the IEEE Industrial Electronics Society*, Vienna, Austria, 2013, pp. 388–393.

Arpitkumar J. Patel is currently pursuing a Ph.D. in Electrical Engineering at Pandit Deendayal Energy University, focusing on the multifunctional control of custom power devices for EV charging stations incorporating Solar PV systems. He holds an M.Tech in Electrical Engineering (Power Systems) from Pandit Deendayal Energy University, where he worked on the control of grid-tied inverters. He completed his B.E. in Electrical Engineering from Gujarat Technological University. His research interests include electric vehicle charging systems, power electronic converters, power quality, and control algorithms.

Amit V. Sant received Ph.D. degree in Power Electronics from the Indian Institute of Technology Delhi, New Delhi, India, in 2013. Presently, he is an Associate Professor in the Department of Electrical Engineering, School of Energy Technology, Pandit Deendayal Energy University (PDEU), Gandhinagar, Gujarat, India. Before joining PDEU, he was a Postdoctoral Research Researcher at the Masdar Institute of Science and Technology, Abu Dhabi, United Arab Emirates. His present research focuses on multilevel inverters, z-source inverters, high gain DC-DC converters, grid integration of renewables, charging infrastructure for electric vehicles, power quality enhancement, smart metering, and applications of artificial intelligence in power electronic systems.

A Soft-Switching Control Method for Dual Active Bridge Converter Over the Full Power and Wide Voltage Regulation Range

Yuhang ZHANG, Yong LI, Jianghu WAN, Tingkun WENG, Jie ZHANG, and Yijia CAO

***Abstract*—The dual active bridge (DAB) has been widely adopted in isolated dc-dc conversion applications due to its capability for bidirectional power transfer. Among the various control strategies for DAB converters, the triple-phase-shift (TPS) control is recognized for its effectiveness. In this article, a soft-switching control method based on TPS control is proposed, which is advantageous for enhancing the efficiency of the DAB converter over the full power and wide voltage regulation range. First, the twelve operating modes of the DAB converter are categorized. And then an innovative methodology is introduced, wherein the DAB converter is equivalently transformed into a four-switch buck-boost (FSBB) converter by decomposing the midpoint voltage waveforms on both the primary and secondary sides. On the basis of the equivalent circuit, a hybrid phase-shift control method based on the soft switching is proposed, which delineates the DAB converter into six operating modes. To secure smooth and seamless transitions between these modes, a unified uni-variate control method is presented, which is simple and readily implementable. Ultimately, a 2.5 kW prototype is constructed, and the correctness and effective-ness of the proposed method are validated via the experimental results.**

***Index Terms*—Dual active bridge, equivalent circuit, full power range, soft-switching, wide voltage regulation range.**

I. Introduction

WITH the rapid development of the new energy industry, the dual active bridge (DAB) converter has been widely applied in fields such as dc micro-grids [1], energy storage systems [2], and electric vehicle onboard charging systems [3] due to its advantages of electrical isolation, high power density, bidirectional energy flow, and ease of achieving soft switching [4], [5].

Manuscript received December 05, 2024; revised February 06, 2025; accepted March 02, 2025. Date of publication June 30, 2025; date of current version April 18, 2025. This work was supported in part by National Nature Science Foundation of China under the Grant U22B200134, 111 Project of China under the Grant B17016, and Science and Technology Innovation Program of Hunan Province under the Grant 2023RC1038. *(Corresponding author: Yong Li.)*

Y. Zhang, Y. Li, T. Weng, and J. Zhang, are with the College of Electrical and Information Engineering, Hunan University, Changsha 410082, China (e-mail: yuhangzhang@hnu.edu.cn; yongli@hnu.edu.cn; vontink@hnu.edu.cn; zj0711@hnu.edu.cn).

J. Wan is with the School of Automation, Central South University, Changsha 410083, China (e-mail: wanjianghu@advancechip.com).

Y. Cao is with the School of Electrical and Information Engineering, Changsha University of Science and Technology, Changsha 410114, China (e-mail: yjcao@csust.edu.cn).

Digital Object Identifier 10.24295/CPSSTPEA.2025.00009

The DAB was originally introduced in 1991 [6]. Over time, phase-shift control has become the primary control method for the DAB [7]. Based on the number of control degrees of freedom, the control methods can be categorized into single-phase-shift (SPS) control, extended-phase-shift (EPS) control, dual-phase-shift (DPS) control, and triple-phase-shift (TPS) control [8]. There is a single phase-shift ratio between the primary and secondary bridges under SPS control, which is the simplest control method. However, during light-load conditions or if the input and output voltages are mismatched, the backflow power and current stress increase, reducing the range of soft-switching conditions [9], [10]. EPS control introduces an phase-shift ratio within the full bridge of one side, while DPS control adds the same phase-shift ratio within the bridges on both sides. Both methods reduce backflow power and current stress, extend the range of soft-switching, and enhance efficiency [11], [12]. TPS control introduces different internal phase-shift ratios within the full bridges on both sides, providing better optimization performance. However, the complexity of control is the highest under TPS control [13].

To further reduce power losses and enhance efficiency, varied solutions have been proposed. Optimized control methods aimed at suppressing backflow power are provided in [14]. A strategy for minimizing current stress is adopted in [15]. A multi-phase-shift control method based on zero-voltage switching (ZVS) is presented in [16]. Nevertheless, the aforementioned methods, which are based on EPS or DPS control, have been validated merely within a single scenario. These methods show limitations in applications with variable port voltages or transmission powers, such as in electric vehicle onboard charging systems.

Regarding achieving TPS control over a wide operating range, there are mainly two ways. One is the lookup table method, and the other is the analytical formula method. In the lookup table method, a multi-mode control method based on the boundary conditions of ZVS is discussed in [17]. However, a few switching devices still suffer hard switching in certain modes. Consequently, an approach involving frequency modulation control is proposed to expand the ZVS range. Both methods require offline computations and the use of online lookup tables. However, the discreteness of the lookup table data impact the optimization effectiveness. To address this, a method relying on artificial intelligence algorithms is given in [18], which

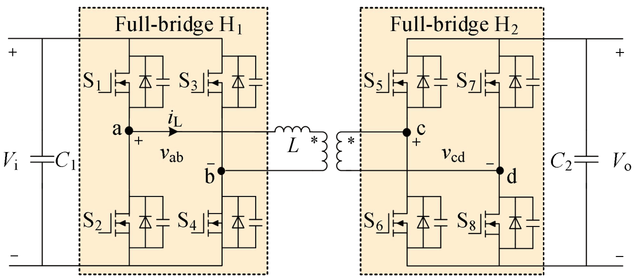

Fig. 1. Topology of the DAB converter.

improves the accuracy of the lookup table method and achieves minimum current stress. But the algorithm requires a amount of storage space, making it challenging to perform real-time calculations on general digital signal processor (DSP) controllers. In the analytical formula method, an optimized scheme that makes the converter operate with minimized root-mean-square (RMS) current across the full power range is presented in [19]. Although the efficiency has been improved under light load conditions, it remains relatively low under heavy-load conditions. A unified phase-shift control approach, aimed at minimizing current stress, is formulated in [20], using the Lagrange multiplier method (LMM). In [21], a current stress minimization control method based on full ZVS is proposed using the LMM. Nonetheless, LMM is typically employed for variable minimization at a given transmission power, posing difficulties in attaining a global optimal solution [14], [22]. The DAB converter is divided into five operating modes, within which the local optimal parameters that minimize current stress are determined in [23]. However, it does not address research on methods for mode transition. Strategies for multi-mode switching are proposed in references [24], [25]. However, the range of soft switching is limited by the voltage conversion ratio and the inductance in [24]. Although full-power-range ZVS is achieved, the efficiency significantly decreases if there is a mismatch between the input and output voltages in [25]. The analytical formula method is easier to implement compared to the lookup table method, but it still involves complex and time-consuming reasoning and calculations.

To address the limitations of existing methods, the article first analyze the division of DAB converter's operating modes under TPS control, providing the criteria and characteristics for each mode. Subsequently, the DAB converter is initially transformed into an equivalent four-switch buck-boost (FSBB) converter by decomposing the midpoint voltage waveforms of both the primary and secondary sides. By drawing parallels with the control strategies of the equivalent converter, a hybrid phase-shift control method achieving soft-switching is presented, which delineates six distinct operating modes of the DAB converter, covering the whole transferred power and a wide voltage regulation range. Furthermore, the transition processes between the modes under step-down and step-up conditions are revealed respectively. On this basis, a unified uni-variate control method is presented, which is simple to implement and achieves a smooth and seamless transition between the modes

TABLE I
THE RANGE OF PHASE-SHIFT RATIOS OF EACH MODE

Mode		The value range of phase-shift ratios	
A	A_1	$0 \leqslant D_2 \leqslant 1$, $1 \leqslant D_2+D_3 \leqslant 2$	$D_1 \leqslant D_2+D_3-1 \leqslant D_2$
	A_2		$D_2+D_3-1 \leqslant D_1 \leqslant D_2$
	A_3		$D_2+D_3-1 \leqslant D_2 \leqslant D_1$
B	B_1	$0 \leqslant D_2 \leqslant 1$, $0 \leqslant D_2+D_3 \leqslant 1$	$D_1 \leqslant D_2 \leqslant D_2+D_3$
	B_2		$D_2 \leqslant D_1 \leqslant D_2+D_3$
	B_3		$D_2 \leqslant D_2+D_3 \leqslant D_1$
C	C_1	$-1 \leqslant D_2 \leqslant 0$, $0 \leqslant D_2+D_3 \leqslant 1$	$D_1 \leqslant D_2+D_3 \leqslant 1+D_2$
	C_2		$D_2+D_3 \leqslant D_1 \leqslant 1+D_2$
	C_3		$D_2+D_3 \leqslant 1+D_2 \leqslant D_1$
D	D_1	$-1 \leqslant D_2 \leqslant 0$, $-1 \leqslant D_2+D_3 \leqslant 0$	$D_1 \leqslant 1+D_2 \leqslant 1+D_2+D_3$
	D_2		$1+D_2 \leqslant D_1 \leqslant 1+D_2+D_3$
	D_3		$1+D_2 \leqslant 1+D_2+D_3 \leqslant D_1$

proposed. Finally, the correctness and effectiveness of the proposed method have been verified by experiments.

The outline of this article is as follows. In Section II, the operating modes of the DAB converter are described under TPS control, and the equivalent circuit is introduced. The hybrid phase-shift control method is proposed in Section III. The unified uni-variate control method is presented in Section IV. The strategy is verified by experimental results obtained from a DAB converter prototype in Section V, followed by conclusion in Section VI.

II. ANALYSIS OF THE EQUIVALENT CIRCUIT

A. Topology of the DAB Converter

The topology of the DAB converter is shown in Fig. 1. $S_1 - S_4$ form the primary full-bridge H_1, and $S_5 - S_8$ form the secondary full-bridge H_2. H_1 and H_2 are connected by a high-frequency AC link, which is consist of an inductor and a transformer. The voltage conversion ratio is defined as $M = V_i / nV_o$, and T_{hs} follows $T_{hs} = 1/2f_s$, where f_s is the switching frequency.

D_1 represents the phase-shift ratio between S_1 and S_4. D_2 denotes the phase-shift ratio between S_1 and S_5. D_3 represents the phase-shift ratio between S_5 and S_8. The value ranges of the phase-shift ratios are as follows: $0 \leqslant D_1 \leqslant 1$, $-1 \leqslant D_2 \leqslant 1$, $0 \leqslant D_3 \leqslant 1$. The operating modes under TPS control are categorized into four classes (i.e., A, B, C, D) as shown in Table I, based on the variation of D_2 from 1 to −1. Within each class, the modes are further divided into three sub-types based on the relative positions of the rising and falling edges of the primary and secondary side midpoint voltage waveforms. This positional relationship within half a period can be reflected through the relationships among the values of D_1, $(D_2 + D_3)$, and D_2. The midpoint voltage waveforms of these modes are depicted in Fig. 2.

It can be observed in Fig. 2 that there are no regions where the primary and secondary midpoint voltages overlap in phase in modes A_1, A_2, A_3, C_3, D_2, and D_3. The peak value of the in-

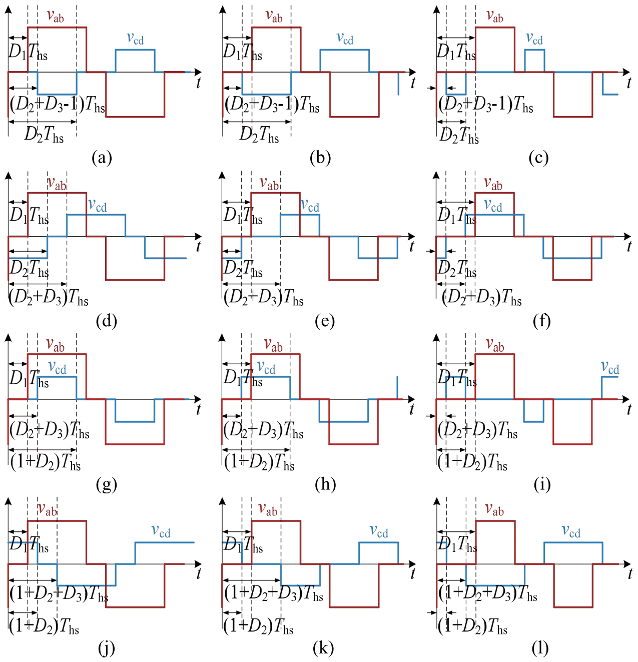

Fig. 2. Midpoint voltage waveforms of each mode under TPS control. (a) Mode A_1. (b) Mode A_2. (c) Mode A_3. (d) Mode B_1. (e) Mode B_2. (f) Mode B_3. (g) Mode C_1. (h) Mode C_2. (i) Mode C_3. (j) Mode D_1. (k) Mode D_2. (l) Mode D_3.

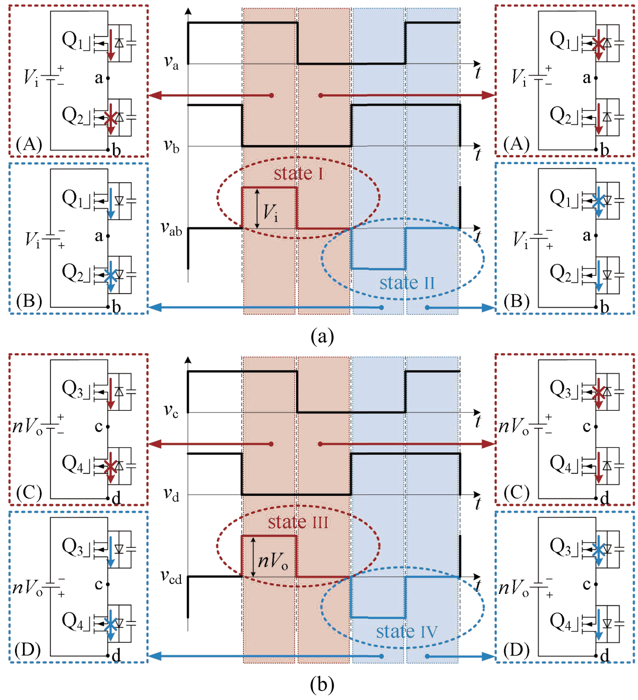

Fig. 3. Midpoint voltage waveforms and equivalent half-bridge circuits. (a) Primary side. (b) Secondary side.

ductor current is higher in these six modes compared to others, resulting in increased conduction losses and reduced efficiency [26]. Besides, conditions involving reverse power, as illustrated by modes C_1, C_2, and D_1, are not discussed. Consequently, modes B_1, B_2, and B_3 emerge as superior choices for enhancing operational efficiency of the DAB converter. Specifically, mode B_1 offers a transferred power range of [0, 1], enabling operation across the full power range. Mode B_2 has a transferred power range of [0, 2/3], while mode B_3 provides a transferred power range of [0, 1/2] [10].

B. The Equivalent Circuit of the DAB Converter

Owing to the relatively complex structure of DAB converter and its complicated control methods, the paper explores the equivalent circuit of the DAB converter from the perspective of circuit structure simplification. Moreover, a control method applicable for the DAB converter is proposed based on the equivalent circuit.

Based on the principle of voltage superposition, the waveform of the primary side midpoint voltage v_{ab} of DAB converter can be decomposed into v_a and v_b, and the decomposed voltage waveforms can be equivalently generated by half-bridge circuits.

As shown in Fig. 3(a), the waveform of v_{ab} within one period is divided into states I and II. In state I, when v_{ab} is high, it can be decomposed into a high voltage v_a and a zero voltage v_b, which is the same as the voltage of points a and b when Q_1 is turned on and Q_2 is off in half-bridge A. When v_{ab} is at zero, it can be decomposed into zero voltages for both v_a and v_b, which is the same as the voltage at points a and b when Q_1 is off and Q_2 is on in half-bridge A. In state II, when v_{ab} is negative, it can be decomposed into a zero voltage v_a and a high voltage v_b, which is the same as the voltage at points a and b when Q_1 is on and Q_2 is off in half-bridge B. When v_{ab} is at zero, it can be divided into high voltages for both v_a and v_b, which is the same as the voltage at points a and b when Q_1 is off and Q_2 is on in half-bridge B. Thus, state I can be equivalently generated by half-bridge A, and state II can be equivalently generated by half-bridge B.

Similarly, the waveform of the secondary side midpoint voltage v_{cd} within one cycle can be decomposed into states III and IV, as illustrated in Fig. 3(b). The waveform of state III can be equivalently generated by half-bridge C, and the waveform of state IV can be equivalently generated by half-bridge D.

On this basis, an equivalent circuit model of DAB converter can be constructed to simplify its structure.

According to the previous analysis, the classification of the operating modes of DAB converter under phase-shift control can be determined by the relative positions of the rising and falling edges of the waveforms for v_{ab} and v_{cd}. In other words, this relative positioning can be reflected through the arbitrary combination of the waveforms for v_{ab} and v_{cd} .

Within the positive half-cycle of v_{ab}, there exist two possible combinations of v_{ab} and v_{cd}, namely “state I + state III” and “state I + state IV”, as shown in their equivalent circuits in Fig. 4. According to the previous analysis, the combination of “state I + state IV” should be avoided as it lacks any coincident in phase voltage overlap, which results in decreased efficiency. Thus, the circuit of the combination “state I + state III” is selected as the equivalent circuit for DAB converter.

The equivalent circuit illustrated in Fig. 4(a) actually represents the FSBB. A multi-mode ZVS control approach is proposed

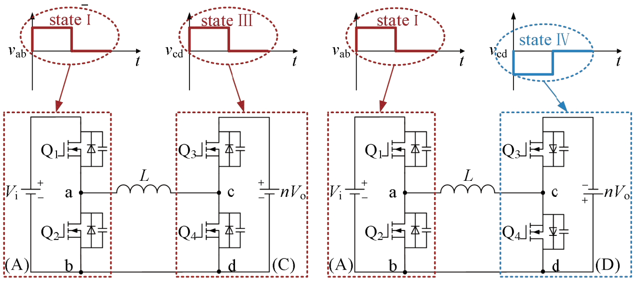

Fig. 4. Equivalent circuits of DAB converter. (a)"State I + state III". (b)"State I + state IV".

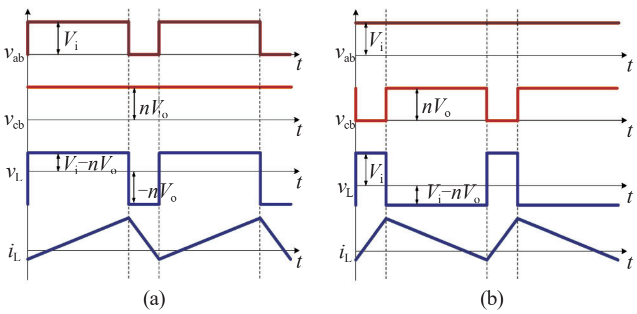

Fig. 5. Waveforms of FSBB. (a) Buck mode. (b) Boost mode.

for this converter in [27]. It indicates that the current stress is lower in both buck and boost modes compared to the Buck-Boost mode. Consequently, conduction losses are lower and operational efficiency is higher. The waveforms for the buck and boost modes are depicted in Fig. 5.

Therefore, the control method of the DAB converter can be optimized based on the buck and boost modes of the FSBB.

III. Hybrid Phase-Shift Control Method

The condition for achieving ZVS is that the current flows through the anti-parallel diodes of the switching device before the gate signal goes high, and the condition for achieving ZCS is that the current flowing through the switching device is zero if the gate signal goes high. The soft-switching conditions of the DAB converter are listed in Table II.

A. The Analysis of Step-Down Condition (M > 1)

The analysis for the step-down condition is grounded in the buck mode of the FSBB. As is shown in Fig. 6(b), S_5 and S_8 remain on during $t_0 - t_2$. S_4 is turned on at t_0, and the energy is directly transferred from the input side to the output side, with the inductor current increasing. S_1 is turned off and S_2 is on at t_1, allowing the energy stored in the inductor to continue being delivered to the output side, resulting in a decrease in current. The difference from the FSBB lies that in the latter, the current drops below zero at t_2, which allows the anti-parallel diode of Q_1 to conduct, enabling ZVS for Q_1 and transitioning to the next cycle. In contrast, the full-bridge structure of the

TABLE II
Soft-Switching Conditions of the DAB Converter

Switching devices	ZVS condition	ZCS condition
S_1, S_4, S_6, S_7	$i_L(t) < 0$	$i_L(t) = 0$
S_2, S_3, S_5, S_8	$i_L(t) > 0$	$i_L(t) = 0$

DAB converter doubles the period. The negative current at t_2 is unable to achieve soft-switching for S_3. Considering this, S_3 should be turned on if the current drops to zero to realize ZCS. Since the transition to the next half-cycle occurs exactly at the zero-crossing point of the current, this mode is termed the buck boundary conduction mode (Buck_BCM). The analysis for the latter half-cycle is similar to the preceding text.

As can be seen from Fig. 6(b), the ZVS conditions listed in Table II are met by the current during the conduction of S_1 and S_2, and the ZCS conditions are met by the current during the conduction of S_3–S_8. Therefore, S_1 and S_2 achieve ZVS, while S_3–S_8 achieve ZCS in the Buck_BCM. The expression of the phase-shift ratios can be further derived as follows

$$\begin{cases} D_1 = D_2 + D_3 \\ D_3 = 0 \\ \dfrac{(V_i - nV_o)(1-D_1)T_{hs}}{L} - \dfrac{nV_oD_2T_{hs}}{L} = 0 \end{cases} \tag{1}$$

Buck_BCM cannot meet the needs of global power operation with the fixed inductance and switching frequency of the DAB converter. Therefore, it is necessary to adjust the transferred power on the basis of Buck_BCM by altering the magnitude or duration of the voltage across the inductor.

If the converter operates under light-load conditions, the reduction in the duration of the inductor voltage can result in discontinuous current, consequently diminishing the power delivery. This mode is defined as the buck discontinuous conduction mode (Buck_DCM), with the operational waveform depicted in Fig. 6(a).

As observed in Fig. 6, it is evident that the current state of the switches at the moment of conduction in the Buck_DCM is consistent with that of the Buck_BCM. Hence, S_1 and S_2 achieve ZVS, and S_3–S_8 achieve ZCS in the Buck_DCM. The expression of the phase-shift ratios can be derived as follows

$$\begin{cases} D_1 = D_2 + D_3 \\ \dfrac{(V_i - nV_o)(1-D_1)T_{hs}}{L} - \dfrac{nV_oD_2T_{hs}}{L} = 0 \end{cases} \tag{2}$$

Under heavy-load conditions, the transferred power can be enhanced by increasing the inductor voltage, which leads to a rapid increase in current. There are two methods to increase the inductor voltage. One method involves increasing the voltage to $V_i + nV_o$, and its operational waveforms is illustrated in red in Fig. 7, with the red shaded area representing the transferred

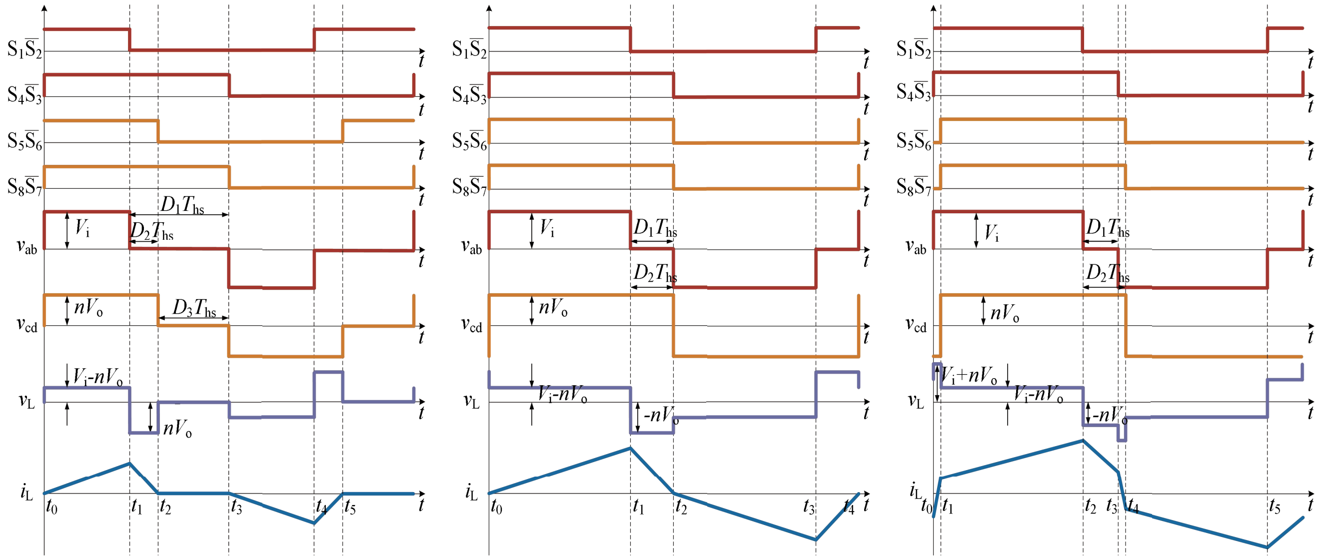

Fig. 6. Operational waveforms of the DAB converter under step-down condition. (a) Buck_DCM. (b) Buck_BCM. (c) Buck_CCM.

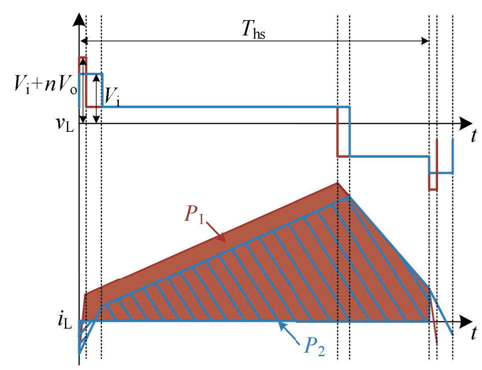

Fig. 7. Comparison of operational waveforms in two methods.

power P_1. The other method involves increasing the voltage to V_i, and its operational waveforms is depicted in blue in Fig. 7, with the blue shaded area representing the transferred power P_2.

Based on the inductor voltage and current waveforms shown in Fig. 7, the expression for the transferred power can be derived as follows

$$P = V_i \cdot \frac{1}{T_{hs}} \int_0^{T_{hs}} i_L(t)\,dt \tag{3}$$

Taking the maximum power P_b of SPS control as [28], the p.u. value of P_1 is

$$\begin{aligned} P_1 &= V_i \cdot \frac{1}{P_b T_{hs}} \int_0^{T_{hs}} i_L(t)\,dt \\ &= \frac{(-MD_1+2MD_2-M+1)^2}{2(M+1)} - \frac{(MD_1+2D_1-2D_2-M+1)^2}{2(M+1)} + \\ &\quad 2(-MD_1+MD_2+D_2)(1-D_2)+2D_1(-MD_1-D_1+2D_2+M-1) \end{aligned} \tag{4}$$

Similarly, the p. u. value of P_2 is

$$\begin{aligned} P_2 &= V_i \cdot \frac{1}{P_b T_{hs}} \int_0^{T_{hs}} i_L(t)\,dt \\ &= \frac{(-MD_1+D_1+2MD_2-D_2-M+1)^2}{2M} - \\ &\quad \frac{(-MD_1-D_1+D_2+M-1)^2}{2M} + 2(-MD_1+D_1+MD_2)(1-D_2)+ \\ &\quad 2D_1(-MD_1+D_2+M-1) \end{aligned} \tag{5}$$

In addition, D_1 and D_2 satisfy the following constraint condition within these two methods:

$$D_1 < D_2 \tag{6}$$

According to (4) − (6), the relationship between the transferred power and the phase shift ratios is plotted for different values of M, as shown in Fig. 8. It can be observed that P_1 is always greater than P_2 under the constraint condition. Thus, elevating the inductor voltage to $V_i + nV_o$ is the optimal choice for enhancing the transferred power under heavy load conditions.

Since the inductor current remains continuously conductive, this mode is defined as the buck continuous conduction mode (Buck_CCM), with its operational waveform presented in Fig. 6(c).

It can be observed in Fig. 6(c) that ZVS conditions indicated in Table II are satisfied by the current of each switch at the moment of conduction. Therefore, S_1–S_8 all achieve ZVS in the Buck_CCM. The expression of the phase-shift ratios can be further derived as follows

$$D_3 = 0 \tag{7}$$

B. The Analysis of Step-Up Condition (M < 1)

The analysis for the step-up operation is based on the boost mode of the FSBB. As is shown in Fig. 9(b), S_1 and S_4 are conductive during $t_0 - t_2$. S_5 is turned on at t_0, and energy from

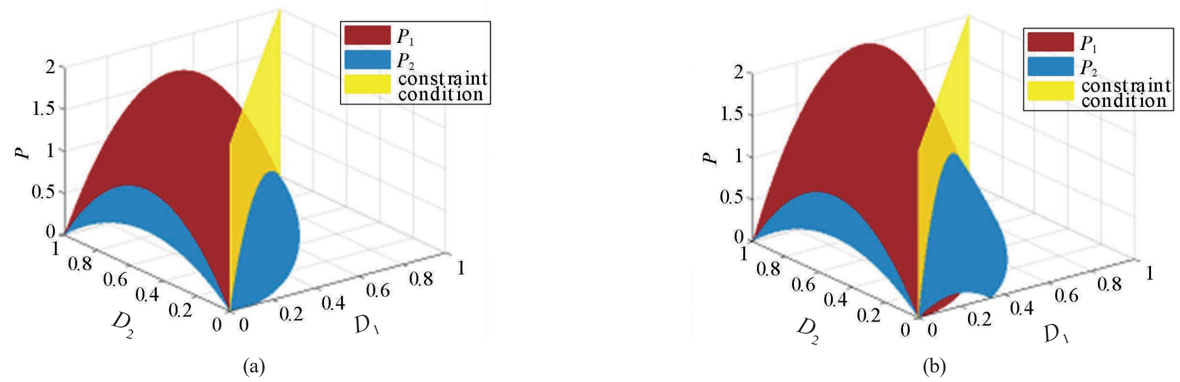

Fig. 8. Comparison of transferred power between two methods. (a) $M = 1.2$. (b) $M = 2$.

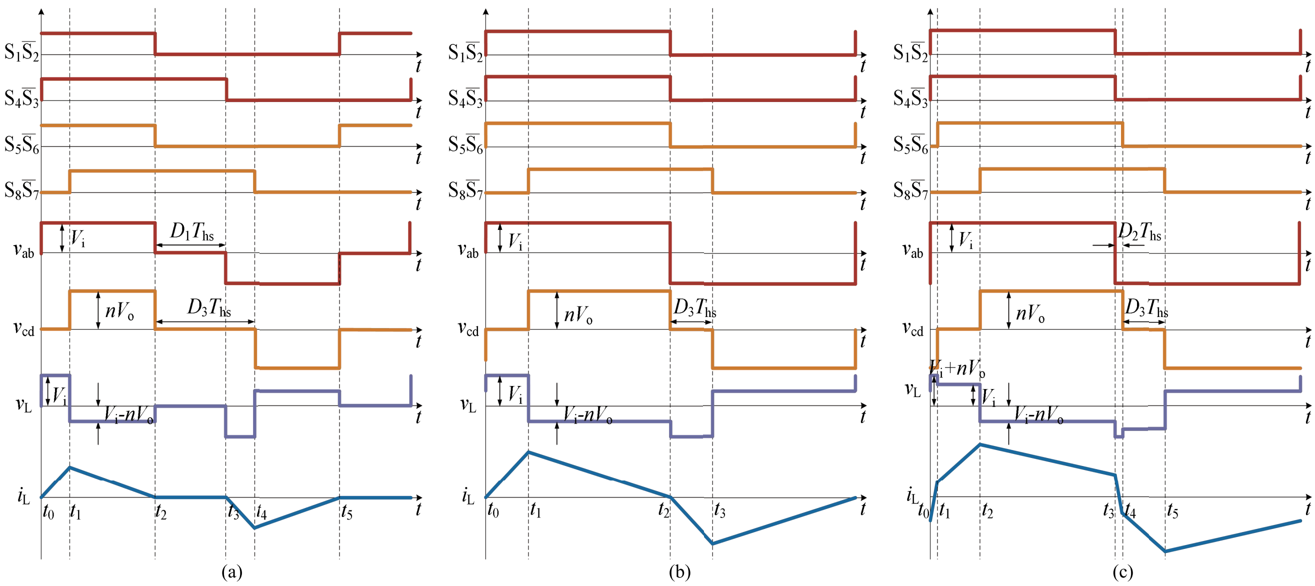

Fig. 9. Operational waveforms of the DAB converter under step-up condition. (a) Boost_DCM. (b) Boost_BCM. (c) Boost_CCM.

the input side is stored in the inductor, with the inductor current increasing. S_7 is turned off and S_8 is on at t_1, causing both the input side and the inductor to transfer energy to the output side, resulting in a decrease in current. The current decreases to zero at t_2, at which point S_6 is turned on with ZCS. Similar to the Buck_BCM, this mode is defined as the boost boundary conduction mode (Boost_BCM).

From Fig. 9(b), it can be seen that the ZVS conditions specified in Table II are met by the current of S_7 and S_8 at the moment of conduction, and the ZCS conditions are met by the current of S_1–S_6 at the moment of conduction. As a result, S_7 and S_8 achieve ZVS, and S_1–S_6 achieve ZCS in the Boost_BCM. The expression of the phase-shift ratios can be further derived as follows

$$\begin{cases} D_1 = D_2 = 0 \\ \dfrac{V_i D_3 T_{hs}}{L} - \dfrac{(V_i - nV_o)(T_{hs} - D_3 T_{hs})}{L} = 0 \end{cases} \tag{8}$$

Under light-load conditions, reducing the duration of the inductor voltage leads to decreased transferred power. This mode is defined as the boost discontinuous conduction mode (Boost_DCM), and its waveform is shown in Fig. 9(a).

In Fig. 9, the current state of the switches at the moment of conduction in Boost_DCM is identical to that of Boost_BCM. Consequently, S_7 and S_8 achieve ZVS, and S_1–S_6 achieve ZCS in Boost_DCM. The expression of the phase-shift ratios can be further derived as follows

$$\begin{cases} D_2 = 0 \\ \dfrac{V_i (D_3 - D_1) T_{hs}}{L} - \dfrac{(V_i - nV_o)(T_{hs} - D_3 T_{hs})}{L} = 0 \end{cases} \tag{9}$$

Under heavy-load operations, the power transferred can be enhanced by raising the inductor voltage to $V_i + nV_o$. This mode is defined as the boost continuous conduction mode (Boost_CCM) because the current remains continuous, with the waveform illustrated in Fig. 9(c).

In Fig. 9(c), ZVS conditions outlined in Table II are satisfied by the current of all switches at the moment of conduction. Therefore, S_1–S_8 all achieve ZVS in the Boost_CCM. The expression of the phase-shift ratios can be further derived as follows

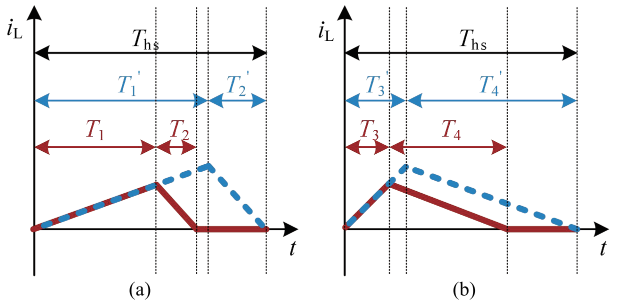

Fig. 10. Inductor current waveforms under DCM and BCM. (a) Buck_DCM and Buck_BCM. (b) Boost_DCM and Boost_BCM.

$$D_1 = 0 \tag{10}$$

This method is termed the hybrid phase-shift control method due to its implementation of multi-mode and multi-phase-shift control.

Regarding the power transmission capability, the six operating modes can be categorized according to the relationships of the phase shift ratios. Buck_CCM and Boost_CCM are grouped under mode B_1 shown in Table I. As analyzed in Section II, this mode covers the entire range of transferred power, enabling the DAB converter to operate under heavy load conditions. Boost_DCM and Boost_BCM are classified as mode B_2, and Buck_DCM and Buck_BCM are classified as mode B_3, with their respective transferred power ranges being [0, 2/3] and [0, 1/2]. These two modes are suitable for the DAB converter to operate under light and medium load conditions.

IV. A Unified Uni-Variate Control Method

To meet diverse transferred power requirements, three operating modes are proposed in the previous section for both step-down and step-up conditions. However, the transferred power is not static, and DAB converter is required to transit seamlessly among the various modes in practical applications. Therefore, a unified uni-variate control method which is simple and feasible is proposed in this section to meet the need of transitions.

A. Transition Method for Discontinuous Conduction of Current

The waveforms of DCM and BCM under both step-down and step-up conditions are illustrated in Fig. 10. The solid red lines represent DCM, and the dashed blue lines represent BCM.

In the Buck_DCM, the inductor current initially rises with a slope of $(V_i-nV_o)/L$ over a period T_1, then falls with a slope of nV_o/L over a period T_2. In the Buck_BCM , the inductor current first increases with a slope of $(V_i-nV_o)/L$ over a period T_1', and then decreases with a slope of nV_o/L over a period T_2'. These two periods satisfy the following expression

$$T_1' + T_2' = T_{hs} \tag{11}$$

It can be observed that as the transferred power increases, T_1 gradually increases to T_1', T_2 increases to T_2'. The periods all satisfy the following expression

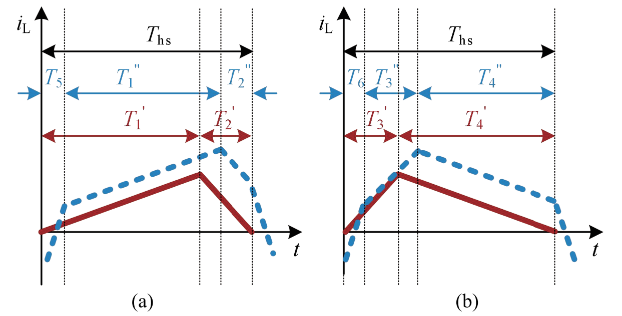

Fig. 11. Inductor current waveforms under BCM and CCM. (a) Buck_BCM and Buck_CCM. (b) Boost_BCM and Boost_CCM.

$$\frac{T_1'}{T_2'} = \frac{T_1}{T_2} = \frac{nV_o}{V_i - nV_o} \tag{12}$$

By solving (11) and (12), T_1' and T_2' can be expressed as

$$\begin{cases} T_1' = \dfrac{nV_o}{V_i} \cdot T_{hs} \\ T_2' = \dfrac{V_i - nV_o}{V_i} \cdot T_{hs} \end{cases} \tag{13}$$

It is evident that T_1 and T_2 are coupled in (12). Therefore, during the transition from Buck_DCM to Buck_BCM, T_2 will be automatically regulated if T_1 is adjusted.

In Boost_DCM, the inductor current first rises with a slope of V_i/L over a time period T_3, then falls with a slope of $(V_i-nV_o)/L$ over a time period T_4. In the Boost_BCM, the inductor current first increases with a slope of V_i/L over a time period T_3', then decreases with a slope of $(V_i-nV_o)/L$ over a time period T_4'. These two periods satisfy the following expression

$$T_3' + T_4' = T_{hs} \tag{14}$$

It can be seen that T_3 gradually increases to T_3', T_4 gradually increases to T_4' with the transferred power increasing. The periods all satisfy the following expression

$$\frac{T_3'}{T_4'} = \frac{T_3}{T_4} = \frac{nV_o - V_i}{V_i} \tag{15}$$

By solving (14) and (15), T_3' and T_4' can be expressed as

$$\begin{cases} T_3' = \dfrac{nV_o - V_i}{nV_o} \cdot T_{hs} \\ T_4' = \dfrac{V_i}{nV_o} \cdot T_{hs} \end{cases} \tag{16}$$

It is apparent that T_3 and T_4 are also coupled in (15). Therefore, the transition from Boost_DCM to Boost_BCM can be achieved by adjusting T_3, and T_4 is regulated accordingly.

B. Transition Method for Continuous Conduction of Current

Fig. 11 gives the waveforms of BCM and CCM under both step-down and step-up conditions, with solid red lines repre-

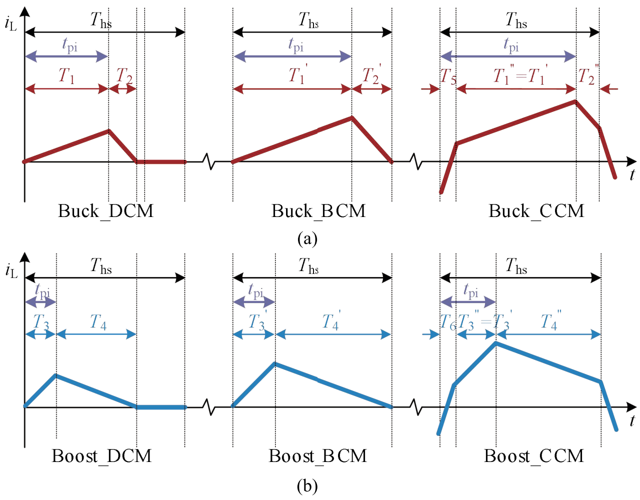

Fig. 12. The transitions among DCM, BCM and CCM. (a) Step-down condition. (b) Step-up condition.

senting BCM and dashed blue lines representing CCM.

In the Buck_CCM waveform shown in Fig. 11(a), the inductor current initially rises with a slope of $(V_i + nV_o)/L$ over a period T_5, then continues to rise with a slope of $(V_i - nV_o)/L$ over a period T_1'', and finally falls with a slope of nV_o/L over a period T_2''. These periods satisfy the following expression

$$T_1'' + T_2'' + T_5 = T_{hs} \tag{17}$$

Based on the analysis in subsection A of Section III, in the shift from Buck_BCM to Buck_CCM, it is optimal to increase the inductor voltage to $V_i + nV_o$, thereby introducing T_5. When the transferred power needs to be adjusted in Buck_CCM, there are three control degrees of freedom (i.e., T_5, T_1'', T_2''), which increase the complexity of control. Thus, it is advisable to keep T_1'' equal to T_1'. When adjusting T_5, T_2'' will be automatically adjusted according to (17).

In Boost_CCM waveform shown in Fig. 11(b), the inductor current first rises with a slope of $(V_i + nV_o)/L$ over a period T_6, then increases with a slope of V_i/L over a period T_3'', and subsequently decreases with a slope of $(nV_o - V_i)/L$ over a period T_4''. These periods satisfy the following expression

$$T_3'' + T_4'' + T_6 = T_{hs} \tag{18}$$

During the transition from Boost_BCM to Boost_CCM, raising the inductor voltage to $V_i + nV_o$, which introduces T_6. In Boost_CCM, by keeping T_3'' equal to T_3', the transferred power can be adjusted by varying T_6, with T_4'' automatically adjusting in accordance with (18).

C. The Principle of the Unified Uni-Variate Control Method

Fig. 12 illustrates the transitions among DCM, BCM and CCM. Based on the analysis from the previous subsections, the transitions can be achieved by adjusting T_1 and T_5 under step-down conditions. To reduce the complexity of control, a unified control variable t_{pi} is defined to regulate T_1 and T_5 in Fig. 12(a).

In Buck_DCM, the value of t_{pi} ranges from $[0, T_1']$, and the expression of t_{pi} is

$$t_{pi} = T_1 \tag{19}$$

Furthermore, the expressions for the phase-shift ratios can be calculated as follows in conjunction with (2)

$$\begin{cases} D_1 = 1 - \dfrac{t_{pi}}{T_{hs}} \\ D_2 = \dfrac{V_i - nV_o}{nV_o} \cdot \dfrac{t_{pi}}{T_{hs}} \\ D_3 = 1 - \dfrac{V_i}{nV_o} \cdot \dfrac{t_{pi}}{T_{hs}} \end{cases} \tag{20}$$

In Buck_BCM, the expression of t_{pi} is

$$t_{pi} = T_1' = \frac{nV_o}{V_i} \cdot T_{hs} \tag{21}$$

At this time, the phase-shift ratios still satisfy (20).

In Buck_CCM, the range of t_{pi} is $[T_1', T_{hs}]$, and the expression of t_{pi} is

$$t_{pi} = T_5 + T_1'' = T_5 + \frac{nV_o}{V_i} \cdot T_{hs} \tag{22}$$

By integrating (7), the expressions for the phase-shift ratios can be derived as follows

$$\begin{cases} D_1 = 1 - \dfrac{t_{pi}}{T_{hs}} \\ D_2 = 1 - \dfrac{nV_o}{V_i} \\ D_3 = 0 \end{cases} \tag{23}$$

As the transferred power increases, the value of t_{pi} will monotonically increase according to (19), (21) and (22). Since t_{pi} changes continuously, the transition process between modes is also continuous and smooth.

Under step-up conditions, the transitions can be realized by controlling T_3 and T_6. Similarly to the step-down conditions, t_{pi} can still be used to regulate T_3 and T_6 in Fig. 12(b).

In Boost_DCM, the value of t_{pi} ranges from $[0, T_3']$, and the expression of t_{pi} is

$$t_{pi} = T_3 \tag{24}$$

The expressions for the phase-shift ratios can be calculated by combining (9) as follows

$$\begin{cases} D_1 = 1 - \dfrac{nV_o}{nV_o - V_1} \cdot \dfrac{t_{pi}}{T_{hs}} \\ D_2 = 0 \\ D_3 = 1 - \dfrac{V_i}{nV_o - V_i} \cdot \dfrac{t_{pi}}{T_{hs}} \end{cases} \tag{25}$$

In Boost_BCM, the expression of t_{pi} is

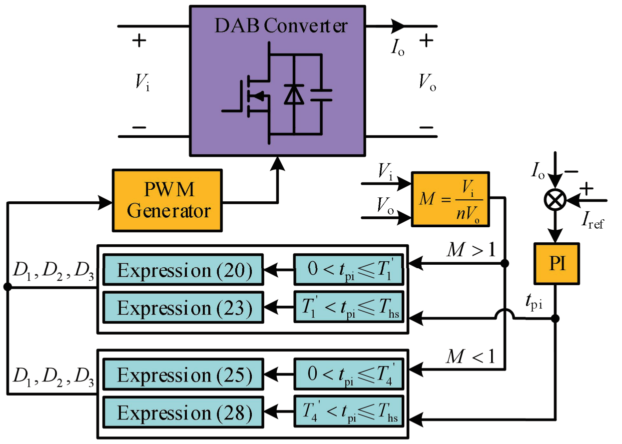

Fig. 13. The closed-loop control system of the unified uni-variate control method.

$$t_{\mathrm{pi}}=T_3^{'}=\frac{nV_{\mathrm{o}}-V_{\mathrm{i}}}{nV_{\mathrm{o}}}\cdot T_{\mathrm{hs}} \tag{26}$$

At this point, the phase-shift ratios still satisfy (25).

In Boost_CCM, the range of t_{pi} is $[T_3^{'}, T_{\mathrm{hs}}]$, and its expression is given by

$$t_{\mathrm{pi}}=T_6+T_3^{''}=T_6+\frac{nV_{\mathrm{o}}-V_{\mathrm{i}}}{nV_{\mathrm{o}}}\cdot T_{\mathrm{hs}} \tag{27}$$

Furthermore, the expressions for the phase-shift ratios can be derived as follows in conjunction with (10)

$$\begin{cases} D_1=0 \\ D_2=\dfrac{t_{\mathrm{pi}}}{T_{\mathrm{hs}}}-\dfrac{nV_{\mathrm{o}}-V_{\mathrm{i}}}{nV_{\mathrm{o}}} \\ D_3=\dfrac{nV_{\mathrm{o}}-V_{\mathrm{i}}}{nV_{\mathrm{o}}} \end{cases} \tag{28}$$

Drawing from (24), (26) and (27), it is evident that the value of t_{pi} increases steadily and monotonically with the transferred power increasing, thereby achieving a smooth transition between modes.

As shown in Fig. 13, the closed-loop control system of the unified uni-variate control method is constructed. First, the input voltage V_{i} and output voltage V_{o} of the DAB converter are sampled to calculate the voltage conversion ratio M, which determines whether the converter is operating under step-down conditions or step-up conditions. Meanwhile, the output current I_{o} is sampled, and the difference between the reference current I_{ref} and I_{o} is fed into a PI controller. The output of the PI controller serves as the unified control variable t_{pi}. Subsequently, V_{i}, V_{o} and t_{pi} are input into the computational model to determine the phase-shift ratios D_1, D_2 and D_3. Finally, the phase-shift ratios are entered into the PWM generator to produce the driving signals, which control the switches of the DAB converter. It is evident that the three phase-shift ratios D_1, D_2 and D_3 can be managed by merely adjusting the value of t_{pi}, thereby reducing the complexity of control. In addition, only four expressions are necessary for the computational model, making the modulation scheme to be readily implemented using general DSP.

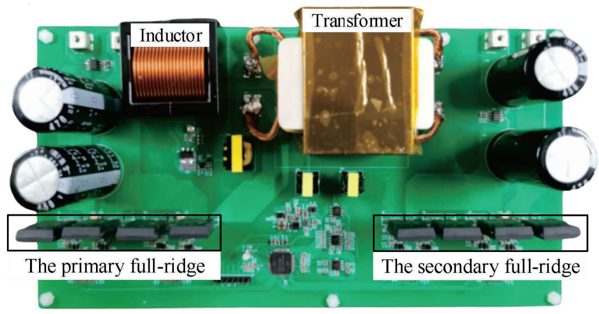

Fig. 14. The 2.5 kW prototype of the DAB converter.

TABLE III
EXPERIMENTAL PARAMETERS

Parameter	Value
Input dc voltage	300 V
Output dc voltage	230–370 V
Inductance	30 μH
Transformer turn ratio	1 : 1
Switching frequency	50 kHz

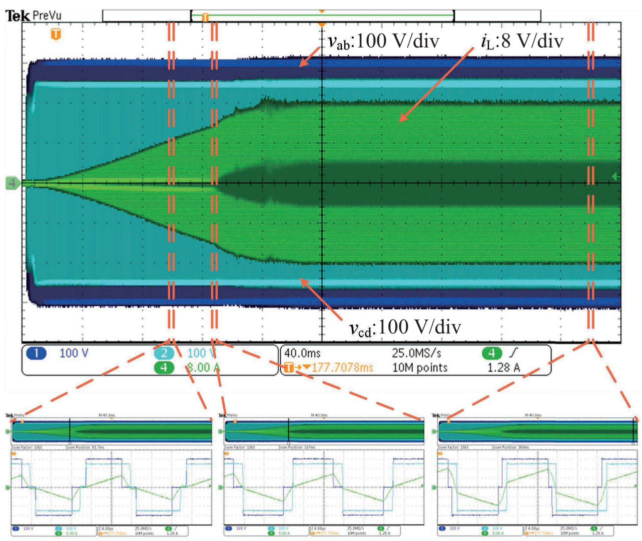

Fig. 15. The waveform over full power range with V_{i} = 300 V, V_{o} = 250 V.

V. Experimental Verification

As shown in Fig. 14, a 2.5 kW prototype of DAB converter is built by SiC MOSFET (i.e., GC3M0040120K) in the laboratory. The control algorithms are implemented by the DSP (i.e., TMS320F280049), and the experimental parameters are listed in Table III. In order to verify the effectiveness of the proposed method under various values of M, experiments are conducted by setting V_{o} to different values.

A. The Experiment Under Step-Down Conditions (M > 1)

An experiment is conducted with the settings V_{i} = 300 V, V_{o} = 250 V. It can be seen from Fig. 15 that as the transferred

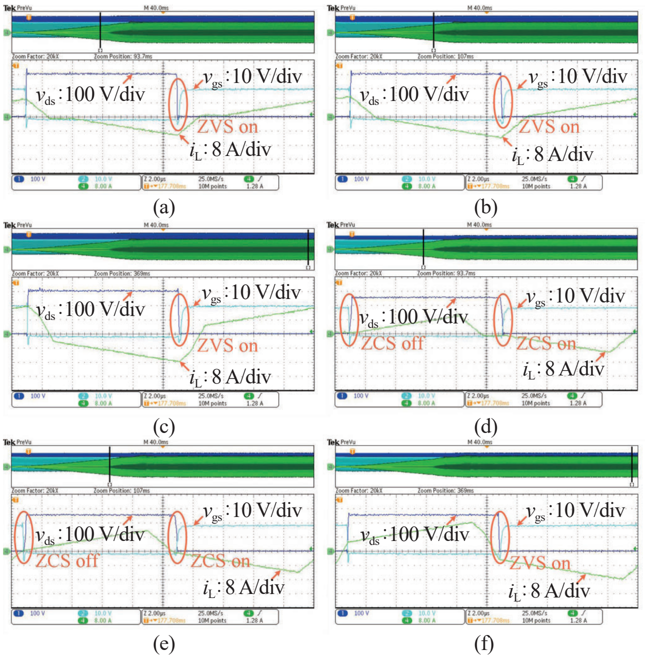

Fig. 16. The switching waveforms with $V_i = 300$ V, $V_o = 250$ V. (a) S_1 in Buck_DCM. (b) S_1 in Buck_BCM. (c) S_1 in Buck_CCM. (d) S_7 in Buck_DCM. (e) S_7 in Buck_BCM. (f) S_7 in Buck_CCM.

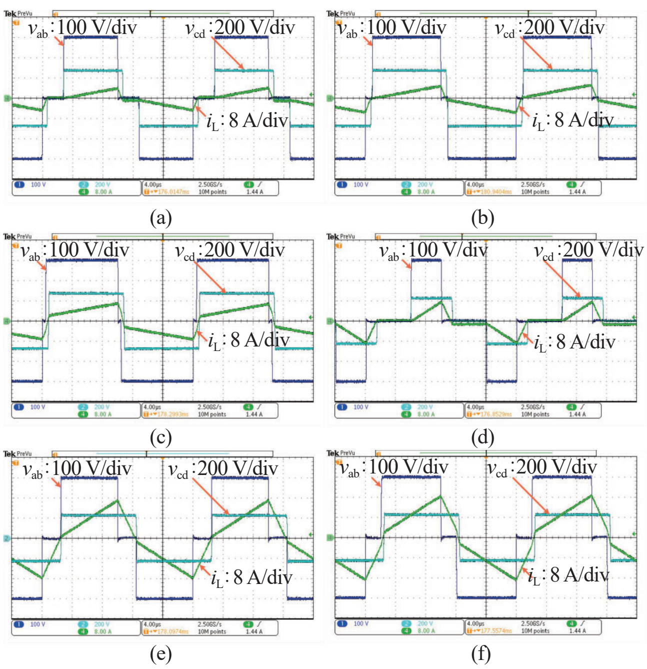

Fig. 17. The waveforms under step-down conditions with $V_i = 300$ V. (a) $V_o = 280$ V in Buck_DCM. (b) $V_o = 280$ V in Buck_BCM. (c) $V_o = 280$ V in Buck_CCM. (d) $V_o = 230$ V in Buck_DCM. (e) $V_o = 230$ V, in Buck_BCM. (f) $V_o = 230$ V in Buck_CCM.

power increases, the converter sequentially operates in Buck_DCM, Buck_BCM, and Buck_CCM, achieving smooth transitions. The switching waveforms of S_1 and S_7 are displayed in Fig. 16. Across all three modes, S_1 consistently achieves ZVS, and S_2 exhibits similar behavior. S_7 achieves ZCS in Buck_DCM and Buck_BCM, and ZVS in Buck_CCM. S_3 − S_6 and

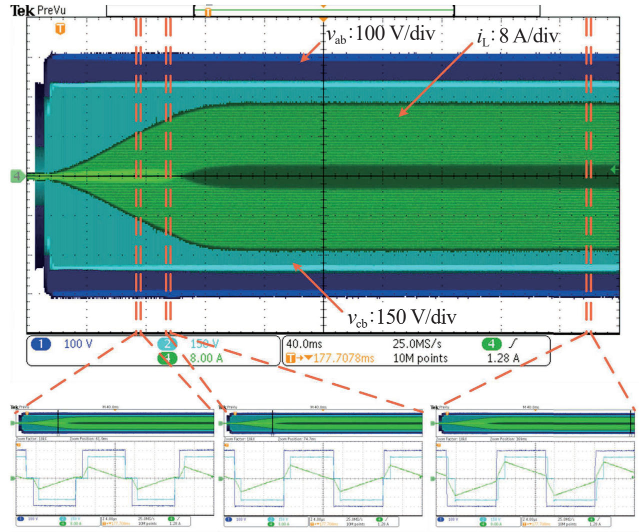

Fig. 18. The waveform over full power range with $V_i = 300$ V, $V_o = 350$ V.

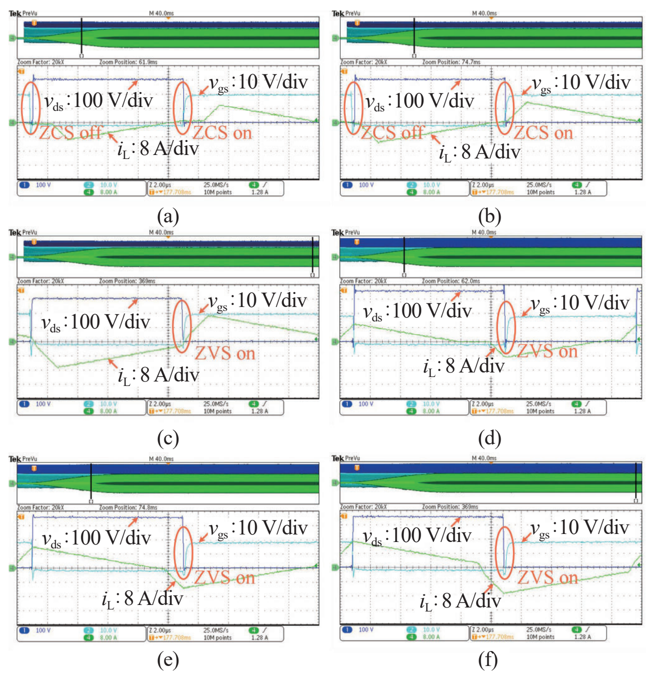

Fig. 19. The switching waveforms with $V_i = 300$ V, $V_o = 350$ V. (a) S_1 in Boost_DCM. (b) S_1 in Boost_BCM. (c) S_1 in Boost_CCM. (d) S_7 in Boost_DCM. (e) S_7 in Boost_BCM. (f) S_7 in Boost_CCM.

S_8 all behave similarly to S_7.

Further experiments are conducted with V_o set to 280 V and 230 V, respectively. The waveforms of Buck_DCM, Buck_BCM and Buck_CCM are presented in Fig. 17, thereby validating the effectiveness of the proposed method across a wide range of output voltage.

B. The Experiment Under Step-Up Conditions (M < 1)

With the settings $V_i = 300$ V, $V_o = 350$ V, Fig. 18 shows that the converter transitions through Boost_DCM, Boost_BCM, and Boost_CCM, seamlessly. The switching waveforms of S_1 and S_7 are depicted in Fig. 19. In Boost_DCM and Boost_

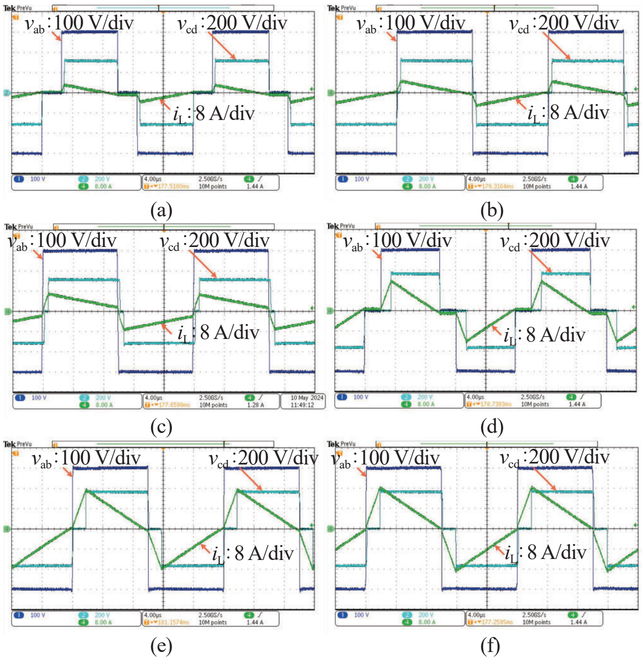

Fig. 20. The waveforms under step-up conditions with V_i = 300 V. (a) V_o = 320 V in Boost_DCM. (b) V_o = 320 V in Boost_BCM. (c) V_o = 320 V in Boost_CCM. (d) V_o = 370 V in Boost_DCM. (e) V_o = 370 V in Boost_BCM. (f) V_o = 370 V in Boost_CCM.

BCM, S_1 achieves ZCS, and in Boost_CCM, it achieves ZVS. $S_2 - S_6$ behave similarly to S_1. S_7 achieves ZVS across all three modes, and S_8 has the same performance as S_7.

Furthermore, experiments are conducted with V_o set to 320 V and 370 V, respectively. The waveforms of Boost_DCM, Boost_BCM, and Boost_CCM are displayed in Fig. 20.

C. Current Stress Analysis

The curves of the current stress by employing the method proposed are illustrated in Fig. 21, and the comparison is made with the optimization methods presented in [21].

As can be observed from Fig. 21(a), under the condition of M = 1.67, the current stress of the proposed method is significantly lower over the full power range compared to other methods. From Fig. 21(b), it is evident that under the condition of M = 0.65, the current stress of the proposed method is smaller over the majority of the power range. During the transition from light load to heavy load, the introduction of the high-slope inductor current in the Boost_CCM mode results in the current stress being slightly higher than that of the TPS-CO within a certain power range. Furthermore, the current stress is obviously decreased under heavy load by the proposed method.

D. Power Losses and Efficiency Performance

Fig. 22 illustrates the power losses in various components of the experimental prototype operating under Buck_DCM and Boost_DCM. The power losses include switching loss, conduction loss, transformer core loss, transformer copper loss, and other loss. The term "other loss" refers to the additional

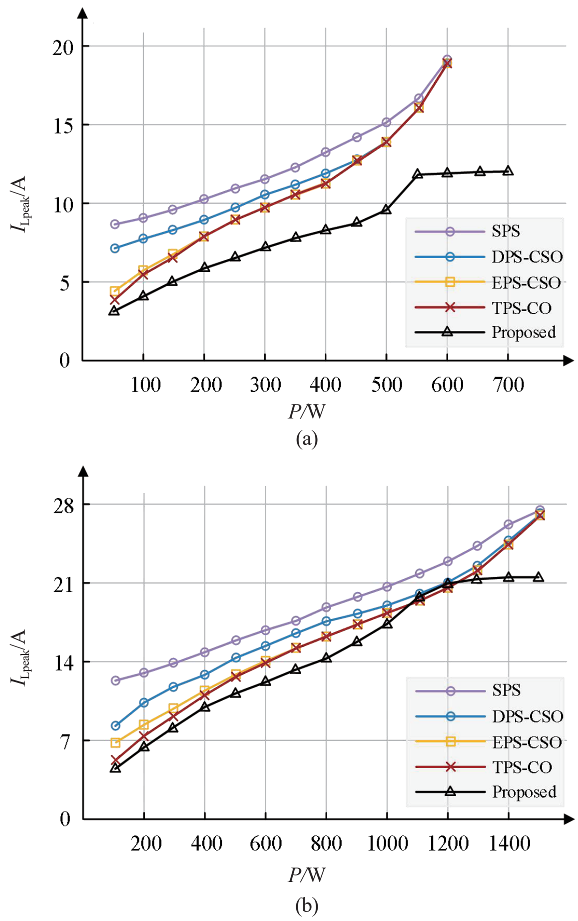

Fig. 21. The curves of the current stress versus transferred power under various control method. (a) Step-down conditions with M = 1.67. (b) Step-up conditions with M = 0.625.

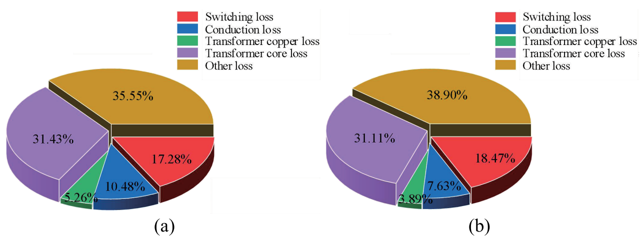

Fig. 22. The power losses of the prototype. (a) Buck_DCM with V_i = 300 V, V_o = 250 V, P = 570 W. (b) Boost_DCM with V_i = 300 V, V_o = 350 V, P = 620 W.

loss caused by sampling circuits, snubber circuits and PCB trace resistances, etc.

The curves of the efficiency under step-down and step-up conditions are presented in Fig. 23, which indicates that the prototype exhibits good excellent operational performance, with an overall high efficiency, peaking at 98.6%.

E. Comparison With Other Methods

A comparison of the proposed method with others is presented in Table IV. As shown in Table IV, while the method in [17] reports the highest efficiency, its performance at higher switching frequencies remains untested. Moreover, its reliance

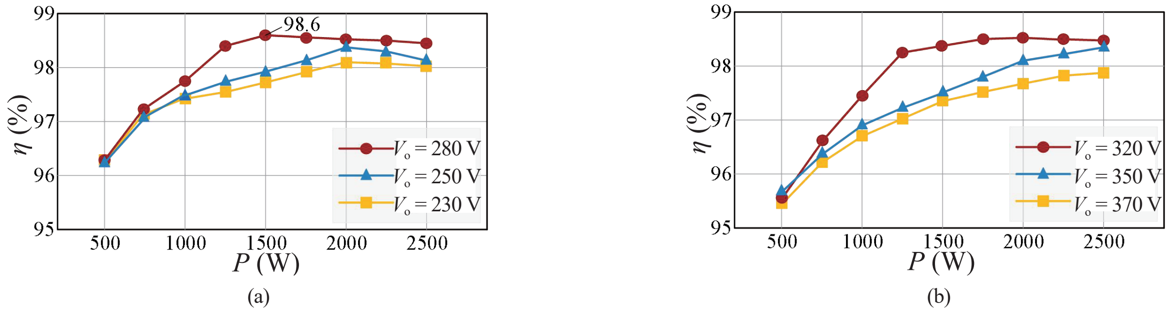

Fig. 23. The curves of the efficiency versus transferred power. (a) Step-down conditions. (b) Step-up conditions.

TABLE IV
EXPERIMENTAL PARAMETERS

The converter	Input dc voltage/V	Output dc voltage/V	Switching frequency/kHz	Controller complexity	Rated power/kW	Max efficiency/%
[17]	640	250–950	25	High	11	98.8
[19]	200	230, 160	20	Middle	1.3	98.3
[23]	70–110	60	20	Middle	1	97.1
[25]	200–400	300	100	Middle	1.2	95.8
Presented	300	230–370	50	Low	2.5	98.6

on lookup tables poses challenges in real-time application. Both the voltage regulation capability and switching frequency in [19] are limited, with efficiency falling below 96% under heavy-load conditions. The switching frequency and the efficiency are lower in [23]. In [25], although the highest frequency is achieved, the efficiency is compromised, reducing its applicability. Moreover, the latter three methods involve complex and time-consuming analysis of mathematical formulas, resulting in increased control difficulty.

VI. Conclusion

This article proposes a soft-switching control method designed for the DAB converter to operate efficiently across the full power and wide voltage regulation range. Utilizing the principle of voltage superposition, the DAB converter is innovatively transformed into an FSBB converter through the decomposition of the midpoint voltage waveforms v_{ab} and v_{cd}. Based on the equivalent circuit, a hybrid phase-shift control method is proposed, which categorizes the DAB converter into six operating modes according to the transferred power, with all six modes facilitating soft-switching of the switching devices. To realize seamless transitions between proposed modes, a unified uni-variate control method is introduced, along with the construction of a closed-loop control system. This method not only simplifies the control process but also facilitates real-time computation, making it compatible with common DSP. The experimental results from the prototype have demonstrated that the proposed method enables the DAB converter to achieve global soft-switching operation over the full power and wide voltage regulation range, resulting in enhanced operational efficiency.

References

[1] S. S. H. Yazdi, K. Rouzbehi, M. J. Carrizosa, A. Heidary, and M. Bagheri, “Modeling, control, and operation of an M-DAB DC-DC converter for interconnection of HVDC grids,” in *IEEE Systems Jouranal*, vol. 17, no. 2, pp. 2652–2663, Jun. 2023.

[2] P. F. S. Costa, P. H. B. Löbler, L. Roggia, and L. Schuch, “Modeling and control of DAB converter applied to batteries charging,” in *IEEE Transactions on Energy Conversion*, vol. 37, no. 1, pp. 175–184, Mar. 2022.

[3] S. Chaurasiya and B. Singh, “A bidirectional fast EV charger for wide voltage range using three-level DAB based on current and voltage stress optimization,” in *IEEE Transactions on Transportation Electrification*,vol. 9, no. 1, pp. 1330–1340, Mar. 2023.

[4] N. Hou and Y. W. Li, “Overview and comparison of modulation and control strategies for a nonresonant single-phase dual-active-bridge DC-DC Converter,” in *IEEE Transactions on Power Electronics*, vol. 35, no. 3, pp. 3148–3172, Mar. 2020.

[5] D. Mou, L. Yuan, Q. Luo, Y. Li, C. Liu, J. Zheng, and Z. Zhao, “Overview of multi-degree-of-freedom modulation techniques for dual active bridge converter,” in *IEEE Journal of Emerging and Selected Topics in Power Electronics*, vol. 11, no. 6, pp. 5724–5737, Dec. 2023.

[6] R. W. A. A. De Doncker, D. M. Divan, and M. H. Kheraluwala, “A three-phase soft-switched high-power-density DC/DC converter for high-power applications,” in *IEEE Transactions on Industry Applications*, vol. 27, no. 1, pp. 63–73, Jan.-Feb. 1991.

[7] Q. Gu, L. Yuan, J. Nie, J. Sun, and Z. Zhao, “Current stress minimization of dual-active-bridge DC-DC converter within the whole operating range,” in *IEEE Journal of Emerging and Selected Topics in Power Electronics*, vol. 7, no. 1, pp. 129–142, Mar. 2019.

[8] B. Zhao, Q. Song, W. Liu, and Y. Sun, “Overview of dual-active-bridge isolated bidirectional DC-DC converter for high-frequency-link power-conversion system,” in *IEEE Transactions on Power Electronics*, vol. 29, no. 8, pp. 4091–4106, Aug. 2014.

[9] H. Bai, Z. Nie, and C. C. Mi, “Experimental comparison of traditional phase-shift, dual-phase-shift, and model-based control of isolated bidirectional DC-DC converters,” in *IEEE Transactions on Power Electronics*, vol. 25, no. 6, pp. 1444–1449, Jun. 2010.

[10] F. Krismer and J. W. Kolar, “Efficiency-optimized high-current dual active bridge converter for automotive applications,” in *IEEE Transactions on Industrial Electronics*, vol. 59, no. 7, pp. 2745–2760, Jul. 2012.

[11] B. Zhao, Q. Yu, and W. Sun, “Extended-phase-shift control of isolated bidirectional DC-DC converter for power distribution in microgrid,” in

IEEE Transactions on Power Electronics, vol. 27, no. 11, pp. 4667–4680, Nov. 2012.

[12] H. Bai and C. Mi, "Eliminate reactive power and increase system efficiency of isolated bidirectional dual-active-bridge DC-DC converters using novel dual-phase-shift control," in *IEEE Transactions on Power Electronics*, vol. 23, no. 6, pp. 2905–2914, Nov. 2008.

[13] P. Wang, X. Chen, C. Tong, P. Jia, and C. Wen, "Large- and small-signal average-value modeling of dual-active-bridge DC-DC converter with triple-phase-shift control," in *IEEE Transactions on Power Electronics*, vol. 36, no. 8, pp. 9237–9250, Aug. 2021.

[14] J. Tian, F. Wang, F. Zhuo, Y. Wang, H. Wang, and Y. Li, "A zero-backflow-power EPS control scheme with multiobjective coupled-relationship optimization in DAB-based converter," in *IEEE Journal of Emerging and Selected Topics in Power Electronics*, vol. 10, no. 4, pp. 4128–4145, Aug. 2022.

[15] L. Xin, Z. Haoyu, Q. Ya, and S. Junkang, "Current stress optimization of dual active bridge converter based on dual phase shift control," in *Proceedings of 2020 IEEE 9th Joint ITAIC*, Chongqing, China, 2020, pp. 717–724.

[16] L. Zhu, A. R. Taylor, G. Liu, and K. Bai, "A multiple-phase-shift control for a SiC-based EV charger to optimize the light-load efficiency, current stress, and power quality," in *IEEE Journal of Emerging and Selected Topics in Power Electronics*, vol. 6, no. 4, pp. 2262–2272, Dec. 2018.

[17] D. Lyu, C. Straathof, T. B. Soeiro, Z. Qin, and P. Bauer, "ZVS-optimized constant and variable switching frequency modulation schemes for dual active bridge converters," in *IEEE Open Journal of Power Electronics*, vol. 4, pp. 801–816, 2023.

[18] X. Li, X. Zhang, F. Lin, C. Sun, and K. Mao, "Artificial-intelligence-based triple phase shift modulation for dual active bridge converter with minimized current stress," in *IEEE Journal of Emerging and Selected Topics in Power Electronics*, vol. 11, no. 4, pp. 4430–4441, Aug. 2023.

[19] A. Tong, L. Hang, G. Li, X. Jiang, and S. Gao, "Modeling and analysis of a dual-active-bridge-isolated bidirectional DC/DC converter to minimize RMS current with whole operating range," in *IEEE Transactions on Power Electronics, vol. 33*, no. 6, pp. 5302–5316, Jun. 2018.

[20] N. Hou, W. Song, and M. Wu, "Minimum-current-stress scheme of dual active bridge DC-DC converter with unified phase-shift control," in *IEEE Transactions on Power Electronics*, vol. 31, no. 12, pp. 8552–8561, Dec. 2016.

[21] Y. Zhang, J. Zong, F. Zhang, X. Li, Y. Wei, and H. Ma, "A comprehensive optimization strategy of DAB converter with minimal current stress and full soft switching in the whole operating range," in *IEEE Journal of Emerging and Selected Topics in Power Electronics*, vol. 12, no. 1, pp. 129–142, Feb. 2024.

[22] Q. Ren and S. Ai. "A three degree freedom optimal control strategy of dual-active-bridge converters for full range operations,"(in Chinese) in *Proceedings of CSEE*, vol. 40, no. 11, pp. 3613–3622, Jun. 2020.

[23] J. Huang, Y. Wang, Z. Li, and W. Lei, "Unified triple-phase-shift control to minimize current stress and achieve full soft-switching of isolated bidirectional DC-DC converter," in *IEEE Transactions on Industrial Electronics*, vol. 63, no. 7, pp. 4169–4179, Jul. 2016.

[24] J. Zhang, D. Sha, and P. Ma, "A dual active bridge DC-DC-based single stage AC-DC converter with seamless mode transition and high power factor," in *IEEE Transactions on Industrial Electronics*, vol. 69, no. 2, pp. 1411–1421, Feb. 2022.

[25] Z. Guo, "Modulation scheme of dual active bridge converter for seamless transitions in multiworking modes compromising ZVS and conduction loss," in *IEEE Transactions on Industrial Electronics*, vol. 67, no. 9, pp. 7399–7409, Sept. 2020.

[26] F. Krismer and J. W. Kolar, "Closed form solution for minimum conduction loss modulation of DAB converters," in *IEEE Transactions on Power Electronics*, vol. 27, no. 1, pp. 174–188, Jan. 2012.

[27] Z. Yu, H. Kapels and K. F. Hoffmann, "High efficiency bidirectional DC-DC converter with wide input and output voltage ranges for battery systems," in *Proceedings of PCIM Europe*, Nuremberg, Germany, 2015, pp. 1–8.

[28] B. Zhao, Q. Song, and W. Liu, "Power characterization of isolated bidirectional dual-active-bridge DC-DC converter with dual-phase-shift control," in *IEEE Transactions on Power Electronics*, vol. 27, no. 9, pp. 4172–4176, Sept. 2012.

Yuhang Zhang was born in Hebei, China. He received the B.S. degree from the College of Electrical and Information Engineering, Hunan University, Changsha, China. He is currently working towards the M.S. degree in electrical engineering at Hunan University, Changsha, China. His current research interests include application and control of bidirectional dc-dc converters.

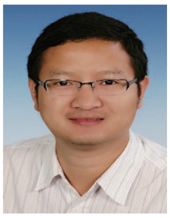

Yong Li received the B.Sc. and Ph.D. degrees from the College of Electrical and Information Engineering, Hunan University, Changsha, China, in 2004 and 2011, respectively. He is currently a full Professor of electrical engineering with Hunan University. His current research interests include power system stability analysis and control, ac/dc energy conversion systems and equipment, analysis and control of power quality, and HVDC and FACTS technologies.

Jianghu Wan was born in Sichuan, China, in 1991. He received the B.S., M.S. and Ph.D. degrees, in 2014, 2017 and 2024, respectively, from Central South University, Changsha, China. His current research interests include bidirectional dc-dc converters, control of three-phrase PWM rectifier, and soft-switching technology.

Tingkun Weng received the M.S. degree in 2024 in electrical engineering from Hunan University, Changsha, China. He is currently working at Technical Skills Training Center of State Grid Hunan Electric Power Company (Changsha Electric Power Technical College). His research interests include flux pump, wireless energy transmission and high temperature superconductivity.

Jie Zhang was born in Chongqing, China, in 1999. He received B.S. degree from the College of Electrical and Information Engineering, Hunan University, Changsha, China, in 2022. He is currently working the M.S. degree in Hunan University, Changsha, China. His research interests include active power decoupling control and bidirectional dc/dc converters.

Yijia Cao was born in Hunan, China, in 1969. He received the graduation degree from Xi'an Jiaotong University, Xi'an, China in 1988, and the M.Sc. and Ph.D. degrees from Huazhong University of Science and Technology (HUST), Wuhan, China, in 1991 and 1994, respectively. From September 1994 to April 2000, he was a Visiting Research Fellow and a Research Fellow with Loughborough University, Loughborough, U.K., Liverpool University, Liverpool, U.K., and the University of the West England, Bristol, U.K. From 2000 to 2001, he was a Professor with HUST, and from 2001 to 2008, he was a Professor with Zhejiang University, Hangzhou, China, and from 2008 to 2018, he was a Professor with Hunan University, Changsha, China. He was appointed as the Vice President of Hunan University in 2008. He is currently a Professor with Changsha University of Science and Technology, Changsha. His research interests include power system stability control and the application of intelligent systems in power systems.

Research on Dead Time Optimization Characteristics of High-Power Three-Phase LLC Resonant Converter

Xianjin HUANG, Hongchao BAI, Zhidong XUE, Yinghui ZHAO, Wenwen SHI, and Linfeng ZHAO

***Abstract*—Reasonable dead time is a prerequisite for realizing zero-voltage turn-on (ZVS) of IGBT in a three-phase LLC converter. At the same time, the operating temperature greatly affects the output capacitance characteristics of IGBT. When the operating temperature of the IGBT rises, it will result in the dead time that has been set is no longer appropriate, thus making the IGBT lose the soft-switching operating characteristics. To address this problem, the article analyzes the soft-switching realization conditions of the three-phase LLC converter and studies the relationship between the soft-switching realization and the dead time. The shutdown characteristics of IGBTs at different operating temperatures are analyzed. It is found that the higher the operating junction temperature of IGBTs in three-phase LLC resonant circuits, the more unfavorable it is to realize soft switching, and the formulas of the minimum dead time and the maximum dead time to ensure the zero-voltage turn-on of IGBTs at the worst operating temperatures are deduced. A 100 kW three-phase LLC converter prototype is constructed for verification. The soft switching can still be realized and the high efficiency can be maintained under the case of higher operating power, which verifies the accuracy of the dead time optimization design.**

***Index Terms*—Dead time, IGBT, soft switching, three-phase LLC resonant converter.**

I. Introduction

THE LLC resonant converter has the advantages of high efficiency, lightweight, small size, and soft-switching characteristics, and is capable of realizing zero-voltage switching (ZVS) conduction of the primary-side switching tube and zero-current switching (ZCS) turn-off of the secondary-side rectifier diode within the full-load range, which greatly improves the efficiency of the converter[1]−[3].To meet the high-power, high-current output requirements, the LLC resonant converter can be a multi-phase staggered parallel connection, the structure on the one hand, can reduce the current stress of each phase of the switching device of the LLC resonant converter, reduce its loss, on the other hand, can reduce the ripple in the output current, improve the service life of the filter capacitor [4]−[8]. In practice, a three-phase LLC converter needs to be controlled with a dead time to maintain the effective turn-off signal until the other switch in the same bridge arm is completely turned off to avoid the occurrence of the two switching tubes in the same bridge arm going straight through [9]. To realize the soft-switching operation of the primary switching tube, the converter needs to operate in the inductive region and the resonant current of the resonant network must be large enough to ensure that the parasitic capacitance of the primary switching tube and the secondary rectifier diode is fully charged and discharged within the dead time [10]. The dead time setting is very important for realizing soft switching and is determined by the parasitic capacitance of the primary-side switching tube and the resonance parameters of the converter. In conventional parametric design, the junction capacitance of the IGBT is often converted to a definite value when determining the dead time, but in practice, the IGBT output capacitance is affected by the voltages at the C- and E-pole terminals and the operating temperature of the IGBT [11]. [12] proposed an efficiency-optimized dead time and excitation inductance design to find the efficiency-optimized dead time design by deriving the relationship between the switching tube loss and the minimum dead time that can satisfy the soft-switching case. The effect of power switching tube junction capacitance variation with the operating environment is not considered. [13] analyzes the principle of selecting the dead time of the LLC converter to realize ZVS in a wide regulation range and uses the data in the MOSFET manual to calculate the minimum value of the dead time of the LLC converter to realize ZVS under the worst operating conditions without considering the effects of the converter's operating power and the switching tube's operating temperature on the switching tube. [14] considered the effect of different operating states of the LLC converter on the dead time and determined the maximum value of the dead time under extreme operating conditions, but did not analyze the minimum dead time. [15] proposed an adaptive deadband modulation scheme, which no longer needs to calculate the deadband time so that the deadband time changes dynamically with the operating conditions to realize soft switching, but the control design is more complex and may affect the performance of the LLC converter using other control methods. [16] proposed a dead time design method considering various controllable factors

Manuscript received December 17, 2024; revised February 28, 2025; accepted March 27, 2025. Date of publication June 30, 2025; date of current version April 18, 2025. This work was supported in part by Intellectual Property Licensing Program under the grant E24ZH200040. *(Corresponding author: Xianjin huang.)*

X. Huang, Z. Xue, and L. Zhao are with the School of Electrical Engineering, Beijing Jiaotong University, Beijing 100044, China (e-mail: xianjinhuang@bjtu.edu.cn; 22121539@bjtu.edu.cn; 23126403@bjtu.edu.cn).

H. Bai, Y. Zhao, and W. Shi are with Shandong Ainuo Instrument Co., Ltd, Jinan 215008, China (e-mail: 81202766@ainuo.com; dcm@ainuo.com; psmd@ainuo.com).

Digital Object Identifier 10.24295/CPSSTPEA.2025.00017

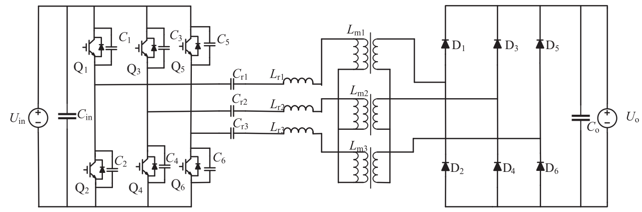

Fig. 1. Three-phase LLC resonant converter topology.

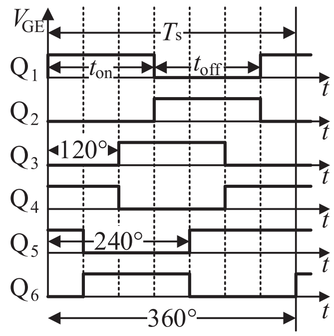

Fig. 2. gate signal.

and noise factors in the LLC resonant circuit, the main principle is to use the Monte Carlo method to simulate the fluctuation characteristics and fluctuation contribution rate of the dead time range, and to optimize the calculated dead time range, but the method requires a large amount of data as a support, and the design process is very cumbersome. [17] proposed a zero-voltage analysis and dead-time design of a half-bridge LLC-DCX converter considering nonlinear capacitance and different load values, analyzed in detail the charging and discharging process of the output capacitance during the dead-time and gave the dead-time formula considering nonlinear capacitance and different load values, but the design process is relatively cumbersome and the analysis is not comprehensive enough, and the junction capacitance is not analyzed from the characteristics of the power switching tubes to analyze the effect of the dead-time. The effect of junction capacitance on the dead time is not analyzed from the characteristics of the power switching tube.

In the high-power converter after a long period of operation of the IGBT module temperature produces a sharp change, this time if the dead time is set unreasonably, the power switching tube will lose the soft switching so that the converter efficiency is reduced, so it is necessary to amend the existing dead time design method. Based on the characteristics of the three-phase LLC circuit topology, this paper analyzes in detail the relationship between dead time and soft switching and obtains the dead time range formula, then analyzes the switching characteristics of the IGBT, studies in detail the relationship between the IGBT output capacitance and its junction temperature and the output load, and determines the size of the worst-case IGBT output capacitance, and makes corrections to the dead time range.

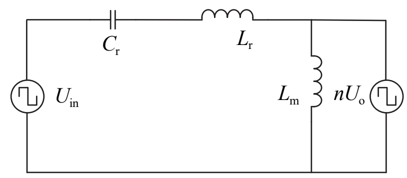

Fig. 3. Equivalent circuit at resonant frequency.

II. Three-Phase LLC Resonant Converter

A. Three-Phase LLC Resonant Converter Working Principle

The three-phase LLC resonant converter circuit topology is shown in Fig. 1, where Q_1~Q_6 are IGBTs, C_1~C_6 are the junction capacitances of the IGBTs, U_{in} is the input voltage, U_o is the output voltage, C_{in} is the input capacitance, C_o is the output capacitance, L_{r1}, L_{r2} and L_{r3} are the resonant inductances, L_{m1}, L_{m2} and L_{m3} are the excitation inductances, C_{r1}, C_{r2} and C_{r3} are the resonant capacitors and n is the transformer turns ratio. The three-phase LLC resonant converter is mainly composed of four parts: inverter bridge, resonant cavity, rectifier bridge and filter capacitor. Among them, in order to solve the problem of uneven power due to uneven current when there is a difference in parameters, the transformer's primary and secondary sides are Y-Y connected three-phase LLC resonant converters. The inverter bridge consists of six power switching tubes, the resonant cavity includes resonant inductor L_r, resonant capacitor C_r, and excitation inductance L_m, and the rectifier bridge consists of six diodes.

The three-phase LLC converter drive signals are shown in Fig. 2, and the three-phase PWM operates with a 120° phase difference between them [18].

B. Calculation of Resonant Current of Three-Phase LLC Resonant Converter

In the ideal case, the resonance parameters between the three phases of the three-phase bidirectional LLC resonant converter are exactly the same, so it can be analyzed as a single phase [19]. The first resonant frequency f_r and the second resonant frequency f_m are shown in (1) and (2). The operating modes of the three-phase LLC resonant converter can be categorized into four operating modes: $f_m < f_s < f_r$, $f_s = f_r$, $f_s > f_r$, and $f_s < f_m$.

$$f_r = \frac{1}{2\pi\sqrt{L_r C_r}} \tag{1}$$

$$f_m = \frac{1}{2\pi\sqrt{(L_m + L_r)C_r}} \tag{2}$$

Fig.3 shows the equivalent circuit of a three-phase LLC operating at the resonant frequency. As for the three-phase LLC converter, operating at the first resonant frequency can realize the ZVS of the primary switching tube and the ZCS of the secondary diode, which can obtain the highest efficiency,

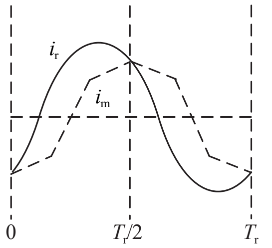

Fig. 4. The resonant current and magnetizing current.

and also can obtain the DC gain that does not change with the load. Moreover, when the switching frequency f_s is close to the resonant frequency f_r, the current in the resonant slot circuit is approximated as a sinusoidal waveform, so the fundamental waveform approximation can be used to simplify the converter into a linear circuit analysis, which can greatly reduce the difficulty of circuit analysis.

Fig. 4 shows the key current waveform of a three-phase LLC operating at the resonant frequency, where i_r is the resonant current and i_m is the excitation current. From Fig. 4, it can be seen that the resonant current at the resonant frequency has a sinusoidal waveform with the expression,

$$i_r = \sqrt{2} I_{rms\_p} \sin(\omega_r t + \theta) \tag{3}$$

where I_{rms_p} is the RMS value of the primary current, θ is the phase difference between the resonant current and the excitation inductor current, and ω_r is the angular frequency of the resonant frequency. From Fig. 4, it can be seen that the excitation current and resonant current are equal at one-half resonant cycle. At this time i_{m_pk} is the peak value of the excitation current and the magnitude is,

$$i_{m\_pk} = \frac{nU_o T_r}{9L_m} \tag{4}$$

where T_r is the resonance period resonance, the average value of the difference between the current and the excitation current is the average value of the output current converted to the primary side. So the following two equations are established,

$$i_r\left(\frac{T_r}{2}\right) = i_{m\_pk} \tag{5}$$

$$\frac{\int_0^{\frac{T_r}{2}} \left[i_r(t) - i_m(t)\right] \mathrm{d}t}{\frac{T_r}{2}} = \frac{nU_o}{3R_L} \tag{6}$$

where R_L is the output load, the expression for the RMS value of the primary current can be introduced from (5) and (6) as,

$$I_{prms} = \frac{U_o \sqrt{18\pi^2 L_m^2 + 2R_L^2 T_s^2 n^4}}{18 L_m R_L n} \tag{7}$$

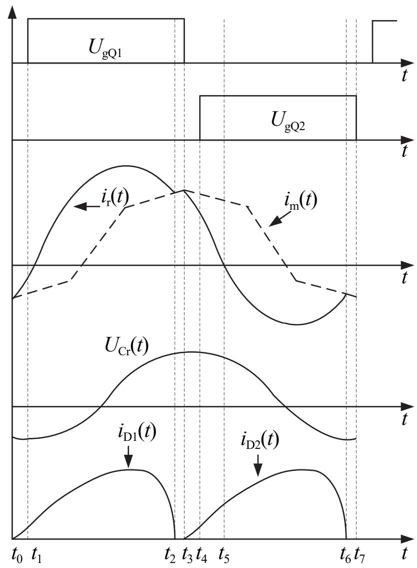

Fig. 5. The key waveform in the under-resonant state.

where T_s is the switching period, the secondary current is equivalent to the difference between the primary resonant current and the excitation current folded to the secondary current, then can get the RMS value of the secondary current as,

$$I_{srms} = \frac{\pi U_o}{3\sqrt{2} R_L} \tag{8}$$

III. Deadband Characterization of Three-Phase LLC Resonant Converter

A. Analysis of Soft-Switching Realization Conditions for LLC Resonant Converter

Generally when designing the LLC resonant converter the closer the switching frequency is to the resonant frequency, the higher the efficiency of the converter, so the switching frequency is usually chosen to be slightly less than the resonant frequency, to be able to realize the ZVS of the primary-side switching tube and the ZCS of the secondary-side diode, whose typical operating waveforms are shown in Fig. 5.

High-power three-phase LLC resonant converters generally use IGBT as a switching tube, and LLC converter IGBT to achieve soft switching prerequisite is that before the arrival of the drive signal, the voltage at both ends of the IGBT junction capacitance has dropped to 0. Let t_d be the dead time; ω_r be the angular frequency for the resonance frequency; t_0 be the time for the resonance current to pass through the zero time, where $t_0 = \theta_0 / \omega_r$; Q_c be the power switching tube junction capacitance charge; Q_s is the resonant current to the junction capacitance charge supply. According to the equivalent model shown in Fig. 4, it can be obtained that,

$$Q_c = C_j U_{in} \tag{9}$$

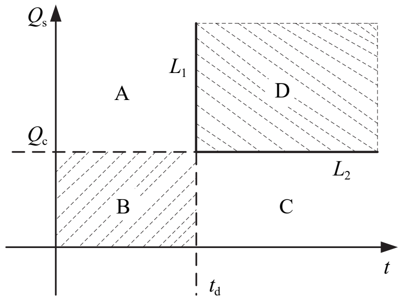

Fig. 6. Distribution figure of operation region.

$$Q_s = \begin{cases} \int_{\frac{T_s}{2}}^{\frac{T_s}{2}+t_d} i_r(t)\mathrm{d}t & \frac{\theta_0}{\omega_r} \geqslant t_d \\ \int_{\frac{T_s}{2}}^{\frac{T_s}{2}+\frac{\theta_0}{\omega_r}} i_r(t)\mathrm{d}t & \frac{\theta_0}{\omega_r} < t_d \end{cases} \tag{10}$$

According to the balanced relationship between the resonant current charge supply and the switching tube junction capacitance charge demand, as well as the magnitude relationship between the current over-zero time and the dead time, the converter can be divided into four operating regions, whose distribution diagrams are shown in Fig. 6. The operating principle of each operating region is analyzed in detail below.

Region A ($t_0 < t_d$, $Q_s > Q_c$). At the moment when the resonant current i_r over 0, the drain-source voltage of switching tube Q_1 has dropped to 0 and the anti-parallel diode conducts. However, since the dead time has not yet ended, the resonant network maintains resonance, resulting in the current reversal during the dead time and D_1 cutoff. Since the drive signal has not yet arrived, the resonant current charges C_1 again, causing the voltage to rise continuously and the soft-switching operating conditions to be destroyed. When the drive signal arrives, the voltage at both ends of D_1 is no longer zero, and this region is the non-soft-switching operating region.

Region B ($t_0 < t_d$, $Q_s < Q_c$). At the moment when the resonant current i_r passes 0, the drain-source voltage of switch Q_1 has current i_r passes 0, and the drain-source voltage of switch Q_1 has not yet dropped to 0. During the $t_0 < t_d$ period, the resonant network operates in the same state as that in region A, where the drain-source voltage is recharged before it drops to 0, and soft-switching operating conditions cannot be created. Therefore this region is also a non-soft-switching operating region.

Region C ($t_0 > t_d$, $Q_s < Q_c$). In this region, although the current back to 0 time is greater than the dead time, the amount of charge that can be provided during the dead time is less than the charge demand. Before the drive signal of Q_1 arrives, the drain-source voltage of Q_1 has not dropped to 0, and the soft-switching operating conditions cannot be created. Therefore this region is a non-soft-switching operating region.

Region D ($t_0 > t_d$, $Q_s > Q_c$). The voltage of Q_1 has dropped to 0 during the dead time, and at the end of the dead time, the anti-parallel diode D_1 of Q_1 maintains conduction, which creates the conditions for the soft-switching operation of Q_1. Therefore, this region is the soft-switching operation region.

According to the above analysis, the soft-switching operating region of the LLC resonant converter is region D and the rest is the non-soft-switching operating region, and the demarcation line between the two is the ray L_1 and the ray L_2 (as shown by the thick solid line in Fig. 6). Thus these two rays constitute the soft-switching boundary curve of the LLC resonant converter, and L_1 and L_2 can be expressed as (11) and (12), respectively.

$$\begin{cases} Q_s \geqslant Q_c \\ \frac{\theta_0}{\omega_r} = t_d \end{cases} \tag{11}$$

$$\begin{cases} Q_s = Q_c \\ \frac{\theta_0}{\omega_r} \geqslant t_d \end{cases} \tag{12}$$

B. Dead Time Design of Three-Phase LLC Resonant Converter

From the boundary analysis of the soft-switching realization in the previous section, it can be seen that in order to realize the ZVS turn-on of the power switching tube, the converter must always work in the above-analyzed region D. If the dead time is too small, the IGBT junction capacitance is not discharged completely, and zero-voltage turn-on can not be realized; if the dead time is too large, the loss will be increased, and it may be out of the soft-switching working condition. After the parameters of the resonant network are determined, the length of the dead time directly determines whether the converter can successfully realize the soft-switching operation within the full design load range. In order to determine the required dead time, the minimum dead time required to realize soft-switching must be considered to ensure that the converter can work in the soft-switching state under the worst condition, which in turn affects the voltage stress of the IGBTs and the efficiency of the converter, and the selection of the dead time is mainly limited by the minimum dead time and the maximum dead time. The first is the determination of the minimum dead time because the parasitic capacitance of the power switching tube must have enough time to be completely discharged during the dead time. As can be seen in Fig. 5 LLC operating waveforms, in i_m through the peak after a very short period of time, it can be assumed that the resonant current value is unchanged, at this time, the power switching tube parasitic capacitance begins to discharge, just when the parasitic dead time when the charge is drained the shortest time. If less than this time, the power switching tube parasitic capacitance has not been completely discharged, can not realize the ZVS open. From the above analysis, to meet the primary power tube ZVS turn on the minimum dead time,

$$t_d \geqslant C_j \frac{\mathrm{d}u}{i_r} \tag{13}$$

where C_j is the parasitic capacitance of the IGBT and du is the

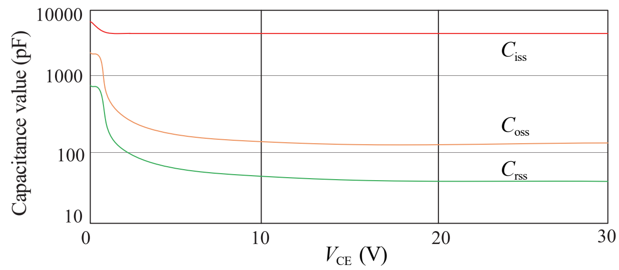

Fig. 7. Relationship between output capacitance and V_{CE}.

differential of the voltage. Minimum dead time to satisfy the turn-on of the primary-side power tube ZVS,

$$t_{\mathrm{dmin}} = C_{\mathrm{j}} \frac{U_{\mathrm{in}}}{i_{\mathrm{m\_pk}}} \tag{14}$$

The maximum dead time must be less than the primary side current reverse over zero time to avoid the output capacitor reverse charging. According to the LLC operating waveform in Fig. 5, it can be seen that at the moment of t_2, the circuit enters the three-element resonant operating state of L_r, C_r, and L_m, and if (15) or (16) is satisfied, the vice-side diode starts to conduct and L_m is clamped. At the moment t_3, the circuit enters the dead time and the parasitic capacitance starts to discharge. At the moment t_5, if the parasitic capacitance is not fully discharged, the power switching tube will lose the ZVS turn-on condition. Therefore, the end of discharging the parasitic capacitance exactly at the moment of t_5 is the critical condition for the ZVS turn-on of the power switching tube, and the maximum dead time is the interval [t_3, t_5].

$$(U_{\mathrm{in}} - U_{\mathrm{Cr}}) \frac{L_{\mathrm{m}}}{L_{\mathrm{m}} + L_{\mathrm{r}}} < -nU_{\mathrm{o}} \tag{15}$$

$$(U_{\mathrm{in}} - U_{\mathrm{Cr}}) \frac{L_{\mathrm{m}}}{L_{\mathrm{m}} + L_{\mathrm{r}}} > nU_{\mathrm{o}} \tag{16}$$

Based on the above analysis, the maximum dead time to satisfy the turn-on of the primary power tube ZVS is obtained.

$$t_{\mathrm{dmin}} = t_{\mathrm{dmin}} + \frac{\tan^{-1}\left(\frac{n^2 U_{\mathrm{o}}^2}{2\pi f_{\mathrm{r}} L_{\mathrm{m}} P_{\mathrm{o}}} \frac{f_{\mathrm{s}}}{f_{\mathrm{r}}}\right)}{2\pi f_{\mathrm{r}}} \tag{17}$$

where P_o is the single-phase output power, and f_r is the series resonant frequency.

IV. Characterization of IGBT Output Capacitance

A. IGBT Output Capacitance

There is a parasitic capacitance between every 2 electrodes of the 3 electrodes of IGBT, which are C_{GE}, C_{GC}, and C_{EC}. The output capacitance C_{oss} of IGBT mainly includes C_{GC} and C_{EC} [20]–[21]. The typical IGBT parasitic capacitance versus voltage is shown in Fig. 7.

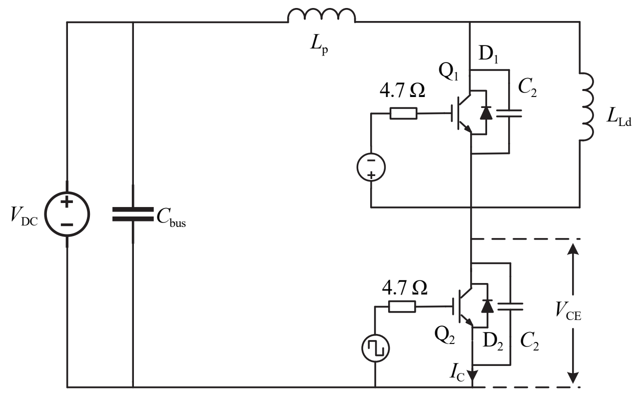

Fig. 8. Double pulse test schematic diagram of the half-bridge IGBT module.

For the three-phase LLC converter whether it can successfully realize the zero-voltage turn-on of IGBT, the output capacitance value of IGBT is very critical data.

According to the previous section on the maximum and minimum dead time limit analysis, if you want to realize the IGBT zero-voltage turn-on, the same bridge arm between the two IGBT drive signal dead time must be greater than its output capacitance charging and discharging time and is less than the primary side of the current reversal over the zero time. In practice, the IGBT output capacitance size is not a constant value, it will receive V_{CE} and operating temperature. Therefore, when V_{CE} is unchanged, the charging time of IGBT output capacitor C_1 (i.e., the time corresponding to the establishment of Q_1 voltage) will vary with the temperature. If the three-phase LLC dead time is calculated based on the typical value in the technical specifications at room temperature, there is a possibility that the charge on the junction capacitor C_1 has not yet been drained by the resonant current and Q_2 has already been turned on in practical applications, thus losing the ZVS turn-on condition. Therefore, the output capacitance of the IGBT should be determined under the worst operating conditions to determine the required dead time.

B. Analysis of the Effect of Temperature Variation on the Operating Characteristics of IGBTs

The study of IGBT operating characteristics is carried out using the double-pulse test method. The test schematic is shown in Fig. 8, in which L_{Ld} is the load inductance, L_p is the line parasitic inductance, and C_{bus} is the bus capacitance. 2 IGBTs form a half-bridge structure.

The upper tube drive applies a negative voltage to ensure that the IGBTs are turned off. In contrast, the lower tube applies a normal drive signal to observe the voltage buildup and current decay characteristics of the lower tube when it is turned off [22]–[23]. Table I shows the parameters of the IGBT test setup.

According to the subsequent prototype parameters bus voltage V_{DC} = 800 V, the on-state current of the IGBT is set at 20 A,

TABLE I
PARAMETERS OF THE IGBT TEST DEVICE

Component	Parameter
Bus capacitance C_{bus} (μF)	2340
Load inductance L_{Ld} (μH)	150
Parasitic inductance L_p (nH)	140

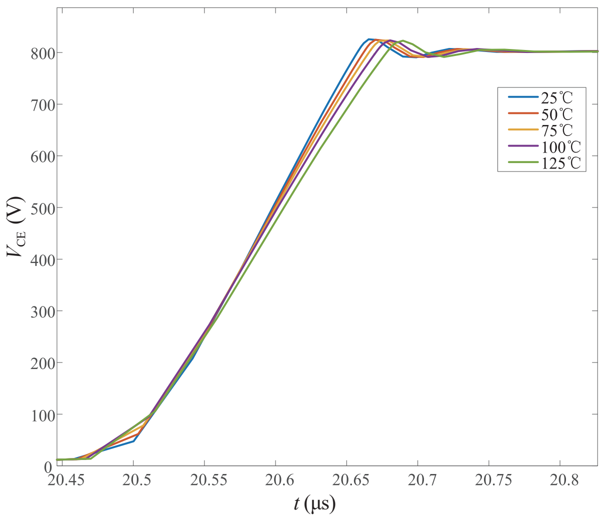

Fig. 9. Turn off voltage waveforms of IGBT at different junction temperatures.

and the temperature of the thermostat box starts from 25 °C, and 1 double-pulse test is carried out for every 25 °C of temperature rise to obtain the waveforms of the voltage at both ends of the IGBTs between the C-pole and the E-pole at different temperatures as shown in Fig. 9.

From Fig. 9, it can be seen that with the same bus voltage and collector current, the dv/dt decreases and the voltage build-up time grows as the junction temperature increases. Finally, the junction capacitance of the IGBT corresponding to the highest junction temperature is used as a reference for the setting of the dead time, and the worst-case junction capacitance size is determined to be 4.5 nF.

V. EXPERIMENTAL VERIFICATION

To verify the accuracy of the proposed theory, a 100 kW three-phase bidirectional LLC resonant converter prototype is designed in this paper with the parameters shown in Table II, and the physical diagram of the prototype is shown in Fig. 10.

During the operation of the LLC circuit, the IGBT output capacitance must be selected according to the maximum value to ensure that the IGBT achieves zero-voltage turn-on in the full temperature range so that the IGBT output capacitor voltage can be discharged to 0 V. The IGBT output capacitance is also selected according to the maximum value. In the worst operating conditions (i.e., the highest operating temperature), the IGBT output capacitance of 4.5 nF, so that the calculation of the dead time selection range of 0.482 μs < t_d < 1.252 μs, in practice, t_{dmin} will be with the temperature and load current

TABLE II
PARAMETERS OF THE PROTOTYPE

Component	Parameter
Power rating P_o (kW)	100
Input voltage U_{in} (V)	800
Output voltage U_o (V)	600
Resonant inductance L_r (μH)	8.5
Excitation inductance L_m (μH)	715.5
Resonant capacitance C_r (μF)	9.4
Switching frequency f_s (kHz)	17
Ratio n	1.333

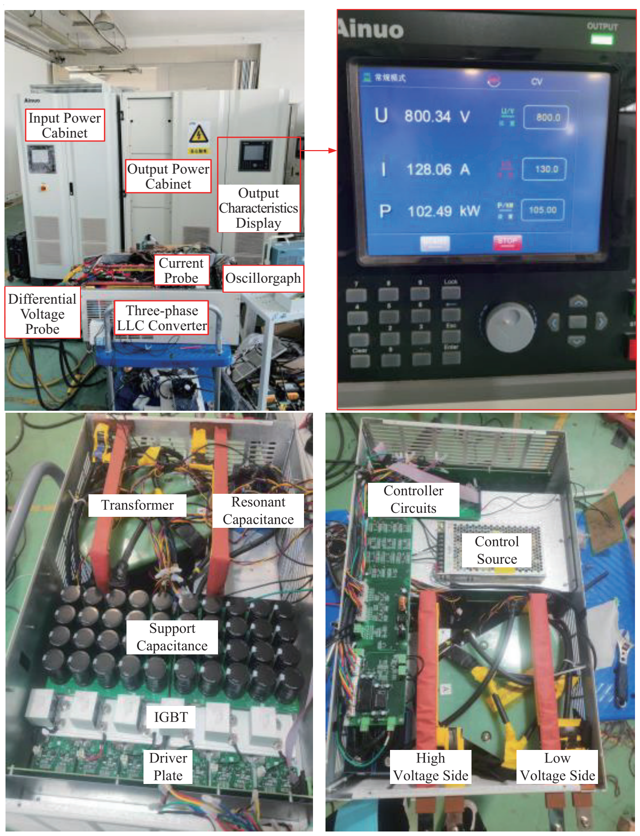

Fig. 10. Efficiency test and experiment platform.

changes, but also to take into account the deviation of the excitation inductance manufacturing and measurement error, so the actual charging and discharging time than the theoretical calculation of the value of the larger, the actual take the dead time. Considering a certain margin, the actual dead time is t_d = 1.1 μs.

The primary-side PWM drive waveform of the three-phase LLC converter prototype is shown in Fig. 11. From the figure, it can be seen that phase A exceeds phase B by one-third of the cycle, and phase B exceeds phase C by one-third of the cycle. Three-phase drive phase difference of 120°, and in each phase of the power switching tube drive there is a certain dead time to meet the drive requirements.

The optimized design dead time t_d=1.1 μs, based on [12]

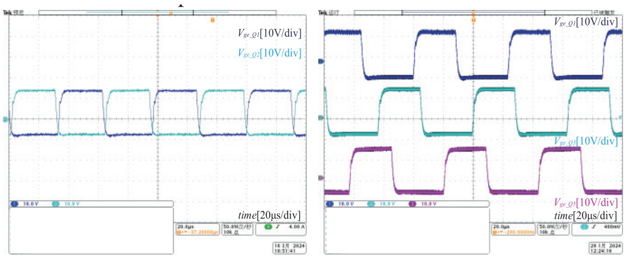

Fig. 11. Three-phase LLC drive waveform. (a) A-phase bridge arm up and down tube driving waveforms. (b) Three-phase driving waveform.

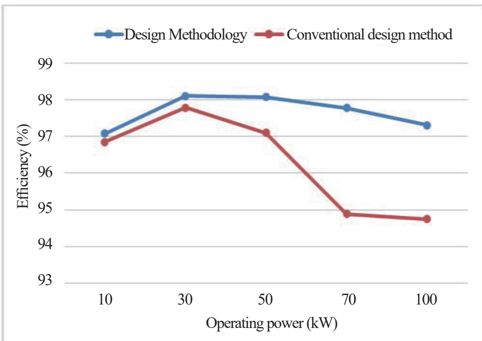

Fig. 12. Efficiency curve comparison chart.

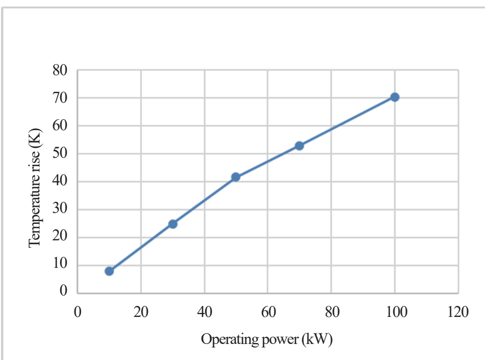

Fig. 13. Working temperature change of prototype.

under the traditional design of the dead time $t_d = 0.8$ μs. Determine the efficiency of the two groups under different power at the rated voltage and the temperature rise of the prototype at an ambient temperature of 25 °C, plot the efficiency comparison curve of the two groups as shown in Fig. 12, and the approximate temperature rise curve of the prototype operation as shown in Fig. 13. The experimental temperature rise diagram of the three-phase LLC resonant converter prototype is shown in Fig. 14. The three-phase LLC prototype startup voltage and current waveforms are shown in Fig. 15, where the dark blue waveform is the input voltage, the light blue waveform is the output voltage, the red waveform is the C-phase resonant current waveform, and the green waveform is the output current waveform.

Analysis of the plotted curve can be seen, in the prototype load is small prototype work stability when the temperature

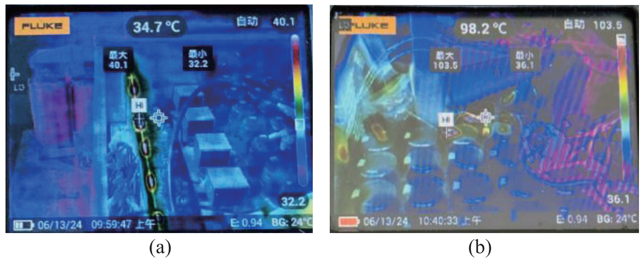

Fig. 14. Photograph of temperature rise of three-phase LLC converter prototype. (a) Starting temperature. (b) Final temperature.

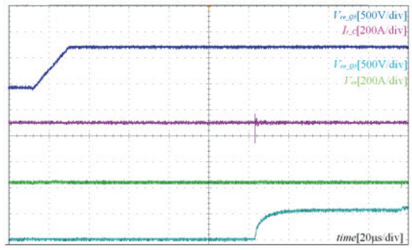

Fig. 15. Three-phase LLC prototype startup voltage and current waveforms.

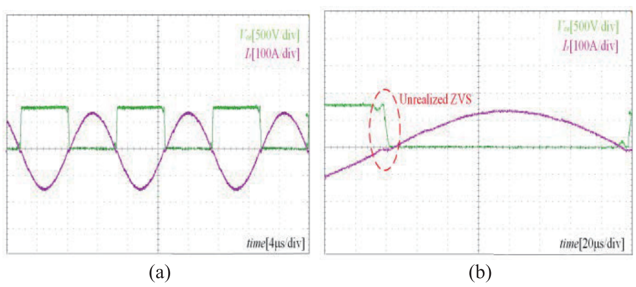

Fig. 16. The prototype loses the soft switching waveform in the traditional design. (a) Power-switching tube soft-switching waveform. (b) Soft-switching detail waveform.

rise is also small, this time the dead time design method proposed in this paper and the traditional dead time design method to get the prototype efficiency is not much difference. In the prototype load aggravation when the IGBT operating temperature becomes high, the IGBT operating characteristics have changed, resulting in the dead time setting being unreasonable, the IGBT lost the soft switching characteristics, as shown in Fig. 16 using the traditional dead time design method of the soft switching characteristics of the waveform, resulting in a great decline in the efficiency of the prototype, the traditional design method compared to this paper's design method, the efficiency of the prototype decreased by 2.5%.

The dead time half-load and full-load operation circuit under the design method in this paper reaches a steady state when the C-phase power switch turn-on voltage and turn-on current signals are shown in Fig. 17, from Fig. 17, it can be seen that in the full load range of the power switch voltage is reduced to 0 before the current begins to increase, the power switch to achieve the ZVS turn-on. Therefore, it can be seen that the dead time optimization method proposed in this paper can still

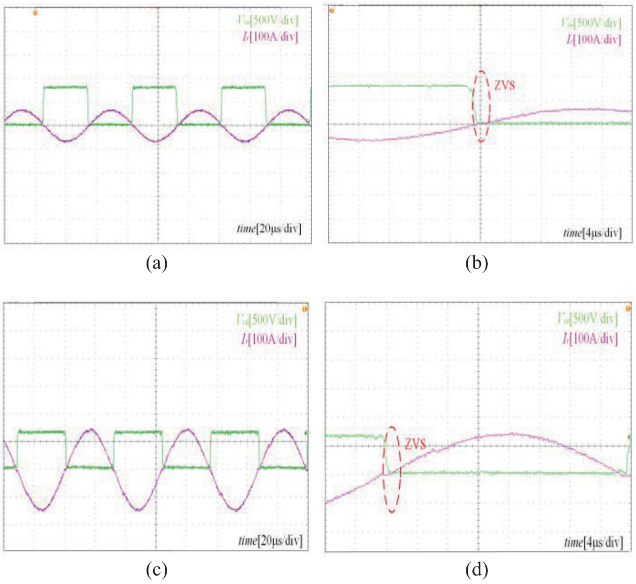

Fig. 17. Realized waveforms of the prototype ZVS under the design methodology of this paper. (a) Full load waveform. (b) Detailed view of full load ZVS waveform. (c) Half load waveform. (d) Detailed view of half-load ZVS waveform.

achieve soft switching and improve the converter's efficiency when the IGBT's operating temperature is high after the workload is aggravated.

In summary, the nonlinear effects of operating temperature and current on the IGBT output capacitance need to be considered in the actual product design. The dead time design needs to be theoretically calculated under the highest junction temperature of the IGBT and the maximum load condition and finally adjusted finely through the test, to ensure that the IGBT can realize soft switching in the full temperature range and the full load range.

VI. Conclusion

In this paper, the operating principle of the three-phase LLC circuit is analyzed, the equivalent model of the converter operating at the resonance point is established and the original and secondary resonant currents are calculated. On this basis, the soft-switching realization range of the switching tubes of the LLC converter is analyzed. The converter is divided into four operating regions in the full input voltage and full load range, of which three are non-soft-switching operating regions, which need to be avoided in the design process. Then this paper analyzes the relationship between the dead time and soft-switching realization of the LLC converter and deduces the mathematical expressions for the maximum and minimum dead times. Then, based on the problem that the ambient temperature in engineering practice will make the IGBT output capacitance undergo a nonlinear transformation, the operating characteristics of IGBT are analyzed, the worst operating condition of the output capacitance is determined, and the dead time setting formula is corrected to make it more in line with engineering practice. Finally, a three-phase LLC converter prototype is constructed to verify the accuracy of the dead time setting method in this paper. This will help promote the three-phase LLC resonant soft-switching technology to realize a wide range of applications in high-power converters.

References

[1] X. Xia, C. Gong, J. Bao, G. Zhu, and Z. Wang, "LLC resonant converter topology with wide gain and high efficiency," in *Power System Protection and Control*, vol. 51, no. 3, pp. 99–107, Feb. 2023.

[2] X. Zhu, K. Liu, K. Ye, L. Jiang, and K. Jin, "Isolated bidirectional hybrid LLC converter based on SiC MOSFET," in *Transactions of China Electrotechnical Society*, vol. 37, no. 16, pp. 4143–4154, Aug. 2022.

[3] Y. Shen, W. Zhao, Z. Chen, and C. Cai, "Full-bridge LLC resonant converter with series-parallel connected transformers for electric vehicle on-board charger," in *IEEE Access*, vol. 6, pp. 13490–13500, 2018.

[4] H. Zhang, M. Han, X. Zhang, and H. Liu, "Interleaved parallel current sharing control for multi-channel LLC resonant converter," in *Electric Power Automation Equipment*, vol. 43, no. 4, pp. 62–68, Apr. 2023.

[5] Z. Chen, K. Chen, X. Xiong, and R. He, "Variable frequency interleaved parallel LLC resonant converter based on variable inductor," in *Electric Machines and Control*, vol. 24, no.12, pp. 97–105, Jun. 2020.

[6] Y. Yang, H. Wu, and T. Guan, "Magnetic integrated current sharing characteristics of interleaved LLC resonant converter," in *Transactions of China Electrotechnical Society*, vol. 34, no. 12, pp. 2529–2538, Jun. 2019.

[7] X. Feng, S. Wang, G. Zhou, and W. Ma, "Current sharing control strategy of three-phase interleaved paralleled LLC resonant converter based on phase-shifting control," in *Electric Power Automation Equipment*, vol. 41, no. 12, pp. 166–171, Dec. 2021.

[8] X. Feng, K. Shao, X. Cui, W. Ma, and Y. Wang, "Control strategy of wide voltage gain LLC resonant converter based on multi-mode switching," in *Transactions of China Electrotechnical Society*, vol. 35, no. 20, pp. 4350–4360, Oct. 2020.

[9] Y. Nakakohara, H. Otake, T. M. Evans, T. Yoshida, M. Tsuruya, and K. Nakahara, "Three-phase LLC series resonant DC/DC converter using SiC MOSFETs to realize high-voltage and high-frequency operation," in *IEEE Transactions on Industrial Electronics*, vol. 63, no. 4, pp. 2103–2110, Apr. 2016.

[10] R. Beiranvand, B. Rashidian, M. R. Zolghadri, and S. M. H. Alavi, "Designing an adjustable wide range regulated current source," in *IEEE Transactions on Power Electronics*, vol. 25, no. 1, pp. 197–208, Jan. 2010.

[11] Y. Yuan and D. Xiang, "Study on effects of different factors on IGBT thermal sensitive electrical parameter dV/dt," in *Journal of Power Supply*, vol. 14, no. 6, pp. 35–39, 66, Dec. 2016.

[12] R. Ren, F. Zhang, and S. Liu, "Optimal design for efficiency based on the dead time and magnetizing inductance of LLC DC transformer," in *Transactions of China Electrotechnical Society*, vol. 29, no. 10, pp. 141–146, May 2014.

[13] Z. Lv, X. Yan, L. Sun, and W. Fan, "Selection and calculation of LLC converter dead-time considering turn-off transient of MOSFET," in *Electric Power Automation Equipment*, vol. 37, no. 3, pp. 175–183, Mar. 2017.

[14] P. Ban, Y. Xie, and Z. Wang, "Design of magnetic integrated LLC converter considering dead time," in *Journal of Magnetic Materials and Devices*, vol. 54, no. 1, pp. 30–35, Jan. 2023.

[15] C. Sun, Q. Sun, R. Wang, Y. Li, and D. Ma, "Adaptive dead-time modulation scheme for bidirectional LLC resonant converter in energy router," in *CSEE Journal of Power and Energy Systems*, vol. 10, no. 4, pp. 1710–1721, Jul. 2024.

[16] J. Tang, P. Rao, W. Xie, and S. Chen, "Robustness design of LLC resonant converter," in *Control and Information Technology*, no. 2, pp. 64–71, 86, 2019.

[17] Y. Sun, Z. Deng, G. Xu, G. Deng, Q. Ouyang, and M. Su, "ZVS analysis and design for half bridge bidirectional LLC-DCX converter with consideration of nonlinear capacitance and different load under synchronous turn-on and turn-off modulation," in *IEEE Transactions on*

Transportation Electrification, vol. 8, no. 2, pp. 2429–2443, Jun. 2022.

[18] M. Noah, S. Kimura, J. Imaoka, W. Martinez, S. Endo, M. Yamamoto, and K. Umetani, "Magnetic design and experimental evaluation of a commercially available single integrated transformer in three-phase LLC resonant converter," in *IEEE Transactions on Industry Applications*, vol. 54, no. 6, pp. 6190–6204, Nov.-Dec. 2018.

[19] H. Cao, Y. Liu, and Y. Wang, "Research on three phase LLC resonant converter, in *Low Voltage Apparatus*, no. 8, pp. 53–59, 2019.

[20] H. Huang, H. Tong, N. Wang, and T. Lu, "Analysis of the influence of IGBT segmented transient model with parasitic oscillation on electromagnetic interference prediction," in *Transactions of China Electrotechnical Society*, vol. 36, no. 12, pp. 2434–2445, Jun. 2021.

[21] B. Wang, W. Zhang, Z. Chen, and Z. Wang, "Wide-band equivalent circuit model of IGBT based on PSPICE," in *Chinese Journal of Power Sources*, no. 12, pp. 2320–2323, 2014.

[22] P. Sun, H. Luo, Y. Dong, W. Li, and X. He, "Junction temperature extraction of high power IGBT module based on turn-off delay time," in *Proceedings of the CSEE*, vol. 35, no. 13, pp. 3366–3372, Jul. 2015.

[23] S. Liu, Y. Chang, W. Li, H. Yang, and R. Zhao, "Dynamic switching characteristics test platform design and parasitic parameter extraction of press-pack IGBT modules," in *Transactions of China Electrotechnical Society*, vol. 32, no. 22, pp. 50–57, Nov. 2017.

Xianjin Huang was born in Hubei, China in 1980. He received the B.S. degree in electrical engineering, the M.S. degree in power electronics and electric drive, and the Ph.D. degree in traffic engineering from Beijing Jiaotong University, Beijing, China, in 2002, 2005, and 2014, respectively. He is currently an Associate Professor with the School of Electrical Engineering, Beijing Jiaotong University. His research interests include traction converter and power semiconductor application for railway systems.

Hongchao Bai was born in June 1983. He received the M.S. degree in Power Electronics and Power Drives from Beihang University in 2007. He is a Senior Engineer and is engaged in the research on converter topologies and their control characteristics as well as the research on the topological characteristics of bidirectional power supplies.

Zhidong Xue was born in Shijiazhuang, China, in 2000. He received the B.Eng. degree in electrical engineering from Beijing Jiaotong University, China, in 2022. His research direction is efficiency optimization design and control method design of bidirectional DC/DC converter.

Yinghui Zhao was born in December 1981. He received the M.S. degree in Communication and Information Systems from Southwest Jiaotong University in 2006. He is a Senior Engineer and a Member of the Chinese Society for Electrical Engineering. His main research focuses on DC-DC topologies and their control as well as bidirectional power systems.

Wenwen Shi was born in November 1992. He received the M.S. degree in Power Electronics and Power Drives from Harbin University of Science and Technology in 2019. He is an Engineer and a Member of the Chinese Society for Electrical Engineering. His main research focuses on AC power supply topologies and their control, linear power amplifiers and precision measurement systems.

Zhao Linfeng was born in Liaoning, China, in 2000. He received the B.Eng. degree in electrical engineering from Hefei University of Technology, China, in 2023. His research directions are the efficiency optimization research of bidirectional converters and the research on radio frequency power supplies.

Mutual Inductance Calculation of Rectangular Coils With Convex Torus Finite Magnetic Shields in Wireless Power Transfer

Zhongqi LI, Qian ZHANG, Lingjun KONG, Changxuan HU, and Shoudao HUANG

***Abstract*—Mutual inductance is one of the critical parameters of wireless power transfer systems, and the accurate calculation of mutual inductance is considered an essential theoretical basis for designing and optimizing wireless power transfer systems. However, the problem of calculating the mutual inductance of a bilateral bounded magnetically shielded rectangular coil with a convex toroid still needs to be solved. Therefore, this article proposes a spatial boundary separation analysis method and derives vector magnetic potential expressions for each region with convex toroidal magnetic shielding structure using the double Fourier transform and Maxwell's equations. The mutual inductance calculation formula under the spatial position are obtained using boundary conditions and spatial geometric relaionships. In contrast to traditional approximation methods, the mutual inductance calculation method of this article permits an accurate numerical solution for the mutual inductance between rectangular coils. The 4.69% difference between calculated and experimental mutual inductance values confirms the accuracy of the computational method in this research. The proposed model of this article matches the transmission efficiency of the conventional rectangular disc coil at over 97% for the same specifications and reduces material usage by 11.12%.**

***Index Terms*—Magnetic shielding, radio energy transmission, reciprocal inductance calculation, rectangular coils.**

I. Introduction

WIRELESS power transfer (WPT) technology is a non-contact power transmission technology [1]−[2] that is gradually surpassing traditional power transmission methods in terms of safety, reliability. Hence, WPT technology holds considerable promise for evolutionary progress in the domain of engineering applications and has been successfully applied to electric vehicles [3]−[4], portable electronics [5]−[6], biomedical science [7]−[8], and power supply for underwater environments [9]−[10], etc., and is now becoming an increasing research focus in the field of electrical engineering. In designing and optimizing the structure of a WPT system, the mutual inductance (MI) is a core variable affected by the transmission performance, and the efficient and accurate calculation of the MI is a crucial component of this process. The structural design of the WPT system shows corresponding differentiation due to the diversity of application scenarios, with different system structures producing different MI coefficients, which in turn have varying degrees of influence on the system transmission efficiency. Therefore, it is of great importance to research methods for accurately calculating the coupling coefficients of MI models.

The coil acts as a crucial element in WPT systems. With the wide application of WPT technology, various types of coils have emerged, including rectangular, circular, polygonal, cross-shaped, and so on. The current coil designs commonly include two primary forms, rectangular and circular. However, from a practical point of view, rectangular coil structures are more necessary and practical in specific application scenarios for WPT systems. This is because lower MI variations are exhibited by rectangular coils compared to circular coils when the coils are shifted relative to each other, which provides more excellent resistance to shifting and results in more stable transmission efficiency. Among them, MI calculation methods in circular coil structures have been the subject of many studies. In contrast, MI calculation methods for rectangular coil structures have been studied less frequently. The work on rectangular coil structures is based on Maxwell's equations, Biot-Savart law [11]−[12], Bessel's function [13]−[14], and Fourier series [15].

In a related study for MI modeling without the addition of magnetic shielding materials, [16] proposes a novel analytical calculation method. This method treats a multi-turn coil as multiple single-turn coils and MI calculation when the coils are vertically offset. Yet, it is not possible to realize MI calculation methodology when the coils in this mod-

Manuscript received December 24, 2024; revised February 28, 2025; accepted March 17, 2025. Date of publication June 30, 2025; date of current version April 18, 2025. This work was supported in part by Natural Science Foundation of Hunan Province under the grant 2022JJ30226, National Key R&D Program Project under the grant 2022YFB3403200, Key Projects of Hunan Provincial Department of Education under the grant 23A0432, Excellent Youth Project of Scientiffc Research of Hunan Provincial Department of Education under the grant 22B0577, National Natural Science Foundation of China (NSFC) Youth Science Fund Project under the grant 62303178, and Scientific Research Fund of Hunan Provincial Education Department under the grant 23C0182. *(Corresponding author: Zhongqi Li.)*

Z. Li, Q. Zhang, L. Kong, and C. Hu are with the College of Traffic Engineering, Hunan University of Technology, Zhuzhou 412007, China (email: my3eee@126.com; 3489734@qq.com; 2119551072@qq.com; 905436194@qq.com).

S. Huang is with the College of Electrical and Information Engineering, Hunan University, Changsha 410082, China (e-mail: hsd1962@hnu.edu.cn).

Digital Object Identifier 10.24295/CPSSTPEA.2025.00015

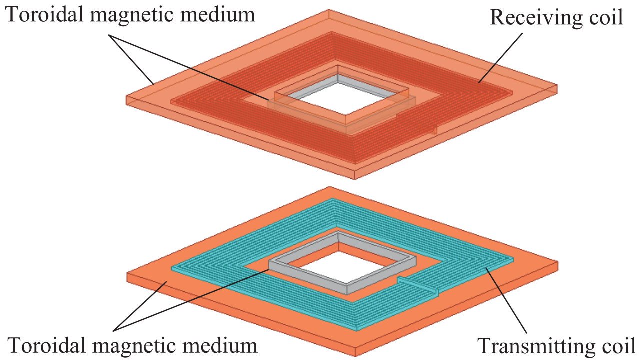

Fig. 1 Three-dimensional view of a rectangular coil of bounded magnetic medium with a convex toroidal type.

el are horizontally misaligned. [17] proposes to construct an MI model using the vertex method to achieve coupling coefficient calculation of rectangular coils of arbitrary dimensions when horizontally offset. Although the MI at the horizontal offset of the coil is calculated by the vertex approach, the MI has not been studied when coils are angularly deflected. In [18], by multiplying the helix factor k, it was realized to determine the MI of a rectangular helical coil at vertical and horizontal offsets as well as at angular deflections. An abstract approach is adopted in [19] by considering wires as ideal line segments of infinitesimal cross-section and calculating the MI between two any positioned quadrilateral coils by accumulating the MI of two straight wires at any position.

In the practical application of WPT systems, magnetic shielding materials are usually integrated the MI model. The addition of magnetic shielding can effec-tively diminish the risk of magnetic radiation, and it changes the magnetic flux path and enhances the inter-coil coupling effect. An analytical model based on Bessel-Fourier transform and dyadic Fourier transform is proposed in [20] to calculate MI for horizontal offsets between the coils with ferrite added on the transmitting coil side, while disregarding the width-thickness ratio. In [21], the MI at any position between rectangular coils with magnetic media on the side of the transmitting coil only and a bounded thickness of the magnetic media is calculated using Fourier integration and spatial transformation methods. However, the length of the magnetic medium is not considered, while in practical applications, the size of the magnetic medium is limited. [22] presents the solution for the calculation of MI between rectangular coils with a boundaried magnetic shielding on the side of the transmitting coils at arbitrary positions, which is based on hyperbolic functions and Fourier series expansions, in contrast to [21] where the boundaries of the magnetic medium are considered. [23] uses the separated variable method in order to calculate the MI of a rectangular coil with both side magnetic shielding. While the dimensions of the magnetic shielding are considered, it is not possible to realize the calculation of MI of a structure with boundaried magnetic shielding and rectangular coils. The MI model has been proposed in [24] by means of a subdomain division based method in order to calculate the MI at an arbitrary location

Step Ⅰ :	The mutual inductance model is partitioned into zones in the x-z plane.
Step Ⅱ :	Solve for the vector magnetic potential in individual region.
Step Ⅲ :	Derivation of unknown coefficients from boundary conditions.
Step Ⅳ :	Combined with the correction factor, the 3-D magnetic flux is obtained.
Step Ⅴ :	For the y-z plane, perform steps I-IV again.
Step Ⅵ :	Calculate mutual inductance using (43).

Fig. 2 MI calculation flowchart.

between rectangular coils with boundaried magnetic shielding. Although the model provides an accurate solution for systems with bilateral bounded magnetic shielding materials, the conservation of magnetic shielding materials has not yet been fully considered. Therefore, the skeletonization of the magnetic shielding material can be considered, but it is inevitable that skeletonization will diminish the performance of the magnetic shielding material. [25] verified the shielding performance of ring-type magnetic shielding material, and it was found that the shielding performance of ring-type magnetic shielding material is similar to that of rectangular disk magnetic shielding material under the same specifications.

In brief, the challenge of calculating the MI of bilateral bounded magnetically shielded rectangular coils with a convex toroidal shape is still unsolved. In view of the above, a computation model for the MI of the bilateral bounded magnetically shielded rectangular coil with a convex toroid has been established in this article, as depicted in Fig. 1.

The computation of MI a rectangular coil with convex toroidal bilateral bounded magnetic shielding is realized using the spatial boundary separation analysis method in this article. In the end, the feasibility and accuracy of putting forward computational methodology are validated through simulation and experiment. Under the exact specifications, the MI can reach over 97% of that of the rectangular disk magnetic shielding transmission structure while saving up to 11.12% of the magnetic shielding material.

II. Analytical Two-Dimensional Model for a Rectangular Coil With Convex Toroidal Magnetic Shielding

The MI calculation process is divided into six steps, as illustrated in Fig. 2. Initially, the MI model is segmented into multiple sectors along the horizontal and vertical directions. Second-

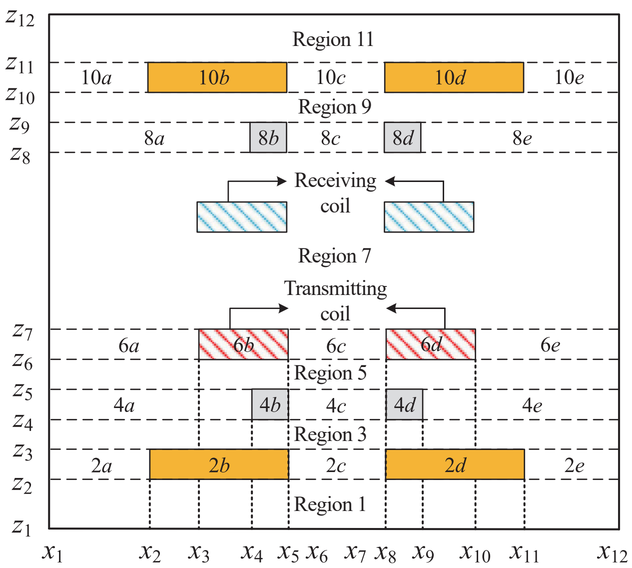

Fig. 3 Cross-sectional view of the *x*-*z* plane for a rectangular coil with a convex torus magnetic shielding.

ly, the vector magnetic potential flux equations of each region are obtained through Poisson and Laplace equations. Then, the unknown coefficients in the vector magnetic potential flux equations are determined by applying boundary conditions, and the correction factors are utilized to correct B-field of the two-dimensional model. The same steps are applied to the *y*-*z* section. Ultimately, magnetic flux density in the 3D model is achieved through superposition calculation, and subsequently, the MI is determined using formula. The detailed steps for the MI calculation are illustrated in Fig. 2.

A. 2D Model Analysis

In order to attain a magnetic shielding performance comparable to that of the rectangular disk magnetic shielding material and to optimize the transmission structure model, adding another layer of magnetic shielding material above the magnetic shielding region of the MI model, thereby constructing a rectangular planar coil structure with a convex-type ring-type magnetic shielding, as depicted in Fig. 3. The system is initially segmented into different sectors according to material properties. Subsequently, the vector magnetic potential were derived for the individual regions. In the end, this includes the solution of unknown coefficients, the coupling of equations, and the transformation of a matrix.

Fig. 1 shows a three-dimensional illustration of the system under consideration. The rectangular coils in the figure are referred to as transmitting and receiving coils or primary and secondary coils, respectively. A zigzag ring-type magnetic shielding material surrounds the dielectric above and below. In the WPT system, the transmitting coil is located above the magnetically shielded region on the transmitting side and the receiving coil is located below the magnetically shielded region on the receiving side. This system uses two rectangular coils with the same geometry and magnetic shielding material. The proposed model is applicable for coils and magnetic shielding of different sizes.

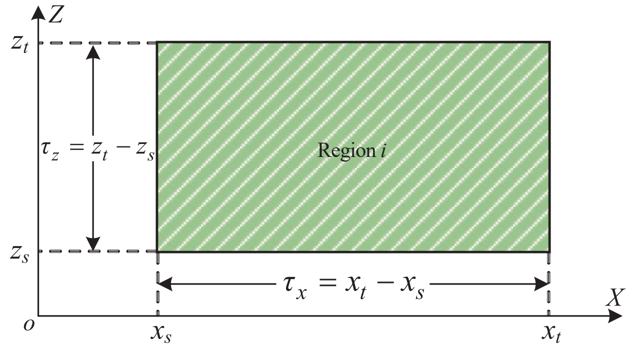

Fig. 4 Cartesian coordinate representation of region *i*.

A detailed *x*-*z* plane cross-section of the system, used to formulate the 2D subdomain model, is illustrated in Fig. 3. The entire system is divided horizontally and vertically into zones based on the nature of the different media and the structure of the system. Region 1 is designated as the air medium below the magnetic shielding material, and region 11 is designated as the air medium above the magnetic shielding material. Regions 2 and 4 and regions 8 and 10 are represented by a cabochon-type magnetic shielding material, typically linear, isotropic, and homogeneous. Regions 2*a*, 4*a*, 8*a*, and 10*a* are located on the left side of the magnetically shielded area and regions 2*e*, 6*e*, 8*e*, and 10*e* are located on the right side of the magnetically shielded area. To save on consumables, the system is hollowed out for the magnetic media, with regions 2*c*, 4*c*, 8*c*, and 10*c* representing the air areas resulting from the hollowing out of the magnetic media. Region 5 denotes an air region, located immediately below the transmitting coil region. Region 7 represents an air region, located immediately above the transmitting coil region. Because the transmitting coil does not carry current, it is not divided into subregions in region 7. Regions 3 and 9 are represented by acceptable air gaps in the middle of the convex ring-type magnetic media. Regions 6*a* and 6*e* denote air regions, immediately adjacent to the transmitting coil in region 6. Regions 6*b* and 6*d* denote current source regions, located above the magnetic shielding region on the transmit side. The region 6*b* is oriented in the same direction as the third direction *y*, and the region 6*d* is oriented in the opposite direction to the third direction *y*. Region 6*c* represents the air region and is located in the middle of the transmitting coil regions 6*b* and 6*d*.

Region *i*, as defined in Fig. 4, can correspond to any region ranging from region 1 to region 11. The boundaries and scope of the area are defined in the diagram.

The initial and terminal coordinates of region *i* are denoted by x_s and x_t in the *x*-direction, and by z_s and z_t in the *z*-direction, respectively. The specific value of x_s, x_t, z_s, and z_t in the *r*-region can be derived in Fig. 3. For instance, if *i*=6*b*, this indicates that the values of x_s, x_t, z_s, and z_t in region 6*b* are x_3, x_5, z_6, and z_7.

The magnetic flux density of the target region can be solved for only if the magnetic vector potential of the target region is calculated, and the vector magnetic potential of each region is derived from (1) and (2). The exact derivation process is presented in the next section.

B. Vector Magnetic Potential Derivation

The stimulation current I_p passes along the transmitting coil, which, under the action of I_p, produces a varying magnetic field. The reason is that the receiving coil exists within the impact of the magnetic field of the transmitting coil. So it achieves electromagnetic coupling and produces a current under the influence of the varying H-field.

To facilitate the computation of the H-field, the magnetic vector potential of the Lorentz norm is introduced. Magnetic vector potential (MVP) is a vector field in classical electromagnetism used to describe magnetic flux density. Magnetic flux density (MFD) is a underlying attribute of H-field, used to depict the distribution of H-field in spatial extent.

In the presence of a current density region, the MVP is controlled by the Poisson equation, as indicated by (1).

$$\frac{\partial^2 A_r}{\partial x^2}+\frac{\partial^2 A_r}{\partial z^2}=0 \tag{1}$$

where J denotes the current density. In other regions with no current density, the MVP is controlled by the Laplace equation, as given by (2).

$$\frac{\partial^2 A_r}{\partial x^2}+\frac{\partial^2 A_r}{\partial z^2}=-\mu_0 J \tag{2}$$

The MVP is determined by deriving (1) and (2) through the method of separation of variables. Then MFD is further calculated.

$$B_r=\nabla\times A_r \tag{3}$$

where A_r represents MVP in the r region. Calculating MFD allows further calculation of H-field.

$$H_r=B_r/\mu_r\,\mu_0 \tag{4}$$

Both μ_r and μ_0 denote the relative magnetic permeability. μ_r denotes the medium in the r region, and μ_0 denotes the air medium.

The generalized formula for MVP in the region 6*b* and 6*d* is obtained by deriving (1). The components of MVP in the MI model are represented by (5). The other regional vector magnetic potential expressions are obtained by solving (2) and are given in (6).

$$A_r=(A^x_r+A^z_r+A^s_r)\vec{e}_r \tag{5}$$

$$A_r=(A^x_r+A^z_r)\vec{e}_y \tag{6}$$

where the y-component of the r-region magnetic vector potential, considering only the $z=z_{s_r}$ and $z=z_{t_r}$ boundary conditions is denoted by A^x_y; similarly, A^z_y represents the y-part of the r-region MVP considering only the $x=x_{s_r}$ and $x=x_{t_r}$ boundary conditions. A^s_y denotes the vector magnetic potential under the current source area, which exists only in region 6*b* and 6*d*. The expressions for the MVP in each region, derived from the solutions of Poisson's or Laplace's equations, will be provided below.

1) Regions 2*b*, 2*d*, 4*b*, 4*d*, 6*b*, 6*d*, 8*b*, 8*d*, 10*b*, 10*d*

The MVP in these regions is derived from (1), with the expressions for A^x_y, A^z_y, and A^s_y being given by (7), (8), and (9), respectively.

$$A^x_y=(z_{t_r}-z)\cdot c_{0_r}+(z-z_{s_r})\cdot d_0+\sum_{N_r=1}^{N_r}\cos\left[a^r_{n_r}(x-x_{s_r})\right]\cdot \left\{\frac{c^x_r\sinh\left[\alpha^r_{x_r}(z_{t_r}-z)\right]}{\alpha^r_{n_r}\sinh(\alpha^r_{n_r}\tau_{z_r})}+\frac{d^x_r\sinh\left[\alpha^r_{n_r}(z-z_{s_r})\right]}{\alpha^r_{n_r}\sinh(\alpha^r_{n_r}\tau_{z_r})}\right\} \tag{7}$$

$$A^z_y=\sum_{l_r=1}^{L_r}\sin\left[\beta^r_{l_r}(z-z_{s_r})\right]\cdot \left\{\frac{f^z_r\cosh\left[\beta^r_{l_r}(x_{t_r}-x)\right]}{\beta^r_{l_r}\sinh(\beta^r_{l_r}\tau_{x_r})}+\frac{e^z_r\cosh\left[\beta^r_{l_r}(x-x_{s_r})\right]}{\beta^r_{l_r}\sinh(\beta^r_{l_r}\tau_{x_r})}\right\} \tag{8}$$

$$A^s_y=-0.5\mu_0 J_y z^2 \tag{9}$$

where a particular region is denoted by r, N_r and L_r denote the number of harmonics in this MI model, where N_r denotes the harmonic parameter in the horizontal direction and L_r denotes the harmonic parameter in the verti-cal direction. And c_{0_r}, d_{0_r}, c^x_r, d^x_r, e^x_r, and f^x_r denote unknown coefficients. $\alpha^r_{n_r}$ and $\beta^r_{n_r}$ denote the spatial frequencies in this MI model. $\alpha^r_{n_r}$ and $\beta^r_{n_r}$ are given by (10).

$$\alpha^r_{n_r}=n_r\pi/\tau_{x_r},\ \beta^r_{l_r}=l_r\pi/\tau_{z_r} \tag{10}$$

2) Regions 3, 5, 7, 9

In regions 3, 5, 7, and 9, the medium may not be air; however, it is assumed to have zero electrical conductivity and a magnetic permeability of μ_0. The magnetic vector potential is also zero when x is x_{s_r} or x_{t_r}. Consequently, the Laplace equation is applied, and (11) provides the vector magnetic potential expression for A^z_y in these regions.

$$A^x_y=\sum_{n_r=1}^{N_r}\sin\left[\alpha^r_{n_r}(x-x_{s_r})\right]\cdot \left\{-\frac{c^x_r\cosh\left[\alpha^r_{n_r}(z_{t_r}-z)\right]}{\alpha^r_{n_r}\sinh(\alpha^r_{n_r}\tau_{z_r})}+\frac{d^x_r\cosh\left[\alpha^r_{n_r}(z-z_{s_r})\right]}{\alpha^r_{n_r}\sinh(\alpha^r_{n_r}\tau_{z_r})}\right\} \tag{11}$$

3) Regions 1, 11

In regions 1 and 11, the range of calculations for the magnetic field is limited. Hence, the MVP is assumed to be 0 under conditions $z=z_1$, $z=z_{12}$, $x=x_1$, and $x=x_{12}$. The vector magnetic potential expression for regions 1 and 11 of $A^z_y=0$ is given by (12), following applying Laplace's equation.

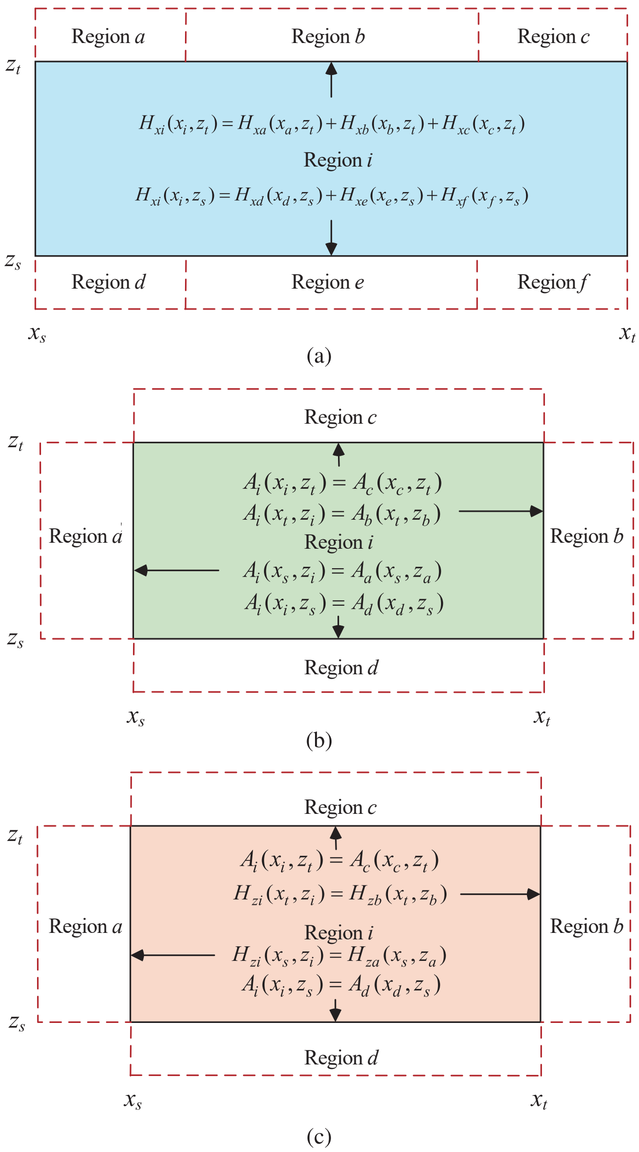

Fig. 5 Boundary condition model (a), (b) and (c).

$$A_y^x=\sum_{n_r=1}^{N_r}\sin\left[\alpha_{n_r}^r(x-x_{s_r})\right]\cdot\left\{-\frac{c_r^x\,\mathrm{cinh}\left[\alpha_{n_r}^r(z_{t_r}-z)\right]}{\alpha_{n_r}^r\cosh(\alpha_{n_r}^r\tau_{z_r})}+\frac{d_r^x\sinh\left[\alpha_{n_r}^r(z-z_{s_r})\right]}{\alpha_{n_r}^r\cosh(\alpha_{n_r}^r\tau_{z_r})}\right\} \tag{12}$$

4) Regions $2c$, $4c$, $6c$, $8c$, $10c$

The medium in all regions is air, indicating that the Laplace equation governs the MFD in these regions. In the derivation process, by applying the critical values of MVP and MFD on the boundaries of these regions as boundary conditions, the generalized form of MVP for these regions can be derived.

$$A_y^x=\sum_{n_r=1}^{N_r}\sin\left[\alpha_{n_r}^r(x-x_{s_r})\right]\cdot\left\{\frac{c_r^x\sinh\left[\alpha_{n_r}^r(z_{t_r}-z)\right]}{\alpha_{n_r}^r\sinh(\alpha_{n_r}^r\tau_{z_r})}+\frac{d_r^x\sinh\left[\alpha_{n_r}^r(z-z_{s_r})\right]}{\alpha_{n_r}^r\sinh(\alpha_{n_r}^r\tau_{z_r})}\right\} \tag{13}$$

$$A_y^z=\sum_{l_r=1}^{L_r}\sin\left[\beta_{l_r}^r(z-z_{s_r})\right]\cdot\left\{\frac{e_r^z\sinh\left[\beta_{l_r}^r(x_{t_r}-x)\right]}{\beta_{l_r}^r\sinh(\beta_{l_r}^r\tau_{x_r})}+\frac{f_r^z\sinh\left[\beta_{l_r}^r(x-x_{s_r})\right]}{\beta_{l_r}^r\sinh(\beta_{l_r}^r\tau_{x_r})}\right\} \tag{14}$$

5) Regions $2a$, $2e$, $4a$, $4e$, $6a$, $6e$, $8a$, $8e$, $10a$, $10e$

The magnetic field in all regions, being an air medium, is controlled by the Laplace equation. The y-part of the MVP in the r-region, A_y^x, is considered concerning only the z-side boundary conditions, and the y-part of the MVP in the r-region, A_y^z is considered concerning only the x-side boundary conditions. Fig. 3 illustrates that the MVP is zero on the x-edge in x_{pr} regions $2a$, $4a$, $6a$, $8a$, and $10a$, and zero on the x-edge x_{qr} in regions $2e$, $4e$, $6e$, $8e$, and $10e$. Thus, $e_r^z=0$ is substituted into (14) to obtain the magnetic vector potentials in regions $2a$, $4a$, $6a$, $8a$, and $10a$. The same can be obtained; however, for regions $2e$, $4e$, $6e$, $8e$, and $10e$, $f_r^z=0$ is substituted into (14) to obtain the magnetic vector potential.

C. Calculation of Unknown Coefficients

As illustrated in Fig. 5, the offered 2D subdomain analysis model showcases three distinct boundary condition patterns. In regions 1, 3, 5, 7, 9, and 11, the boundary condition illustrated in Fig. 5 is to be used. Since more than one region is connected to the z-edge of region r, the boundary conditions $F(x)$ and $G(x)$ on the z-edge are represented as segmented mapping. For region 1, x_{pr} applied at the lower boundary is zero, while for region 11, x_{qr} applied at the upper boundary is zero.

The pattern of boundary conditions in Fig. 5 must be applied in regions $2a$, $2c$, $4a$, $4c$, $6a$, $6c$, $8a$, $8c$, $10a$, $10c$, $2e$, $4e$, $6e$, $8e$, and $10e$. The A_y^z on the left boundary x_s is zero in regions $2a$, $4a$, $6a$, $8a$, and $10a$, and the A_y^z on the correct boundary x_t is also zero in regions $2e$, $4e$, $6e$, $8e$, and $10e$, according to the special boundary relationship between regions. The boundary condition illustrated in Fig. 5 is to be used in regions $2b$, $2d$, $4b$, $4d$, $6b$, $6d$, $8b$, $8d$, $10b$, and $10d$.

After determining the boundary conditions between the 11 partitions and 31 subregions of the MI model, the coefficients to be determined for individual regions are calculated by the system of coupled equations. The subsequent part is dedicated to the derivation of the unknown coefficients within the vector magnetic potential. To elucidate the derivation progression, one of the neighboring side of region $6b$ is utilized as a case study.

In accordance with (7), The following expression for $A_{y_{6b}}^x$ on the edge of the bottom $z=z_6$ of region $6b$ can be obtained.

$$A_{y_{6b}}\big|_{z=z_6}=\tau_{z_{6b}}\cdot c_{0_{6b}}+\sum_{n_{6b}=1}^{N_{6b}}\frac{c_{6b}^x}{\alpha_{n_{6b}}^{6b}}\cdot\cos\left[\alpha_{n_{6b}}^{6b}(x-x_3)\right]+A_{y_{6b}}^s\big|_{z=z_6} \tag{15}$$

The relationship between $\boldsymbol{A}_{y_{6b}}$ and $\boldsymbol{A}_{y_5}$ is obtained by applying the MVP as a boundary condition on $z=z_6$, ensuring the continuity of the MVP between the regions.

$$A_{y_5}|_{z=z_6} - \overset{s}{A}_{y_{6b}}|_{z=z_6} = \tau_{z_{11}} \cdot c_{0_{6b}} + \sum_{n_{6b}=1}^{N_{6b}} \frac{\overset{x}{c}_{6b}}{\overset{6b}{\alpha}_{n_{6b}}} \cdot \cos\left[\overset{6b}{\alpha}_{n_{6b}}(x-x_3)\right] \tag{16}$$

In the above equation, the series in the equation is viewed as the Fourier Series (FS) containing just the cosine factor. On the interval $[x_3, x_4]$, the FS expansion of $L(x) = A_{y_5}|_{z=z_6} - \overset{8}{A}_{y_{6b}}|_{z=z_6}$ is performed to determine the coefficients $c_{0_{6b}}$ and $\overset{x}{c}_{6b}$.

$$c_{0_{6b}} = \frac{1}{\tau_{x_{11}}} \cdot \frac{1}{\tau_{z_{11}}} \cdot \int_{x_3}^{x_4} L(x)\,\mathrm{d}x \tag{17}$$

$$\overset{x}{c}_{6b} = \frac{2}{\tau_{x_{11}}} \int_{x_3}^{x_4} \overset{6b}{\alpha}_{n_{6b}} \cdot L(x) \cdot \cos\left[\overset{6b}{\alpha}_{n_{6b}}(x-x_3)\right]\mathrm{d}x \tag{18}$$

After the expression for $\boldsymbol{A}_{y_5}|_{z=z_6}$ has been substituted into $c_{0_{6b}}$ and $\overset{x}{c}_{6b}$, (17) and (18) can be rewritten as (19) and (20), where $n_{6b}=1,2,3 \cdots N_{6b}$.

$$c_{0_{6b}} + \sum_{n_5=1}^{N_5}\left[\overset{x}{c}_{_{6b}} \cdot Tc(n_5) + \overset{x}{d}_{_{6b}} \cdot Td(n_5)\right] = e \tag{19}$$

$$\overset{x}{c}_{_{6b}} + \sum_{n_5=1}^{N_5}\left[\overset{x}{c}_{_{6b}} \cdot Tc(n_{6b}, n_5) + \overset{x}{d}_{_{6b}} \cdot Td(n_{6b}, n_5)\right] = 0 \tag{20}$$

In (19), $Tc(n5)$ and $Td(n5)$ are related only to n_5. The variable s is related to the current source.

$$Tc(n_5) = \frac{\operatorname{csch}(\overset{5}{\alpha}_{n_5} \cdot \tau_{z_5})}{\tau_{x_{6b}} \cdot \tau_{z_{6b}} \cdot \overset{5}{\alpha}_{n_5}} \int_{x_3}^{x_4} \sin\left[\overset{5}{\alpha}_{n_5}(x-x_1)\right]\mathrm{d}x \tag{21}$$

$$Td(n_5) = \frac{-\coth(\overset{5}{\alpha}_{n_5} \cdot \tau_{z_5})}{\tau_{x_{6b}} \cdot \tau_{z_{6b}} \cdot \overset{5}{\alpha}_{n_5}} \int_{x_3}^{x_4} \sin\left[\overset{5}{\alpha}_{n_5}(x-x_1)\right]\mathrm{d}x \tag{22}$$

$$e = -\frac{\overset{s}{A}_y|_{z=z_6}}{\tau_{z_{6b}}} = \frac{0.5\mu_0 \cdot \mu_{6b} \cdot J_y \cdot z_6^2}{\tau_{z_{6b}}} \tag{23}$$

In (20), $Tc(n_{6b}, n_5)$ and $Td(n_{6b}, n_5)$ are determined by n_{6b} and n_5.

$$Tc(n_{6b}, n_5) = \frac{2\overset{6b}{\alpha}_{n_{6b}} \cdot \csc(\overset{5}{\alpha}_{n_5} \cdot \tau_{z_5})}{\tau_{x_{6b}} \cdot \overset{5}{\alpha}_{n_5}} \cdot \int_{x_3}^{x_4} \sin\left[\overset{5}{\alpha}_{n_5}(x-x_1)\right] \cdot \cos\left[\overset{6b}{\alpha}_{n_{6b}}(x-x_3)\right]\mathrm{d}x \tag{24}$$

$$Tc(n_{6b}, n_5) = -\frac{2\overset{6b}{\alpha}_{n_{6b}} \cdot \coth(\overset{5}{\alpha}_{n_5} \cdot \tau_{z_5})}{\tau_{x_{6b}} \cdot \overset{5}{\alpha}_{n_5}} \cdot \int_{x_3}^{x_4} \sin\left[\overset{5}{\alpha}_{n_5}(x-x_1)\right] \cdot \cos\left[\overset{6b}{\alpha}_{n_{6b}}(x-x_3)\right]\mathrm{d}x \tag{25}$$

Matrix representations are more readable, concise, and expandable than systems of equations, thus the coefficients to be determined for regions 5 and $6b$ are defined by the matrix, this matrix is a column vector of $(2N_5 + 1 + N_{6b}) * 1$. The current source matrix is a column vector of $(1 + N_{6b}) * 1$.

$$[D_{5\&6b}] = [\overset{x}{c}_1 \ \ \overset{x}{c}_5 \overset{x}{d}_1 \ \ \overset{x}{d}_5 c_{0_{6b}} \overset{x}{c}_1 \ \ \overset{x}{c}_{6b}]^{\mathrm{T}} \tag{26}$$

$$[O_{5\&6b}] = \left[-\frac{\overset{s}{A}_y|_{z=z_6}}{\tau_{z_{6b}}} 0 \ \ 0\right]^{\mathrm{T}} \tag{27}$$

According to the array of equations, the length of the matrices of $c_{0_{6b}}$ and $\overset{x}{c}_{6b}$ in region $6b$ is $(1 + \mathrm{N}_{6b} * 1)$.The above system of equations can be expressed by (28).

$$[K_{5\&6b}]\,[D_{5\&6b}] = [O_{5\&6b}] \tag{28}$$

In the above equation, $[K_{5\&6b}]$ is the system information matrix that is associated with regions 5 and $6b$, which encompasses the dimensions, relative permeability,and conductivity of the two-dimensional subdomain model.

$$[K_{5\&6b}] = [\,[T_{5\&6b}]\,[I_{5\&6b}]\,] \tag{29}$$

where $[T_{5\&6b}]$ is the matrix of $(1 + N_{6b}) * 2N_5$ and $[I_{5\&6b}]$ is the unit matrix that is of $(1 + N_{6b}) * (1 + N_{6b})$.

The complete form of (28) can be obtained by determining the coefficients by repeating the above method, utilizing other boundary conditions in each region, as demonstrated in (30).

$$[K]\,[D] = [O] \tag{30}$$

$[D]$ is a column vector of length $L_{\max} * 1$, including all undetermined coefficients in the entire region.

$$[D] = [\,[D_1]^{\mathrm{T}}\,[D_2]^{\mathrm{T}} \cdots [D_{31}]^{\mathrm{T}}\,]^{\mathrm{T}} \tag{31}$$

$[D_r]$ is the matrix of coefficients to be determined for a region in a two-dimensional subdomain, and $L_{\max}$ is the sum of the number of coefficients to be determined in the subdomain, $L_{\max}$ is denoted by (32).

$$L_{\max} = N_1 + 2N_2 + L_2 + \cdots + 2(N_{4b} + 1 + L_{4b}) + \cdots + N_{31} \tag{32}$$

$[K]$ represents the $L_{\max} * L_{\max}$ system information matrix, and [O] is the electromagnetic source matrix of length $L_{\max} * 1$. The coefficients to be determined can ultimately be calculated using (33).

$$[\mathrm{D}] = [\mathrm{K}]^{-1}\,[\mathrm{O}] \tag{33}$$

III. Mutual Inductance Calculation for Rectangular Coils Enclosed by Convex Toroidal Magnetic Shielding

From the derivation of the first part of the equation, it is possible to calculate the MVP for individual regions. It is assumed that the extent of the third orthogonal plane is infinite, but the extent of the third orthogonal plane is finite in the actual MI

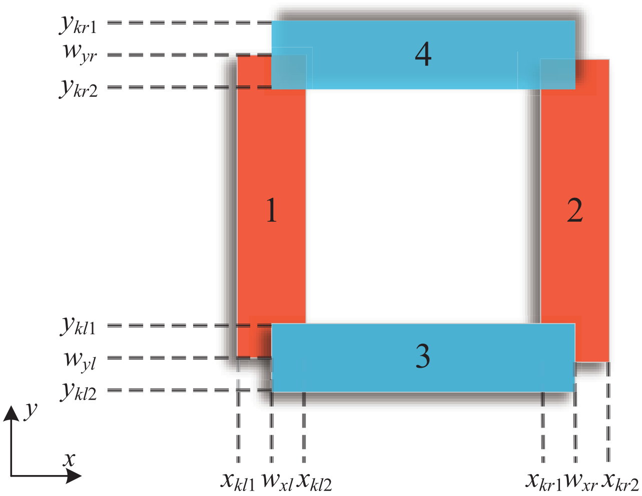

Fig. 6 Simplified model of the coil.

model. Hence, the MVP is made to vary in the third orthogonal plane by the calibration factor. In a coordinate system, the third direction is the three-dimensional space formed perpendicular to the plane comprising the coordinate system and extending outward from that direction. In Fig. 3 the third direction is the y-direction [26].

According to the Biot-Savart law [27], the calibration factor is defined as the ratio of the MFD of an infinite-length linear excitation to the MFD of a finite-length linear excitation.

The rectangular helical coil can be abstracted into four separate conductors, as shown in Fig. 8. The lengths of conductors 1 and 2 in the y-direction are w_{yr} - w_{yl}, and the lengths of conductors 3 and 4 in the x-direction are w_{xr} - w_{xl}, where the parameter representations can be calculated from (34).

$$\begin{cases} \omega_{xl}=(x_{kl1}+x_{kl2})/2 \\ \omega_{xr}=(x_{kr1}+x_{kr2})/2 \\ \omega_{yl}=(y_{kl1}+y_{kl2})/2 \\ \omega_{yr}=(y_{kr1}+y_{kr2})/2 \end{cases} \tag{34}$$

(35) gives the MFD at a point in an unenclosed region due to two infinitely long parallel conductors, 1 and 2, being excited.

$$B^{\inf}_{1,2}=\left[\left(\frac{k}{h_1}\right)^2+\left(\frac{k}{h_2}\right)^2-2\left(\frac{k^2}{h_1 h_2}\right)\cdot\cos(\pi-\gamma_1-\gamma_2)\right]^{\frac{1}{2}} \tag{35}$$

where the excitation current is I_p, $\Gamma_{xl}=x\text{-}w_{xl}$, $\Gamma_{xr}=x\text{-}w_{xr}$, $\Gamma z=z\text{-}z_v$, $z_v=z_7\text{-}z_6$, $k=\mu_0 I_p/2\pi$, the rest of the parameters can be calculated from (36).

$$\begin{cases} \cos\,\alpha_1=(x-w_{xl})/g_1 \\ \cos\,\alpha_2=(w_{xl}-x)/g_1 \\ h_1=[(\Gamma_{xl})^2+(\Gamma_z)^2]^{\frac{1}{2}} \\ h_2=[(\Gamma_{xr})^2+(\Gamma_z)^2]^{\frac{1}{2}} \end{cases} \tag{36}$$

(37) gives the MFD in the unconfined area excited by two finite-length conductors, 1 and 2.

$$B^f_{1,2}=\left[(B^f_1)^2+(B^f_2)^2-2B^f_1 B^f_2\cdot\cos(\pi-\gamma_1-\gamma_2)\right]^{\frac{1}{2}} \tag{37}$$

$$B^f_1=\frac{\mu_0 I_p}{4\pi h_1}\cdot\left(\frac{h_4}{\sqrt{h_1^2+h_4^2}}-\frac{h_3}{\sqrt{h_1^2+h_3^2}}\right) \tag{38}$$

$$B^f_2=\frac{\mu_0 I_p}{4\pi h_2}\cdot\left(\frac{h_4}{\sqrt{h_2^2+h_4^2}}-\frac{h_3}{\sqrt{h_2^2+h_3^2}}\right) \tag{39}$$

where $h_3=y_{kl1}-y$, $h_4=y_{kr2}-y$. y_{kl1} and y_{kr2} denote the dimension on the third direction y in the mutual induction model. The flux density excited by a straight line of finite length can be calculated by substituting the derived B^f_1 and B^f_2 into (37). The calibration factor in the MI model is derived from (40). In the MI model, the calibration factor for the third orthogonal plane can be similarly derived by the above steps.

$$j_{xz}(u,v,w)=\frac{B^f_{1,2}}{B^{\inf}_{1,2}} \tag{40}$$

The literature proposes the coefficient function $g(\mu_i)$ [23], where μ_i denotes the relative permeability of the medium, and $g(\mu_i)$ is a function of μ_i , which reduces the error generated by the relative permeability.

$$g(\mu_i)=\frac{B_z^{3DFEA}(\mu_i)}{B_z^{2DFEA}(\mu_i)}\cdot\frac{B_z^{2DFEA}(\mu_i=1)}{B_z^{3DFEA}(\mu_i=1)} \tag{41}$$

In the above equation, the z-axis of the MFD derived from the three dimensional and two dimensional FEA models of μ_r at relative permeability are denoted by $B_z^{3DFEA}(\mu_i)$ and $B_z^{2DFEA}(\mu_i)$. The MFD in the z-direction derived from three dimensional and two dimensional FEA models of the unconfined region are also denoted by $B_z^{3DFEA}(\mu_i=1)$ and $B_z^{2DFEA}(\mu_i=1)$, respectively.

Since the coils are parallel to each other, only the perpendicular z-axis of MFD exists, which plays a role in determining the MI. In this WPT system, the total MFD under the three-dimensional areas is found by summing the subflux densities in each plane and then reducing the error by using calibration factors and coefficient functions $g(\mu_i)$, where the formula is calculated as (42).

$$\begin{cases} B_{zr}^{3D}(u,v,w)=B_{xz}^{2D}+B_{yz}^{2D} \\ B_{xz}^{2D}(u,v,w)=B_{zr}^{xz}(x,z)\cdot g(\mu_i)\cdot j_{xz}(u,v,w) \\ B_{yz}^{2D}(u,v,w)=B_{zr}^{yz}(y,z)\cdot g(\mu_i)\cdot j_{xz}(u,v,w) \end{cases} \tag{42}$$

$B_{zr}^{xz}(u, w)$ and $B_{zr}^{yz}(v, w)$ are the z-components of the MFD in the r-region derived from the individual planes in the MI model. Depending on the location of the receiving coil, it is

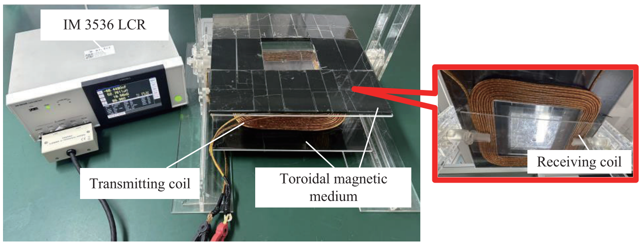

Fig. 7 Experimental equipment.

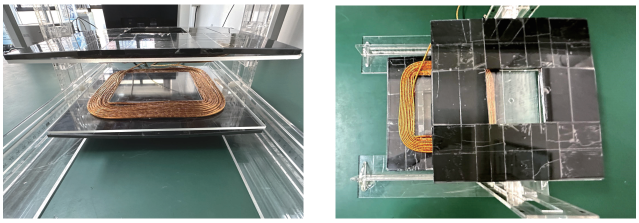

(a) (b)

Fig. 8 Relative position change of experimental model coils. (a) Vertical offset. (b) Horizontal offset.

therefore necessary to find $B_{zr}^{3D}(u, v, w)$ to further calculate the MI of this WPT system. The MI is given by (43).

$$M=\sum_{e_r=1}^{E_r}\left(\oint_{S_{er}} B_{z_7}^{3D}(u,v,w)\mathrm{d}x\mathrm{d}y\right)/I_p \tag{43}$$

where E_r denotes the winding count of the receiving coil, e_r denotes coil per turn, and S_{er} denotes the effective receiving area per winding count of the coil.

IV. Verification

Accuracy for (43) is verified through simulations conducted using ANSYS Maxwell software. As shown in Fig. 7, impedance tester, acrylic frame and other devices is used for the measurements. The experiments are conducted on a non-magnetic wooden table with an acrylic frame, and an impedance tester is used for testing. The transmitting and receiving side magnetic shields are constructed of 5 mm high permeability cabochon ring type magnetic shields placed outside the transceiver coils, respectively. The copper wire coil has a radius of 4 mm and contains ten turns. Current frequency set to 85 KHz. Coil and dielectric material parameters and coil harmonic parameters are illustrated in Table I and Table II.

This section will examine the offset variation of the coil in the horizontal and vertical directions. During the experiment, the transmitting side device was kept fixed and the receiving side device was adjusted for vertical and horizontal relative offset positions. The variation of the relative places of the coils in the experimental model is illustrated in Fig. 8.

A. Vertical Offset

For the receiving coil vertical offset experiment, set the initial distance between the receiving and transmitting coils to 30 mm, and the receiving side unit is gradually moved to 120 mm in 10 mm increments along the z-direction. The offset schematic is depicted in Fig. 9.

TABLE I
Coil and Dielectric Material Parameters

Symbol	Parameter	Value
N_p	Transmitting coil winding count	10
N_s	Receiving coil winding count	10
L_c	Copper wire diameter	4 mm
L_g	Gap between coil and magnetic shield	5 mm
μ_r	Relative permeability of ferrite	2800
I_p	Transmitting coil excitation current	10 A
f	Current frequency	85 kHz
H_e	Height of inner edge	5 mm
L_x	Coil size in x-direction	256 mm
L_y	Coil size in y-direction	261 mm

TABLE II
Coil Harmonic Parameters

Harmonic number	Value
Harmonic (N_{2a}, N_{2b}, N_{2c}, N_{2d}, N_{2e}, N_{4a}, N_{4b}, N_{4c}, N_{4d}, N_{4e}, N_{8a}, N_{8b}, N_{8c}, N_{8d}, N_{8e}, N_{10a}, N_{10b}, N_{10c}, N_{10d}, N_{10e})	40
Harmonic (N_1, N_3, N_5, N_9, N_{11}, N_{6a}, N_{6b}, N_{6c}, N_{6d}, N_{6e}, L_{6a}, L_{6b}, L_{6c}, L_{6d}, L_{6e}, N_7)	100
Harmonic (L_{2a}, L_{2b}, L_{2c}, L_{2d}, L_{2e}, L_{4a}, L_{4b}, L_{4c}, L_{4d}, L_{4e}, L_{8a}, L_{8b}, L_{8c}, L_{8d}, L_{8e}, L_{10a}, L_{10b}, L_{10c}, L_{10d}, L_{10e})	40

In Fig. 9, Δz denotes the dynamic spacing between coils. The green dashed line signifies the location of the receiving coil before the vertical offset, the blue solid line signifies the position of the receiving coil after the vertical offset, and the red solid line indicates the place of the transmitting coil. The MI data and error comparisons after the vertical offset of the receiving coil are recorded in Table III. Where M_c represents computational MI, M_s represents simulated MI, and M_e represents experimental MI. ε_1 denotes the mistake between the MI of the M_c and M_s. ε_2 denotes the bias between the MI of the M_c and M_e. Such expressions will be adhered to in the following parts of this article. The expressions for ε_1 and ε_2 are given by (44) and (45), respectively.

$$\varepsilon_1=\frac{|M_c-M_s|}{M_c}\times 100\% \tag{44}$$

$$\varepsilon_2=\frac{|M_c-M_e|}{M_c}\times 100\% \tag{45}$$

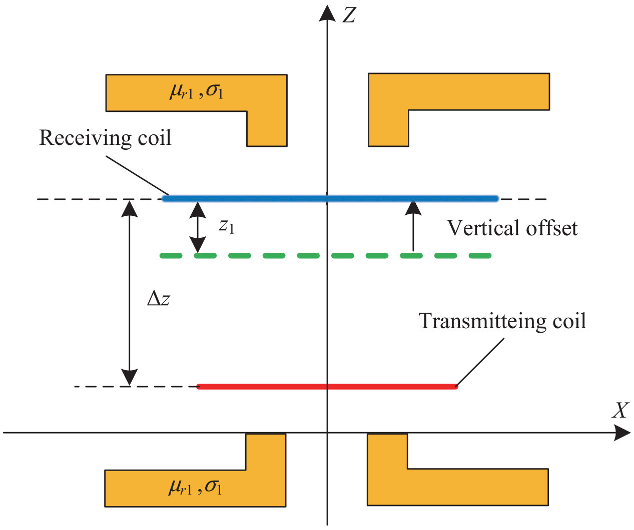

Fig. 9 Schematic diagram of the vertical offset of the receiving coil.

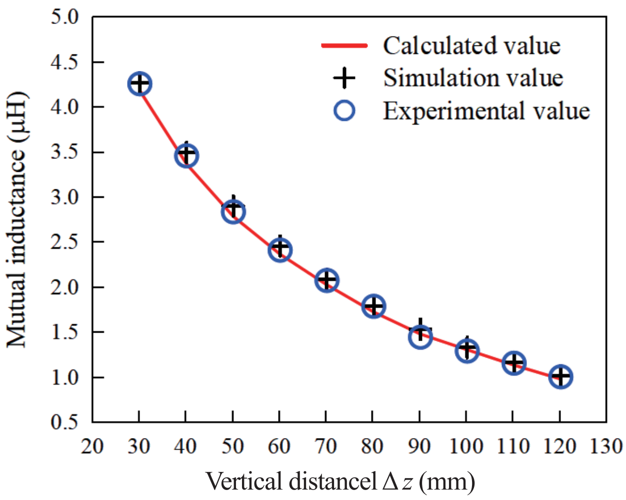

Fig. 10 MI variation curve with vertical distance of receiving coil.

Analysis of the data in Table III reveals that the error ε_1 between the M_c and M_s remains below 4.55%, and the error ε_2 between the M_c and M_e does not exceed 4.69% for Δz ranging from 30 mm-120 mm. The error between the M_c, M_s and M_e values of mutual inductance is within 5% and the experimental results are in better agreement. Based on Table III, a plot of MI versus vertical distance between coils was illustrated as exhibited in Fig. 10.

The curve in Fig. 10 shows that MI decreases gradually with increasing Δz. This is due to the fact that the increase in Δz causes a gradual decrease in MFD in the MI model and hence the MI value of this system gradually decreases.

B. Horizontal Offset

For the receiving coil horizontal offset experiment, Δz in the MI model is maintained at a constant 40 mm. In the experiment, the receiving coil is positioned in the horizontal directions in increments of 10 mm, beginning from the horizontal coordinate $x = 0$ mm and extending to $x = 50$ mm and $x = -50$ mm, respectively. The offset schematic is depicted in Fig. 11. The MI measurements and their error comparisons when the receiving coil is horizontally offset are recorded in Table IV. In the table, x denotes the horizontal offset of the receiving coil, and this notation will be used in the subsequent sections.

TABLE III
MUTUAL INDUCTANCE AND DEVIATION AT VERTICAL OFFSET

Δz(mm)	M_c(μH)	M_s(μH)	M_e(μH)	ε_1	ε_2
30	4.0896	4.2756	4.2667	4.55%	4.33%
40	3.3774	3.504	3.2189	3.75%	4.69%
50	2.7956	2.9119	2.7281	4.16%	2.41%
60	2.3771	2.4677	2.4234	3.81%	1.95%
70	2.0385	2.0965	2.0876	2.85%	2.41%
80	1.7372	1.7985	1.8011	3.53%	3.68%
90	1.4926	1.5451	1.4591	3.52%	2.24%
100	1.3194	1.3424	1.3053	1.74%	1.07%
110	1.1485	1.1802	1.1712	2.76%	1.98%
120	0.9943	1.0314	1.0194	3.73%	2.52%

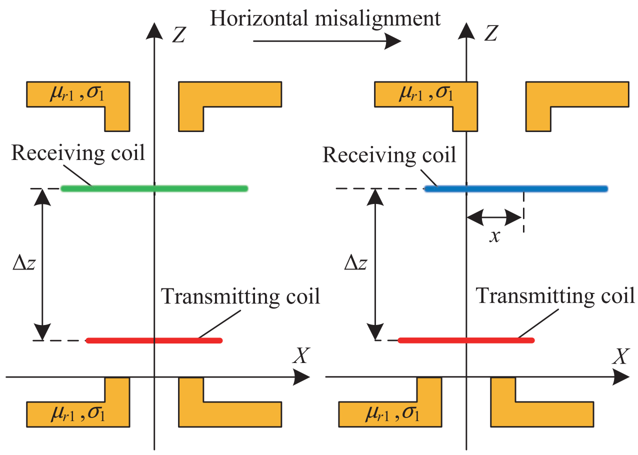

Fig. 11 Schematic diagram of the horizontal offset of the receiving coil.

Analysis of the findings in Table IV indicates that when the horizontal offset range $x = -20$ mm, the error between the M_c and M_s values does not exceed 4.0% in all cases except for the MI where the deviation ε_1 between the M_c and M_s is 4.41%. The error ε_2 between the M_c and M_e of MI does not exceed a maximum of 4.31% and reaches a minimum of 1.77%. This indicates a high level of agreement among the results of calculated MI, simulated MI, and experimental MI. According to Table IV, the modification of MI with horizontal offset distance between the coils is graphed as exhibited in Fig. 12.

Fig. 12 exhibits that when the vertical height is maintained constant, the receiving coil is moved in horizontal direction. MI decreases as the distance from the center position increases. This is due to the fact that in this system the magnetic flux

TABLE IV
HORIZONTAL OFFSET MUTUAL INDUCTANCE AND ERROR AT VERTICAL DISTANCE Δz=40 MM

x(mm)	M_c(μH)	M_s(μH)	M_e(μH)	ε_1	ε_2
−50	2.6969	2.7442	2.5936	1.75%	3.83%
−40	2.8982	2.9817	2.8163	2.88%	2.83%
−30	3.0775	3.1801	2.9628	3.33%	3.73%
−20	3.1967	3.3376	3.0590	4.41%	4.31%
−10	3.3036	3.4344	3.2349	3.96%	2.08%
0	3.4097	3.5029	3.2773	2.73%	3.88%
10	3.3253	3.4241	3.2427	2.97%	2.48%
20	3.2013	3.3218	3.1446	3.76%	1.77%
30	3.0781	3.1664	2.9458	2.87%	4.30%
40	2.8909	2.9732	2.8125	2.85%	2.71%
50	2.6876	2.7391	2.5774	1.92%	4.10%

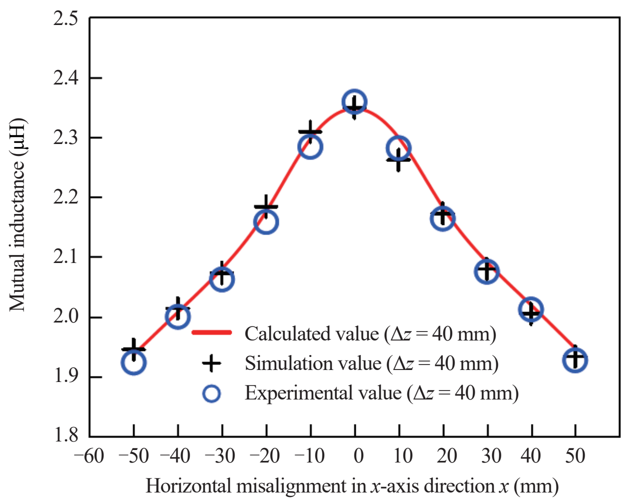

Fig. 12 MI variation curve with horizontal offset of receiving coil.

decreases gradually from the center to the edges and hence the value of MI decreases gradually as x increases.

C. Comparison

The speed of the computational model presented in the article is compared with the simulation software ANSYS Maxwell for solving MI under the same conditions using the computational software MATLAB. Ignoring the time spent on ANSYS Maxwell modeling, the MI model of a bounded magnetically shielded rectangular coil with a convex toroidal type has been computed in MATLAB and simulated in ANSYS Maxwell using the same hardware configuration. The results of the comparison of the solution speeds of the two methods are presented in Table V. In the table, t_c represents the time taken for testing, $t_{1–5}$ indicates the average time taken for ANSYS Maxwell simulation, and $t_{6–10}$ indicates the average time taken for MATLAB computation. T_a indicates the duration for the computation or

TABLE V
COMPARISON OF TIME TAKEN FOR COMPUTATION AND SIMULATION OF MUTUAL INDUCTANCE

t_c(s)	T_a(s)	T_b(s)	T_c(s)
t_1	82.56	95.66	79.37
t_2	86.46	94.24	81.34
t_3	84.56	92.69	81.09
t_4	82.56	97.66	80.45
t_5	81.67	91.23	77.13
t_6	8.41	8.89	6.90
t_7	7.23	8.79	7.32
t_8	8.65	8.63	6.90
t_9	7.89	9.69	8.30
t_{10}	8.79	8.32	8.12

simulation of the MI value at vertical offset. T_b indicates the duration for the computation or simulation of the MI value at the horizontal offset. T_c indicates the duration for the computation or simulation of the MI values at horizontal and vertical offsets. The data analysis in Table V reveals that the fastest time for ANSYS Maxwell simulation is 77.13 seconds. In contrast, the longest time taken by the MATLAB programme employing the methodology of this article was 9.79 seconds, which is considerably shorter than the simulation time of ANSYS Maxwell. This demonstrates the significant computational efficiency advantage of the method used in this article.

The parameters from Tables I and II are incorporated into the system, and the ANSYS Maxwell model output depicting the z-x magnetic field distribution cross-section for the coaxial state with Δz = 40 mm and the horizontal offset state with x = −50 mm is presented in Fig. 13.

Fig. 13 represents a graphical representation of the spatial distribution of MVP in this system at Δz = 40 mm. The coaxial state and the horizontal offset state magnetic field distribution comparison graph indicate that MFD shows a gradual increase in the horizontal direction, followed by a gradual decrease, consistent with the distributional properties of MFD in this structure.

For the comparison of the calculation methodology used in the cited literature with the methodology presented in this article, the outcome are shown in Table VI, where VO represents vertical offsets, HO represents horizontal offsets, MS represents with magnetic shielding, FMS represents with bounded magnetic shielding, and SM represents the ability to save consumables.

The convex ring type magnetic shielding materiall presented in the article is replaced with the rectangular disc magnetic shielding material of the exact specifications, according to the parameters in Tables I and II. This article compares it to the transmission structure. The findings indicate that the material consumption is lowered by 11.12% with the convex ring type magnetic shielding material, compared to the rectangular disc

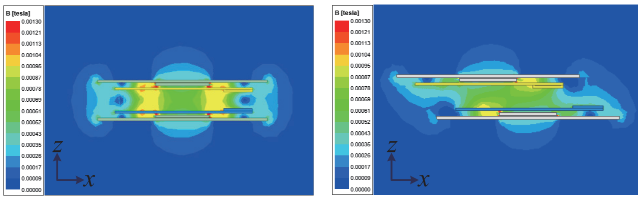

Fig. 13 Comparative analysis of magnetic field morphology.

TABLE VI
COMPARISON OF CALCULATION METHODS

	VO	HO	MS	FMS	SM
[19]	√	×	×	×	×
[20]	√	√	×	×	×
[23]	×	√	√	×	×
[24]	√	√	√	×	×
[26]	×	×	√	√	×
[27]	√	√	√	√	×
This paper	√	√	√	√	√

magnetic shielding material. Furthermore, the percentage of material savings for this model increases even more as the area of the transmission structure skeletonized with the toroidal magnetic shielding material increases.

Additionally, the investigation is conducted to examine the difference in the impact of magnetic shielding material on MI between a convex ring type and a rectangular disc using the same coil structure. With Table I and Table II, two kinds of power transmission models are constructed. The MI ratio is compared through simulation analysis when the magnetic medium is a convex ring type versus a rectangular disc. In this comparison, the rectangular disc magnetic shielding area is identical to the cabochon ring type, 300 mm×300 mm. The other coils and related parameters remain unchanged from those of the cabochon ring-type magnetic shielding transmission structure.

Within conventional mutual-inductance models, for instance those utilizing a rectangular plate magnetic shielding transmission system, that system performance stays relatively stable. Should the performance of the MI model presented in this study surpass 97% of that of the original model, it can be inferred that this WPT system has effectively met the objectives of diminishing production expenses while concurrently preserving transmission performance. Therefore, the simulated MI ratio data for the two trans- mission structures in the case of vertical offset and horizontal offset are provided in this article, as shown in Tables VII and VIII. In these tables, Δz represents the vertical offset distance, and x denotes the horizontal offset distance. ε_3 denotes the ratio of MI values between the convex annular magnetic medium and the rectangular disc magnetic medium in the WPT system. M_u and M_v respectively indicate the MI for the convex ring and rectangular disc magnetically shielded structures. The expression for ε_3 is presented in (46).

TABLE VII
COMPARISON WITH RECTANGULAR DISC MAGNETICALLY SHIELDED TRANSMISSION STRUCTURE IN VERTICAL OFFSET SIMULATION OF MUTUAL INDUCTANCE

Δz(mm)	M_u(μH)	M_v(μH)	ε_3
30	4.2756	4.2667	99.79%
40	3.5040	3.4989	99.85%
50	2.9119	2.9081	99.87%
60	2.4677	2.4434	99.02%
70	2.0965	2.0876	99.58%
80	1.7985	1.7911	99.59%
90	1.5451	1.5191	98.32%
100	1.3424	1.3193	98.28%
110	1.1802	1.1712	99.24%
120	1.0314	1.0194	98.84%

TABLE VIII
COMPARISON OF MAGNETIC SHIELDED TRANSMISSION STRUCTURES WITH RECTANGULAR DISCS IN HORIZONTAL OFFSET SIMULATION OF MUTUAL INDUCTANCE

x(mm)	M_u(μH)	M_v(μH)	ε_3
−50	2.7442	2.6969	98.28%
−40	2.9817	2.8982	97.20%
−30	3.1801	3.0775	96.77%
−20	3.3376	3.2967	98.77%
−10	3.4344	3.3536	97.65%
0	3.5029	3.4097	97.34%
10	3.4241	3.3253	97.11%
20	3.3218	3.2713	98.48%
30	3.1664	3.0781	97.21%
40	2.9732	2.8909	97.23%
50	2.7391	2.6876	98.12%

$$\varepsilon_3=\frac{M_v}{M_u}\times 100\% \tag{46}$$

In summary, whether a vertical offset or a horizontal offset, the simulated ratio of MI between the convex ring-type magnetic shielding transmission structure and the rectangular disc magnetic shielding transmission structure remains above 97.11%. Additionally, ε_3 achieve a maximum of 99.87%. This indicates that this WPT system has largely maintained the transmission performance of the original MI model. Hence, material savings are achieved with convex ring-type magnetically shielded power transmission structures while maintaining transmission efficiencies nearly identical to those of rectangular disc magnetically shielded structures. The manufacturing cost of this WPT system has also been effectively lowered.

V. Conclusion

This article presents a model for MI calculation of a rectangular coil with a convex toroidal bounded magnetic shield, proposing an analytical method leveraging spatial boundary separation for precise calculations in complex regions. The method solves the MI calculation formulas in each region through the double Fourier transform, Maxwell's system of equations, and the Biot-Savart law. The calculated results are verified for validity through simulation and experiment, with the findings indicating that the maximum error between them is 4.55%. The MI calculated, simulated, and experimental values are in agreement. The model achieves an 11.12% material saving over the conventional rectangular magnetic shielding transmission structure, with savings increasing with the openwork area of the ring magnetic shielding.

Simultaneously, the MI value of this WPT system can achieve 99.87% of conventional WPT systems. The design can maximize material savings in the structure while ensuring transmission efficiency, possessing more pro- nounced practical functionality and widespread applicability. In addition, the proposed coil structure model and the results of the study provide theoretical support for the optimisation of the structure and variable of WPT systems, while also instituting a practical basis for the further advancement of MI calculation methods for WPT systems and the widespread application of more reliable and affordable wireless power transfer equipment.

In the end, this study provides a valuable reference and guideline for subsequent research on MI calculations for solenoid-type magnetically shielded rectangular coil structures.

Appendix A

In the matrix transformation process, (30) can be further derived as (33). $[D]$ indicates the unknown in MVP, which contains the the elements of the unknown coefficients. $[K]$ indicates denotes the coefficients of the unknowns, which contains the elements of the known coefficients. $[O]$ and the matrixis populated with elements representing the current sources in the equation. (47) and (48) give the extended forms of $[D]$ and $[O]$, respectively.

$$\begin{aligned}[D] = [\ &[D_1][D_{2a}][D_{2b}][D_{2c}][D_{2d}][D_{2e}][D_3][D_{4a}][D_{4b}] \\ &[D_{4c}][D_{4d}][D_{4e}][D_5][D_{6a}][D_{6b}][D_{6c}][D_{6d}][D_{6e}][D_7] \\ &[D_{8a}][D_{8b}][D_{8c}][D_{8d}][D_{8e}][D_9][D_{10a}][D_{10b}][D_{10c}] \\ &[D_{10d}][D_{10e}][D_{11}]\ ]^T\end{aligned} \tag{47}$$

Each element of $[D]$ consists of a submatrix, the elements of which represent the unknown coefficients of vector magnetic potential.

$$\begin{aligned}[O] = [\ &[O_1][O_{2a}][O_{2b}][O_{2c}][O_{2d}][O_{2e}][O_3][O_{4a}][O_{4b}] \\ &[O_{4c}][O_{4d}][O_{4e}][O_5][O_{6a}][O_{6b}][O_{6c}][O_{6d}][O_{6e}][O_7] \\ &[O_{8a}][O_{8b}][O_{8c}][O_{8d}][O_{8e}][O_9][O_{10a}][O_{10b}][O_{10c}] \\ &[O_{10d}][O_{10e}][O_{11}]\ ]^T\end{aligned} \tag{48}$$

where each element of the $[O]$ is a submatrix, the elements represent the current sources contained within the vector magnetic potentials. $[K]$ and its elements are provided by (49).

$$[K]=\begin{bmatrix}
[V_1] & [V_0] & [V_0] & [V_0] & [V_0] & [V_0] & [V_0] & [V_0] & [V_0] & [V_0] & [V_0] \\
[V_0] & [V_{2a\&2e}] & [V_0] & [V_0] & [V_0] & [V_0] & [V_0] & [V_0] & [V_0] & [V_0] & [V_0] \\
[V_0] & [V_0] & [V_3] & [V_0] & [V_0] & [V_0] & [V_0] & [V_0] & [V_0] & [V_0] & [V_0] \\
[V_0] & [V_0] & [V_0] & [V_{4a\&4e}] & [V_0] & [V_0] & [V_0] & [V_0] & [V_0] & [V_0] & [V_0] \\
[V_0] & [V_0] & [V_0] & [V_0] & [V_5] & [V_0] & [V_0] & [V_0] & [V_0] & [V_0] & [V_0] \\
[V_0] & [V_0] & [V_0] & [V_0] & [V_0] & [V_{6a\&6e}] & [V_0] & [V_0] & [V_0] & [V_0] & [V_0] \\
[V_0] & [V_0] & [V_0] & [V_0] & [V_0] & [V_0] & [V_7] & [V_0] & [V_0] & [V_0] & [V_0] \\
[V_0] & [V_0] & [V_0] & [V_0] & [V_0] & [V_0] & [V_0] & [V_{8a\&8e}] & [V_0] & [V_0] & [V_0] \\
[V_0] & [V_0] & [V_0] & [V_0] & [V_0] & [V_0] & [V_0] & [V_0] & [V_9] & [V_0] & [V_0] \\
[V_0] & [V_0] & [V_0] & [V_0] & [V_0] & [V_0] & [V_0] & [V_0] & [V_0] & [V_{10a\&10e}] & [V_0] \\
[V_0] & [V_0] & [V_0] & [V_0] & [V_0] & [V_0] & [V_0] & [V_0] & [V_0] & [V_0] & [V_{11}]
\end{bmatrix} \tag{49}$$

where $[V]$ is a submatrix within $[K]$. Each element of matrix $[V]$ is also a submatrix, where $[V_0]$ represents the zero matrix, and the elements of other submatrices represent known coefficients of the vector magnetic potential. The submatrices of $[V]$ are specifically represented from (50) to (60).

$$[V_1]=[\ [I]\ [C_1^{2a}]\ [C_1^{2b}]\ [C_1^{2c}]\ [C_1^{2d}]\ [C_1^{2e}]\ ] \tag{50}$$

$$\begin{aligned}[V_3]=[\ &[C_3^{2a}]\ [C_3^{2b}]\ [C_3^{2c}]\ [C_3^{2d}]\ [C_3^{2e}] \\ &[I]\ [C_3^{4a}]\ [C_3^{4b}]\ [C_3^{4c}]\ [C_3^{4d}]\ [C_3^{4e}]\ ]\end{aligned} \tag{51}$$

$$\begin{aligned}[V_5]=[\ &[C_5^{4a}]\ [C_5^{4b}]\ [C_5^{4c}]\ [C_5^{4d}]\ [C_5^{4e}] \\ &[I]\ [C_5^{6a}]\ [C_5^{6b}]\ [C_5^{6c}]\ [C_5^{6d}]\ [C_5^{6e}]\ ]\end{aligned} \tag{52}$$

$$\begin{aligned}[V_7]=[\ &[C_7^{6a}]\ [C_7^{6b}]\ [C_7^{6c}]\ [C_7^{6d}]\ [C_7^{6e}] \\ &[I]\ [C_7^{8a}]\ [C_7^{8b}]\ [C_7^{8c}]\ [C_7^{8d}]\ [C_7^{8e}]\ ]\end{aligned} \tag{53}$$

$$\begin{aligned}[V_9]=[\ &[C_9^{8a}]\ [C_9^{8b}]\ [C_9^{8c}]\ [C_9^{8d}]\ [C_9^{8e}] \\ &[I]\ [C_9^{10a}]\ [C_9^{10b}]\ [C_9^{10c}]\ [C_9^{10d}]\ [C_9^{10e}]\ ]\end{aligned} \tag{54}$$

$$[V_{11}]=[\ [C_{11}^{10a}]\ [C_{11}^{10b}]\ [C_{11}^{10c}]\ [C_{11}^{10d}]\ [C_{11}^{10e}]\ [I]\ ] \tag{55}$$

$$[V_{2a\&2e}]=\begin{bmatrix} [C^{1}_{2a}] & [I] & [C^{2b}_{2a}] & [0] & [0] & [0] & [C^{3}_{2a}] \\ [C^{1}_{2b}] & [C^{2a}_{2b}] & [I] & [C^{2c}_{2b}] & [0] & [0] & [C^{3}_{2b}] \\ [C^{1}_{2c}] & [0] & [C^{2b}_{2c}] & [I] & [C^{2d}_{2c}] & [0] & [C^{3}_{2c}] \\ [C^{1}_{2d}] & [0] & [0] & [C^{2c}_{2d}] & [I] & [C^{2e}_{2d}] & [C^{3}_{2d}] \\ [C^{1}_{2e}] & [0] & [0] & [0] & [C^{2d}_{2e}] & [I] & [C^{3}_{2e}] \end{bmatrix} \tag{56}$$

$$[V_{4a\&4e}]=\begin{bmatrix} [C^{3}_{4a}] & [I] & [C^{4b}_{4a}] & [0] & [0] & [0] & [C^{5}_{4a}] \\ [C^{3}_{4b}] & [C^{4a}_{4b}] & [I] & [C^{4c}_{4b}] & [0] & [0] & [C^{5}_{4b}] \\ [C^{3}_{4c}] & [0] & [C^{4b}_{4c}] & [I] & [C^{4d}_{4c}] & [0] & [C^{5}_{4c}] \\ [C^{3}_{4d}] & [0] & [0] & [C^{4c}_{4d}] & [I] & [C^{4e}_{4d}] & [C^{5}_{4d}] \\ [C^{3}_{4e}] & [0] & [0] & [0] & [C^{4d}_{4e}] & [I] & [C^{5}_{4e}] \end{bmatrix} \tag{57}$$

$$[V_{6a\&6e}]=\begin{bmatrix} [C^{5}_{6a}] & [I] & [C^{6b}_{6a}] & [0] & [0] & [0] & [C^{7}_{6a}] \\ [C^{5}_{6b}] & [C^{6a}_{6b}] & [I] & [C^{6c}_{6b}] & [0] & [0] & [C^{7}_{6b}] \\ [C^{5}_{6c}] & [0] & [C^{6b}_{6c}] & [I] & [C^{6d}_{6c}] & [0] & [C^{7}_{6c}] \\ [C^{5}_{6d}] & [0] & [0] & [C^{6c}_{6d}] & [I] & [C^{6e}_{6d}] & [C^{7}_{6d}] \\ [C^{5}_{6e}] & [0] & [0] & [0] & [C^{6d}_{6e}] & [I] & [C^{7}_{6e}] \end{bmatrix} \tag{58}$$

$$[V_{8a\&8e}]=\begin{bmatrix} [C^{7}_{8a}] & [I] & [C^{8b}_{8a}] & [0] & [0] & [0] & [C^{9}_{8a}] \\ [C^{7}_{8b}] & [C^{8a}_{8b}] & [I] & [C^{8c}_{8b}] & [0] & [0] & [C^{9}_{8b}] \\ [C^{7}_{8c}] & [0] & [C^{8b}_{8c}] & [I] & [C^{8d}_{8c}] & [0] & [C^{9}_{8c}] \\ [C^{7}_{8d}] & [0] & [0] & [C^{8c}_{8d}] & [I] & [C^{8e}_{8d}] & [C^{9}_{8d}] \\ [C^{7}_{8e}] & [0] & [0] & [0] & [C^{8d}_{8e}] & [I] & [C^{9}_{8e}] \end{bmatrix} \tag{59}$$

$$[V_{10a\&10e}]=\begin{bmatrix} [C^{9}_{10a}] & [I] & [C^{10b}_{10a}] & [0] & [0] & [0] & [C^{11}_{10a}] \\ [C^{9}_{10b}] & [C^{10a}_{10b}] & [I] & [C^{10c}_{10b}] & [0] & [0] & [C^{11}_{10b}] \\ [C^{9}_{10c}] & [0] & [C^{10b}_{10c}] & [I] & [C^{10d}_{10c}] & [0] & [C^{11}_{10c}] \\ [C^{9}_{10d}] & [0] & [0] & [C^{10c}_{10d}] & [I] & [C^{10e}_{10d}] & [C^{11}_{10d}] \\ [C^{9}_{10e}] & [0] & [0] & [0] & [C^{10d}_{10e}] & [I] & [C^{11}_{10e}] \end{bmatrix} \tag{60}$$

where $[I]$ signifies the unit matrix. The submatrix $[C]$ signifies the coefficients of the array of equations. And a linear equation represents each row of the matrix.

References

[1] Y. Wang and C. C. Mi, "Guest editorial: special issue on advanced and emerging technologies of high efficiency and long-distance wireless power transfer systems," in *IEEE Transactions on Industry Applications*, vol. 58, no. 1, pp. 1006–1009, Jan.-Feb. 2022.

[2] S. Y. R. Hui, "Past, present and future trends of non-radiative wireless power transfer," in *CPSS Transactions on Power Electronics and Applications*, vol. 1, no. 1, pp. 83–91, Dec. 2016.

[3] S. Y. Chu, X. Cui, X. Zan, and A. -T. Avestruz, "Transfer-power measurement using a non-contact method for fair and accurate metering of wireless power transfer in electric vehicles," in *IEEE Transactions on Power Electronics*, vol. 37, no. 2, pp. 1244–1271, Feb. 2022.

[4] M. Liang, K. E. K. Drissi, and C. Pasquier, "Frequency domain analysis of a dynamic wireless transfer system for electric vehicles," in *IEEE Access*, vol. 12, pp. 72777–72793, 2024.

[5] P. K. Chittoor and C. Bharatiraja, "Wireless-sensor communication based wireless-charging coil positioning system for UAVs with maximum power point tracking," in *IEEE Sensors Journal*, vol. 22, no. 8, pp. 8175–8182, Apr. 2022.

[6] D. Kim and S. Lee, "Propulsion and control of microrobot using a multi-selective wireless power transfer coil," in *IEEE Transactions on Magnetics*, vol. 59, no. 11, pp. 1–6, Nov. 2023.

[7] Q. Wang, W. Che, M. Mongiardo, and G. Monti, "Wireless power transfer system with high misalignment tolerance for bio-medical implants," in *IEEE Transactions on Circuits and Systems II: Express Briefs*, vol. 67, no. 12, pp. 3023–3027, Dec. 2020.

[8] T. Campi, S. Cruciani, F. Maradei, A. Montalto, F. Musumeci, and M. Feliziani, "Centralized high power supply system for implanted medical devices using wireless power transfer technology," in *IEEE Transactions on Medical Robotics and Bionics*, vol. 3, no. 4, pp. 992–1001, Nov. 2021.

[9] A. Wibisono, M. H. Alsharif, H. -K. Song, and B. M. Lee, "A survey on underwater wireless power and data transfer system," in *IEEE Access*, vol. 12, pp. 34942–34957, 2024.

[10] Z. Yan, B. Song, Y. Zhang, K. Zhang, Z. Mao, and Y. Hu, "A rotation-free wireless power transfer system with stable output power and efficiency for autonomous underwater vehicles," in *IEEE Transactions on Power Electronics*, vol. 34, no. 5, pp. 4005–4008, May 2019.

[11] D. Wu, C. Huang, F. Yang, and Q. Sun, "Analytical calculations of self- and mutual inductance for rectangular coils with lateral misalignment in inductive power transfer," in *IET Power Electronics*, vol. 12, no. 15, Oct.

2019.

[12] R. Oliveira and P. Lehn, "An improved mutual inductance electromagnetic model for inductive power transfer systems under misalignment conditions," in *IEEE Transactions on Vehicular Technology*, vol. 69, no. 6, pp. 6079–6093, Jun. 2020.

[13] J. T. Conway, "Inductance calculations for circular coils of rectangular cross section and parallel axes using bessel and struve functions," in *IEEE Transactions on Magnetics*, vol. 46, no. 1, pp. 75–81, Jan. 2010.

[14] S. Babic, F. Sirois, C. Akyel, G. Lemarquand, V. Lemarquand, and R. Ravaud, "New formulas for mutual inductance and axial magnetic force between a thin wall solenoid and a thick circular coil of rectangular cross-section," in *IEEE Transactions on Magnetics*, vol. 47, no. 8, pp. 2034–2044, Aug. 2011.

[15] I. Jeong and K. Nam, "Analytic expressions of torque and inductances via polynomial approximations of flux linkages," in *IEEE Transactions on Magnetics*, vol. 51, no. 7, pp. 1–9, Jul. 2015.

[16] Y. Cheng and Y. Shu, "A new analytical calculation of the mutual inductance of the coaxial spiral rectangular coils," in *IEEE Transactions on Magnetics*, vol. 50, no. 4, pp. 1–6, Apr. 2014.

[17] D. Wu, Q. Sun, X. Wang, and F, Yang, "Analytical model of mutual coupling between rectangular spiral coils with lateral misalignment for wireless power applications," in *IET Power Electronics*, vol. 11, no. 5, pp. 781–786, May 2018.

[18] D. Wu, F. Cheng, and C. Huang, "Analytical computation of mutual inductance between two rectangular spiral coils with misalignments for wireless power applications," in *Microwave and Optical Technology Letters*, vol. 62, Oct. 2019.

[19] Y. Cheng and Y. Shu, "Mutual inductance calculation between arbitrarily positioned rectangular filaments," in *International Journal of Applied Electromagnetics and Mechanics*, vol. 46, no. 1, pp. 287–298, Feb. 2014.

[20] Z. Luo and X. Wei, "Analysis of square and circular planar spiral coils in wireless power transfer system for electric vehicles," in *IEEE Transactions on Industrial Electronics*, vol. 65, no. 1, pp. 331–341, Jan. 2018.

[21] Z. Li, J. Li, C. Quan, X. Zhang, and S. Huang, "Mutual inductance calculation of arbitrarily positioned rectangular coils with magnetic shielding in wireless power transfer systems," in *Transactions of China Electrotechnical Society*, vol. 37, no. 17, pp. 4294–4305, Sept. 2022.

[22] B. K. Kushwaha, G. Rituraj, and P. Kumar, "3-d analytical model for computation of mutual inductance for different misalignments with shielding in wireless power transfer system," in *IEEE Transactions on Transportation Electrification*, vol. 3, no. 2, pp. 332–342, Jun. 2017.

[23] B. K. Kushwaha, G. Rituraj, and P. Kumar, "A subdomain analytical model of coil system with magnetic shields of finite dimensions and finite permeability for wireless power transfer systems," in *IEEE Transactions on Magnetics*, vol. 56, no. 12, pp. 1–11, Dec. 2020.

[24] Z. Chen, Z. Li, Z. Lin, J. Li, and Y. Zhang, "Mutual inductance calculation of rectangular coils at arbitrary position with bilateral finite magnetic shields in wireless power transfer systems," in *IEEE Transactions on Power Electronics*, vol. 39, no. 10, pp. 14065–14076, Oct. 2024.

[25] H. Li, C. Wang, Z. Wei, and D. Li, "Research of shield structure for wireless power transfer system," in *Advanced Technology of Electrical Engineering and Energy*, vol. 38, no. 05, pp. 74–83, May 2019.

[26] A. Demenko, R. M. Wojciechowski, and J. K. Sykulski, "2-d versus 3-d electromagnetic field modeling in electromechanical energy converters," in *IEEE Transactions on Magnetics*, vol. 50, no. 2, pp. 897–900, Feb. 2014.

[27] Z. Zhang, M. Shao, K. Shang. X. Li, C. Huang, J. Shi, H. Cui, and Y. Dong, "Mutual inductance calculation between arbitrarily positioned polygonal coils," in *Transactions of Nanjing University of Aeronautics & Astronautics*, vol. 39, no. S1, pp. 120–126, Oct. 2022.

Zhongqi Li was born in China in 1985. He received the M.Sc. degree from Hunan University of Technology in 2012, and the Ph.D. degree from the Hunan University in 2016. From 2016, he is working assistant professor in Hunan University of Technology. From 2020, he is now working post-doctoral fellow in Hunan University. His research interests include wireless power transfer systems and soft-switching power converters.

Qian Zhang was born in China in 1999. He received a bachelor's degree in software engineering from Wuhan Polytechnic University in 2023. He is currently pursuing the Master's degree in Control Science and Engineering at Hunan University of Technology. His current research interests include wireless power transfer systems.

Lingjun Kong was born in China in 1998. He received a bachelor's degree in Electrical Engineering and Automation from Xuchang University, Xuchang, China, in 2020. He is currently pursuing the Master's degree in Energy Power at Hunan University of Technology. His current research interests include wireless power transfer systems.

Changxuan Hu was born in China in 1999. He received a bachelor's degree from School of Electrical Engineering, Henan Polytechnic University in 2021. He is pursuing a Master's degree in the School of Rail Transportation at Hunan University of Technology, majoring in wireless power transfer technology.

Shoudao Huang received the B.Eng. and Ph.D. degrees in electrical engineering from the College of Electrical and Information Engineering, Hunan University, Changsha, China, in 1983, and 2005, respectively. He is currently a Full-Time Professor with the College of Electrical and Information Engineering, Hunan University. His research interests include motor design and control, power electronic system and control, and wind energy conversion systems.

Static Identification of Inductance Parameters and Initial Rotor Position in Permanent Magnet Synchronous Motor

Liyuan GUO, Chuanqiang LIAN, Guanda XU, Jilong LIU, Xin TANG, and Kun WANG

***Abstract*—Accurate determination of inductance parameters and rotor initial position is of paramount importance in ensuring optimal control accuracy and stability in the context of permanent magnet synchronous motors. This paper proposes a novel static identification method for both the inductance parameters and rotor initial position of a permanent magnet synchronous motor, to achieve simultaneous identification of both parameters. The method involves the injection of high-frequency quadrature voltage signals into the motor, followed by the decomposition of the high-frequency response current using the recursive least squares method. This results in the identification of the motor inductance parameters and rotor initial position, based on the outcomes of the motor rotor polarity identification. Compared with traditional methods, this approach has the advantages of eliminating the delay effect of digital system sampling and control, and of not requiring filters to demodulate the high-frequency response current. Furthermore, the identification results are less affected by the nonlinearity of the inverter. Both simulation and experimental validation support the validity of the method. The experimental results demonstrate that the errors between the identified values of the inductance of the cross and straight axes and the design value are 0.15% and 0.97%, respectively. Additionally, the deviation between the identified results and the actual value of the initial position of the rotor is 1.76°, indicating a high level of identification accuracy.**

***Index Terms*—High frequency injection; inductance parameter identification; initial position identification; permanent magnet synchronous motor.**

I. Introduction

The permanent magnet synchronous machine (PMSM) is distinguished by its simple structure, high power density, high efficiency and low failure rate. It has found widespread application in a variety of fields, including aerospace, ships and vessels, and new energy vehicles.

The conventional identification methodologies for motor parameters can be categorised into two distinct approaches: offline identification methods, which include finite element analysis and experimental measurement [1], and online identification methods, encompassing recursive least squares [2]–[4], Kalman filter [5], [6] and artificial intelligence algorithms [7]. The offline identification method is characterized by its simplicity; however, it necessitates a substantial workload and often encounters challenges in achieving precise identification under full working conditions. Conversely, online identification can achieve identification under full working conditions, but the challenge of under-ranking remains. The inductance identification method based on finite element analysis considers the influence of the cross-saturation effect on the inductance of PMSM in the cross and straight axes. The obtained steady-state inductance parameters are essentially consistent with the actual measurement results, but the calculation process is more complicated. Another method identified in [1] involves the use of high-frequency square-wave voltage injection to identify the inductance parameters. This method takes into account the influence of inverter nonlinearity on the identification results. However, the delay caused by the digital system sampling is approximated by one carrier cycle. The inductor parameter identification method based on the recursive least squares method is mentioned in [2], and the computational amount of this method is smaller than that of the traditional least squares method. However, it is prone to the phenomenon of "data saturation". In order to address this problem, [3] mentions the combination of dynamic forgetting factor and recursive least squares method for inductor identification. Another inductor identification method is proposed in [8], which is based on double time scale stochastic approximation theory. This method is more accurate than the traditional recursive least squares algorithm. Additionally, an inductive parameter identification method based on Kalman filtering has been developed. This method utilizes the a posteriori probability density of the previous moment to iteratively obtain the a posteriori probability density of the subsequent moment. The results of this method are accurate; however, it is only applicable to linear systems. In addressing this limitation, subsequent scholars have proposed an extended Kalman filtering method for identifying motor inductance. This method involves the application of Kalman

Manuscript received January 01, 2025; revised March 02, 2025; accepted March 06, 2025. Date of publication June 30, 2025; date of current version April 18, 2025. This work was supported in part by China National Science Foundation under the Grant 52177202 and 52407230. *(Corresponding author: Chuanqiang Lian.)*

All authors are with National Key Laboratory of Electromagnetic Energy, Naval University of Engineering, Wuhan 430033, China (e-mail: glyisgreat@163.com; wzdslcq@163.com; 3150101258@zju.edu.cn; 66976@163.com; tangxin11@alumni.nudt.edu.cn; 28076622@qq.com).

Digital Object Identifier 10.24295/CPSSTPEA.2025.00012

filtering in nonlinear systems, as outlined in [7]. The proposed approach utilizes a chaotic initialization and a chaotic variation strategy to facilitate rapid identification of inductance parameters. However, the complexity of this method hinders its practical application in engineering contexts.

The conventional approach to rotor initial position identification can be categorized into two distinct methods: the dynamic identification method, which includes the rotor pre-positioning method [9], and the static identification method, which encompasses various high-frequency signal injection methods [10]–[16]. The high-frequency injection signals employed in these methods include high-frequency rotating voltage [10], high-frequency pulsating voltage [11], [12], high-frequency square-wave voltage [13]–[15], and triangular wave voltage [16]. The dynamic identification method is straightforward in principle, but it has certain requirements on the operating environment of the motor, and the identification results are easily affected by the rotation of the motor. Static identification can achieve high-precision identification, but the principle is more complex. [9] proposed a rotor initial pre-positioning method to identify the initial position, the essence of which is to inject a constant voltage vector into the motor for a certain period of time so that the motor rotor reaches a predetermined position. The method is simple but time-consuming and prone to phenomena such as reversal. A rotor initial position identification method based on high-frequency rotating voltage injection is introduced in [11]. The method involves the injection of a high-frequency rotating voltage into a stationary coordinate system, the extraction of the phase difference of the positive-sequence current to compensate for the phase of the negative-sequence current, and the final determination of the initial position of the rotor through the inverse tangent operation. This method has been demonstrated to exhibit high measurement accuracy; however, it necessitates the implementation of a low-pass filter to facilitate the demodulation of the response current. Moreover, it does not consider the impact of sampling and control delays that are inherent to digital systems. In contrast, [12] introduces a rotor initial position identification method based on high-frequency pulsed vibration injection. This method involves injecting a high-frequency pulsed vibration voltage into the estimated d-axis, demodulating the estimated d-axis currents and q-axis currents, and then locking the phase, thereby obtaining the initial position of the rotor. This method eliminates the need for a low-pass filter to demodulate the response current; however, it does not account for the effects of sampling and control delays in digital systems. [15] expounds on a rotor initial position recognition method that is predicated on high-frequency square wave injection. The fundamental principle underlying this method entails the injection of a high-frequency square wave signal into the estimated d-axis, followed by the acquisition of the initial rotor position through the analysis and processing of the estimated q-axis current response. The method exhibits reduced phase delay and enhanced detection accuracy; however, it is susceptible to inverter nonlinearity and switching loss, and its robustness is inadequate.

In light of the challenges posed by the conventional high-frequency injection technique, this paper puts forward a static identification method for the parameters of permanent magnet synchronous motor inductance and the initial rotor position. The proposed method involves the injection of high-frequency quadrature voltage signals into permanent magnet synchronous motor, utilising the recursive least-squares method. The method involves decomposing the high-frequency response currents of the motor orthogonally, thereby obtaining an estimation of the motor's inductance parameters and the initial position of its rotor. This process culminates in the identification of the rotor's polarity by leveraging the saturation characteristics of the inductance to rectify the estimated value. The saturation property of the inductor is then employed to identify the rotor polarity, and the estimated value of the rotor's initial position is corrected.The method's feasibility and effectiveness are verified by simulation and experimental results. In comparison with traditional methods, the proposed approach offers distinct advantages. It facilitates the simultaneous identification of inductor parameters and initial position, while also compensating for phase differences caused by sampling and control delays in the digital system during the identification process. This eliminates the necessity for approximate compensation with a fixed delay time, enhancing the accuracy of the parameter identification results. Furthermore, the method in this paper employs the recursive least squares method to demodulate the response current, obviating the necessity for a filter for demodulation. This approach effectively circumvents the signal delay and distortion problems that arise from the filter.

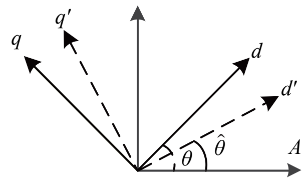

Fig. 1. Relationship between rotation coordinate system and estimated rotation coordinate system.

II. PMSM High Frequency Mathematical Modelling

The model of a three-phase permanent magnet synchronous motor at high frequency signals can be equated to a purely inductive model, as illustrated below:

$$\begin{cases} \dot{i}_{d\mathrm{h}} = \dfrac{1}{L_d} u_{d\mathrm{h}} \\ \dot{i}_{q\mathrm{h}} = \dfrac{1}{L_q} u_{q\mathrm{h}} \end{cases} \tag{1}$$

where, $u_{d\mathrm{h}}$、 $u_{q\mathrm{h}}$ is d, q-axis voltage; $i_{d\mathrm{h}}$、 $i_{q\mathrm{h}}$ is d, q-axis current; L_d、 L_q is d, q-axis inductance.

As illustrated in Fig. 1, the rotational coordinate system is shown to be related to the estimated rotational coordinate system. In this paper, the estimated rotational coordinate system is assumed to be in front of the A-phase winding axis θ , and the rotational coordinate system d-axis is shown to be ahead of the

A-phase winding axis $\hat{\theta}$. The size of $\hat{\theta}$ can vary, and to simplify the calculation, this paper sets $\hat{\theta} = 0$. The angle difference between the rotational coordinate system and the estimated rotational coordinate system is $\Delta\theta = \theta - \hat{\theta} = \theta$, which is also the initial position of the motor rotor.

As illustrated in Fig. 1, the relationship between the motor voltage and current in the rotating coordinate system and the estimated motor voltage and current in the rotating coordinate system is

$$\begin{bmatrix} u_{dh} \\ u_{qh} \end{bmatrix} = \begin{bmatrix} \cos\Delta\theta & \sin\Delta\theta \\ -\sin\Delta\theta & \cos\Delta\theta \end{bmatrix} \begin{bmatrix} u'_{dh} \\ u'_{qh} \end{bmatrix}$$
$$\begin{bmatrix} i_{dh} \\ i_{qh} \end{bmatrix} = \begin{bmatrix} \cos\Delta\theta & \sin\Delta\theta \\ -\sin\Delta\theta & \cos\Delta\theta \end{bmatrix} \begin{bmatrix} i'_{dh} \\ i'_{qh} \end{bmatrix} \tag{2}$$

Combining (1) and (2), the voltage equation of the three-phase permanent magnet synchronous motor in the estimated rotational coordinate system can be expressed as:

$$\begin{bmatrix} i'_{dh} \\ i'_{qh} \end{bmatrix} = \begin{bmatrix} a_{11} & a_{12} \\ a_{21} & a_{22} \end{bmatrix} \begin{bmatrix} u'_{dh} \\ u'_{qh} \end{bmatrix} \tag{3}$$

In (3), u'_{dh}、 u'_{qh}、 i'_{dh}、 i'_{qh} represent the high-frequency voltage and high-frequency current, respectively, in the estimated rotating coordinate system. Let $m = (L_d+L_q)/L_dL_q$, $n = (L_d - L_q)/L_dL_q$, then

$$\begin{cases} a_{11} = \dfrac{m}{2} + \dfrac{n}{2}\cos(2\Delta\theta) \\ a_{12} = a_{21} = \dfrac{n}{2}\sin(2\Delta\theta) \\ a_{22} = \dfrac{m}{2} - \dfrac{n}{2}\cos(2\Delta\theta) \end{cases} \tag{4}$$

III. The Principle of Inductor Parameter and Initial Position Recognition in PMSM

As demonstrated in (4), the response current signal of the permanent magnet synchronous motor contains information regarding the inductance parameter and the initial position of the rotor. In this paper, an orthogonal decomposition of the high-frequency response current of the motor is employed, in conjunction with mathematical analysis, to ascertain the inductance parameter and the initial position of the rotor of the permanent magnet synchronous motor.

Firstly, it is necessary to set the angle between the estimated rotational coordinate system and the axis of the A-phase winding of the right-angle coordinate system to 0. Following this, a high-frequency quadrature voltage signal should be injected into the estimated rotational coordinate system of the permanent magnet synchronous motor. The given value of the high-frequency quadrature voltage at this time is

$$\begin{cases} u'_{dh}{}^* = U_h\cos(\omega_h t) \\ u'_{qh}{}^* = U_h\sin(\omega_h t) \end{cases} \tag{5}$$

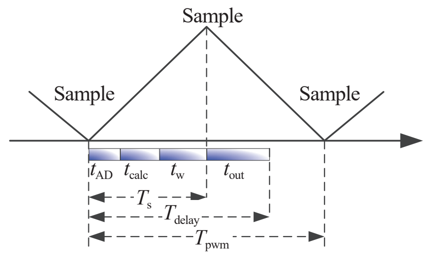

Fig. 2. PWM irregular sampling timing chart.

where, U_h is the high-frequency injection voltage amplitude and ω_h is the high-frequency injection voltage frequency.

In the context of an open-loop vector control system for a permanent magnet synchronous motor, it is evident that the digital system exhibits a delay phenomenon, resulting in a deviation between the actual and the desired voltage values. As illustrated in Fig. 2, the timing diagram of pulse width modulation (PWM) irregular sampling, the causes of the delay phenomenon include the signal A/D conversion time t_{AD}, the calculation time of the control algorithm t_{calc}, the waiting time to avoid the modulating signal and the carrier signal intercepted several times t_w, and the delay of the PWM output t_{out}. As the delay time of the digital system cannot be accurately measured, the conventional approach assumes that the delay time of the digital system is compensated by a fixed value. However, there is a discrepancy between this compensation value and the actual digital system delay time. This discrepancy generates a phase difference in the control system, thereby affecting the recognition accuracy of the motor parameters.

As demonstrated in Fig. 3, the time-domain waveforms of the injected voltage at varying frequencies are presented. The solid line waveform denotes the actual waveform, while the dashed line waveform indicates the given waveform. It is observed that as the frequency of the injected voltage increases, the phase difference between the actual and given waveforms also rises.

The method proposed in this paper is capable of cancelling the phase difference caused by the delay of the digital system in the identification process. This is due to the fact that the delay of the digital system is not a factor in this process. The high-frequency quadrature voltage signal after considering the digital system delay can be expressed as follows:

$$\begin{cases} u'_{dh} = U_h\cos(\omega_h t + \varphi_e) \\ u'_{qh} = U_h\sin(\omega_h t + \varphi_e) \end{cases} \tag{6}$$

where, φ_e is the phase difference of the injected quadrature voltage signal caused by the sampling and control delay of the digital system.

When combined with (3), the estimated high-frequency response current of the motor in the rotating coordinate system is expressed as follows:

$$\begin{cases} i'_{dh} = \dfrac{U_h}{\omega_h}\left[A_{11}\sin(\omega_h t) + A_{12}\cos(\omega_h t)\right] \\ i'_{qh} = \dfrac{U_h}{\omega_h}\left[A_{21}\sin(\omega_h t) + A_{22}\cos(\omega_h t)\right] \end{cases} \tag{7}$$

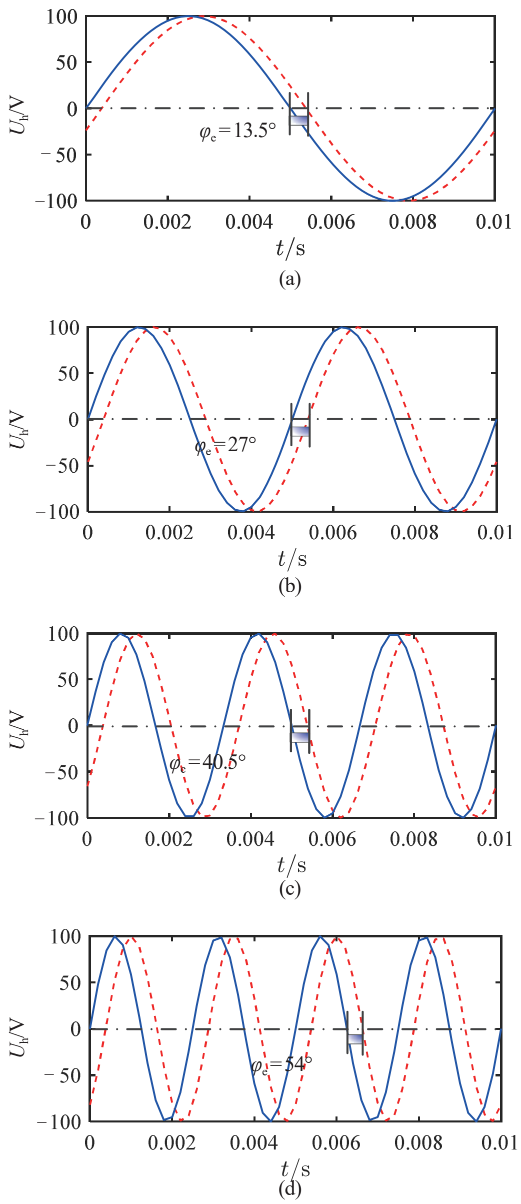

Fig. 3. Actual and given waveforms of injected voltage at different frequencies. (a) $|U_h| = 100$ V, $f_h = 100$ Hz. (b) $|U_h| = 100$ V, $f_h = 200$ Hz. (c) $|U_h| = 100$ V, $f_h = 300$ Hz. (d) $|U_h| = 100$ V, $f_h = 400$ Hz.

where,

$$\begin{cases} A_{11} = a_{11}\cos\varphi_e + a_{12}\sin\varphi_e \\ A_{12} = a_{11}\sin\varphi_e - a_{12}\cos\varphi_e \\ A_{21} = a_{21}\cos\varphi_e + a_{22}\sin\varphi_e \\ A_{22} = a_{21}\sin\varphi_e - a_{22}\cos\varphi_e \end{cases} \tag{8}$$

Meanwhile, (7) can be expressed as follows:

$$Y = \Phi^{\mathrm{T}} w \tag{9}$$

where,

$$Y = [\, i'_{dh} \;\; i'_{qh} \,]^{\mathrm{T}} \tag{10}$$

$$\Phi^{\mathrm{T}} = \begin{bmatrix} \frac{U_h}{\omega_h}\sin(\omega_h t) & \frac{U_h}{\omega_h}\cos(\omega_h t) \\ \frac{U_h}{\omega_h}\sin(\omega_h t) & \frac{U_h}{\omega_h}\cos(\omega_h t) \end{bmatrix} \tag{11}$$

$$w = \begin{bmatrix} A_{11} & A_{21} \\ A_{12} & A_{22} \end{bmatrix} \tag{12}$$

The coefficients A_{11}, A_{12}, A_{21} and A_{22} contain the inductance parameter and the initial position information of the rotor. The present paper adopts the recursive least squares method to determine the size of the coefficients as follows:

$$\begin{cases} K(k) = P(k-1)\Phi(k)\left[\lambda I + \Phi^{\mathrm{T}}(k)P(k-1)\Phi(k)\right]^{-1} \\ P(k) = \frac{1}{\lambda}\left[I - K(k)\Phi^{\mathrm{T}}(k)\right]P(k-1) \\ e(k) = Y(k) - \Phi^{\mathrm{T}}(k)w(k-1) \\ w(k) = w(k-1) + K(k)e(k) \end{cases} \tag{13}$$

Following the determination of the coefficients A_{11}, A_{12}, A_{21} and A_{22}, which contain the motor inductance parameter and the rotor initial position parameter. The following assumption is made:

$$\begin{cases} y_1 = A_{11} - A_{22} = m\cos\varphi_e \\ y_2 = A_{12} + A_{21} = m\sin\varphi_e \\ y_3 = A_{11} + A_{22} = n\cos(2\Delta\theta - \varphi_e) \\ y_4 = A_{12} - A_{21} = -n\sin(2\Delta\theta - \varphi_e) \\ x_1 = \sqrt{y_1^2 + y_2^2} = m \\ x_2 = \sqrt{y_3^2 + y_4^2} = n \end{cases} \tag{14}$$

where,

$$\begin{cases} m = \frac{L_d + L_q}{L_d L_q} \\ n = \frac{L_d - L_q}{L_d L_q} \end{cases} \tag{15}$$

Performing mathematical analysis and derivation of (14), it can be demonstrated that the phase difference φ_e, caused by the digital system delay, can be eliminated. Consequently, the calculation formula for the motor inductance parameter and the initial position of the rotor can be obtained as follows:

$$\begin{cases} L_d = \frac{2}{x_1 + x_2} \\ L_q = \frac{2}{x_1 - x_2} \\ \Delta\theta = \frac{1}{2}\arctan\left(\frac{-y_4}{y_3}\right) + \frac{1}{2}\arctan\left(\frac{y_2}{y_1}\right) \end{cases} \tag{16}$$

In the absence of knowledge regarding the polarity of the motor rotor, the rotor initial position $\Delta\theta$, as specified in (16),

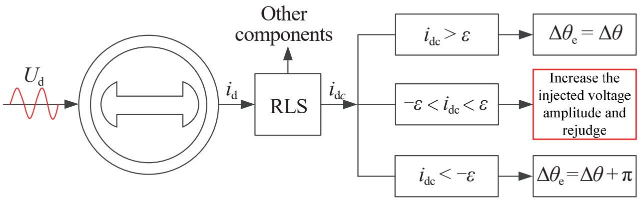

Fig. 4. Rotor polarity recognition strategy.

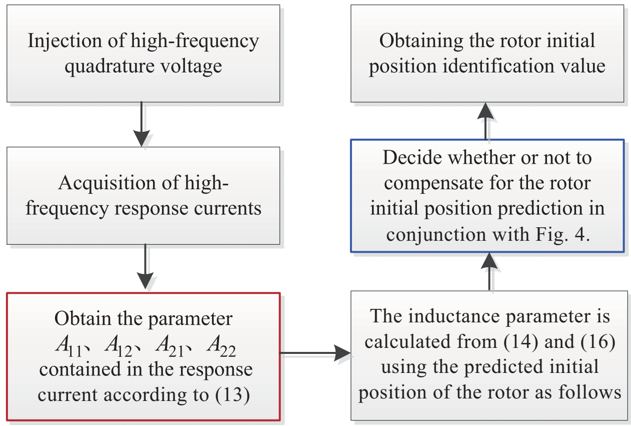

Fig. 5. Schematic flow diagram of the methodology of this paper.

may correspond to the actual rotor initial position $\Delta\theta_e$, or may be in a direction antithetical to the actual rotor initial position $\Delta\theta_e$. Consequently, this paper aims to ascertain whether the rotor initial position necessitates compensation, contingent on an assessment of the motor rotor's polarity. The present paper introduces a method of detecting the average value of the DC component of the response current to verify the polarity of the rotor, as proposed in [17]. According to the saturation characteristics of the inductor, the magnitude of the DC component of the response current is determined to establish whether or not it is necessary to compensate for the initial rotor position. The specific polarity identification strategy is shown in Fig. 4.

In order to circumvent the impact of uncontrollable factors on the rotor polarity judgement in the context of actual engineering applications, this paper proposes a comparison parameter ε. When the response current DC component i_{dc} exceeds ε, the calculated rotor initial position aligns with the actual rotor initial position, obviating the necessity for compensation. Conversely, when the response current DC component i_{dc} falls short of $-\varepsilon$, the The calculated value of the rotor initial position is reversed with the actual position, and then the initial position is compensated by 180°. When the response current DC component i_{dc} is between $-\varepsilon$ and ε, the saturation characteristic of the motor magnetic circuit is not obvious, which is easy to cause the error of judging the rotor polarity. In this case, it is necessary to increase the amplitude of the injected voltage and judge the rotor polarity again.

As illustrated in Fig. 5, the method described in this paper is represented by a schematic flow diagram.

IV. Impact of Inverter Nonlinearity on Identification Results

A. Inverter Non-Linear Analysis

In a real motor drive system, the deadband of the inverter and the voltage drop of the switching devices have the capacity to distort the high frequency quadrature voltage signal that has been injected. This phenomenon is known as the inverter's non-linearity.

Subsequently, the high-frequency injection voltage of the permanent magnet synchronous motor, considering the inverter nonlinearity, can be expressed as:

$$\begin{cases} u'_{dh} = U_h \cos(\omega_h t + \varphi_e) + D_d V_{dead} \\ u'_{qh} = U_h \sin(\omega_h t + \varphi_e) + D_q V_{dead} \end{cases} \tag{17}$$

where,

$$\begin{cases} D_d = \dfrac{4}{3}\cos(\mathrm{int}\left\{3(\theta_e + \gamma + \dfrac{\pi}{6})/\pi\right\}\dfrac{\pi}{3}) \\ D_q = \dfrac{4}{3}\sin(\mathrm{int}\left\{3(\theta_e + \gamma + \dfrac{\pi}{6})/\pi\right\}\dfrac{\pi}{3}) \end{cases} \tag{18}$$

$$V_{dead} = \frac{T_d + T_{ON} - T_{OFF}}{T_{pwm}}(V_{dc} - V_{sat} + V_f) + \frac{V_{sat} + V_f}{2} \tag{19}$$

In this system, the distortion coefficients of high-frequency quadrature voltage signal in the estimated rotating coordinate system are denoted by D_d and D_q. The electrical angle is indicated by θ_e, the current vector angle by γ, the dead time by T_d, the switching device turn-on and turn-off delays by T_{ON} and T_{OFF}, respectively, the switching period by T_{pwm}, the inverter DC voltage by V_{dc}, the voltage drop of the power supply switch by V_{sat} and the voltage drop of the switching device by V_f.

According to (17) and (18), the voltage deviation of the inverter due to its nonlinear characteristic is different when the rotor position is different. This change in voltage deviation will further change the amplitude of the high-frequency injected voltage, and the change in the amplitude of the high-frequency injected voltage will ultimately have an impact on the results of the identification of the inductor parameters with the initial position of the rotor. Fig. 6 provides a visual representation of the waveforms used to estimate the distortion coefficients in the rotating coordinate system. These waveforms are obtained by comparing the distortion coefficients with a given high-frequency injected voltage, which is used as a high-frequency fundamental noise reference.

B. Effect of Inverter Non-Linear on Parameter Identification Results

Combining (6) and (17) reveals that the voltage deviations caused by the inverter are $D_d V_{dead}$ and $D_q V_{dead}$. As illustrated in Fig. 6, this voltage deviation assumes the form of a square wave. According to the Fourier decomposition, the square wave can be expressed in the following:

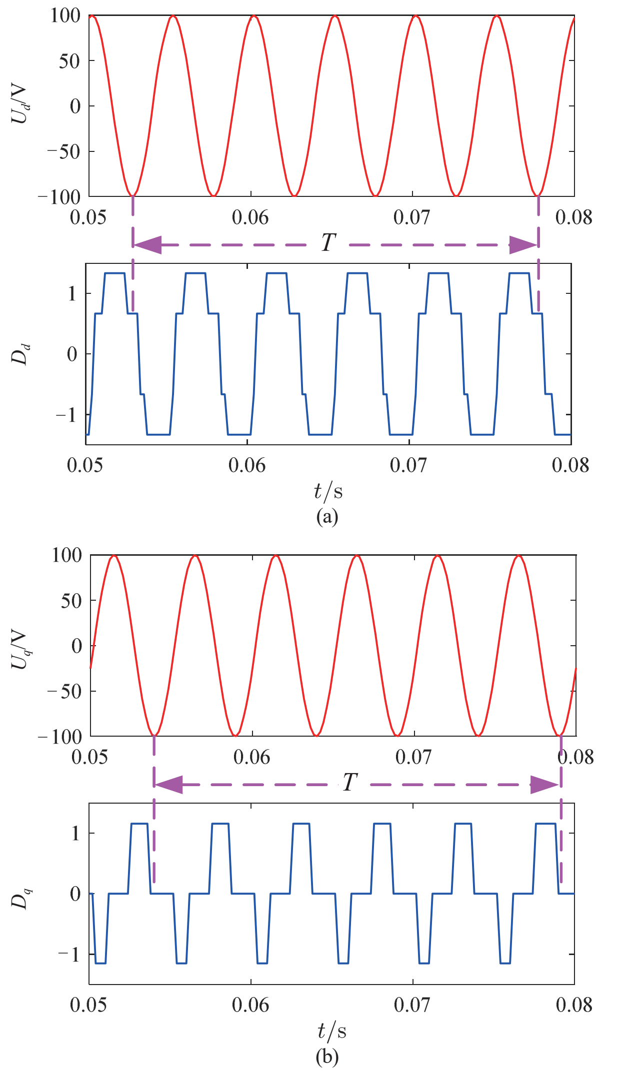

Fig. 6. Estimation of waveforms of distortion coefficients in a rotating coordinate system. (a) d-axis injection voltage and d-axis twist factor waveforms. (b) q-axis injection voltage and q-axis twist factor waveforms.

$$\begin{cases} D_d V_{\text{dead}} = a_0 + \sum\limits_{n=1}^{\infty} a_n \sin(n\omega_{\text{h}} t) + \sum\limits_{n=1}^{\infty} b_n \cos(n\omega_{\text{h}} t) \\ D_q V_{\text{dead}} = c_0 + \sum\limits_{n=1}^{\infty} c_n \sin(n\omega_{\text{h}} t) + \sum\limits_{n=1}^{\infty} d_n \cos(n\omega_{\text{h}} t) \end{cases} \tag{20}$$

As demonstrated in (7) to (16), the parameter identification process is confined to the high-frequency injected voltage sine and cosine fundamental components. That is to say, the parameters a_1, b_1, c_1 and d_1 in (20) have a significant impact on the outcomes of the parameter identification process. In order to obtain the values of a_1 , b_1 , c_1 and d_1 , a filter is first used to remove the high-frequency sine and cosine components of the voltage deviation. Then, the values of a_1 , b_1 , c_1 and d_1 are fitted using the recursive least squares method, and the fitting equations are as follows:

$$\begin{bmatrix} \Delta U_{d1} \\ \Delta U_{q1} \end{bmatrix} = \begin{bmatrix} 1 & \sin(\omega_{\text{h}} t) & \cos(\omega_{\text{h}} t) \\ 1 & \sin(\omega_{\text{h}} t) & \cos(\omega_{\text{h}} t) \end{bmatrix} \begin{bmatrix} a_0 & c_0 \\ a_1 & c_1 \\ b_1 & d_1 \end{bmatrix} \tag{21}$$

where, ΔU_{d1} and ΔU_{q1} are the voltage deviations with the high frequency sine and cosine components removed.

Subsequently, the high-frequency response current deviation resulting from this voltage deviation is as follows:

$$\begin{cases} \Delta i'_{d\text{h}} = \dfrac{U_{\text{h}}}{\omega_{\text{h}}} [\Delta A_{11} \sin(\omega_{\text{h}} t) + \Delta A_{12} \cos(\omega_{\text{h}} t)] \\ \Delta i'_{q\text{h}} = \dfrac{U_{\text{h}}}{\omega_{\text{h}}} [\Delta A_{21} \sin(\omega_{\text{h}} t) + \Delta A_{22} \cos(\omega_{\text{h}} t)] \end{cases} \tag{22}$$

where,

$$\begin{cases} \Delta A_{11} = (a_{11} b_1 + a_{12} d_1)/U_{\text{h}} \\ \Delta A_{12} = -(a_{11} a_1 + a_{12} c_1)/U_{\text{h}} \\ \Delta A_{21} = (a_{21} b_1 + a_{22} d_1)/U_{\text{h}} \\ \Delta A_{22} = -(a_{21} a_1 + a_{22} c_1)/U_{\text{h}} \end{cases} \tag{23}$$

The following equation is postulated:

$$\begin{cases} \Delta y_1 = \Delta A_{11} - \Delta A_{22} \\ \Delta y_2 = \Delta A_{12} + \Delta A_{21} \\ \Delta y_3 = \Delta A_{11} + \Delta A_{22} \\ \Delta y_4 = \Delta A_{12} - \Delta A_{21} \end{cases} \tag{24}$$

By combining (14), (16) and (24), the motor parameter identification equation that is independent of inverter nonlinearity can be introduced as follows:

$$\begin{cases} L'_d = \dfrac{2}{x'_1 + x'_2} \\ L'_q = \dfrac{2}{x'_1 - x'_2} \\ \Delta\theta' = \dfrac{1}{2}\arctan\left(\dfrac{-y_4 + \Delta y_4}{y_3 - \Delta y_3}\right) + \dfrac{1}{2}\arctan\left(\dfrac{y_2 - \Delta y_2}{y_1 - \Delta y_1}\right) \end{cases} \tag{25}$$

where,

$$\begin{cases} x'_1 = \sqrt{(y_1 - \Delta y_1)^2 + (y_2 - \Delta y_2)^2} \\ x'_2 = \sqrt{(y_3 - \Delta y_3)^2 + (y_4 - \Delta y_4)^2} \end{cases} \tag{26}$$

In this paper, (16) and (25) are utilised in the simulation to obtain the identification results of the motor parameters affected by the inverter nonlinearity and to remove the inverter nonlinearity, respectively. The deviations of these two equations are analysed under different dead times and different rotor positions. The d-axis inductance parameter is set to 3.1 mH and the q-axis inductance parameter is set to 6.8 mH, and the scalar values of the motor d-axis inductance parameter, q-axis inductance parameter and the rotor initial position deviation results are given in Figs. 7–9, respectively. As is apparent from Figs. 7–9, the identification error of the d-axis inductance parameter caused by the inverter nonlinearity is between 0.8% and 0.95%; the identification error of the q-axis inductance parameter is between 0.4% and 0.55%; and the identification error of the rotor initial position does not exceed 0.04°. The inverter nonlinearity

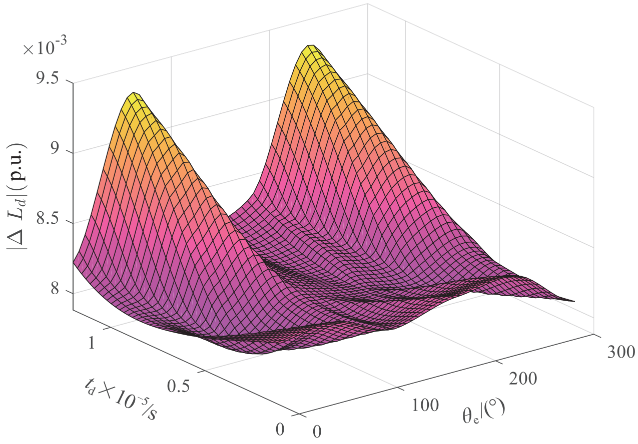

Fig. 7. *d*-axis inductor parameter identification deviation.

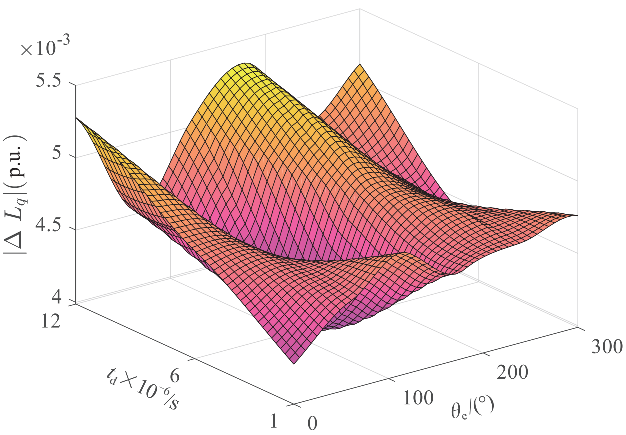

Fig. 8. *q*-axis inductance parameter identification deviation.

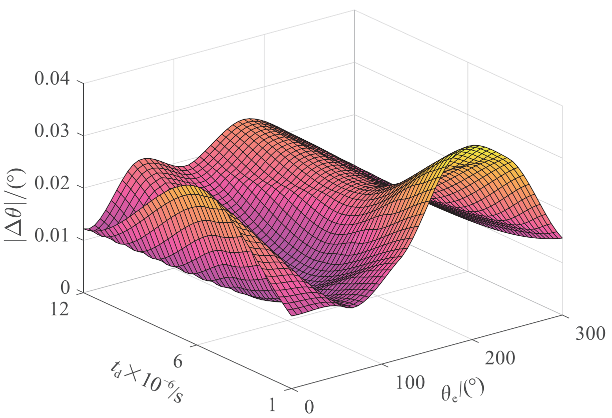

Fig. 9. Rotor initial position recognition deviation.

exerts a lesser influence on the motor parameter identification method proposed in this paper.

V. Simulation and Experimental Verification

A. Simulation Verification

In this paper, a proposed method of identifying the inductance parameter and rotor initial position of a permanent magnet synchronous motor is simulated and verified. The simulation model is constructed in MATLAB/Simulink according to the control block diagram in Fig. 10, and the relevant motor parameters during the simulation are presented in Table I.

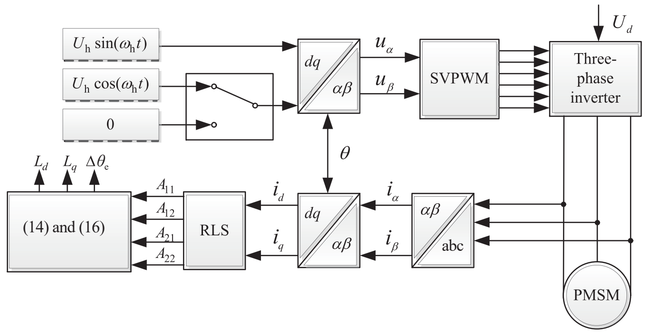

Fig. 10. Control strategy diagram.

TABLE I
Main Parameters of PMSM

Parameters	Value
Rated power	30 kW
Rated current	60 A
Stator resistance	0.05 Ω
Chain of permanent magnets	1.357 Wb
Moment of inertia (mechanics)	1 kg•m^2
d-axis inductance	3.1 mH
q-axis inductance	6.8 mH
Initial rotor position during simulation	0
Initial rotor position during experiment	180°
Sampling period	200×10^{-6} s
Polar logarithm	3

As illustrated in Fig. 11, the high-frequency injection voltage waveform and high-frequency response current waveform of the PMSM during simulation are shown, respectively. It is considered that the frequency of the high-frequency injection voltage should be set to 0.1−0.2 times the switching frequency. This is because if the frequency is set too high, it can easily generate other harmonic signals. However, if the frequency is set too low, it can easily separate from the fundamental signal. In this paper, the high-frequency injection voltage with an amplitude of 100 V and a frequency of 200 Hz is selected.

As illustrated in Fig. 12, the simulation results of the inductance parameters of the permanent magnet synchronous motor and the initial position of the rotor are presented. The parameter identification results converge within approximately 30 ms, with the identification results of the *d*-axis inductance and the *q*-axis inductance being 3.096 mH and 6.787 mH, respectively. The design value is only found in the error of 0.13% and 0.19%, respectively. It should be noted that the simulation of the motor model does not include saturation characteristics. Consequently, this paper does not include the simulation of motor rotor polarity

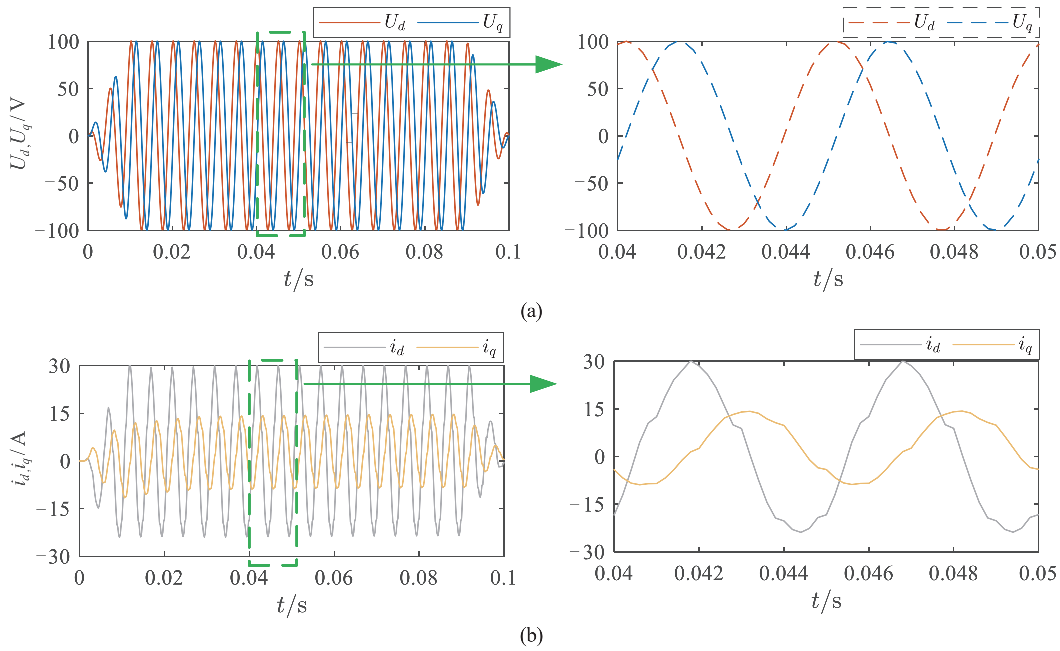

Fig. 11. High-frequency injection voltage and response current waveforms of PMSM during simulation. (a) High-frequency injection voltage waveform during simulation. (b) Response current waveform during simulation.

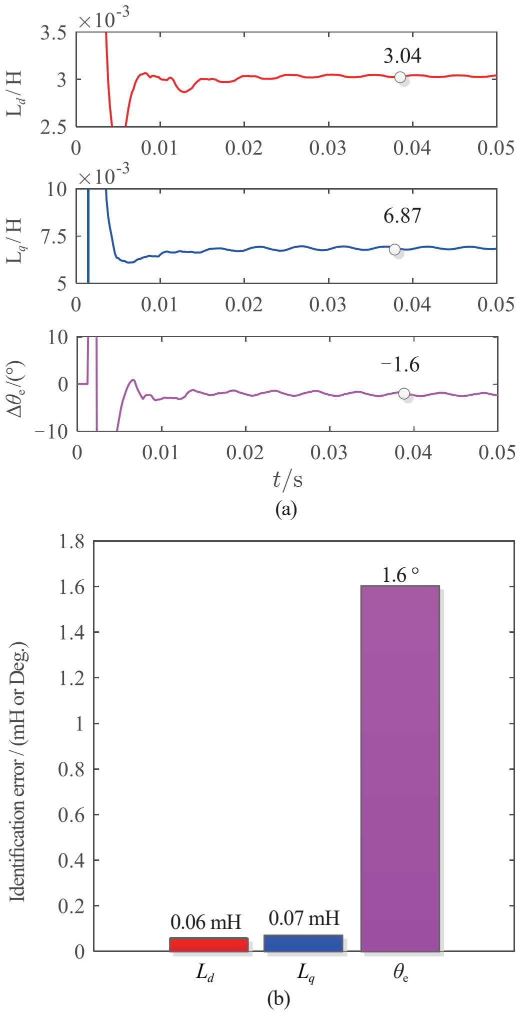

Fig. 12. Simulation identification results. (a) Simulation results. (b) Identification error.

identification, the default identification of the rotor initial position, and the actual rotor position in the same direction. However, in actual engineering applications, it is still necessary to carry out rotor polarity identification to determine the correctness of the rotor initial position identification results. This is demonstrated in 4.2 of the experimental demonstration. The identification results of the motor rotor initial position are −0.041°, and the simulation of the design value difference of 0.041°. The simulation results can better identify the motor parameters, and the identification results of the error are small.

Furthermore, the paper selects the motor parameters in Table I and applies the high-frequency pulse vibration injection method proposed in [12] and the high-frequency square wave injection method proposed in [15] to identify the motor parameters respectively. As the traditional high-frequency signal injection method is primarily used to identify the initial rotor position, this paper only focuses on the identification of the initial rotor position for comparative analysis. Fig. 13 illustrates the corresponding waveforms of the injected voltage and the identification results of the initial rotor position of the traditional method. As demonstrated in Fig. 13, the high-frequency pulsed voltage injection method requires approximately 70 milliseconds to complete the rotor initial position identification, yielding an identification error of 3.56°. In comparison, the high-frequency square-wave voltage injection method requires around 50 milliseconds to accomplish the same task, resulting in an identification error of 2.16°. A comparison of these two traditional methods with the method proposed in this paper clearly demonstrates the former's clear disadvantages in terms of rotor initial position identification, due to the fact that the proposed method is not only more accurate, but also faster.

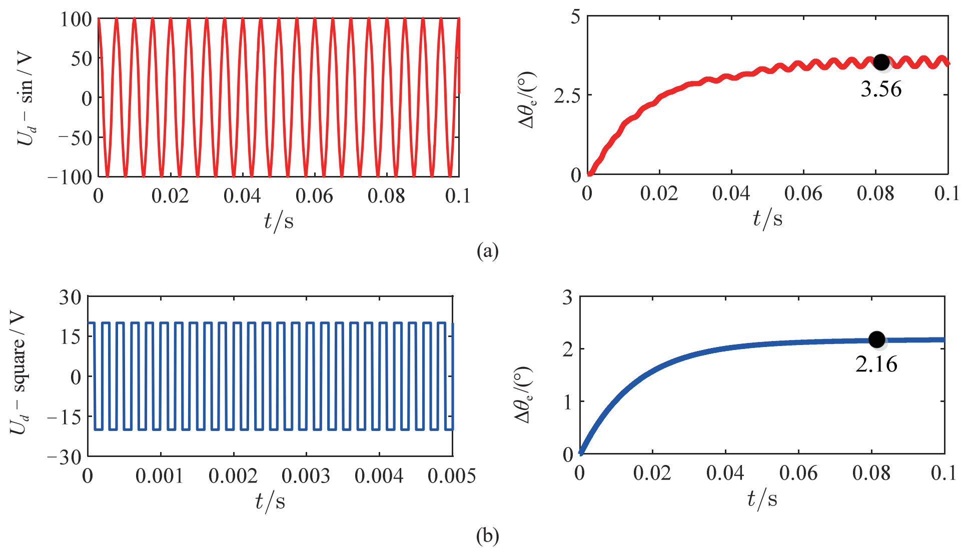

Fig. 13. Results of rotor initial position identification by conventional high-frequency injection method. (a) Localised map of PMSM rotor initial position identification results with injected signals based on high frequency pulsed vibration signal injection. (b) Localised map of PMSM rotor initial position identification results with injected signals based on high-frequency square-wave signal injection.

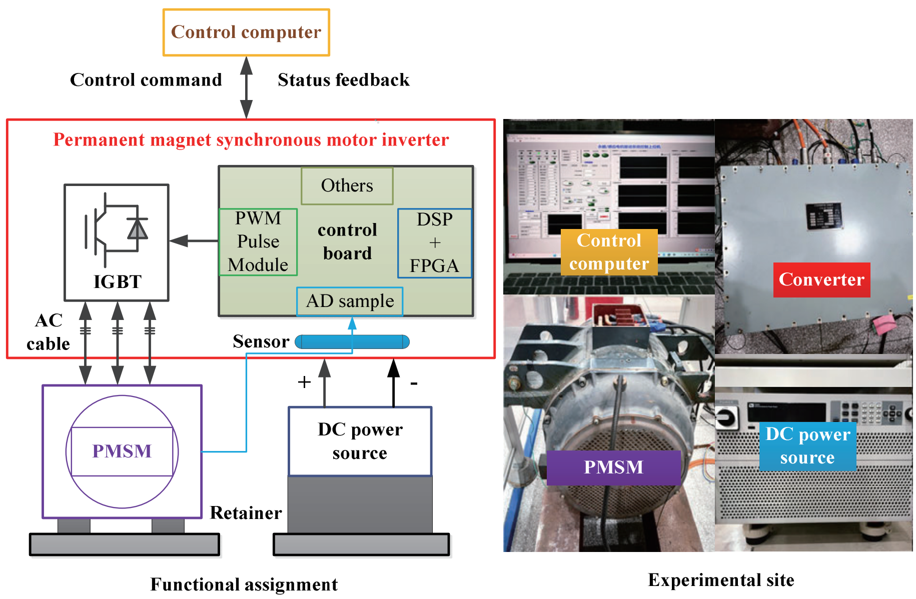

Fig. 14. Experimental platforms.

B. Experimental Verification

In this paper, the proposed method of identifying the inductance parameters and initial rotor position of permanent magnet synchronous motor is experimentally verified. The experimental platform is shown in Fig. 14, which mainly includes the power supply, inverter, permanent magnet synchronous motor and host computer, in which the inverter is a TMS320F28335 DSP and Cyclone IV FPGA as the core control chip. The parameters of the permanent magnet synchronous motor used in the experiment are shown in Table I. The DC side voltage is set to 500 V and the SVPWM switching frequency is 1 kHZ for the experiment.

In this experiment, $\hat{\theta}$ is assumed to be 0 at the moment 0, and a high-frequency quadrature voltage signal with an amplitude of 100 V and a frequency of 200 Hz is injected into the estimated rotating coordinate system of the PMSM. The computation of the inductance parameter and the estimated value of the rotor initial position is performed within the time frame of 0 to 0.1 s, while the rotor polarity identification and the correction of the estimated value of the rotor initial position is performed within the time frame of 0.1 to 0.16 s.

As illustrated in Fig. 15(a), the high-frequency injected voltage waveform of the PMSM during the experiment has been presented. In order to mitigate the impact effect on the motor when the quadrature voltage is injected, the amplitude change has been incorporated into the ramp function over a period of 0.01 s. Fig. 15(b) provides a representation of the high-frequency

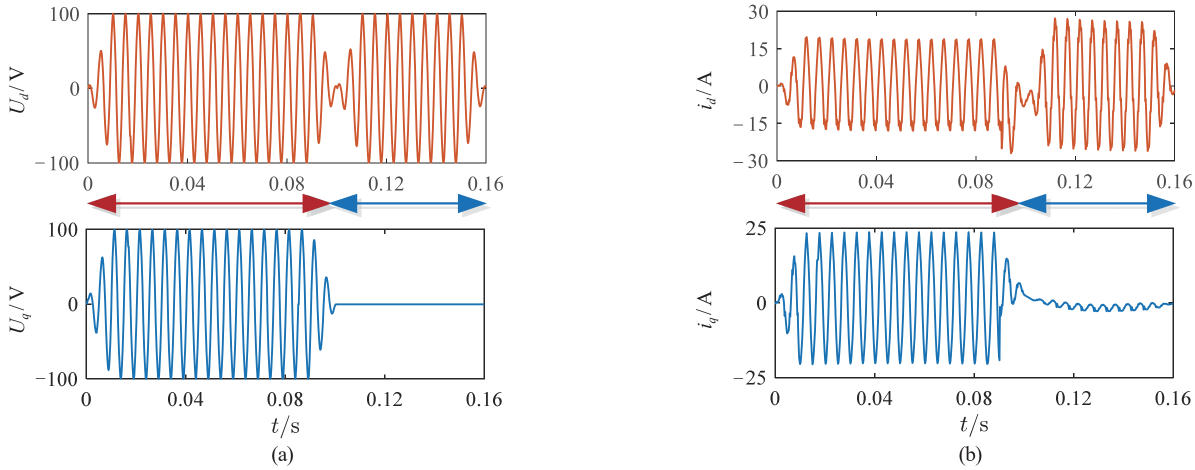

Fig. 15. High-frequency injection voltage and response current waveforms of PMSM during the experiment. (a) High frequency injection voltage wave form during experiment. (b) High frequency response current waveform during experiment.

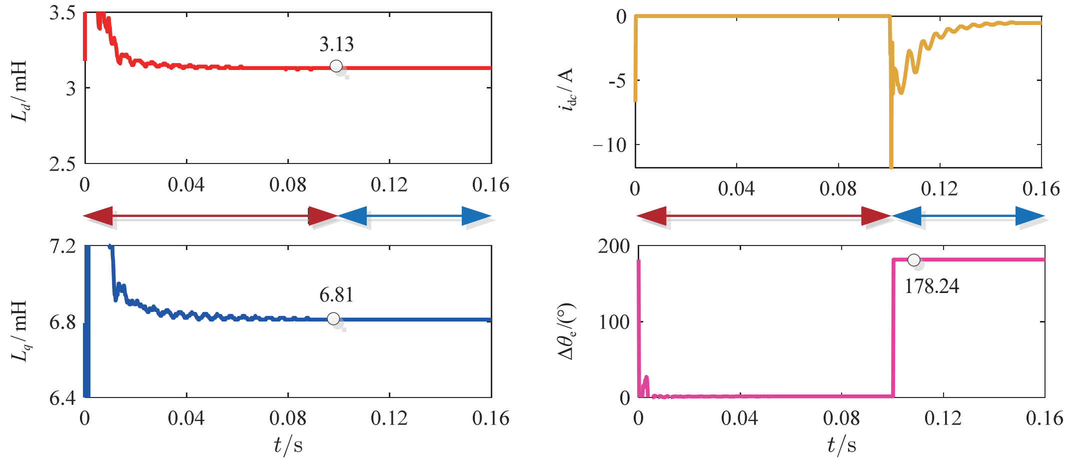

Fig. 16. Experimental identification results.

response current waveform of the PMSM.

As illustrated in Fig. 16, the results of identifying the DC component of the d-axis response current in the PMSM polarity identification stage are presented. The d-axis inductance, the q-axis inductance and the initial position of the rotor at the time of the experiment are used as the basis for these results. As demonstrated in the figure, the DC component is found to be negative. In accordance with the principle of polarity identification and compensation outlined in Fig. 4, it is evident that the calculated position of the rotor is opposite to its actual position at this time. The identification results of the d-axis inductance and the q-axis inductance have an error of 0.97% and 0.15%, respectively, compared with the design values of the PMSM in Table I. The initial rotor position of the motor used in the experiment is 180°, and the initial rotor position identified in this paper is 178.24°, which is close to each other. In summary, the identification results of this paper are accurate, and can complete the identification of inductance parameters in approximately 50 ms, and complete the identification of rotor initial position parameters in 160 ms.

In addition to the foregoing, a series of experiments were conducted in which the amplitude and frequency of the high-frequency injection voltage were varied. The inductance parameter specification obtained from these experiments is shown in Fig.17(a), while the deviation value of the rotor initial position recognition results is shown in Fig.17(b). It is evident from the data that, for a constant injection frequency, an increase in the amplitude of the selected injection voltage results in a reduction of the error between the identification results and the motor design values. Furthermore, it is evident that an enhancement in the high-frequency response current of the motor leads to a reduction in the parameter identification error and more accurate identification results.

VI. Conclusion

The control performance of permanent magnet synchronous motors (PMSM) is contingent upon the precise measurement of inductance parameters and the determination of the rotor's initial position. In this paper, a static identification method for the inductance parameters and rotor initial position of a permanent magnet synchronous motor is proposed. The proposed methodology involves the injection of high-frequency quadrature voltage signals into the motor, followed by the utilisation

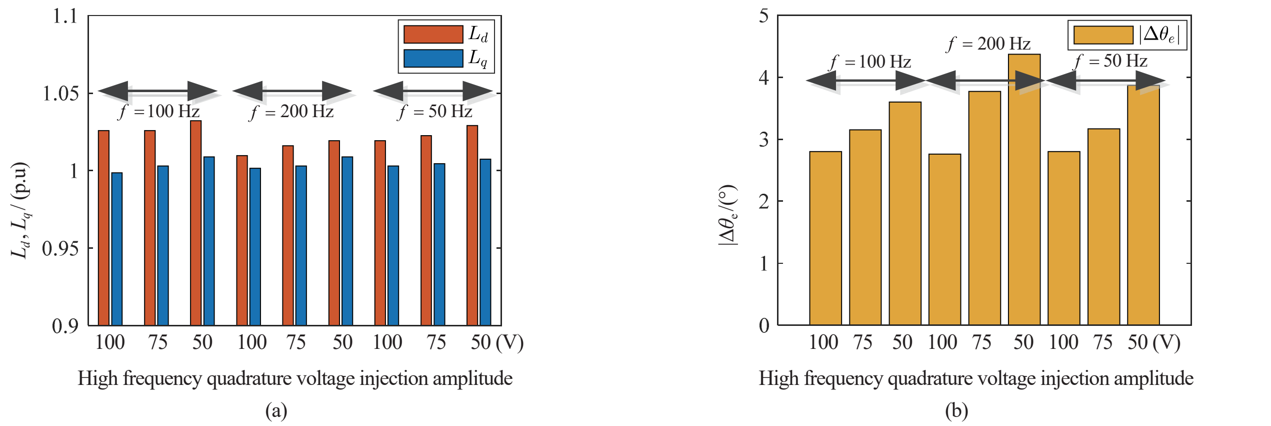

Fig. 17. Identification results for different injection voltages. (a) The process of inductive identification invariably results in the identification of the youngest valus. (b) The result of the identification of the initial position of the rotor exhibits a deviation value.

of the recursive least squares method for the decomposition of the high-frequency response currents of the motor. This process enables the estimation of the motor's inductance parameters and the initial rotor position. Subsequently, the estimated value of the initial rotor position is corrected in accordance with the saturation characteristics of the inductance. In comparison with the traditional method, the novel approach has the capacity to offset the phase difference caused by the sampling and control delay of the digital system. Furthermore, there is no necessity to utilise a filter for demodulation, which effectively avoids the signal delay and distortion caused by the filter. Additionally, it is less affected by the nonlinearity of the inverter.

In response to the research conducted in this paper, future endeavours will primarily encompass the reduction of the time required for the identification of the inductor parameters and the initial position of the rotor, as well as the compensation method for the inverter nonlinearity in the identification.

References

[1] K. Huang, J. Zhou, S. Liu, and S. Huang,"Inductance identification method of permanent magnet synchronous motor considering inverter nonlinearity based on high-frequency injection," in *Transactions of China Electrotechnical Society*, vol. 36, no. 8, pp. 1607–1616, 2021.

[2] J. Zhang, F. Peng, Y. Huang, Y. Hao, and Z. Zhu, "Online inductance identification using PWM current ripple for position sensorless drive of high-speed surface-mounted permanent magnet synchronous machines," in *IEEE Transactions on Industrial Electronics*, vol. 69, no. 12, pp. 12426–12436, Dec. 2022.

[3] Z. Ma, W. Zhang, J. He, and H. Jin, "Multi-parameter online identification of permanent magnet synchronous motor based on dynamic forgetting factor recursive least squares," in *Proceedings of 2022 IEEE 5th International Electrical and Energy Conference (CIEEC)*, 2022, pp. 4865–4870.

[4] C. Y. Jia, X. D. Wang, and K. Zhou, "Predictive control of built-in permanent magnet synchronous motor current model based on inductance identification," in *Journal of Electrical Machines and Control*, vol. 25, no. 11, pp. 75–82, 2021.

[5] Y. Zhang, Y. Bi, and S. Wang, "Parameter identification of permanent magnet synchronous motor based on extended Kalman filter and Gradient correction," in *Proceedings of 2020 IEEE International Conference on Mechatronics and Automation (ICMA)*, 2020, pp. 718–722.

[6] T. Hu, J. Liu, J. Cao, and L. Li, "On-line parameter identification of permanent magnet synchronous motor based on extended Kalman filter," in *Proceedings of 2022 25th International Conference on Electrical Machines and Systems (ICEMS)*, 2022, pp.1–6.

[7] H. Li and X. Jian, "Parameter identification of permanent magnet synchronous motor based on CGCRAO algorithm," in *IEEE Access*, vol. 11, pp. 124319–124330, 2023.

[8] C. Lian, F. Xiao, S. Gao, and J. Long, "Parameter identification for interior permanent magnet synchronous motor based on experimental calibration and stochastic approximation theory with two time scales," in *Proceedings of the CSEE*, vol. 39, no. 16, pp. 4892–4898, 4991, 2019.

[9] J. Liu, F. Xiao, Y. Shen, Z. Mai, and C. Li, "Position-sensorless control technology of permanent-magnet synchronous motor-a review," in *Transactions of China Electrotechnical Society*, vol. 32, no. 16, pp. 76–88, 2017.

[10] J. Yang, S. Yang, H. Li, and X. Zhang, "Initial rotor position estimation for IPMSM based on high frequency rotating voltage injection," in *Transactions of China Electrotechnical Society*, vol. 33, no. 15, pp. 3547–3555, 2018.

[11] A. Yu, L. Liu, Z. Kan, and C. Zhang, "Initial position identification of PMSM with filterless high frequency pulse signal injection method," in *Transactions of China Electrotechnical Society*, vol. 36, no. 4, pp. 801–809, 2021.

[12] Z. Mai, F. Xiao, K. Fu, J. Liu, C. Lian, K. Li, and W. Zhang, "HF pulsating carrier voltage injection method based on improved position error signal extraction strategy for PMSM position sensorless control," in *IEEE Transactions on Power Electronics*, vol. 36, no. 8, pp. 9348–9360, Aug. 2021.

[13] W. Li, J. Liu, and S. Chen, "Permanent magnet synchronous motor rotor position detection method based on high-frequency square-wave signal injection," in *Transactions of China Electrotechnical Society*, vol. 33, no. 24, pp. 5821–5829, 2018.

[14] C. Li, G. Wang, G. Zhang, N. Zhao, and D. Xu, "Adaptive pseudorandom high-frequency square-wave voltage injection based sensorless control for SynRM drives," in *IEEE Transactions on Power Electronics*, vol. 36, no. 3, pp. 3200–3210, Mar. 2021.

[15] K. Yu and Z. Wang, "Position sensorless control of IPMSM using adjustable frequency setting square-wave voltage injection," in *IEEE Transactions on Power Electronics*, vol. 37, no. 11, pp. 12973–12979, Nov. 2022.

[16] M. Sun, Y. He, X. Qiu, T. Tao, and W. Zhang, "Random frequency triangular wave injection based sensorless control of PMSM drives for audible noise reduction," in *Transactions of China Electrotechnical Society*, vol. 38, no. 6, pp. 1460–1471, 2023.

[17] B. Liu, "Research on rotor position detection technology of permanent magnet synchronous motor based on pulse high-frequency signal injection," Ph.D. dissertation, Dept. Elect. Eng., Nanjing University of Aeronautics and Astronautics, Nanjing, China, 2018.

Liyuan Guo was born in Shanxi, China, in 1999. He received the B.S. degree in electrical engineering from Shanxi University, Taiyuan, China, in 2022. He is currently working toward the M.S. degree with the National Key Laboratory of Electromagnetic Energy, Naval University of Engineering, Wuhan, China. His current research area is high-performance control of permanent magnet synchronous motors.

Chuanqiang Lian received the B.S. degree in automation from the Department of Automation, Tsinghua University, Beijing, China, in 2008, and the M.S. and Ph.D. degrees from the College of Mechatronic Engineering and Automation (CMA), National University of Defense Technology (NUDT), Changsha, China, in 2010 and 2016, respectively. He is currently an Associate Professor with the National Key Laboratory of Electromagnetic Energy, Naval University of Engineering, Wuhan, China. He has co-authored over twenty papers in international journals and conferences. His current research interests include AC motor control and flywheel energy storage.

Guanda Xu was born in Jiangxi, China, in 1998. He received the B.S. degree in electrical engineering from Zhejiang University, Hangzhou, China, in 2019, and the M.S. degree from the Naval University of Engineering, Wuhan, China, in 2021. He is currently working toward the Ph.D. degree with the National Key Laboratory of Electromagnetic Energy, Naval University of Engineering, Wuhan, China. His research interests include position and current sensorless control of AC motors and electric vehicle drives.

Jilong Liu was born in Hebei, China, in 1988. He received the B.S. and Ph.D. degrees in electrical engineering from the School of Electrical Engineering, Xi'an Jiaotong University, Xi'an, China, in 2010 and 2015, respectively. From 2015 to 2017, he was a Lecturer with the National Key Laboratory of Electromagnetic Energy, Naval University of Engineering, Wuhan, China, where he was promoted to an Associate Professor in 2017, and to a Full Professor in 2022. His current research interests include modular multilevel converter and AC motor control.

Tang Xin was born in Sichuan, China, in 1989. He received the B.S. degree in mechanical engineering from Jilin University, China, in 2011; the M.S. and Ph.D. degrees in mechatronics engineering from the National University of Defense Technology, China, in 2014 and 2018, respectively. He is currently a lecturer at the Naval University of Engineering, Wuhan, China. His research interests mainly include condition monitoring, fault diagnosis and related AI modeling methods of power electronic devices.

Kun Wang was born in 1985, holds a master's degree in electrical engineering. He is currently a lecturer at the Naval University of Engineering, Wuhan, China.

Simulation and Analysis of Core Losses Under High-Frequency PWM Wave Voltage Excitations

Zhikang FU, Jinghui WANG, Juntao XIAO, and Wei CHEN

Abstract—**The core losses quantification of magnetic components with geometrically diverse cores for power converters remains a challenge and an area of active research. By using finite element analysis software Ansys Maxwell, a simulation method for core losses calculation under PWM voltage excitation is proposed based on the modified Steinmetz equation (MSE) in this paper. The magnetic properties measurement and model of core material are specified, which are basis of core losses simulation. Furthermore, the work conducts a comprehensive error analysis to identify primary sources of simulation inaccuracies, accompanied by targeted mitigation strategies. To validate the methodology, core losses of a ferrite EE shaped core are simulated and subsequently compared with experimental measurements acquired through the DC power method. The close agreement between simulated and empirical results demonstrates the efficacy of the proposed methodology.**

Index Terms—**Core loss model, core losses simulation, DC power method, finite element analysis, PWM wave excitation.**

I. Introduction

MAGNETIC components are important passive component in power converters, and their losses are important indicators for the optimal design of power converters. The losses of magnetic component include winding loss and core losses. The winding loss which is of a linear nature can be accurately obtained by using an impedance analyzer or finite element software when the winding's material is solid conductor. However, the accurate quantification of Litz wire winding losses remains a difficult problem [1]–[2]. The core losses are of a nonlinear nature and are affected by numerous factors. Not only do the excitation voltage waveform, frequency, amplitude, as well as the working environment and temperature affect the core losses, but also the core material, core shape and size have an impact on the core losses. As the frequency, efficiency and power density of power converters are getting higher and higher [3]–[4], the shapes of cores are becoming more and more diverse. The error will be very large if we only use the mathematical model of core losses to predict the core losses of cores with various shapes. Although the losses of magnetic components can be obtained through measurement, it is extremely unrealistic and uneconomical to measure the losses of each designed product after prototyping to verify whether it meets the design requirements [5]–[6].

Finite element analysis (FEA) is a numerical analysis method for analyzing the magnetic flux density distribution of irregular cores. In the industry, it tends to be used to obtain the core losses of magnetic components with different core shapes. Ansys Maxwell is the most commonly used FEA simulation software in the industry. Based on the accurate calculation of the magnetic flux density distribution within the core, the core losses prediction models which come with software are utilized to obtain the core losses of magnetic components. There are three types of core losses prediction models built into the software: the Steinmetz equation (SE) model, the loss separation model and the P_{cv}-B_m curve. The SE model is only applicable to the core losses calculation under sinusoidal excitation. Based on the core losses under sinusoidal excitation, the loss separation model divides the core losses into hysteresis loss, classical eddy current loss and excess eddy loss according to the physical mechanism of core losses[7], [8]–[9] proposed an improved loss separation model, and extended it to core losses calculation under non-sinusoidal excitation. The P_{cv}-B_m curve is directly the numerical relationship between the core losses density P_{cv} and the peak value of the magnetic flux density B_m. However, the P_{cv}-B_m relationship curves for different excitation frequencies are different, so it is only applicable to the core losses simulation at a single frequency. Finite element (FE) software is used to obtain the core losses of cores with different structures, which is beneficial to enterprises to reducing research and development costs. However, the core losses simulation methods of existing software are not applicable to core losses calculation of magnetic components in power converters.

Accurate core losses measurement is the basis of core losses simulation and also the means of verifying the core losses simulation accuracy. The existing core losses measurement methods are mainly divided into non-electrical methods and electrical methods. Calorimeter method is recognized as the most accurate non-electrical measurement method for core losses. However, it is complicated to operate, time-consuming

Manuscript received January 04, 2025; revised February 19, 2025; accepted March 14, 2025. Date of publication June 30, 2025; date of current version April 18, 2025. This work was supported in part by National Natural Science Foundation of China under the grant 51777036. *(Corresponding author: Jinghui Wang.)*

Z. Fu, J. Wang, and W. Chen are with the College of Electrical Engineering and Automation, Fuzhou University, Fuzhou 350108, China (e-mail: 417423447@qq.com; wjh@fzu.edu.cn; chw@fzu.edu.cn).

J. Xiao is with the Delta Electronics Shanghai Co., Ltd., Shanghai 201209, China (e-mail: 645138025@qq.com).

Digital Object Identifier 10.24295/CPSSTPEA.2025.00014

and has strict environmental requirements [10]–[11]. Electrical methods mainly include the Two-Winding AC power method and the DC power method. Regarding the Two-Winding AC power method, the voltage on the sensing winding and the current on the excitation winding of the magnetic component are sampled, and the core losses can be obtained by calculating the average value of the product of the two. When the impedance angle of the tested component is close to 90°, a tiny phase-difference error will lead to a very large measurement error [12]–[13]. [13] utilizes reactive power compensation to reduce the phase difference between the sampled voltage and current so as to improve the measurement accuracy of the Two-Winding AC power method. Regarding the DC power method, an inverter circuit is used to convert the DC voltage into a high-frequency PWM wave and apply it to the magnetic component. The output power of the DC voltage is measured to obtain the losses of the magnetic component, which effectively circumvents the problem that the measurement error of the Two-Winding AC power method is sensitive to the phase difference error. The loss of the inverter circuit is the main error source of the DC power method. An air-core inductor is used for calibration to verify the losses of the inverter circuit so as to improve the measurement accuracy of the DC power method [14]. The differential DC power method is proposed to broaden the inductance range of the tested components based on the DC power method [15].

In this paper, based on the modified Steinmetz equation (MSE), a simulation scheme for the core losses of magnetic components under high-frequency PWM wave voltage excitation by using the FE software Ansys Maxwell is proposed. The sources of calculation errors are analyzed in detail and corresponding solutions are put forward. Finally, based on the accurate measurement and models of the magnetic properties of core materials, the core losses of EE-shaped cores made of the same material are simulated and analyzed by utilizing the proposed simulation scheme. The simulation results are compared with the measured values of core losses to verify the feasibility and accuracy of the simulation scheme.

II. Simulation Scheme for Core Losses under High-Frequency PWM Wave Excitation

There are two key factors in the core losses calculation of magnetic components using the FE software Ansys Maxwell: 1) The mathematical prediction model of core losses density and magnetic flux density. The core losses are closely related to magnetic flux density, and an accurate mathematical model of core losses density is a guarantee for the core losses simulation of magnetic components. 2) The determination of the magnetic-flux-density distribution inside the core. FEA is to solve the Poisson equation or Laplace equation with known field-domain boundary conditions to obtain the magnetic vector potential. The curl of the magnetic vector potential is the magnetic-flux density. Among them, the permeability of the core-material is essential. Therefore, the accurate acquisition of the magnetization characteristics of the core material is the basis for the FE simulation of core losses.

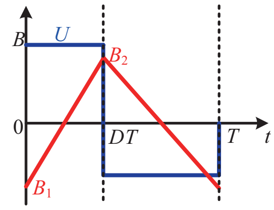

Fig. 1. Flux density waveform under PWM voltage excitation.

A. High-Frequency PWM Core Losses Mathematical Model

The Steinmetz equation is often used for the core losses calculation of magnetic components under sinusoidal excitation. [16] proposed an MSE for the core losses calculation of magnetic components under arbitrary waveform excitation. The weighted average magnetic flux density change rate B_w is introduced, as shown in (1).

$$B_{\mathrm{w}} = \frac{1}{2B_{\mathrm{m}}}\int_T \left(\frac{\mathrm{d}B}{\mathrm{d}t}\right)^2 \mathrm{d}t \tag{1}$$

The equivalent sinusoidal wave frequency $f_{\mathrm{sin\_eq}}$ of an arbitrary waveform is obtained according to the equality of B_w for arbitrary-waveform excitation and sinusoidal-waveform excitation, as shown in (2).

$$f_{\mathrm{sin\_eq}} = \frac{2}{\Delta B^2 \cdot \pi^2} \cdot \int_T \left(\frac{\mathrm{d}B}{\mathrm{d}t}\right)^2 \mathrm{d}t \tag{2}$$

The core losses density under arbitrary waveform excitation $P_{\mathrm{cv\_arb}}$ can be obtained by using the core losses density under sinusoidal waveform excitation with a frequency of $f_{\mathrm{sin\_eq}}$, as shown in (3).

$$P_{\mathrm{cv\_arb}} = (k \cdot f_{\mathrm{sin\_eq}}^{\alpha-1} \cdot B_{\mathrm{m}}^{\beta}) \cdot f_{\mathrm{s}} \tag{3}$$

where B_m is the peak value of AC magnetic flux density, k, α, and β are SE parameters of $f_{\mathrm{sin\_eq}}$, ΔB is the peak-to-peak value of the magnetic flux density, f_s is the excitation frequency of the arbitrary waveform.

The voltage excitation waveform and the magnetic flux density waveform of the PWM wave with a duty cycle of D and a frequency of f_s are shown in Fig. 1, and the magnetic flux density $B(t)$ is shown in (4).

$$B(t) = \begin{cases} B_1 + \dfrac{B_2 - B_1}{D} \cdot f_{\mathrm{s}} \cdot t & 0 \leqslant t \leqslant DT \\ B_2 - \dfrac{B_2 - B_1}{(1-D)} \cdot f_{\mathrm{s}} \cdot (t - DT) & DT \leqslant t \leqslant T \end{cases} \tag{4}$$

The core losses density $P_{\mathrm{cv\_PWM}}$ under PWM wave voltage excitation can be obtained by combining (2), (3) and (4), as shown in (5).

$$P_{\mathrm{cv\_PWM}} = \left(\frac{\pi^2 \cdot D \cdot (1-D)}{2}\right) \cdot k \cdot f_{\mathrm{sin\_eq}}^{\alpha} \cdot B_{\mathrm{m}}^{\beta} \tag{5}$$

The sinusoidal wave voltage excitation with frequency f_s is applied to the magnetic component, and the SE is used for the core losses calculation. Then, the PWM wave voltage excitation with a frequency f_s is applied to the magnetic component, and the MSE is used for its core losses calculation. When the peak values of the magnetic flux densities of the two are equal, the ratio of the core losses densities P_{cv_PWM}/P_{cv_sin} is shown in (6).

$$\frac{P_{cv\_PWM}}{P_{cv\_sin}} = \frac{(k \cdot f_{sin\_eq}^{\alpha-1} \cdot B_m^{\beta}) \cdot f_s}{k \cdot f_s^{\alpha} \cdot B_m^{\beta}} = (\frac{f_{sin\_eq}}{f_s})^{\alpha-1} \tag{6}$$

where P_{cv_sin} is the core losses density under sinusoidal wave voltage excitation, as shown in (7).

$$P_{cv\_sin} = k \cdot f_s^{\alpha} \cdot B_m^{\beta} \tag{7}$$

Thus the core losses density P_{cv_PWM} under PWM wave voltage excitation is shown in (8).

$$\begin{cases} P_{cv\_PWM} = \gamma \cdot k \cdot f_s^{\alpha} \cdot B_m^{\beta} = \gamma \cdot P_{cv\_sin} \\ \gamma = (\dfrac{2}{\pi^2 D(1-D)})^{\alpha-1} \\ k' = (\dfrac{2}{\pi^2 D(1-D)})^{\alpha-1} \cdot k \end{cases} \tag{8}$$

It can be derived from (8) that the ratio of the core losses under PWM wave excitation to that under sinusoidal wave excitation is a coefficient related to the duty cycle and the coefficient α when the excitation frequency and the peak value of the magnetic flux density are equal. Therefore, based on the core losses under sinusoidal wave excitation, the core losses under PWM wave voltage excitation can be simulated and calculated by using the eddy current field solver or the transient field solver of Maxwell software.

B. Simulation Process for Core Losses under High-Frequency PWM Wave Excitation

The flow chart of simulation scheme for core losses under high-frequency PWM voltage excitation is shown in Fig. 2. After establishing the simulation physical model, the modified Steinmetz parameters k', α, β and, the AC magnetization curve are assigned to the core material, and the copper material is assigned to the winding. Either the transient field solver or the eddy current field solver can be selected.

If the transient field solver is chosen, the PWM wave voltage excitation is applied to the magnetic component, and the magnetic flux density distribution inside the core is obtained. The core losses density distribution inside the core is calculated by using the field calculator. Finally, the core losses of the magnetic component can be obtained by integrating the core losses density with the core volume.

If the eddy current field solver is chosen, the sinusoidal wave voltage excitation is applied to the magnetic component.

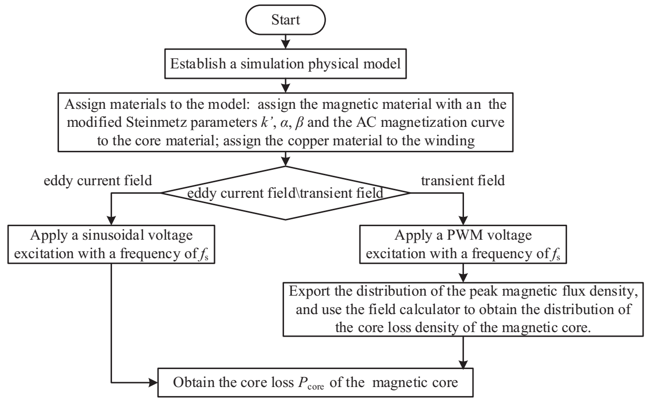

Fig. 2. Flow chart of core losses simulation for high-frequency PWM voltage excitation.

Then, the distribution of magnetic flux density peak inside the core can be directly obtained, and thus the core losses of magnetic components can be directly obtained. However, the sinusoidal wave voltage excitation can only be applied in the eddy current field solver. Therefore, it is necessary to determine the corresponding relationship between the sinusoidal-wave excitation voltage amplitude and the PWM excitation voltage amplitude, in order to ensure that the magnetic flux density amplitude of the two excitations is equal.

The relationships of the sinusoidal wave voltage amplitude U_{m_sin}, the peak-to-peak value of the PWM-wave voltage U_{pp_PWM} and the peak value of the magnetic flux density are shown in (9).

$$\begin{cases} U_{m\_sin} = 2 \cdot \pi \cdot f_s \cdot N \cdot A_e \cdot B_{m\_sin} \\ U_{pp\_PWM} = \dfrac{2 \cdot f_s \cdot N \cdot A_e}{D \cdot (1-D)} \cdot B_{m\_PWM} \end{cases} \tag{9}$$

If the core and winding turns of the magnetic component are the same, and the excitation frequency and the peak value of the magnetic flux density are also the same, the relationship between U_{m_sin} and U_{pp_PWM} is shown in (10).

$$\frac{U_{m\_sin}}{U_{pp\_PWM}} = \pi \cdot D \cdot (1-D) \tag{10}$$

C. Measurement of Magnetic Properties of Core Materials

As can be seen from Fig. 2, the accurate measurement of the magnetic properties of core material is the basis for the FE analysis and calculation of the core losses of magnetic components. This includes the measurement of the AC magnetization curve and the core losses under sinusoidal wave excitation.

In general, a magnetic ring with a relatively small ratio of outer diameter to inner diameter is used as the device under test (DUT) to obtain the magnetic properties of core material. In this paper, ferrite (TPG33B) is taken as the research object, and the ferrite T22 magnetic ring is employed to acquire the magnetic properties of core material. Its dimensional parameters are presented in Table I, and the effective

TABLE I
SIZE PARAMETERS OF FERRITE (TPG33B) T22 STANDARD MAGNETIC RING

parameter	value	parameter	value
OD (mm)	21.99	A_e (mm^2)	40.02
ID (mm)	14.05	V_e (mm^3)	2265.5
h (mm)	10.08	N (number of turns)	6
l_e (mm)	56	L (μH)	112.7

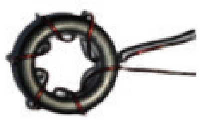

Fig. 3. Ferrite (TPG33B) T22 magnetic ring.

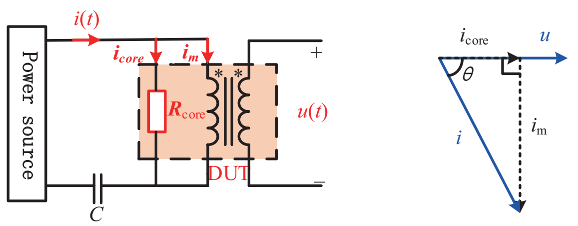

(a) (b)

Fig. 4. Schematic diagram of the measurement principle of the large-signal AC method. (a) Equivalent circuit diagram. (b) Current and voltage vector diagram.

parameters A_e, l_e, and V_e are calculated with (11), and the specimen under test is shown in Fig. 3.

$$\begin{cases} A_e = \dfrac{(OD-ID)\cdot h}{2} \\ l_e = \dfrac{\pi\cdot(OD-ID)}{\ln(OD/ID)} \\ V_e = \pi\cdot h\cdot\left[\left(\dfrac{OD}{2}\right)^2-\left(\dfrac{ID}{2}\right)^2\right] \end{cases} \tag{11}$$

The large-signal AC method is usually used to measure the AC magnetization curve and core losses under sinusoidal wave excitation. The measurement principle is shown in Fig. 4. In the figure, the capacitor C is a DC-blocking capacitor. The DUT is wound with a double-winding. A large-signal AC excitation is applied to the DUT. The induced voltage $u(t)$ of the secondary side and the exciting current $i(t)$ of the primary side of DUT are sampled. According to Faraday's law of electromagnetic induction and Ampere's circuital law, the magnetic flux density $B(t)$ and the magnetic field intensity $H(t)$ are shown in (12).

$$\begin{cases} B(t) = \dfrac{1}{N\cdot A_e}\displaystyle\int_0^t u(t)\mathrm{d}t \\ H(t) = \dfrac{N\cdot i(t)}{l_e} \end{cases} \tag{12}$$

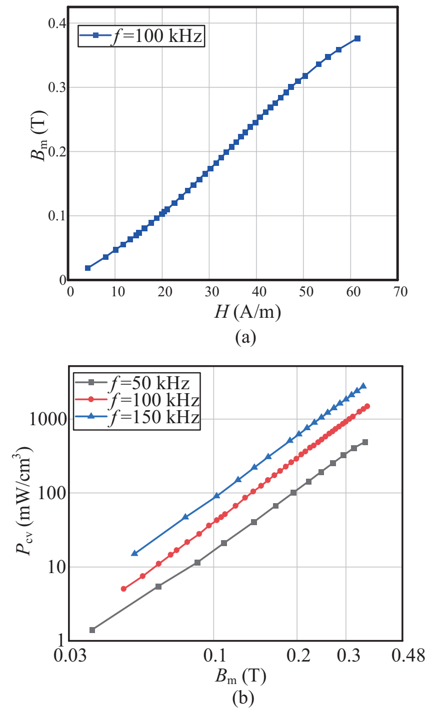

Fig. 5. Magnetic characteristic curves of ferrite (TPG33B) T22. (a) AC magnetization curve. (b) Core loss under sinusoidal wave excitation.

where A_e is the effective cross-sectional area, l_e is the effective magnetic path length, N is the winding turns, T is the period.

The hysteresis loop can be drawn according to (12). Connecting the peak points of the hysteresis loops excited by different voltages amplitudes yields the AC magnetization curve. Meanwhile, the product of the exciting current $i(t)$ and the induced voltage $u(t)$ is integrated over one period to obtain the core losses P_{core}, as shown in (13).

$$P_{core} = \frac{1}{T}\int_0^T u(t)\cdot i(t)\cdot\mathrm{d}t \tag{13}$$

The magnetization curve of the ferrite TPG33B under 100 kHz sinusoidal wave voltage excitation is shown in Fig. 5(a). The mathematical model of the magnetization curve $B_m(H)$ is shown in (14).

$$B_m(H) = B_s\cdot\frac{(H/H_0)^{\beta_2}}{1+(H/H_0)^{\beta_2}} \tag{14}$$

where B_s, H_0, and β_2 are the parameters related to the core material, and these are obtained by the least squares method as shown in Table II.

The core losses under sinusoidal wave voltages excitation whose frequency range is from 50 kHz to 150 kHz are shown in Fig. 5(b). The mathematical model of the core losses density $P_{cv}(B_m)$ is shown in (15).

$$P_{cv}(B_m) = k\cdot f^{\alpha}\cdot B_m^{\beta} \tag{15}$$

where k, α, and β are the parameters related to the core

TABLE II
MAGNETIC CHARACTERISTIC PARAMETERS OF FERRITE (TPG33B) T22

parameter	value	parameter	value
B_s	1.16653	k	0.07691
H_0	100.53436	α	1.70366
β_2	1.43403	β	2.75142

material, and these are obtained by the least squares method as shown in Table II.

III. ERROR ANALYSIS OF CORE LOSSES CALCULATION FOR HIGH-FREQUENCY PWM WAVE EXCITATION

There are mainly three errors of core losses calculation under PWM wave voltage excitation by using FE software Maxwell: the measurement error of magnetic characteristics of core material, the error of core losses mathematical model, and the error caused by applying different types of excitation sources.

A. The Measurement Error of Magnetic Characteristics of Core Material

The magnetic ring with a relatively small outer-to-inner diameter ratio is usually used as DUT to obtain the magnetic characteristics of core materials. It is assumed that the magnetic flux density inside the magnetic ring is uniformly distributed and is equal to the magnetic flux density at the effective magnetic path length. However, in reality, the magnetic flux density distribution inside the magnetic ring is non-uniform, which will thus lead to the magnetic characteristics measurement error of the core material.

In this paper, the T22 magnetic ring is used to obtain the magnetic characteristics of core material, and the ratio of its outer diameter to inner diameter is 1.57. If the magnetic flux density inside the magnetic ring is uniformly distributed and is equal to the magnetic flux density at the effective magnetic path length, then the magnetic field intensity H_m, magnetic flux density B_{m_ideal} inside the core and core losses P_{core_ideal} are shown in (16).

$$\begin{cases} H_{m} = \dfrac{N \cdot I_{pk}}{l_{e}} \\ B_{m\_ideal} = B_{s} \cdot \dfrac{(H_{m}/H_{0})^{\beta_2}}{1+(H_{m}/H_{0})^{\beta_2}} \\ P_{core\_ideal} = k \cdot f^{\alpha} \cdot B_{m\_ideal}^{\beta} \cdot V_{e} \end{cases} \tag{16}$$

where I_{pk} is the current peak value. f is exciting frequency, with a value of 100 kHz. B_s, H_0, β_2, k, α, and β are shown in TABLE II.

If the magnetic flux density distribution inside the core is non-uniform, then the core losses P_{core_Integ} is shown in (17).

$$P_{core\_Integ} = 2\cdot\pi\cdot h\cdot k\cdot f^{\alpha}\cdot \int_{r_2}^{r_1}\left(B_{s}\cdot\frac{\left(\dfrac{N\cdot I_{pk}}{2\cdot\pi\cdot r\cdot H_{0}}\right)^{\beta_2}}{1+\left(\dfrac{N\cdot I_{pk}}{2\cdot\pi\cdot r\cdot H_{0}}\right)^{\beta_2}}\right)^{\beta}\cdot r\mathrm{d}r \tag{17}$$

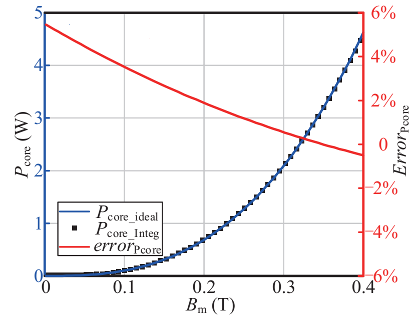

Fig. 6. Relationship diagram between core loss calculation error and magnetic flux density.

where r_1 is the outer diameter of the T22 magnetic ring, r_2 is the inner diameter of the T22 magnetic ring. Therefore, the relative error which is caused by using the T22 to measure the magnetic characteristics of core material is as shown in (18).

$$error_{P_{core}} = \frac{P_{core\_Integ} - P_{core\_ideal}}{P_{core\_Integ}} \cdot 100\% \tag{18}$$

The relative measurement error curve e is plotted according to (16), (17) and (18), as shown in Fig. 6. It can be seen from the figure that the curves of P_{core_ideal} and P_{core_Integ} coincide, and the maximum relative error between the two curves is only 5.46%. Therefore, the magnetic characteristics of core material can be accurately obtained by using the magnetic ring T22.

B. Error of the Mathematical Model for Core Losses

In the transient field solver, the instantaneous value of the core losses is obtained using the equivalent elliptical loop (EEL) model [17] which is based on the parameters k, α, and β of the SE equation, as shown in (19).

$$\begin{cases} C = \pm\dfrac{1}{C_{\alpha\beta}} k \cdot \left|B_{m}\cos(\theta)\right|^{\beta-\alpha} \\ C_{\alpha\beta} = (2\pi)^{\alpha}\cdot\dfrac{2}{\pi}\displaystyle\int_{0}^{\frac{\pi}{2}}\cos^{\beta}(\theta)\cdot \mathrm{d}\theta \\ p_{cv}(t) = |C|\cdot\left|\dfrac{\mathrm{d}B}{\mathrm{d}t}\right|^{\alpha} \end{cases} \tag{19}$$

The MSE is proposed for core losses simulation in this paper. Taking the ferrite T22 magnetic ring as the research object, the calculation errors of the two methods are analyzed. The core losses under PWM wave voltage excitation are calculated using the MSE and the EEL model respectively, and the exciting frequency is set to 100 kHz. After that, the calculation results are compared with the measured value of

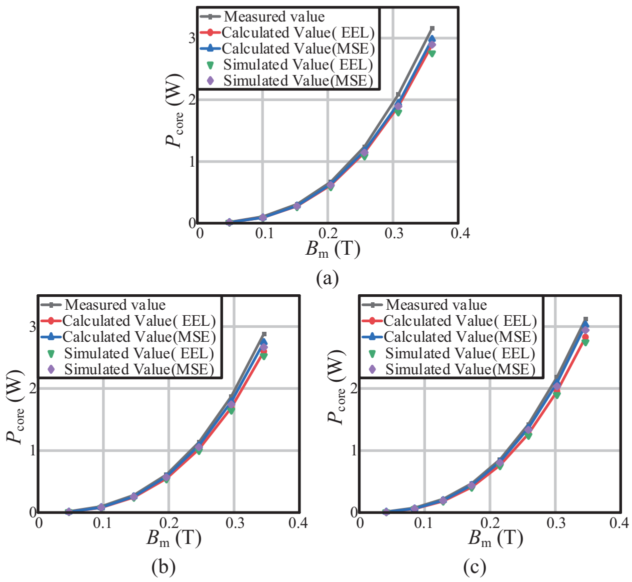

Fig. 7. Core loss of ferrite (TPG33B) T22 magnetic ring under PWM excitation at different duty cycles. (a) Duty = 0.5. (b) Duty = 0.4. (C) Duty = 0.3.

core losses, as shown in Fig. 7. It can be seen from the figure that under different duty cycles, the calculation error of core losses by using the MSE model is smaller than that of the EEL model. Therefore, the simulation scheme which is by using the MSE model is proposed to analyze the core losses under PWM wave voltage excitation in this paper.

Furthermore, the simulation results of EEL are compared with these of the proposed scheme, as shown in Fig. 7. The conclusion is consistent with the calculated conclusion. And the maximum absolute error for the magnetic ring in Fig. 7 is 0.26 W, corresponding to a relative error of 8.36%.

C. Errors of Different Excitation Types

In the FE software Maxwell, the voltage excitation can be applied to magnetic components, or the corresponding current excitation can also be applied. Due to the differences between the ways of applying the two types of excitations, the FE calculation processes of the two will result in calculation errors.

Taking the T22 magnetic ring as the research object, the error caused by different excitation types is analyzed. The core and winding of the magnetic component which is wound with T22 magnetic ring have a planar symmetric structure. Therefore, the three-dimensional model can be simplified into a two-dimensional model for simulation. Using the xoy plane as the cross-section, the simulation physical model is established in rectangular coordinate system, as shown in Fig. 8.

The transient field solver is selected. The sinusoidal voltage excitation with a frequency of 100 kHz and an amplitude of 30 V, or the sinusoidal current excitation with an amplitude of 0.31 A is applied to the magnetic component. The corresponding magnetic flux density peaks are both 0.2 T. The voltage and current waveforms on the magnetic component, as well as the instantaneous value of core losses, are shown in Fig. 9.

From Fig. 9, when the sinusoidal excitation voltage is applied to the magnetic component, the instantaneous values of the excitation current and the core losses are close to sinusoidal

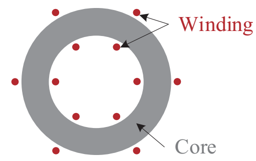

Fig. 8. Simulated physical model of ferrite (TPG33B) T22 magnetic ring.

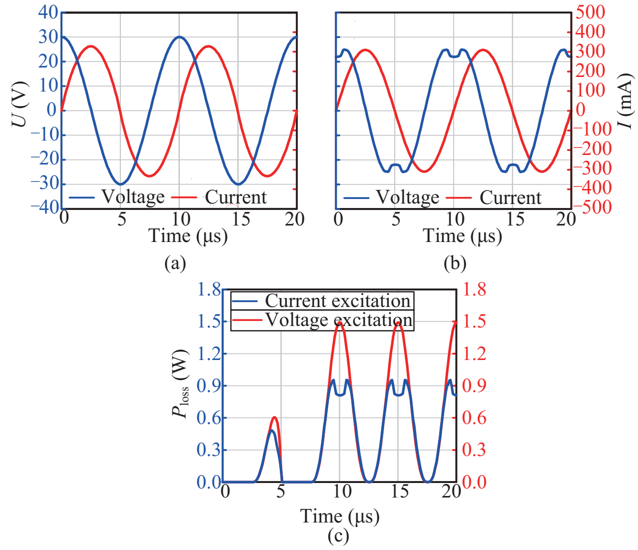

Fig. 9. Waveform diagram of excitation voltage, current and loss in transient field simulation. (a) Voltage and current of the core winding under voltage excitation. (b) Voltage and current of the core winding under current excitation. (c) Simulation diagrams of instantaneous core loss under voltage excitation or current excitation.

waves, which is consistent with the actual waveform. However, when the sinusoidal current excitation is applied to the magnetic component, there are depression phenomena at the peak of the excitation voltage and the instantaneous value of the core losses, which is inconsistent with the actual waveform. This is because the magnetic permeability of the core material has non-linear properties, resulting in differences during the FE analysis process for different excitation types.

In addition to the influence of different excitation types on the exciting waveform and core losses of magnetic ring, different excitation types also have different effects on magnetic components with air gap. When the core is of the EE type or RQ type and the magnetic component is wound by splicing two halves, there is usually an installation air gap l_g. This installation air gap is difficult to measure accurately and affects the core losses. When a voltage excitation $u(t)$ is applied to the magnetic component, the magnetic flux density $B(t)$ inside the core can be obtained with (20).

$$B(t) = \frac{\int u(t)\mathrm{d}t}{N \cdot A_e} \tag{20}$$

When a current excitation i(t) is applied to the magnetic component, the magnetomotive force and the magnetic potential drop in the air gap satisfy the ampere-turn balance, then the magnetic flux density $B(t)$ inside the core can be

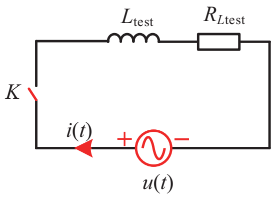

Fig. 10. Equivalent circuit diagram of the core series model.

obtained with (21).

$$B(t) = \mu_0 \cdot \frac{i(t) \cdot N}{l_{\text{g}}} \tag{21}$$

From (20) and (21), when the voltage excitation is applied to the magnetic component, the magnetic flux density distribution inside the core is independent of the air gap. However, when the current excitation is applied, the magnetic flux density distribution in the core is closely related to the air gap. Therefore, voltage excitation can effectively avoid the magnetic flux density distribution calculation error caused by the air gap, thereby reducing the core losses calculation error.

When a sinusoidal voltage excitation is applied to DUT, as shown in (22).

$$u(t) = U_{\text{m}} \cos(\omega t + \varphi_{\text{k}}) \tag{22}$$

where φ_{k} is the initial phase, and its range is from −90° to + 90°.

The R-L series equivalent circuit of the magnetic component is shown in Fig. 10. The Kirchhoff voltage circuit equation can be obtained, as shown in (23).

$$\begin{cases} L_{\text{test}} \dfrac{\mathrm{d}i}{\mathrm{d}t} + R_{L\text{test}} \cdot i = U_{\text{m}} \cdot \cos(\omega t + \varphi_{\text{k}}) \\ \tan\varphi = \dfrac{\omega \cdot L_{\text{test}}}{R_{L\text{test}}} \end{cases} \tag{23}$$

where L_{test} is the equivalent inductance of the DUT, R_{test} is the equivalent resistance of the DUT.

The excitation current which will not experience sudden changes can be obtained with (24).

$$\begin{aligned} i = &\frac{U_{\text{m}}}{\sqrt{R_{L\text{test}}{}^2 + (\omega \cdot L_{\text{test}})^2}} \cdot \cos(\omega t + \varphi_{\text{k}} - \varphi) - \\ &\frac{U_{\text{m}}}{\sqrt{R_{L\text{test}}{}^2 + (\omega \cdot L_{\text{test}})^2}} \cdot \cos(\varphi_{\text{k}} - \varphi) \cdot e^{-\frac{t}{\tau}} \end{aligned} \tag{24}$$

where τ is time constant. When the time approaches ∞, the current becomes stable. In practice, when the time reaches 5τ (at the millisecond level), the current becomes stable. However, when the difference between φ_{k} and φ is 90°, there is no transient process in the circuit.

In the transient field solver of FE software Maxwell, voltage excitations with different initial phases are applied to the magnetic component (as shown in Fig. 8), and the excitation voltage and current waveforms are shown in Fig. 11. When

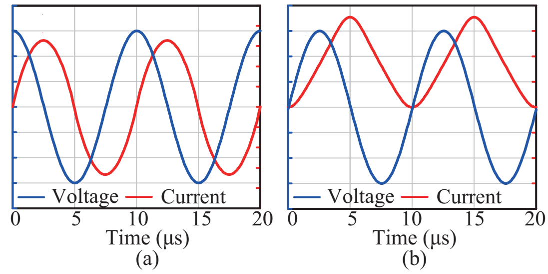

Fig. 11. Voltage and current waveforms in transient field simulation with different initial phases. (a) $\varphi_{\text{k}} = 0°$. (b) $\varphi_{\text{k}} = 90°$.

the initial phase is 0, the circuit quickly reaches a steady state; when the initial phase is 90°, there is an initial DC bias current and the current does not reach a stable state. Therefore, when the initial phase of the cosine voltage excitation is zero, the calculation time can be effectively saved.

In conclusion, when the core losses of magnetic components are calculated using the FE software Maxwell, a sinusoidal wave voltage excitation with an initial phase of zero should be applied to the magnetic components. In other words, the voltage excitation should be applied to the magnetic components, and initial state of the circuit should be zero in order that the stable state is reached in advance.

IV. Accuracy Verification of the Core Losses Simulation Scheme

In this section, the EE41 type core is taken as the research object. Based on the magnetic characteristics of the core material obtained from the ferrite T22 magnetic ring, the proposed simulation scheme for core losses is used to analyze the core losses under PWM wave voltage excitation. The simulation results are then compared with the measured values of the core losses to verify the feasibility and calculation accuracy of the scheme.

A. Core Losses Measurement Under PWM Wave Voltage Excitation

The equivalent circuit model of the magnetic component is shown in Fig. 4(a). When the large-signal AC method is utilized for core losses measurement under PWM wave voltage excitation, the waveforms of i_{L}, i_{core}, and i_{m} are shown in Fig. 12. Δt is the delay between the sampled voltage and current, and the relative measurement error δ is shown in (25).

$$\delta = \frac{\Delta P_{\text{core}}}{P_{\text{core}}} \approx \frac{I_{\text{m\_pp}} \cdot \Delta t}{D \cdot (1-D) \cdot I_{\text{core\_pp}} \cdot T} \tag{25}$$

where $I_{\text{m\_pp}}$ is the peak to peak of i_{m}, $I_{\text{core\_pp}}$ is the peak to peak of i_{core}, as shown in (24).

$$\begin{cases} I_{\text{m\_pp}} = \dfrac{U_{2\text{pp}} \cdot D \cdot (1-D)}{f \cdot L} \\ I_{\text{core\_pp}} = \dfrac{U_{2\text{pp}}}{R_{\text{core}}} \end{cases} \tag{26}$$

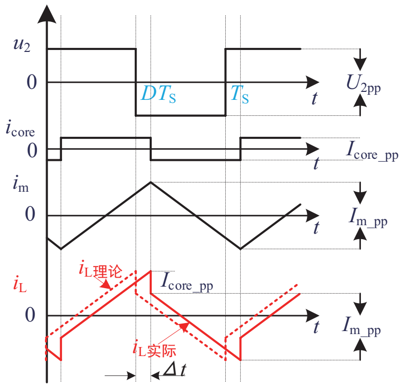

Fig. 12. Voltage and current waveforms under rectangular wave excitation.

where U_{2pp} is the peak-to-peak value of the exciting voltage.

By combining (25) and (26), the relative measurement error is shown in (27).

$$\delta = \frac{\Delta P_{core}}{P_{core}} \approx \tan\theta \cdot \Delta\theta \cdot \frac{R_{rec\_core}}{R_{sin\_core}} \tag{27}$$

where θ is the impedance angle of the magnetic component. R_{rec_core} is the equivalent resistance of the core losses under PWM wave voltage excitation. R_{sin_core} is the equivalent resistance of the core losses under sinusoidal wave voltage excitation. When the impedance angle θ is close to 90°, a tiny delay will lead to a very large measurement error. When the excitation frequency and magnetic flux density are the same, and the duty cycle is greater than 0.282 as known from (5), the measurement error of PWM voltage excitation is greater than that of sinusoidal wave excitation. In addition, the PWM wave voltage has a steep rising edge and contains high-order harmonics, so the measurement error is further increased.

Therefore, the DC power method is utilized to measure the core losses under high-frequency PWM wave excitation in this paper. The measurement principle of DC power method is shown in Fig. 13(a). The DC voltage source is converted into a PWM wave voltage through the inverter circuit and applied to the magnetic component. The magnetic component losses P_L can be obtained by subtracting the inverter circuit losses P_{ex} from the output power P_{in} of the DC voltage source, as shown in (28).

$$\begin{cases} P_L = P_{in} - P_{ex} \\ P_{in} = U_{in} \cdot I_{in} \end{cases} \tag{28}$$

where I_{in} is the DC component of the input current i_{in}, U_{in} is the input voltage.

A multimeter is only utilized to measure the DC components of the input voltage and input current to obtain the magnetic component losses by the DC power method. It avoids the problem that the measurement accuracy of the large-signal AC method is sensitive to delay errors. In [14], based on the optimized design to minimize the inverter circuit losses P_{ex}, the air-core inductor is utilized to calibrate P_{ex} to improve the

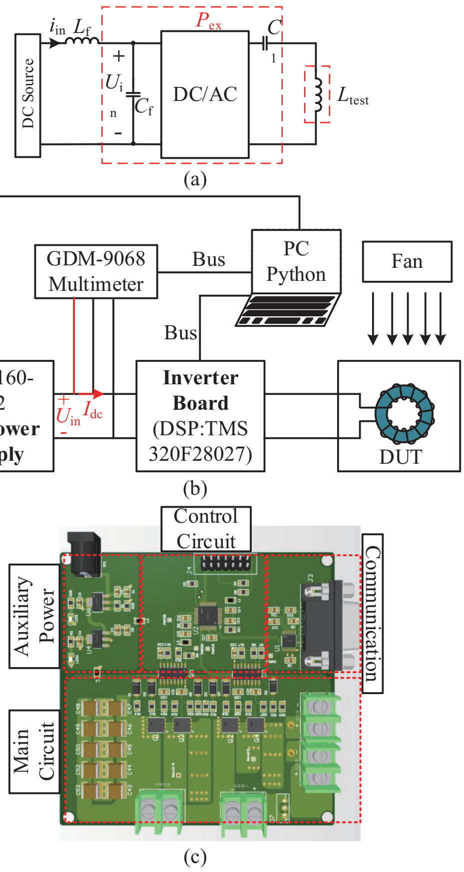

Fig. 13. DC power method measurement system. (a) DC power method measurement schematic diagram. (b) System diagram. (c) The inverter board's PCB layout (top view).

measurement accuracy of the DC power method. [18] proposes a separation scheme for core losses and winding loss of PWM wave excitation based on the DC power method. The system diagram and the inverter board's PCB layout (top view) of the DC power method are shown in Fig. 13(b) and (c).

B. Verification of the Simulation Accuracy of Core losses Under PWM Wave Voltage Excitation

The dimensions of the EE41 core and the wound specimen are shown in Fig. 14(a). The EE-type core has structural symmetry, so the three-dimensional model can be simplified to a two-dimensional model for simulation. The established two-dimensional simulation physical model is shown in Fig. 14 (b). The Polyline in the figure is a line drawn for analyzing the magnetic flux density inside the core.

The PWM wave voltage excitation (with a frequency of 100 kHz, a duty cycle of 0.5, and voltage amplitudes of 30 V and 70 V respectively) is applied to the magnetic component. The distribution of its magnetic flux density peak is shown in Fig. 15. The distribution of the magnetic flux density in the EE-shaped core is uneven, with relatively large magnetic flux density at the inner corners of the magnetic column and relatively small magnetic flux density at the outer corners. The span of the magnetic flux density distribution and the core losses density of the EE-shaped core is wide.

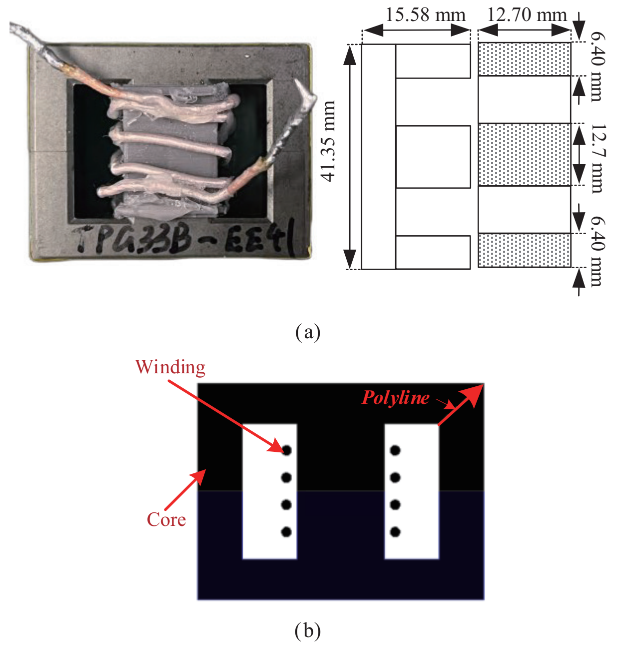

Fig. 14. Parameters of ferrite (TPG33B) EE-shaped core. (a) Dimensions of ferrite (TPG33B) EE-shaped core. (b) Two-dimensional simulation model of ferrite (TPG33B) EE-shaped core.

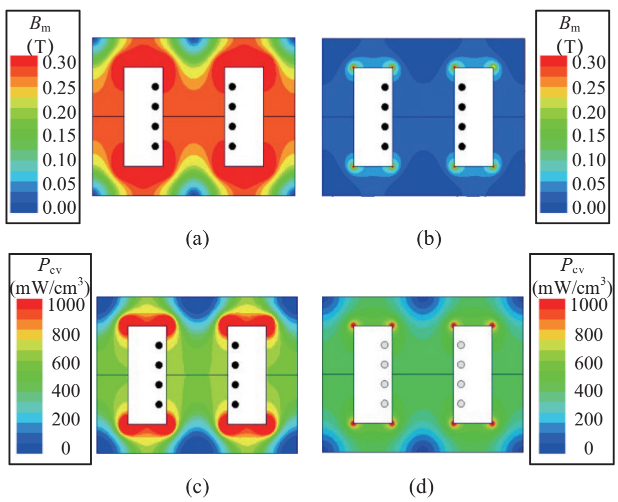

Fig. 15. Field distribution diagram of ferrite (TPG33B) EE core. (a) Peak distribution of magnetic flux density (excitation voltage: 70 V). (b) Peak distribution of magnetic flux density (excitation voltage: 30 V). (c) Distribution of core loss density (excitation voltage: 70 V). (d) Distribution of core loss density (excitation voltage: 30 V).

The distribution of the magnetic flux density peak on the Polyline is shown in Fig. 16. The span of the distribution of the magnetic flux density peak is from 0 T to 0.5 T, and its distribution is complex. A comparison between the simulation results and measurements of the core losses of the EE-shaped core is shown in Fig. 17. The abscissa in the figure represents the amplitude of the excitation voltage. It can be seen from the figure that the simulation results and measurements of the core losses at different duty cycles are basically in agreement. When the amplitude of the excitation voltage is relatively large, the absolute error is relatively large. This is because the distribution range of the magnetic flux density is too wide, and the mathematical model of the core losses density for a wide range of magnetic flux densities needs to be further improved.

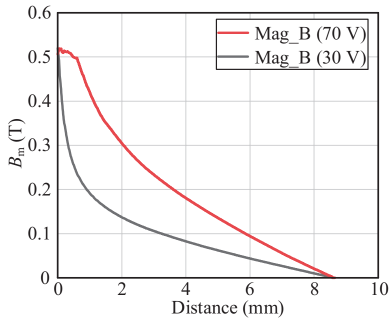

Fig. 16. Peak distribution of magnetic flux density along the Polyline of the Ferrite (TPG33B) EE core.

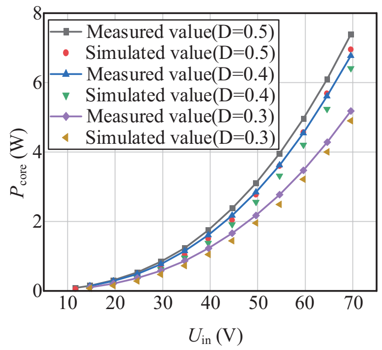

Fig. 17. Core loss diagram of ferrite (TPG33B) EE core under PWM excitation.

V. Conclusion

By using FE software Ansys Maxwell, this paper proposes a simulation scheme for core losses calculation of magnetic components with different core structures in power converters. The core losses model under PWM wave voltage excitation is derived based on MSE, and it is equal to the core losses under sinusoidal wave voltage excitation multiplied by a coefficient which relates to duty cycle and the SE coefficient α. Therefore, based on the core losses under sinusoidal wave voltage excitation, either the transient field solver or the eddy current field solver of FE software Ansys Maxwell can be selected for core losses simulation.

The magnetic properties of core material serve as basis for accurate core losses simulation. The large-signal AC method is used for magnetic properties measurement of core materials under sinusoidal wave voltage excitation. The measurement and modeling of AC magnetization curves and core losses of ferrite (TPG33B) are obtained with magnetic ring T22. Furthermore, the main simulation error sources are analyzed. The magnetic property measurement error is due to the uneven distribution of magnetic flux density inside the magnetic ring. An accurate core losses model ensures the accuracy of core losses simulation. For the core losses of PWM wave voltage excitation, the EEL model which is the software's built-in core losses model has poorer accuracy than MSE. The FE calculation processes of different excitation types will result in calculation errors. The voltage excitation with an initial phase of zero, when initial value of the exciting current is zero, should be applied to the magnetic components.

The large-signal AC method which is used for core losses measurement under PWM wave excitation is widely inaccurate. Therefore, the core losses simulation results are compared with measurement results with DC power method, and the comparison results validated the practicability and accuracy of the proposed simulation method. The maximum absolute error for the EE-shaped magnetic core is only 0.428 W, corresponding to a relative error of 5.79%.

However, the span of magnetic flux density distribution in non-ring core is a wide range (several mT to saturation magnetic flux density), and the core losses model of wide range magnetic flux density should be further improved.

REFERENCES

[1] T. Wang, R. Luo, J. Wen, M. Zhang, and J. Tian, "A measurement method of winding loss for high-frequency transformer based on auxiliary winding," in *Transactions of China Electrotechnical Society,* vol. 37, no. 10, pp. 2622–2630, May 2022.

[2] C. Peng, G. Chen, B. Wang, and J. Song, "Semi-analytical AC resistance prediction model for Litz wire winding in high-frequency transformer," in *IEEE Transactions on Power Electronics*, vol. 38, no. 10, pp. 12730–12742, Oct. 2023.

[3] S. Zhang, W. Sun, T. Fan, X. Wen, and D. Zhang, "Research on high power density silicon carbide motor controller based on parallel connection of discrete devices," in *Transactions of China Electrotechnical Society*, vol. 38, no. 22, pp. 5999–6014, Nov. 2023.

[4] X. Huang, Y. Lei, Y. Zhou, W. Du, and J. Zhang, "An ultra-high efficiency high power density 140W PD3.1 AC-DC adapter using GaN power ICs," in *2023 IEEE Applied Power Electronics Conference and Exposition (APEC)*, Orlando, FL, USA, 2023, pp. 1252–1258.

[5] L. Yi and J. Moon, "Accurately disentangling core and winding losses in experimental, in-situ magnetic loss measurement for power electronic circuits and applications," in *IEEE Journal of Emerging and Selected Topics in Power Electronics*, vol. 12, no. 6, pp. 5568–5578, Dec. 2024.

[6] A. Huang, X. Wang, H. Zhang, C. Hwang, D. Pommerenke, and J. Fan, "Improved current shunt characterization method for core loss measurement," in *IEEE Transactions on Power Electronics*, vol. 37, no. 7, pp. 8290–8300, Jul. 2022.

[7] G. Bertotti, "General properties of power losses in soft ferromagnetic materials," in *IEEE Transactions on Magnetics*, vol. 24, no. 1, pp. 621–630, Jan. 1988.

[8] N. Zhang, L. Li, and X. Wei, "Calculation method and experimental verification of core losses under non-sinusoidal excitation," in *Transactions of China Electrotechnical Society*, vol. 31, no. 17, pp. 224–232, Sept. 2016.

[9] Z. Zhao, Q. Lin, J. Ji, and X. Ma, "Wideband loss separation models of ferromagnetic materials considering skin effect," in *Proceedings of the Chinese Society of Electrical Engineering*, vol. 42, no. 14, pp. 5374–5382, Jul. 2022.

[10] J. H. Wang and W. Chen, "Study of calorimetric method to measure loss of super low loss angle core," in *Advanced Technology of Electrical Engineering and Energy*, vol. 31, no. 4, pp. 6–9, Apr. 2012.

[11] J. Wang, P. Fan, S. Lin, F. Huang, and W. Chen, "Comparative calorimetric method for magnetic component losses measurement with high frequency," in *IEEE Journal of Emerging and Selected Topics in Power Electronics*, vol. 12, no. 5, pp. 5112–5122, Oct. 2024.

[12] M. Mu, Q. Li, D. J. Gilham, F. C. Lee, and K. D. T. Ngo, "New core loss measurement method for high-frequency magnetic materials," in *IEEE Transactions on Power Electronics*, vol. 29, no. 8, pp. 4374–4381, Aug. 2014.

[13] D. Hou, M. Mu, F. C. Lee, and Q. Li, "New high-frequency core loss measurement method with partial cancellation concept," in *IEEE Transactions on Power Electronics*, vol. 32, no. 4, pp. 2987–2994, Apr. 2017.

[14] B. Liu, W. Chen, J. Wang, and Q. Chen, "A practical inductor loss testing scheme and device with high frequency pulsewidth modulation excitations," in *IEEE Transactions on Industrial Electronics*, vol. 68, no. 5, pp. 4457–4467, May 2021.

[15] J. Ye and W. Chen, "The method and device based on the differential power for measurement of high-frequency core losses," in *Proceedings of the Chinese Society of Electrical Engineering*, vol. 37, no. 16, pp. 4834–4841, Aug. 2017.

[16] J. Reinert, A. Brockmeyer, and R. W. De Doncker, "Calculation of losses in ferro- and ferrimagnetic materials based on the modified Steinmetz equation," in *Conference Record of the 1999 IEEE Industry Applications Conference. Thirty-Forth IAS Annual Meeting*, Phoenix, AZ, USA, 1999, pp. 2087–2092.

[17] D. Lin, P. Zhou, W. N. Fu, Z. Badics, and Z. J. Cendes, "A dynamic core loss model for soft ferromagnetic and power ferrite materials in transient finite element analysis," in *IEEE Transactions on Magnetics*, vol. 40, no. 2, pp. 1318–1321, Mar. 2004.

[18] D. Yang, B. Wang, S. Shao, and J. Zhang, "A novel DC differential method for high frequency core loss measurement," in *IEEE Transactions on Power Electronics*, vol. 39, no. 10, pp. 13459–13470, Oct. 2024.

Zhikang Fu was born in Jiangxi, China, in 1999. He is currently pursuing the master's degree with the Fuzhou University, Fuzhou. His research interest includes high frequency magnetic technology, engineering electromagnetic field analysis and application, etc.

Jinghui Wang was born in Jiangxi, China. She received the B.E., M.S., and Ph.D. degrees in electrical engineering from Fuzhou University, Fuzhou, China, in 1997, 2000, and 2012, respectively. She is currently an Associate Professor at Fuzhou University. Her main research interests include power electronic high frequency magnetic technology and electromagnetic characteristic measurement and model study of magnetic elements.

Juntao Xiao was born in Jiangxi, China, in 1997. He obtained her master's degree from Fuzhou University in 2023. His research interest includes magnetic component design, magnetic core loss testing technology, etc.

Wei Chen (Fellow, CPSS) was born in Jiangxi, China. He received the M.S. and Ph.D degrees in electrical engineering from Fuzhou University, Fuzhou, China, in 1987 and 1990, espectively. He worked as a Senior Visiting Professor with Center for Power Electronics Systems (CPES) of Virginia Tech, Blacksburg, VA, USA, from 1996 to 1998. His research interests include power conversion, high-frequency magnetic technology, EMI debug and solution, wireless power transfer, electromagnetic field analysis, and applications, etc.

Accurate Calculation of Parasitic Capacitance of High Frequency Inductors

Jiangtao TU, Kaining FU, Wei CHEN, and Yanhui QIU

***Abstract*—High-frequency inductors are important devices in power converters. The parasitic capacitance not only affects the electromagnetic interference suppression effect of filter inductors, but also causes efficiency degradation and other problems. In order to predict the impedance characteristics of high-frequency inductors, this paper proposes a method to accurately calculate the parasitic capacitance of inductors. Firstly, the effect of the winding structure parameters on the electric field distribution between adjacent turns is investigated. Then, the calculation method is optimized, which can be used to accurately describe the electric field distribution. Secondly, the effect of core parasitic capacitance on the total capacitance is further investigated. Finally, a calculation method for the parasitic capacitance of high-frequency inductors is established. In the experiments, the impedance test and finite element simulation are used as references to compare the calculation results. The maximum calculation error is only within 5.05%, which verifies the validity and accuracy of the proposed calculation method.**

***Index Terms*—Electric field distribution, finite element simulation, inductors, parasitic capacitance.**

I. Introduction

WITH the increasing switching frequency, the electromagnetic parameters design of magnetic components has become a major bottleneck limiting the power converter to further increase the switching frequency and power density [1]−[2]. This is because the parasitic parameters of magnetic components cause high-frequency voltage oscillations, which not only lead to higher EMI noise, but also reduce the efficiency of the power converter [3]−[4]. More and more researchers are focusing on the high-frequency parasitic parameters characterization of magnetic components [5].

As shown in Fig. 1, the high-frequency model of the inductor contains the inductance L, the parasitic capacitance C_p, and the equivalent parallel resistance R_s. It can be found that accurate measurement or calculation of the parasitic capacitance C_p is essential to accurately predict the high-frequency impedance characteristics of an inductor. Parasitic capacitance C_p contains the capacitance inside the winding and the capacitance between the winding and the core. In addition, the capacitance inside the winding can be categorized into turn-to-turn capacitance and layer-to-layer capacitance. In order to optimize the high-frequency characteristics of inductors at the design level, it is necessary to propose an analytical method for theoretically calculating the parasitic capacitance of inductors. In [6], a theoretical calculation method for parasitic capacitance of single-layer winding is presented. Further, a calculation method for parasitic capacitance of multilayer winding is presented in [7] and used to evaluate the size of parasitic capacitance of transformers and EMI chokes [8]−[9]. However, these methods do not take into account the effect of the parasitic capacitance between the winding and the core on the total capacitance [10]. In addition, the application of these techniques is strictly limited to the distance between the windings and the core, making it difficult to apply them widely [11].

Finite element simulations can be used to analyze the parasitic parameter characteristics under various complex core and winding structures. However, 3D finite element simulation suffers from time-consuming and non-convergence problems due to large mesh sizes and limitations in computer computational resources. As a result, parasitic capacitance is difficult to realize fast prediction by simulation [12]−[13]. In [14], parasitic capacitance of an inductors can be extracted by impedance test. This method cannot be used to predict the size of parasitic capacitance at the design stage. [15] proposed a method to calculate the turn-to-turn capacitance, but the core parasitic capacitance was not studied in depth. This results in a large error between the calculated and measured values. For inductor design, the parasitic capacitance should be reduced as small as possible. Once the winding arrangement of the inductor is determined, the parasitic capacitance can be accurately calculated by the proposed method. Hence, the proposed calculation method can be used to predict the parasitic capacitance of the inductor in the design stage.

This paper is organized as follows. In Section II, the characteristics of the electric field distribution between adjacent

Manuscript received January 22, 2025; revised March 25, 2025; accepted April 14, 2025. Date of publication June 30, 2025; date of current version May 12, 2025. This work was supported in part by National Natural Science Foundation of China under the grant 51777036, Natural Science Foundation of Xiamen, China under the grant 3502Z202372043, and Research start-up fund of Xiamen University of Technology under the grant YKJ23008R.
(Corresponding author: Kaining Fu.)

J. Tu and Y. Qiu are with School of Electrical Engineering and Automation, Xiamen University of Technology, Xiamen 361024, China (e-mail: 1092111621@qq.com; 512621898@qq.com).

K. Fu is with Xiamen Key Laboratory of Frontier Electric Power Equipment and Intelligent Control, the School of Electrical Engineering and Automation, Xiamen University of Technology, Xiamen 361024, China (e-mail: fkn@xmut.edu.cn).

W. Chen is with School of Electrical Engineering and Automation, Fuzhou University, Fuzhou 350108, China (e-mail: chw@fzu.edu.cn).

Digital Object Identifier 10.24295/CPSSTPEA.2025.00018

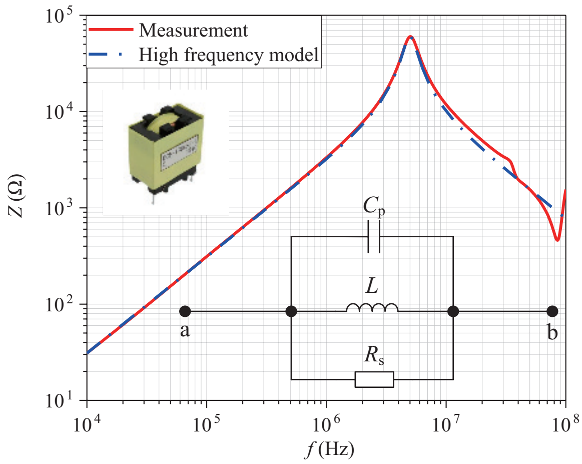

Fig. 1. Equivalent circuit of inductor.

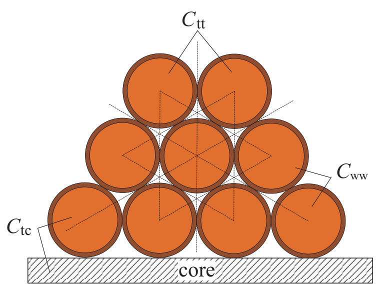

Fig. 2. Cross-section of an inductor with three winding layers.

turns of the winding are explored, and the parasitic capacitance of the windings are deduced using electromagnetic field equations. In Section III, the core parasitic capacitance between winding and core is analyzed and calculated. In Section IV, the calculation model on the description of electric field is further optimized. In Section V, the accuracy of the proposed calculation method is verified by finite element method (FEM) simulation and impedance measurement. Section VI gives the conclusion of this paper.

II. Parasitic Capacitance Model of Winding

As illustrated in Fig. 1, the impedance characteristics of the inductor exhibit capacitive impedance after the resonance point due to the presence of parasitic capacitance. For better and clearer understanding the distribution of parasitic capacitance, Fig. 2 shows the cross-section view of an inductor with three layers of windings. The parasitic capacitance consists of the following three components:

1. Turn-to-turn parasitic capacitance in the same layer of the winding (C_{tt});
2. Turn-to-turn parasitic capacitance between adjacent layers of the winding (C_{ww});
3. Parasitic capacitance between winding and core (C_{tc}).

Both turn-to-turn capacitance C_{tt} and C_{ww} are determined by the winding arrangement. This is because the winding arrangement affects the distribution of electric field lines between turns, which in turn affects the size of the parasitic capacitance. The parasitic capacitance between the winding and the core is

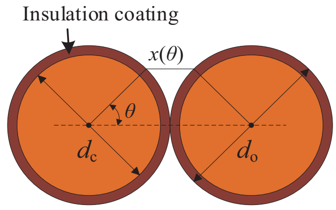

Fig. 3. Cross-section of turn-to-turn.

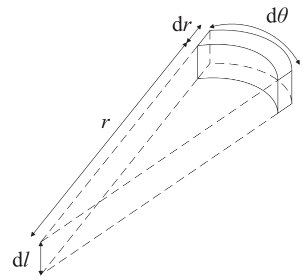

Fig. 4. Insulation coating.

affected not only by the area between the winding and the core, but also by the dielectric properties of the core material.

Fig. 3 shows the cross-section view of the same layer winding, where the windings are densely wound. d_c and d_o are the diameter of bare conductors and conductors with insulation coatings, respectively. $x(\theta)$ is the path of the electric field lines through the air. As can be seen in Fig. 3, the electric field lines between adjacent turns need to pass through the insulating coating and air. Thus, the equivalent parasitic capacitance between the adjacent turns of conductor consists of an insulating coating capacitance and an air capacitance connected in series.

A. Capacitance of Insulation Coating

The unit of insulation coating is shown in Fig. 4, where r is the radius of the bare conductor. The capacitance can be expressed as:

$$\mathrm{d}C = \varepsilon \frac{\mathrm{d}S}{x} \tag{1}$$

Then, the capacitance of the insulation coating can be expressed as:

$$\mathrm{d}C = \frac{\varepsilon_0 \varepsilon_r r}{2\mathrm{d}r} \mathrm{d}\theta \mathrm{d}l \tag{2}$$

where ε_r is the relative permittivity of the insulation material.

Combined with (2) and the relevant parameters shown in Fig. 3 and Fig. 4, the capacitance of insulation coatings can be further expressed as:

$$\mathrm{d}C_{ttc} = \varepsilon_0 \varepsilon_r \mathrm{d}\theta \int_0^{l_t} \mathrm{d}l \int_{\frac{d_o}{2}}^{\frac{d_c}{2}} \frac{r}{2\mathrm{d}r} = \frac{\varepsilon_0 \varepsilon_r l_t}{2\ln \frac{d_o}{d_c}} \mathrm{d}\theta \tag{3}$$

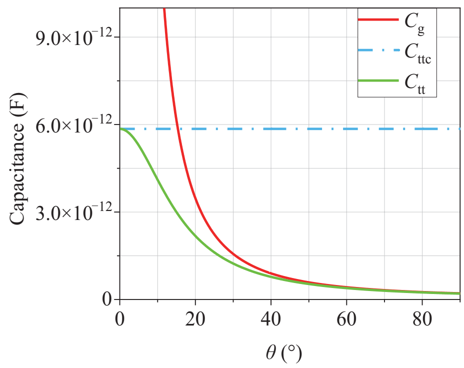

Fig. 5. Capacitance microelement value distribution.

Then, the insulation capacitance can be further simplified as:

$$\frac{\mathrm{d}C_{\mathrm{ttc}}}{\mathrm{d}\theta}=\frac{\varepsilon_0\varepsilon_{\mathrm{r}}l_{\mathrm{t}}}{2\ln\dfrac{d_{\mathrm{o}}}{d_{\mathrm{c}}}} \tag{4}$$

B. Air Capacitance

As shown in Fig. 3, assuming that the path of electric field lines in the air is a straight line, the length of the electric field lines at angle θ, $x(\theta)$, can be expressed as:

$$x(\theta)=d_{\mathrm{o}}(1-\cos\theta) \tag{5}$$

Combined with (1) and (5), the air capacitance can be expressed as:

$$\frac{\mathrm{d}C_{\mathrm{g}}(\theta)}{\mathrm{d}\theta}=\varepsilon_0\frac{l_{\mathrm{t}}d_{\mathrm{o}}}{2(1-\cos\theta)} \tag{6}$$

C. Total Capacitance Between Turn-to-Turn

Since the air capacitance $\mathrm{d}C_g$ and the insulation capacitance $\mathrm{d}C_{ttc}$ are in series connection, the total capacitance between turn-to-turn can be calculated. Combining (4) and (6), the turn-to-turn capacitance at angle θ, can be given as:

$$\mathrm{d}C_{\mathrm{tt}}(\theta)=\frac{\mathrm{d}C_{\mathrm{ttc}}\mathrm{d}C_{\mathrm{g}}}{\mathrm{d}C_{\mathrm{ttc}}+\mathrm{d}C_{\mathrm{g}}}=\frac{\varepsilon_0 l_{\mathrm{t}}}{2}\frac{1}{1+\dfrac{1}{\varepsilon_{\mathrm{r}}}\ln(\dfrac{d_{\mathrm{o}}}{d_{\mathrm{c}}})-\cos\theta}\mathrm{d}\theta \tag{7}$$

Based on (7), the turn-to-turn capacitance C_{tt} can be further calculated as:

$$C_{\mathrm{tt}}=\varepsilon_0 l_{\mathrm{t}}\int_0^{\frac{\pi}{2}}\frac{1}{1+\dfrac{1}{\varepsilon_{\mathrm{r}}}\ln(\dfrac{d_{\mathrm{o}}}{d_{\mathrm{c}}})-\cos\theta}\mathrm{d}\theta \tag{8}$$

where the capacitance C_{tt} is determined not only by the structure parameters but also by the integration range.

Fig. 5 shows the capacitance value at different angles θ, including air capacitance, insulation capacitance, and turn-to-turn capacitance. The insulation capacitance remains constant at different θ. Air capacitance C_g is changed versus angel θ. According to (8), the turn-to-turn capacitance C_{tt} is also changed versus angel.

Since the air capacitance in the range of [30°, 90°] is smaller than that in the range of [0°, 30°], the integration range [0°, 30°] is chosen to calculate the capacitance [15].

In order to show the influence of integration range on calculation results, an example is given as following: d_o=0.3 mm, d_c=0.34 mm, l_t=47 mm. The 3D FEM simulation result is used as a reference (The simulated capacitance is 4.6782 pF). For the integration range used in [15], i.e., [0°, 30°], the calculated result is 3.4489 pF, resulting in 26.28% relative error. If the integration range is further extended to [0°, 90°], the calculation result is 4.4654 pF, and the corresponding relative error is reduced to 4.549%.

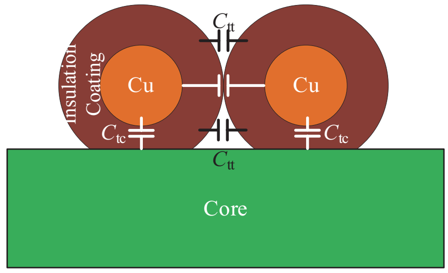

Fig. 6. Parasitic capacitance between winding and core.

III. Parasitic Capacitance Between Winding and Core

As shown in Fig. 6, there are parasitic capacitances C_{tc} between the winding and the core. If the winding is wound directly on the core without the use of a bobbin, the parasitic capacitance C_{tc} and the turn-to-turn capacitance C_{tt} satisfy: C_{tc}=2C_{tt}. However, this assumption can only be applied to magnetic components without bobbin, such as toroidal inductors, and does not apply to magnetic components with bobbins such as EE, EI, and PQ type cores.

Since the winding is wound on a bobbin, the parasitic capacitance between the winding and the core should consider the dielectric effect due to the bobbin. In addition, the presence of bobbin makes the windings to be located at different distances from the core center columns, side columns, and yoke. These factors cause the parasitic capacitance C_{tc} and the winding turn-to-turn capacitance C_{tt} no longer meet the requirements: C_{tc}=2C_{tt}.

In order to accurately calculate the parasitic capacitance C_{tc}, a sub-area calculation method is used. As shown in Fig. 7, the parasitic capacitance between the winding and the core can be calculated in three parts:

1. Capacitance between the winding and the core center column (C_{cw1});

2. Capacitance between the winding and the core side column (C_{cw2});

3. Capacitance between the winding and the yoke (C_{cw3}).

The total capacitance C_{cw} between the core and the winding consists of three parts, C_{cw1}, C_{cw2}, and C_{cw3}, which can be expressed as:

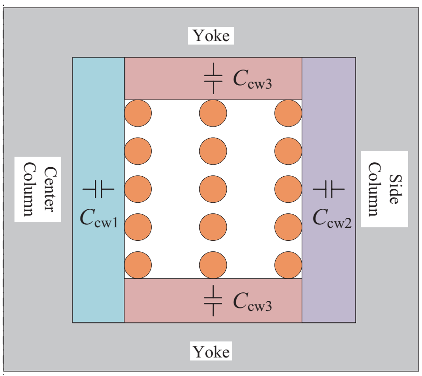

Fig. 7. Capacitance distribution between winding and core.

$$C_{cw}=k_{cw1}\cdot C_{cw1}+k_{cw2}\cdot C_{cw2}+k_{cw3}\cdot C_{cw3} \tag{9}$$

where k_{cw1}, k_{cw2} and k_{cw3} are the normalization factors for the capacitance of each part.

In order to calculate the parasitic capacitance between each part of the core and the winding, the type of core should be considered in detail. The calculation can be done using the parallel plate capacitance formula and the coaxial cylindrical capacitance formula, respectively. They can be expressed as:

$$C_x=\begin{cases}\alpha_x\varepsilon_0\varepsilon_x\dfrac{2\pi h_x r_x}{d_x}\\ \alpha_x\varepsilon_0\varepsilon_x\dfrac{2\pi h_x}{\ln(1+\dfrac{d_x}{r_x})}\end{cases}\quad x=\text{cw1,cw2,cw3} \tag{10}$$

where ε_0 is the vacuum permittivity constant, ε_x is the relative permittivity of the material, h_x and r_x are the height and radius, respectively. d_x is the distance between two plates or coaxial cylindrical plates, and α_x is the weighting factor.

There are two factors that require attention: one is the selection of capacitance formula, and the other is the determination of weighting factor α_{cw2}. For the first factor, the structure type of magnetic core should be considered. For the inductor with an EE core, the calculation formula for parasitic capacitance should be chosen as the parallel plate capacitance formula. For the inductor with a PQ core, the calculation formula for parasitic capacitance should be chosen as the coaxial cylindrical capacitance formula.

For the second factor, the weight factor α_{cw2} should be determined according to type of magnetic core. For PQ-type inductors, the degree of side column enclosure to the windings can be represented by α_{cw2} = 1/2. For pot-type inductors, it can be represented by α_{cw2} = 8/9. For the EE-type inductor, it can be represented by α_{cw2} = 1.

Since the research object is the PQ core, the coaxial cylindrical capacitance formula was chosen for the calculation of the structural capacitance between the winding and core. Fig. 8 shows the identification of the structural parameters for the quantitative calculation of the capacitance between the windings and the core.

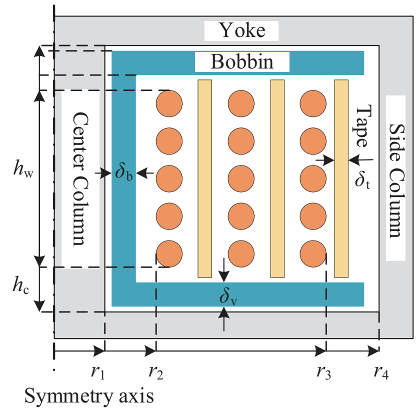

Fig. 8. Structural parameters of inductors.

A. Calculation of C_{cw1}

This part of capacitance refers to the capacitance between the innermost winding and the center column of the core. The dielectric material of the capacitance C_{cw1} is composed by air and bobbin. The relevant parameters can be calculated by the following equation:

$$\begin{cases}\alpha_{cw1}=1\\ h_{cw1}=h_c\\ d_{cw1}=r_2-r_1+\dfrac{d_o}{2}\\ r_{cw1}=r_1+\dfrac{d_{cw1}}{2}\\ \varepsilon_{cw1}=\dfrac{\varepsilon_a\varepsilon_b d_{cw1}}{\varepsilon_a\delta_b(r_2-r_1-\delta_b)}\end{cases} \tag{11}$$

where ε_{cw1} is the relative permittivity of the composite dielectric made up of the air and the bobbin.

The capacitance C_{cw1} can be calculated by substituting (11) into (10).

B. Calculation of C_{cw2}

This part of capacitance is between the outermost winding and the core side column. As the number of winding layers p increases, the outer radius r_3 of the winding gradually increases, resulting in C_{cw2} becoming non-negligible part of the core capacitance. The relevant parameters can be obtained by the following equations:

$$\begin{cases}h_{cw2}=h_c\\ d_{cw2}=r_4-r_3+\dfrac{d_o}{2}\\ r_{cw2}=r_3+\dfrac{d_{cw2}}{2}\\ \varepsilon_{cw2}=\dfrac{\varepsilon_a\varepsilon_t d_{cw2}}{\varepsilon_a\delta_t+\varepsilon_t(d_{cw2}-\delta_t)}\end{cases} \tag{12}$$

where ε_{cw2} is the relative permittivity of the composite dielectric formed by air and insulation tape.

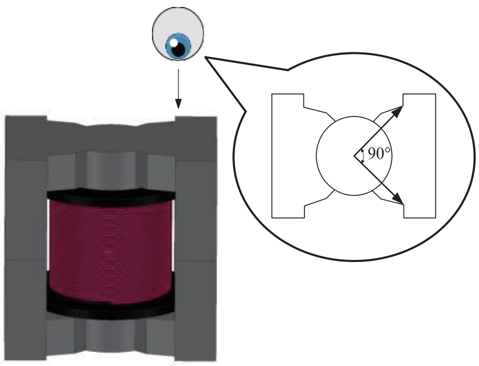

Fig. 9. PQ2625 inductor overhead view.

The weighting factor α_{cw2} in (10) depends on the degree of enclosure of the winding by the side column.

For most cores, the side columns are partially surrounded by the winding, rather than the entire 360° circumference of the winding. Fig. 9 shows an inductor with a PQ magnetic core, where the single side column enclosing the winding at an angle of 90°. Thus, the entire core side column surrounds the winding by 50%. For other types of cores, the weighting factor α_{cw2} need to be determined for specific structures. The parasitic capacitance C_{cw2} can be calculated by substituting (12) into (10).

C. Calculation of C_{cw3}

The capacitance C_{cw3} consists of winding to the top and bottom yokes, respectively. It increases with the number of winding layers p and the wire diameter d_o. The relevant parameters can be calculated by:

$$\begin{cases} \alpha_{cw3}=1 \\ A_{cw3}\approx\dfrac{\pi}{2}(r_3{}^2-r_2{}^2) \\ d_{cw3}=\dfrac{h_c-h_w}{2}+\dfrac{d_o}{2} \\ \varepsilon_{cw3}=\dfrac{\varepsilon_a\varepsilon_b d_{cw3}}{\varepsilon_a\delta_v+\varepsilon_b(\dfrac{h_c}{2}-\dfrac{h_w}{2}-\delta_v)} \end{cases} \tag{13}$$

where ε_{cw3} is the relative permittivity of the composite dielectric consisting of air and the bobbin. The parasitic capacitance C_{cw3} between the yoke and the winding can be calculated by substituting (13) into (10).

D. Normalization Factors $k_{cw1}, k_{cw2}, k_{cw3}$

When the leakage inductance is far smaller than the magnetizing inductance, the potential distribution of the winding can be regarded as linearly distributed along the height direction. The calculation process of C_{cw1} will be taken as an example. As shown in Fig. 10, the potential difference between the winding and the core at one terminal is U_{D1} and the potential difference between the winding and the core at the other end is U_{D2}, then the total energy stored in this capacitance can be expressed as:

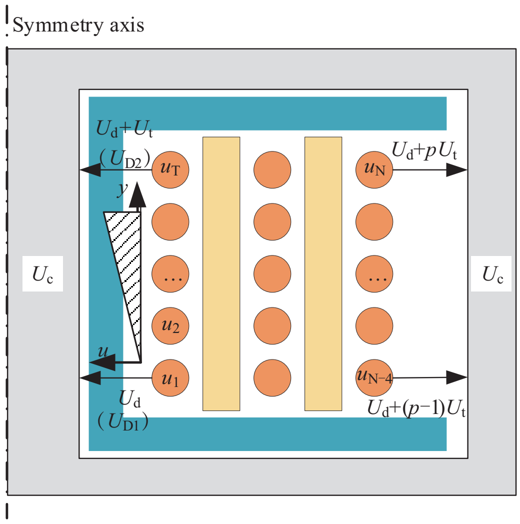

Fig. 10. Inductor winding potential distribution.

$$W=\frac{C_x}{6}(U_{D1}^2+U_{D1}U_{D2}+U_{D2}^2) \tag{14}$$

The energy stored on the parasitic capacitances C_{cw1}, C_{cw2} and C_{cw3} between each part of the core and the winding can be calculated according to (14), respectively:

$$\begin{cases} W_{cw1}=C_{cw1}\dfrac{3U_d^2+3U_dU_t+U_t^2}{6} \\ W_{cw2}=C_{cw2}\dfrac{3U_d^2+(6p-3)U_dU_t+(3p^2-3p+1)U_t^2}{6} \\ W_{cw3}=C_{cw3}\dfrac{6U_d^2+6pU_dU_t+(2p^2-p+1)U_t^2}{6} \end{cases} \tag{15}$$

where p is the number of winding layers and U_t is the voltage drop of the innermost layer.

The energy stored in the parasitic capacitance between each part of the core and the winding can be expressed as:

$$W_x=\frac{C_x}{2}(pU_t)^2 \qquad x=\text{cw1,cw2,cw3} \tag{16}$$

The Normalization factors k_{cw1}, k_{cw2}, k_{cw3} can be derived from (15) and (16):

$$\begin{cases} k_{cw1}=\dfrac{3k_U^2+3k_U+1}{3p^2} \\ k_{cw2}=\dfrac{3k_U^2+(6p-3)k_U+(3p^2-3p+1)}{3p^2} \\ k_{cw3}=\dfrac{6k_U^2+6pk_U+(2p^2-p+1)}{3p^2} \end{cases} \tag{17}$$

where k_U is the core potential factor, which will be analyzed in the following.

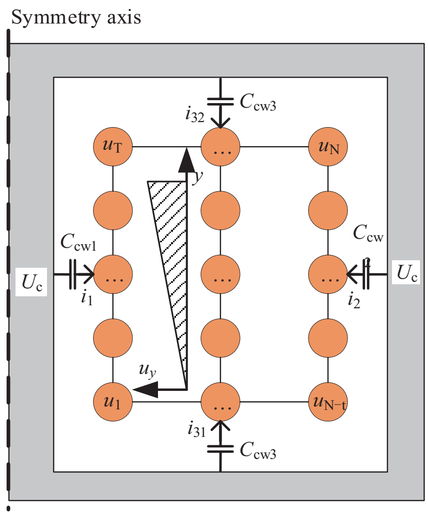

Fig. 11. System equivalent circuits for cores and winding.

E. Core Potential Coefficient

In order to calculate the stored electric energy in the core, the core potential should be solved. As shown in Fig. 11, the potential of each turn of the winding are provided. The calculation of center column capacitance, C_{cw1}, is used as an example. The potentials of the first and last turns of the first layer of the winding are U_1 and U_T, respectively. The potential at the height y of the innermost layer is given by:

$$U_y = U_1 + (U_T - U_1)\frac{y}{h_w} \tag{18}$$

The capacitance between the winding and the core at the height y is:

$$C_y = \alpha_{cw1}\varepsilon_0\varepsilon_{cw1}\frac{2\pi\,dy}{\ln(1+\dfrac{d_{cw1}}{r_{cw1}})} \tag{19}$$

Therefore, the displacement current i_1 flowing through the core from the innermost layer is:

$$i_1 = \int_0^{h_w}(U_y - U_c)C_y = \frac{U_1 + U_t - 2U_c}{2}C_{cw1} \tag{20}$$

Similarly, the displacement currents i_2, i_{31} and i_{32} flowing through the rest part of the core can be calculated as:

$$\begin{cases} i_2 = \dfrac{2U_1 + (2p-1)U_t - 2U_c}{2}C_{cw2} \\ i_{31} = \dfrac{2U_1 + (p-1)U_t - 2U_c}{2}C_{cw3} \\ i_{32} = \dfrac{U_1 + (p+1)U_t - 2U_c}{2}C_{cw3} \end{cases} \tag{21}$$

According to KCL law, the displacement current i_1, i_2, i_{31} and i_{32} meet the following relationship:

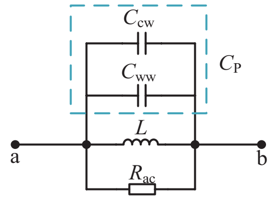

Fig. 12. Equivalent circuit of inductor.

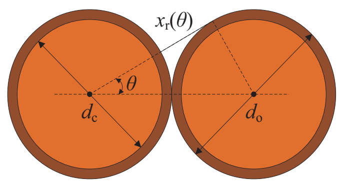

Fig. 13. Radial extension of electric field lines.

$$i_1 + i_2 + i_{31} + i_{32} = 0 \tag{22}$$

According to (18)–(22), the core potential U_c can be solved as:

$$U_c = U_1 + \frac{C_{cw1} + (2p-1)C_{cw2} + 2pC_{cw3}}{2C_{cw1} + 2C_{cw2} + 4C_{cw3}}U_t \tag{23}$$

Based on (18)–(23), the core potential coefficient k_U in (17) is calculated as:

$$\begin{aligned} k_U &= \frac{U_d}{U_t} = \frac{U_1 - U_c}{U_t} \\ &= -\frac{C_{cw1} + (2p-1)C_{cw2} + 2pC_{cw3}}{2C_{cw1} + 2C_{cw2} + 4C_{cw3}} \end{aligned} \tag{24}$$

By calculating the parasitic capacitance and normalization factors between each part of the core and the winding and applying (9), the total capacitance C_{cw} between the core and the winding can be obtained.

As shown in Fig. 12, since the parasitic capacitance C_{cw} and C_{ww} are gauged to the input terminals of the inductor, the parasitic capacitance C_{cw} and C_{ww} are in parallel. The total parasitic capacitance C_p of the inductor satisfies the following relationship:

$$C_P = C_{cw} + C_{ww} \tag{25}$$

IV. The Effect of Electric Field Path

A. Type of Electric Field Line Model

The electric field distribution between adjacent turns affects the size of the parasitic capacitance. As shown in Fig. 3, the existing calculation method of turn-to-turn capacitance uses a straight line to represent electric field lines [15]. As shown in

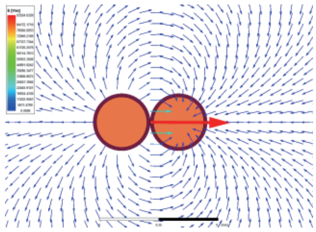

Fig. 14. Electric field line distribution of adjacent turns.

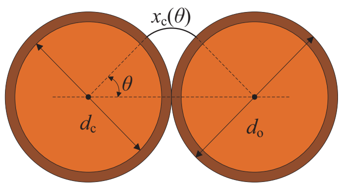

Fig. 15. Arc model of electric field line.

Fig. 13, [16] proposes an electric line model for capacitance calculations assuming that the electric field line extend in the radial direction right up to the surfaces of adjacent turn.

According to geometric analysis, the expression for the path length of this model can be derived as:

$$x_r(\theta) = d_o\left(\cos\theta \pm \sqrt{\cos^2\theta - \frac{3}{4} - \frac{1}{2}}\right) \tag{26}$$

Fig. 14 shows the distribution of the electric field lines between adjacent turns. It can be noticed that the electric field line is not a straight line but an arc.

Comparing Figs. 13 and 14, it is clear that the simulated electric field line profiles are quite different from the straight-line assumption as well as the radial-extension assumption. Therefore, the expression in (5) and (26) cannot accurately characterize the electric field distribution between the adjacent turn. Therefore, [17] proposes an arc model to represent the distribution of the electric field line, as shown in Fig. 15.

The path length of the electric field lines for the arc model can be expressed as:

$$x_c(\theta) = \frac{d_o(1-\cos\theta)}{2\sin\theta} \tag{27}$$

However, compared to the simulated electric field lines shown in Fig. 14, there is a discrepancy between the arc model and the electric field lines, which lead to a large error in the calculation of the turn-to-turn capacitance. The detail comparisons will be provided in the experimental section.

The micro-arc model used in this paper is shown in Fig.16, and its corresponding expression is:

$$x_m(\theta)=\theta\, d_o \tan\frac{\theta}{2} \tag{28}$$

In order to verify the accuracy of these four electric

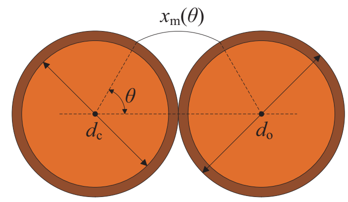

Fig. 16. Micro-arc model of electric field line.

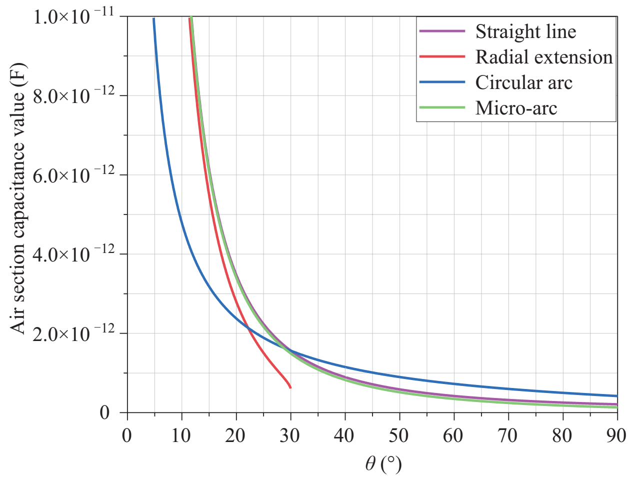

Fig. 17. Air capacitance calculation with four models.

TABLE I
COMPARISON OF CALCULATION RESULTS

Model	Calculation/pF	Simulation/pF	Relative error/%
Straight line	4.465		4.503
Radial	3.235	4.273	24.292
extension Arc	4.026		5.780
Micro-arc	4.316		0.996

field line models on the results of turn-to-turn capacitance calculations, enameled wires, with d_o=0.34 mm, d_c=0.3 mm, are used as the study object for capacitance calculations. The calculation results are shown in Fig. 17. It can find that the radial extension of electric field line model is only applicable for $0° \leqslant \theta \leqslant 30°$. This is because when $\theta > 30°$, the electric field lines extend to infinity. The air capacitance only has a value at $0° \leqslant \theta \leqslant 30°$. However, compared to the simulation results shown in Fig. 14, there are electric field lines at $30° < \theta \leqslant 90°$. This leads to a large deviation.

For the arc model, it is significantly different from the other three model in the range $0° \leqslant \theta \leqslant 90°$. The difference between parasitic capacitance calculated by using straight line model and micro-arc model is tiny in the range of $0° < \theta \leqslant 90°$, and the accuracy between the two models needs to be further analyzed.

Table I shows the comparison results of the turn-to-turn capacitance. It can be found that the errors in the calculation results of the straight-line model and micro-arc model are

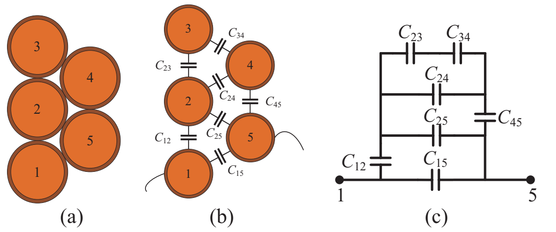

Fig. 18. Staggered winding structure. (a) Section view, (b) Turn-to-turn capacitance, (c) Equivalent circuit .

smaller than the those of the other two models, with relative errors of 4.49% and 0.99%, respectively. Since the micro-arc electric field line model represent the electric field line distribution between adjacent turns more precisely, the calculation error is smaller compared to the use of the straight-line model.

B. Impact of Integration Domain

For single-layer windings, the domain of integration chosen for the calculation of the turn-to-turn capacitance is [−90°, 90°], which is determined by the actual electric field line distribution. For theoretical calculations, the choice of too large or too small integration domain will bring large errors to the calculation results. For multilayer staggered windings, the staggered arrangement of the conductors leads to a change in the electric field distribution between adjacent turns compared to single-layer windings. Therefore, the selection of the integration domain has a significant influence on the accuracy of the calculation results.

Fig. 18(a) shows a staggered winding structure, and with the corresponding turn-to-turn capacitance distribution shown in Fig. 18(b). Fig. 18(c) shows the equivalent circuit for the turn-to-turn capacitance.

If the integration domain is the same as that of the single-layer winding, i.e., [−90°, 90°], the turn-to-turn capacitance is 4.465 pF. In order to verify the influence of the integration domain on the calculation results, 2D FEM simulation is used for the verification as shown in Fig. 18(a). The capacitance C_{15} given by simulation is 3.968 pF. The relative error between the calculation and the simulation is 12.5%. The error is due to the fact that coils numbered #1 and #5 are affected by coil #2, which changes the distribution of electric field between coils #1 and #5.

To minimize this part of the error, the upper part of the integration domain is [0°, 30°], while the lower part of the integration domain is [−90°, 0°]. Therefore, when calculating the turn-to-turn capacitance between coils #1 and #5, the integration domain is chosen as [−90°, 30°].

Based on the above considerations, the calculation result is 3.9572 pF with a relative error of 0.2611%. Similarly, Table II gives the capacitance between any two turns. According to the equivalent circuit shown in Fig.18(c), the lumped capacitance of the winding can be calculated as 6.312 pF. The simulation result is 6.299 pF. As a result, the relative error of the calculation is only 0.207%.

TABLE II
TURN-TO-TURN CAPACITANCE

Capacitor	Simulation capacitance value /pF	Calculated value/pF	Relative error /%
C_{12}	3.9454	3.9572	0.2991
C_{15}	3.9675	3.9572	0.2611
C_{23}	3.9497	3.9572	0.1901
C_{24}	3.3503	3.4489	2.4991
C_{25}	3.3486	3.4489	2.5422
C_{34}	3.9592	3.9572	0.0507
C_{45}	4.2035	4.1045	2.5093
C_{in}	6.2990	6.3120	0.2064

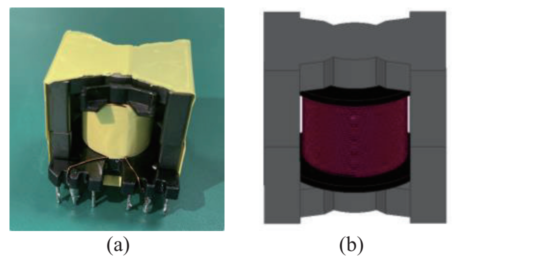

Fig. 19. Wire-wound inductor with PQ magnetic core. (a) Prototype, (b) Simulation model.

TABLE III
WINDING STRUCTURE PARAMETER

Parameter	Symbol	Unit	Value
Turns	n	-	36
Layers	p	-	1
Diameter (without insulation layer)	d_c	mm	0.3
Diameter (with insulation layer)	d_o	mm	0.34
Length of per turn	l_t	mm	47.2

If the integral domain [−90°, 90°] is still used in the calculation of turn-to-turn capacitance, the lumped capacitance is 7.213 pF, which results in a relative error of 12.668%. Therefore, the accuracy of the proposed calculation method can be improved by 12.461%. The proposed calculation method is applicable to any winding arrangement. Hence, the calculation method is the same for the inductors with different winding methods. Besides, different winding arrangements of inductor can result in varying parasitic capacitance, but the calculation method is the same.

Based on the above analysis, the selection of the integration domain is another key factor that affects the calculation error of parasitic capacitance.

V. EXPERIMENTAL VERIFICATION

In order to verify the accuracy of the proposed parasitic capacitance calculation method, an inductor was wound as shown in Fig. 19(a) and its detail specifications are listed in Table III. Fig. 19(b) shows the simulation model of the inductor used to validate the proposed calculation method. Combining (2)–(8),

TABLE IV
CALCULATION PARAMETERS FOR MAGNETIC CORE RELATED CAPACITORS

Parameters	Symbol	Unit	Value
Radius of central column	r_1	mm	6
Distance from center axis to winding	r_2	mm	7.35
Type thickness	δ_t	mm	0.05
Relative dielectric constant of type	ε_t	-	3
Core window height	h_c	mm	20.55
Relative dielectric constant of bobbin	ε_b	-	3
Thickness of bobbin	δ_b	mm	0.67
Radius of winding	r_3	mm	7.69
Radius of side column	r_4	mm	11
Skeleton thickness	δ_v	mm	1.05
Winding height	h_w	mm	12.24

the turn-to-turn capacitance C_{tt} can be calculated to be 4.465 pF. Further, based on the energy conversion rule, the total winding capacitance C_{in} is calculated to be 0.1276 pF.

Based on the core-related parameters indicated in Fig. 8, the core-related parameters are calculated as shown in Table IV, where the weighting factors are α_{cw1}=1, α_{cw2}=0.5, α_{cw3}=1. According to (9)−(24), the capacitance C_{cw} can be calculated as 0.954 pF. Further, the total parasitic capacitance of the inductor can be calculated as 1.082 pF by (25).

Manufactured inductors made of different core materials demonstrate different impedance characteristics due to different permeability. When the permeability is enough high, it only impacts the value of the inductance and it does not influence the value of parasitic capacitance. The parasitic capacitance is determined by the electric field distribution and is independent of the permeability. When the permeability is too low, the magnetic flux linkage differs between each turn of the winding is different, leading to a variation in the winding's potential distribution. In this case, the permeability affects the value of the parasitic capacitance.

In order to verify the analysis, Fig. 20 show the comparison results of the impedance characteristics under different permeability value. Table V lists the corresponding inductance and capacitance values. It can be clearly observed that as permeability increases, inductance also increases. The parasitic capacitance remains unchanged under different permeability, as shown in Fig. 20 and Table V.

For inductors with or without air gaps, the parasitic capacitances of the windings are identical in both cases. The inductance of an inductor is determined by the length of the air gap. When the permeability is sufficiently high, the magnetizing flux is far larger than the leakage flux. This means that the flux linkage each turns of the winding is the same. The voltage potential distribution across the winding remains linear and continuous unaffected by changes in air gap length.

Fig. 21 shows the impedance test platform for the tested

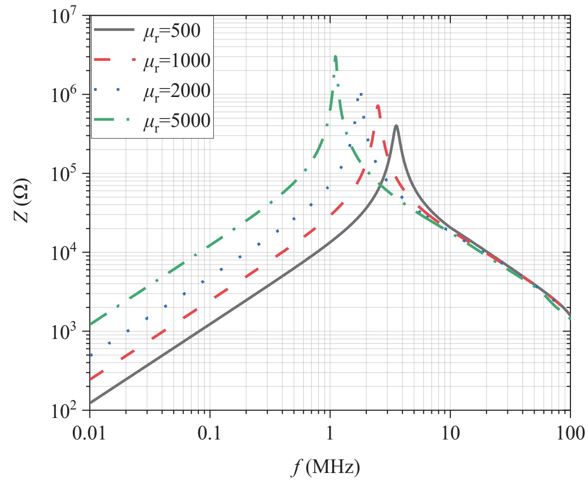

Fig. 20. Impedance characteristic versus under different permeability.

TABLE V
INDUCTANCE AND CAPACITANCE

Relative permeability	Inductance/mH	Resonant frequency/MHz	Capacitance/pF
500	1.955	3.565	1.030
1000	3.881	2.489	1.054
2000	7.736	1.754	1.064
5000	19.305	1.117	1.052

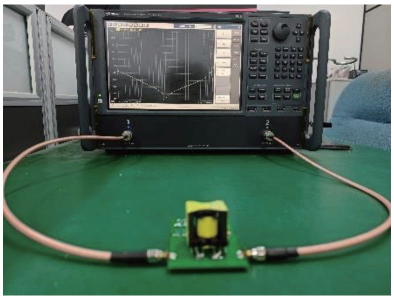

Fig. 21. Two-port test of network analyzer.

inductor, where a network analyzer, KEYSIGHT E5080A, is used to measure S-parameters and convert them into Z-parameters through post-processing. Firstly, the S-parameter test is performed under the two-port measurement in the frequency range of 100 kHz to 100 MHz. Then the impedance characteristic curve versus frequency of the inductor is obtained by converting the S-parameter to the Z-parameter.

The transformed impedance curve of the tested inductor is shown in Fig. 22 indicated by red solid line. The simulated impedance curve is also shown as green dashed line in Fig. 22. It can be found that the simulated parasitic capacitance of the inductor calculated from the resonance point location is 1.054 pF. As a result, the error between the calculated and simulated value is only 2.657%. Similarly, the measured parasitic capacitance is 1.03 pF.

As shown in Fig. 22, the resonant frequency point of the measured impedance, simulated impedance and the calculated

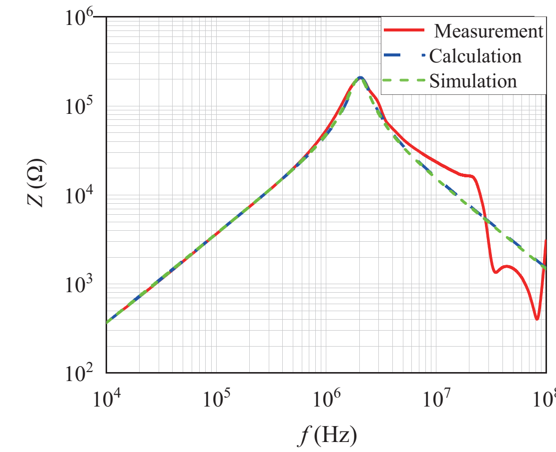

Fig. 22. Comparison of impedance curves.

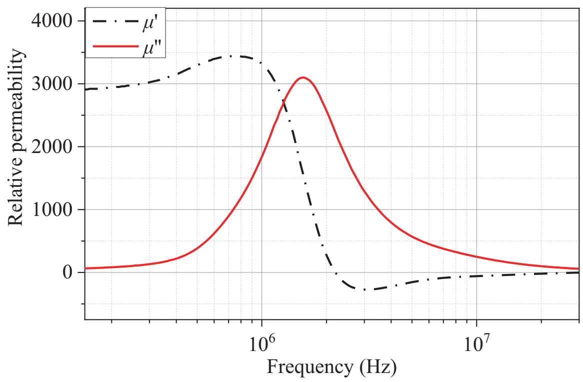

Fig. 23. Complex permeability of magnetic core.

impedance agree very well. The calculated results have a relative error 5.05% compared the measured results. Due to the unavoidable manual winding deviation during the actual winding process, the winding structure parameters of the actual inductor, such as the distance between the winding and each part of the magnetic core, the distance between the winding turns, etc., differ from the theoretical calculation results. The structure parameters of the simulation model are the same as those of the theoretical calculation. Therefore, the deviation between simulation and theoretical calculation is smaller than the deviation between measurement and theoretical calculation. The reason why the measured impedance does not conform well with the calculation results in the high frequency range is due to the influence of permeability variation with frequency. As shown in Fig. 23, it can be observed that when the frequency is higher than 1 MHz, the real portion of permeability decreases rapidly, leading to significant variations between magnetizing flux and leakage flux. Consequently, when the permeability is sufficiently low, the potential distribution along each turn is influenced by the frequency-dependent permeability. This causes parasitic capacitance variations as a function of frequency.

The proposed calculation method can be used to quickly calculate the parasitic capacitance as the calculation error is still within reasonable limits. The FEM simulation results used in this paper is to verify the accuracy of the proposed calculation method. Compared with the FEM simulation method, the proposed calculation method has merit of computational efficiency and solution speed.

In this paper, the influence of temperature on parasitic capacitance is neglected. This is because that when the temperature is lower than curie temperature, the permeability is larger enough. For this consideration, the flux linkage each turn of the winding is the same. Then, the potential distribution along each winding can be regarded as linearly and continuedly. Hence, the temperature does not affect the parasitic capacitance of the inductor.

In summary, the calculation method in this paper can predict the parasitic capacitance of inductors more accurately and efficiently and guide the optimization of parasitic capacitance.

VI. Conclusion

This paper discusses the theoretical calculation of inductor parasitic capacitance. The conclusions are as follows.

1. The electric filed distribution between adjacent turns determines the value of parasitic capacitance. A proper integral line model and integration domain can improve the accuracy of parasitic capacitance prediction.
2. The parasitic capacitance between the magnetic core and the winding is divided into several areas to calculate the total parasitic capacitance.
3. Compared with the finite element simulation, the proposed calculation method has a faster solving speed, and the error between the calculated results and the measured results is kept within 5.05%.

References

[1] J. He, Y. Liu, D. Bi, and X. Li, "Review of conducted electromagnetic interference suppression strategies for switching converters," in *Transactions of China Electrotechnical Society*, vol. 37, no. 6, pp. 1455–1472, Mar. 2022.

[2] W. Shen, F. Wang, D. Boroyevich, and C. W. Tipton IV, "High-density nanocrystalline core transformer for high-power high-frequency resonant converter," in *IEEE Transactions on Industry Applications*, vol. 44, no. 1, pp. 213–222, Jan.-Feb. 2008.

[3] Y. Gao, V. Sankaranarayanan, E. M. Dade, Y. Zhou, F. Zhou, R. W. Erickson, and D. Maksimović, "Modeling and design of high-power, high-current-ripple planar inductors," in *IEEE Transactions on Power Electronics*, vol. 37, no. 5, pp. 5816–5832, May 2022.

[4] Y. Lan, X. Zeng, W. Chen, and Q. Chen, "High-frequency model of common-mode choke in electromagnetic interference filters," in *Transactions of China Electrotechnical Society*, vol. 40, no. 6, pp. 1–11, Mar. 2025.

[5] L. Gao, C. Xu, G. Dong, C. Gong, and F. Zhang, "Common mode electro-magnetic interference modeling method of planar transformers based on CST software and its application," in *Transactions of China Electrotechnical Society*, vol. 35, no. 24, pp. 5057–5563, Dec. 2020.

[6] B. Ahmad, P. Jayathurathnage, W. Martinez, and J. Kyyrä, "Parameter extraction technique for evaluation of inductive and capacitive elements of three-winding coupled inductor," in *IEEE Journal of Emerging and Selected Topics in Industrial Electronics*, vol. 3, no. 3, pp. 616–625, Jul. 2022.

[7] G. Grandi, M. K. Kazimierczuk, A. Massarini, and U. Reggiani, "Stray capacitances of single-layer solenoid air-core inductors," in *IEEE Transactions on Industry Applications*, vol. 35, no. 5, pp. 1162–1168, Sept.-Oct. 1999.

[8] W. Shen, "Design of high-density transformers for high-frequency high-power converters," Ph.D. dissertation, Virginia Polytechnic Institute

and State University, 2006.

[9] K. Nguyen-Duy, Z. Ouyang, A. Knott, and M. A. E. Andersen, "Minimization of the transformer inter-winding parasitic capacitance for modular stacking power supply applications," in *2014 16th European Conference on Power Electronics and Applications*, Lappeenranta, Finland, 2014, pp. 1–10.

[10] A. Roc'h, H. Bergsma, D. Zhao, B. Ferreira, and F. Leferink, "A new behavioural model for performance evaluation of common mode chokes," in *2007 18th International Zurich Symposium on Electromagnetic Compatibility*, Munich, Germany, 2007, pp. 501–504.

[11] S. W. Pasko, M. K. Kazimierczuk, and B. Grzesik, "Self-capacitance of coupled toroidal inductors for EMI filters," in *IEEE Transactions on Electromagnetic Compatibility*, vol. 57, no. 2, pp. 216–223, Apr. 2015.

[12] Qin Yu and T. W. Holmes, "A study on stray capacitance modeling of inductors by using the finite element method," in *IEEE Transactions on Electromagnetic Compatibility*, vol. 43, no. 1, pp. 88–93, Feb. 2001.

[13] Z. De Grève, O. Deblecker, and J. Lobry, "Numerical modeling of capacitive effects in HF multiwinding transformers—part I: A rigorous formalism based on the electrostatic equations," in *IEEE Transactions on Magnetics*, vol. 49, no. 5, pp. 2017–2020, May 2013.

[14] M. Popov, R. P. P. Smeets, L. van der Sluis, H. de Herdt, and J. Declercq, "Experimental and theoretical analysis of vacuum circuit breaker prestrike effect on a transformer," in *IEEE Transactions on Power Delivery*, vol. 24, no. 3, pp. 1266–1274, Jul. 2009.

[15] A. Massarini and M. K. Kazimierczuk, "Self-capacitance of inductors," in *IEEE Transactions on Power Electronics*, vol. 12, no. 4, pp. 671–676, Jul. 1997.

[16] X. Liu, Y. Wang, J. Zhu, Y. Guo, G. Lei, and C. Liu, "Calculation of capacitance in high-frequency transformer windings," in *IEEE Transactions on Magnetics*, vol. 52, no. 7, pp. 1–4, Jul. 2016.

[17] M. Kovacic, Z. Hanic, S. Stipetic, S. Krishnamurthy, and D. Zarko, "Analytical wideband model of a common-mode choke," in *IEEE Transactions on Power Electronics*, vol. 27, no. 7, pp. 3173–3185, Jul. 2012.

Jiangtao Tu was born in Datian, Fujian, in 2001. He is presently working towards his M.S. degree in the College of Electrical Engineering and Automation, Xiamen University of Technology, Xiamen, China. His current research interest includes electromagnetic interference in power converters.

Kaining Fu was born in Xiamen, China, in 1993. He received his M.S. and Ph.D. degrees from Fuzhou University, Fuzhou, China, in 2018 and 2021, respectively. He is presently working as a Lecturer in the College of Electrical Engineering and Automation, Xiamen University of Technology, Xiamen, China. He is a member of the Magnetic Technology Committee of the China Power of Supply Society (CPSS). His current research interests include power conversion, high-frequency magnetics, EMI debugging and solutions, and electromagnetic field analysis and applications.

Wei Chen was born in Fuzhou, China. He received his M.S. and Ph.D. degrees from Fuzhou University, Fuzhou, China, in 1987 and 1990, respectively. He worked as a Senior Visiting Professor in the Center for Power Electronics Systems (CPES), Virginia Tech, Blacksburg, Virginia, USA, from 1996 to 1998. He was with Delta Electronics Co., Ltd., as a R&D manager in the Delta Power Electronics Center, Shanghai, China, from 1999 to 2008. He has published more than 80 technical papers, including IEEE transactions and proceedings. He has held more than 40 approved patents in China and the USA. His current research interests include power conversion, high-frequency magnetic technology, EMI debugging and solutions, wireless power transfer, and electromagnetic field analysis and its applications. Professor Chen is an executive member of the council of the China Power of Supply Society (CPSS) and he served as chairman of the Magnetic Component Specialty Committee of the CPSS.

Yanhui Qiu was born in Sanming, China, in 1988, received the Ph.D. in Electrical Engineering and Automation College of Fuzhou University in 2017. He is presently working as a Lecturer in the Xiamen University of Technology in 2023. His current research interests include power electronic technology and new energy generation technology.

IEEE PEAS 2025

The 3rd IEEE International Power Electronics and Application Symposium

November 7–10, 2025 Shenzhen, China

Call for Papers

Honorary Chairs
Fred C. Lee, *Virginia Tech.*
Dehong Xu, *Zhejiang Univ.*

General Chair
Jinjun Liu, *Xi'an Jiaotong Univ.*

Technical Program Chairs
Wuhua Li, *Zhejiang Univ.*
Kai Sun, *Tsinghua Univ.*
Jiabing Hu, *Huazhong Univ. of Sci. and Tech.*
Xiaoqiang Guo, *Yanshan Univ.*
Chris Mi, *San Diego State University*
Pedro Rodriguez, *Universitat Politècnica de Catalunya*
Luiz Henrique Silva Colado Barreto, *Federal University of Ceará*
Fei Gao, *University of Technology of Belfort-Montbeliard*
Henry Chung, *City Univ. of Hong Kong*
Ningyi Dai, *Univ. of Macau*
Sanjib Panda, *National Univ. of Singapore*
Jung-Ik Ha, *Seoul National Univ.*
Junichi Itoh, *Nagaoka Univ. of Tech.*
Chushan Li, *Zhejiang Univ.*

Tutorial Committee Chairs
Xinbo Ruan, *Nanjing Univ. of Aeronautics and Astronautics*
Pinjia Zhang, *Tsinghua Univ.*
Yijie Wang, *Harbin Univ. of Tech.*

Industry Session Committee Chairs
Jinfa Zhang, *Delta Electronics*
Junming Zhang, *Zhejiang Univ.*
Yaojie Sun, *Fudan Univ.*

Organization Committee Chair
Hao Ma, *Zhejiang Univ.*

Global Submit Committee Chair
Xiaoming Yuan, *Huazhong Univ. of Sci. and Tech.*

Special Activity Committee Chair
Xiong Du, *Chongqing Univ.*

Publications Committee Chair
Hao Ma, *Zhejiang Univ.*

Sponsored by

China Power Supply Society
IEEE Power Electronics Society

Technical Sponsores
Guangdong Power Supply Society

Secretariat of PEAS 2025
Email: peas@cpss.org.cn
Phone: +86-22-83575728、27686709
Fax: +86-22-27687886
Address: China Power Supply Society
10th Floor, Datong Building, No.467 Huanghe Road, Nankai District, Tianjin, 300110, China

IEEE International Power Electronics and Application Symposium (PEAS) is an international symposium for presentation and discussion of the state-of-the-art in power electronics, energy conversion and its applications. The IEEE PEAS 2025 is the third meeting of PEAS, which will be held in Shenzhen, China, during November 7-10, 2025. The 4th China Power Electronics and Energy Conversion Congress and Exposition & The 28th China Power Supply Society Conference will be held during the PEAS 2025.

The worldwide power electronic industry, research, and academia are cordially invited to participate in an array of presentations, tutorials, and social activities for the advancement of science, technology, engineering education, and fellowship. Technical interests of the symposium include, but are not limited to:

- **Advanced DC/DC converters and Power Factor Correction Converters**
- **Advanced DC/AC Inverter Topologies, Modulations, and Controls**
- **Advanced Control, Modeling, Simulation, and Stability of Power Electronics Systems**
- **Advanced Power Devices (Si, SiC, GaN devices etc) and Their Applications**
- **Magnetics, EMI, Passive Integration and Digital Manufacture Technology**
- **Reliability, Diagnosis, Prognosis and Protection of Power Electronics**
- **Conversion and Control Technologies for Renewable Energy and Storage Systems**
- **Power Electronics for Transmission and Distribution**
- **Power Electronics for Motor Drives and Transportations**
- **Power Electronics for Converter Dominated Grid-Forming Power System**
- **Power Electronics for Wireless Power Transfer**
- **Power Electronics for Data Centers, Consumer Electronics, Energy Harvesting, Power ICs, etc.**
- **Power-to-X and Green Hydrogen Energy Systems**
- **Big Data, Artificial Intelligence, and Security in Power Electronics Systems**
- **Invited Topics and Emerging Topics in Power Electronics**

Paper Submission

The working language of the symposium is English. Prospective authors are invited to electronically submit digests of their work in English (Maximum 6 pages in double space, in pdf format), following the instructions available on the website: http://peas.cpss.org.cn/. The digest is a summary of your paper including the digest title, abstract, digest text and references.
Accepted and presented papers will be published in the symposium proceedings, and submitted to the IEEE Xplore on-line digital library and EI Compendex.

Important Deadlines

Submission of digests	**Jun. 30th, 2025**
Submission of Industry Session	**Jul. 15th, 2025**
Submission of Tutorial	**Jul. 15th, 2025**
Notification of paper acceptance	**Aug. 15th, 2025**
Submission of final papers	**Sept. 15th, 2025**

For more information: peas.cpss.org.cn


Welcome to Shenzhen China

Shenzhen, a dynamic metropolis in southern China adjacent to Hong Kong, is celebrated as the “Silicon Valley of China” and the “Window of Reform”. From a humble fishing village to a global innovation powerhouse, its meteoric rise mirrors China’s modernization miracle.

As a vibrant metropolis, Shenzhen blends modernity with natural beauty. Skyscrapers like Ping An Finance Centre contrast with lush parks and coastline. Must-visit spots include Window of the World, Shenzhen Bay Park, OCT-LOFT Creative Culture Park, Dapeng Ancient Fortress, and Lianhua Mountain Park, where innovation meets history and greenery.

Shenzhen is also a culinary hotspot, offering Cantonese delicacies, international cuisine, and bustling night markets. Don’t miss its iconic seafood and innovative fusion dishes.

Beyond its role as an economic powerhouse, the city hosts cultural gems like Design Society and Shenzhen Museum, showcasing its pioneering spirit. While engaging in symposium activities, we encourage you to explore Shenzhen’s dynamic culture, cutting-edge tech scene, and coastal charm. Welcome to experience the energy of this "City of the Future"!

■ More Participation Opportunities

Tutorials

Several high-quality tutorials will be offered on Friday, November 7, 2025.
Prospective lecturers are invited to send a proposal before July 15, 2025 to the Tutorial Chair: Xinbo Ruan, on https://jsj.top/f/Ztxd8O
The proposal should be including:

- Tutorial title
- Name, affiliation, and short bio(s) of the lecturer(s)
- Objectives and audience
- Synopsis

Industry Session Presentations

In order to strengthen the cooperation among industries with academics, PEAS 2025 will arrange industry sessions during the symposium. Speakers are invited to make a presentation only without submitting a formal paper. These presentations will be included in the PEAS 2025 symposium proceeding. Each presentation should be limited within 30 minutes (25 minutes for presentation, plus 5 minutes for Q&A). We seek technical presentations rather than marketing-oriented talks.
Please submit the proposal before July 15, 2025 to https://jsj.top/f/tqdMih including:

- Title of the presentation
- Summary of the presentation content
- Description of the target audience
- Short professional biography of the speaker

Other wonderful content

- **Plenary Session:** Leading experts from academia, industry, and research institutes will be invited to share their insights on technology developments and future trends.
- **Other Events:** The 4th China Power Electronics and Energy Conversion Congress and Exposition & The 28th China Power Supply Society Conference, the 11th Student Design Competition on Power Electronics, Award ceremony of CPSS Science and Technology Award, Young Professional forum, Power supply Engineer in Women forum will be held during the PEAS 2025.

CHINA POWER SUPPLY SOCIETY

China Power Supply Society (CPSS) founded in 1983 is a nonprofit, non-governmental academic and professional organization of scientists and engineers in the power supply & power electronics fields. CPSS is dedicated to achieving scientific and technological progress of power supply and the advancement of the power supply industry. CPSS website is www.cpss.org.cn.

CPSS TRANSACTIONS ON
POWER ELECTRONICS AND APPLICATIONS

(Quarterly, Started in 2016)

Vol. 10 No. 2 Jun. 30, 2025

Sponsored by: China Power Supply Society (CPSS)

Technically Co-Sponsored by: IEEE Power Electronics Society (IEEE PELS)

Supported by: Sungrow Power Supply Co., Ltd.
Xiamen Kehua Hengsheng Co., Ltd.
Shenzhen Inovance Technology Co., Ltd.
StarPower Semiconductor Ltd.

Editor-in-Chief: Jinjun Liu

Published by: Editorial Office of CPSS TPEA

Address: 10th Floor, Datong Building, No. 467 Huanghe Road,
Nankai Dist., Tianjin, 300110, China

Tel: +86-22-27680796-18#

Fax: +86-22-27687886

E-mail: tpea@cpss.org.cn

Website: tpea.cpss.org.cn